Numerical simulation of drop impact and evaporation on superheated surfaces at low and high ambient pressures

Schlawitschek, Christiane

(2020)

Numerical simulation of drop impact and evaporation on superheated surfaces at low and high ambient pressures

Dissertation
Christiane Schlawitschek

TECHNISCHE
UNIVERSITÄT
DARMSTADT

Numerische Simulation von Tropfenaufprall und -verdampfung auf geheizten Oberflächen bei niedrigem und hohem Umgebungsdruck

Numerical simulation of drop impact and evaporation on superheated surfaces at low and high ambient pressures

Doctoral thesis
by Christiane Schlawitschek

submitted in fulfillment of the requirements for the
degree of Doktoringenieur
(Dr.-Ing.)

at the Department of Mechanical Engineering
of the Technische Universität Darmstadt

First Examiner:	Apl. Prof. Dr. Tatiana Gambaryan-Roisman
Second Examiner:	Prof. Dr.-Ing. Peter Stephan
Third Examiner:	Prof. Dr.-Ing. Christian Hasse

Darmstadt 2020

Christiane Schlawitschek:
Numerical simulation of drop impact and evaporation on superheated surfaces at low and high ambient pressures

Darmstadt, Technische Universität Darmstadt

Date of oral exam: November 3, 2020
Thesis published online on TUprints in 2020

Please cite this thesis as:
URN: urn:nbn:de:tuda-tuprints-118001
URL: https://tuprints.ulb.tu-darmstadt.de/11800

Danksagung

Die vorliegende Ausarbeitung entstand während meiner Anstellung als wissenschaftliche Mitarbeiterin am Institut für Technische Thermodynamik der Technischen Universität Darmstadt. Ich bedanke mich herzlich bei Herrn Prof. Peter Stephan für die Möglichkeit, diese Arbeit an seinem Institut durchführen zu können, sein kontinuierliches Vertrauen in mich und meine Arbeit, für den mir eingeräumten Freiraum sowie für die vielen fachlichen und fachübergreifenden Gespräche und Ratschläge. Des Weiteren bedanke ich mich herzlich bei Frau Apl. Prof. Tatiana Gambaryan-Roisman für die engagierte Betreuung, ideenreiche Impulse und ein stets offenes Ohr für wissenschaftliche Herausforderungen. Das äußerst positive Arbeitsklima am Institut und in der Forschungsgruppe waren wichtige Voraussetzungen für das Gelingen dieser Arbeit. Ebenfalls gilt mein herzlicher Dank Prof. Christian Hasse für die Übernahme des Koreferats.

Darüber hinaus möchte ich mich bei jenen Personen bedanken, die mich während meines Studiums und der parallelen HiWi-Tätigkeit an der Brandenburgischen Technischen Universität Cottbus betreut und mir geholfen haben, meine Freude an der Thermodynamik zu erkennen und zu erhalten, insbesondere Herrn Prof. Fabian Mauß. Während dieser Zeit konnte ich wertvolle Erfahrungen sammeln, die deutlich über eine normale Wissensvermittlung im Studium hinausgingen.

Mein herzlicher Dank gilt Dr. Daniel Rettenmaier, Dr. Daniel Deising, Benjamin Franz, Thomas Antritter und Yun Ouedraogo für den fachlich wertvollen Austausch bei regelmäßigen Numerik-Kolloquien. Ebenfalls möchte ich mich herzlich bei meinen Studenten Pascal Steffens, Kilian Köbschall und Simon Homes bedanken, die mit ihren Arbeiten wertvolle Impulse geliefert haben.

Ich möchte mich bei meinen Kolleginnen und Kollegen am TTD für die gute Arbeitsatmosphäre am Institut bedanken. Zahlreiche fachliche und darüber hinausgehende Gespräche waren in der Zeit am Institut prägend für mich ebenso wie die Einstellung, Probleme nicht hinzunehmen, sondern sie gemeinsam zu diskutieren und zu lösen. Dies gilt insbesondere für Dr. Felix Crößmann, Dr. Axel Sielaff, Dr. Jochen Dietl, Dr. Martin Still, Dr. Timm Winterling, Dr. Niklas Preußer, Dr. Achim Bender und Dr. Axel Dietrich. Ein besonderer Dank gilt den drei Letztgenannten für die Durchsicht der Ausarbeitung, welche jeweils mit größter Sorgfalt durchgeführt und äußerst konstruktiv kommuniziert wurde.

Bei meiner Familie, ganz besonders bei meinen Eltern, möchte ich mich für die Unterstützung, den Rückhalt und Freiraum in allen Lebenslagen ganz herzlich bedanken. Sie haben mich gefördert und angespornt und somit den Weg zur Promotion geebnet.

Abstract

Abstract

This thesis presents the numerical simulation of fluid dynamics, as well as heat and mass transfer for drop impingement on a hot solid surface for low and high ambient pressures. The technical application ranges from effective thermal management strategies using spray cooling, safety aspects in high pressure nuclear reactors to process technology in chemical or food industry.

It is reported in literature that wetting characteristics depend on the ambient pressure. Drop splash is suppressed at low ambient pressure. High ambient pressure encourages compressibility effects. The compressibility of both the liquid and vapour phase increases with increasing pressure. Thereby, the effects of compressibility on drop impingement is of interest. Up to now, no attempt has been made to investigate a full pressure range for the evaporative drop impingement process.

In order to provide insights into evaporative drop impingement processes under various ambient pressures, numerical simulations are performed. CFD simulations are conducted using a finite volume discretisation method solving the Navier-Stokes equations. The volume of fluid method is utilised to resolve two-phase flow. The solver accounts for compressible fluid flow, heat and mass transfer due to evaporation across the free liquid-vapour interface, evaporation in the vicinity of the three-phase contact line, as well as for heat conduction within the solid substrate. The dynamic contact angle is implemented using a subscale model. Effects of low and high ambient pressure on the three-phase contact line are investigated in the well established so-called micro region model.

Zusammenfassung

Die vorliegende Arbeit behandelt numerische Simulationen zum hydrodynamischen Verhalten sowie zum Wärme- und Stofftransport beim Tropfenaufprall auf eine heiße, feste Oberfläche bei niedrigen und hohen Umgebungsdrücken. Die Anwendungsfelder reichen vom leistungsfähigen Thermomanagement mittels Sprühkühlung, sicherheitsrelevanten Aspekten bei Hochdruck-Nuklearreaktoren, bis hin zur Verfahrenstechnik in der Chemie- und Lebensmittelindustrie.

Aus der Literatur ist bekannt, dass sich die Benetzungseigenschaften ändern, wenn sich der Umgebungsdruck ändert. Splashing wird bei niedrigem Umgebungsdruck unterdrückt. Hoher Umgebungsdruck begünstigt Kompressibilitätseffekte. Die Kompressibilität der Flüssigkeit und der Dampfphase erhöht sich bei steigendem Druck. Bisher wurden jedoch keine Studien durchgeführt, die einen breiten Druckbereich des Tropfenaufpralls bei gleichzeitiger Verdampfung abdecken.

Zum Erlangen von Erkenntnissen beim Tropfenaufprall mit Verdampfung bei verschiedenen Umgebungsdrücken werden numerische Simulationen durchgeführt. In den CFD Simulationen wird die Finite Volumen Methode genutzt, und es werden Navier-Stokes Gleichungen gelöst. Der Löser berücksichtigt kompressible Fluidströmung, Wärme- und Stofftransport über die freie Flüssigkeits-Dampf Phasengrenze und in der Nähe der Dreiphasen-Kontaktlinie aufgrund von Verdampfung, sowie Wärmeleitung im Feststoff. Der dynamische Kontaktwinkel ist über ein Subskalenmodell eingebunden. Der Einfluss von niedrigem und hohem Umgebungsdruck in der Nähe der Dreiphasen-Kontaktlinie wird mittels eines bekannten Mikrozonenmodells untersucht.

The focus is the non-splashing drop-wall collision in a non-boiling, single-component evaporation regime. Ambient pressure ratios ranging between $p/p_{cr} = \left[8 \cdot 10^{-3} \dots 0.5\right]$, Reynolds and Weber numbers ranging between $Re = [600 \dots 1300]$ and $We = [10 \dots 50]$ are investigated. The wall temperature is above saturation but below Leidenfrost temperature. The wall superheat is in the order of $\Delta T = 10\,\mathrm{K}$. Different parameter studies are dedicated to investigate the influence of low and high ambient pressures on the evaporative drop impact processes. Within one parameter study, dimensional drop impact parameters are kept constant, such as drop diameter, impact velocity and wall superheat. Caused by the variation in ambient pressure, material properties of the fluid change. Consequently, non-dimensional groups are changing, indicating a shift in dominant forces. Another parameter study keeps non-dimensional groups constant. Further parameter studies focus on the influence of the vapour phase on the drop impact outcome, especially for high ambient pressure.

Within this work, results are presented for different length scales. The modelling of the vicinity of an evaporating three-phase contact line indicates a strong influence of the ambient pressure on the apparent contact angle and the heat being transferred in the micro region. For increasing pressure, the contact angle increases whereas the transferred heat has a local maximum within the investigated pressure range. For the macroscale drop impingement process, strong influence on the fluid dynamics and heat transfer is identified.

In summary, numerical simulations of the evaporative drop impact and the modelling of microscale thermodynamic effects for low and high ambient pressure are investigated in the present thesis. The results increase the understanding of the influence of pressure on the fluid dynamics, as well as the heat and mass transfer. Correlations for the maximum spreading ratio, spreading duration, as well as transferred energy and mass are reported. The findings are expected to improve design concepts for technical applications within the investigated parameter range.

Der Fokus liegt auf einer Tropfen-Wand Kollision ohne Splashing jedoch mit Verdampfung im Bereich des stillen Siedens. Das Verhältnis vom Umgebungs- zum kritischen Druck des Fluides beträgt $p/p_{cr} = \left[8 \cdot 10^{-3} \dots 0.5\right]$, wobei die Reynolds- und Weber-Zahlen im Bereich von $Re = [600 \dots 1300]$ und $We = [10 \dots 50]$ variieren. Die Wandtemperatur liegt oberhalb der Sättigungs-, jedoch unterhalb der Leidenfrosttemperatur. Die Wandüberhitzung liegt in der Größenordnung von $\Delta T = 10\,\mathrm{K}$. Verschiedene Parameterstudien widmen sich dem Einfluss von niedrigem und hohem Umgebungsdruck bei Tropfenaufprall mit Verdampfung. In einer Studie bleiben die Aufprallparameter, wie Tropfendurchmesser, Aufprallgeschwindigkeit und Wandüberhitzung konstant. Der Umgebungsdruck beeinflusst die Eigenschaften des Fluides und somit die dimensionslosen Kennzahlen, was auf eine Verschiebung der dominanten Kräfte hindeutet. In einer zweiten Studie sind dagegen die dimensionslosen Kennzahlen identisch. Zusätzlich werden Parameterstudien durchgeführt, die sich mit dem Einfluss der Dampfphase auf den Aufprall beschäftigen, besonders bei hohem Druck.

Im Rahmen dieser Arbeit werden Ergebnisse für unterschiedliche Längenskalen gezeigt. Die Modellierung in der Nähe der Dreiphasen-Kontaktlinie weist einen starken Einfluss des Umgebungsdruckes auf den Kontaktwinkel und die übertragene Wärme innerhalb der Mikrozone auf. Bei steigendem Druck steigt der Kontaktwinkel, wohingegen die übertragene Wärme ein lokales Maximum im untersuchten Druckbereich zeigt. Für den makroskopischen Tropfenaufprall zeichnet sich ein starker Einfluss auf die Hydrodynamik und den Wärmetransport ab.

Durch die Simulationen zum Tropfenaufprall mit Verdampfung und die modellierten thermodynamischen Effekte innerhalb der Mikrozone wird das Verständnis für den Einfluss auf die Fluiddynamik und den Wärme- und Stofftransport bei niedrigen und hohen Umgebungsdrücken erweitert. Korrelationen für die maximale Spreizung, Ausbreitungsdauer sowie die übertragene Wärme und Masse werden diskutiert. Diese Erkenntnisse werden als nützlich bei dem Design und Optimieren von technischen Apparaten innerhalb des untersuchten Druckbereichs angesehen.

Contents

Nomenclature

Abbreviation	Description
CFD	Computational Fluid Dynamics
CIIP	Constant Initial Impact Parameters study
CNDG	Constant Non-Dimensional Groups study
CSF	Continuum Surface Force
EoS	Equation of State
LGB	Locally Grid-Based front tracking
MULES	Multi-Dimensional Limiter For Explicit Solution
ODE	Ordinary Differential Equation
PISO	Pressure-Implicit Split-Operator
PLIC	Piecewise Linear Interface Reconstruction
VoF	Volume of Fluid

Latin Symbol	Description	Unit
A	dispersion constant	J
a	speed of sound	m/s
c	specific heat capacity	J/(kg K)
c_α	compression coefficient	-
D	diameter	m
D	distance	m
D	non-dimensional group	-
$\tilde{D}$	constant for diffusion equation	m^2
f	condensation coefficient	-
$\mathbf{f}$	volumetric force	N/m^3
$\mathbf{g}$, g	gravitational acceleration	m/s^2
Δh_v	enthalpy of vaporisation	J/kg
K	curvature	1/m
k	thermal conductivity	W/(m K)
L	length scale	m
M	mass	kg
$\dot{M}$	mass flow	kg/s
$\overline{M}$	molar mass	kg/kmol
$\dot{m}$	mass flux	$kg/(m^2\,s)$
N	number	-
N_l, N_v	scaling factors	-
$\mathbf{n}$	unit normal vector	m
p	pressure	N/m^2
Q	heat	J

Continued on next page

Latin Symbol (continued)	Description	Unit
$\dot{Q}$	heat flow	W
$\dot{Q}_{\mathrm{mic}}$	integrated heat flux across micro region	W/m
$\dot{q}$	heat flux	$\mathrm{W/m^2}$
R	thermal resistance	$(\mathrm{m^2\,K})/\mathrm{W}$
R_{cl}	contact line radius	m
R_{gas}	specific gas constant	$\mathrm{J/(kg\,K)}$
$\overline{R}$	molar gas constant	$\mathrm{J/(kmol\,K)}$
r	radial coordinate	m
S	spreading ratio	-
S	surface area	$\mathrm{m^2}$
$\mathbf{S}$	surface vector	$\mathrm{m^2}$
T	temperature	K
t	time	s
Δt	time step	s
$\mathbf{u}, u$	velocity	m/s
V	volume	$\mathrm{m^3}$
v	mass specific volume	$\mathrm{m^3/kg}$
$\overline{v}$	molar volume	$\mathrm{m^3/kmol}$
w	weighting factor	-
$\mathbf{x}$	point vector	m
$\mathbf{x}_{\Sigma}$	centroid vector of a segment	m
$\mathbf{x}_{\mathrm{c}}$	centroid vector of a computational cell	m
$\mathbf{x}_{\mathrm{f}}$	centroid vector of an internal face	m
Δx	grid size	m
x, y, z	Cartesian coordinates	m

Greek Symbol	Description	Unit
α	volume fraction	$\mathrm{m^3/m^3}$
β	angle between cell centroids	deg
γ	various material properties	various
δ	film thickness, film height	m
ε	relative error	-
ε_1,ε_2	perturbation	-
η	local coordinate perpendicular to wall	m
θ	contact angle	deg
κ	isentropic exponent	-
μ	dynamic viscosity	$\mathrm{kg/(m\,s)}$
ν	kinematic viscosity	$\mathrm{m^2/s}$
ξ	local coordinate along wall	m
ρ	density	$\mathrm{kg/m^3}$
$\dot{\rho}$	mass source term	$\mathrm{kg/(m^3\,s)}$
$\overline{\rho}$	molar density	$\mathrm{kmol/m^3}$
Σ	various source terms	various
σ	surface tension	N/m
τ	non-dimensional time	-
χ	thermodynamic compressibility	$\mathrm{Pa^{-1}}$
ψ	mathematical compressibility	$\mathrm{s^2/m^2}$

Subscript	Description
0	initial conditions; reference state
ad	adsorbed layer/film
c	capillary
cell	computational cell
cl	contact line
cr	critical point of fluid
cum	cumulated
drop	drop
end	end
evap	evaporation
exp	experiments
fluid	fluid
f	face
in	input
int	interface
Kap	Kapitza
l	liquid
lin	linearised
liq	liquid
max	maximum
mac	macroscopic
mic	micro region
min	minimum
p	isobaric
p	point
PR	Peng–Robinson EoS
r	receding phase
rel	relative
ref	reference
S	isentropic
s	spreading phase
solid	solid
sat	saturation conditions
T	isothermal
th	thermal
trans	transition zone
v	isochoric
v	vapour
w	wall
Φ	capillary wave
∞	far field value

Superscript	Description
$'$	derivative with respect to coordinate
$\cdot$	derivative with respect to time
$*$	non-dimensional

Non-dimensional groups

Symbol	Description	Definition
Bo	Bond number	$\rho g D_0^2/(4\sigma)$
Ca	Capillary number	$\mu_\mathrm{l} u_\mathrm{cl}/\sigma$
Co	Courant number	$u\Delta t/\Delta x$
E^*	non-dimensional heat	$6Q/(\pi\rho D_0^3 \Delta h_\mathrm{v})$
Ja	Jakob number	$c\Delta T/\Delta h_\mathrm{v}$
M^*	non-dimensional evaporated mass	$6M_\mathrm{evap}/(\pi\rho_\mathrm{l} D_0^3)$
Ma	Mach number	u_0/a
Oh	Ohnesorge number	$\mathrm{We}^{1/2}/\mathrm{Re}$
P^*	relative pressure	p/p_cr
Pr	Prandtl number	$c\mu/k$
$\dot{Q}^*$	non-dimensional heat flow	$6\dot{Q}/(\pi\rho D_0^2 u_0 \Delta h_\mathrm{v})$
$\dot{Q}^*_\mathrm{mic}$	non-dimensional integrated heat flux	$\dot{Q}_\mathrm{mic}/(k_\mathrm{l}\Delta T)$
Re	Reynolds number	$\rho D_0 u_0/\mu$
We	Weber number	$\rho D_0 u_0^2/\sigma$

CHAPTER 1

Introduction

1.1 Motivation and practical relevance

Thermal management addresses heating and cooling strategies for the supply or removal of thermal energy from a technical component. The constant effort for a reduction of the component mass and size on the one hand and an increasing demand for performance and power on the other hand is the driving force behind research and application of effective, safe, sustainable, reliable, cost and resource efficient cooling strategies. The design requirements for thermal management concern critical system temperatures or heat fluxes and play a vital role in achieving high system performance. Thermal management spans over a range of applications within the automotive sector [50], aviation, electronics [52, 103], the nuclear industry, or chemical and food industry. In the electronic industry, for example, thermal energy of the electronic components needs to be removed sufficiently to prevent material damage or, in the case of battery pack cooling [86], thermal runaway[1].

Two-phase cooling methods utilise the phase change enthalpy, which allows heat transfer with lower temperature differences compared to single-phase cooling methods. Among several two-phase cooling methods, such as immersed body pool boiling, heat pipes, and jet impingement, evaporative spray cooling creates extremely high heat transfer coefficients [52, 93].

The ambient pressure of the spray is found to influence spray characteristics, drop dynamics, and hence the surface cooling rate [24, 64, 66]. Current literature on spray cooling concentrates mainly on the influence on the full spray. Without doubt, research on the full spray cooling is of tremendous interest. However, to understand the physical effects of various ambient pressures on spray cooling, it is helpful to step back in length and time scales and to focus on the initial phase of single drop impact. So far, only a few studies have been published on the influence of various ambient pressures on single drop impact. None of them takes heat and mass transfer in a non-boiling but yet evaporative regime into account.

The objective of this thesis is to investigate the contribution of low and high ambient pressure on single drop hot wall collision for a non-boiling, single-component evaporation regime. Comprehensive numerical simulations are conducted including the potentially compressible nature of the event, as well as the description of the fluid dynamics and thermodynamics in the vicinity of the three-phase contact line. This thesis can be considered as a step towards the understanding of the complex underlying physical phenomena. The pressure's influence on the drop impact and evaporation can be directly linked to the drop impact morphology and its influence on the heat transfer. The findings are useful for improving system design on an engineering scale.

[1] Exceeding a critical system temperature, further chemical reactions are triggered resulting in higher energy release and hence higher temperatures, leading to a complete destruction of the affected battery cells.

1.2 Fundamentals in drop impact phenomena on hot walls

A brief introduction is given on the drop impacting on hot walls. Relevant non-dimensional groups are listed and used throughout this thesis. In literature, drop impact regimes on a hot wall are categorised from a heat transfer perspective or from a hydrodynamics perspective. The wall temperature influences the heat transfer mechanisms during the drop impact. Furthermore, the fluid dynamics during drop impact on hot walls are of interest, which are strongly influenced by the heat transfer mechanisms.

Relevant non-dimensional numbers

When a drop hits a solid surface, its morphology outcome differs strongly depending on initial and ambient conditions. The drop might stick, spread, disintegrate, rebound or undergo a combination of these phenomena. The impact parameters, such as impact velocity u_0 and initial drop diameter D_0, but also fluid properties such as viscosity μ_l, surface tension σ and density of the liquid ρ_l, are identified in many studies to play a vital role on drop impact phenomena. To compare results from different systems, non-dimensional numbers are helpful. The ratio of inertia to viscous forces is used for the Reynolds number

$$Re = \frac{\rho_\mathrm{l} D_0 u_0}{\mu_\mathrm{l}}. \tag{1.1}$$

The ratio of inertia to surface forces is represented in the Weber number

$$We = \frac{\rho_\mathrm{l} D_0 u_0^2}{\sigma}. \tag{1.2}$$

The Bond number scales external volume forces to surface forces. In case of solely gravitational external forces, the Bond number for a drop reads

$$Bo = \frac{\rho_\mathrm{l} g D_0^2}{4\sigma}, \tag{1.3}$$

where g denotes the gravitational acceleration. Small Bond numbers indicate strong surface forces compared to the volume forces. Hence, the drop tends to a spherical shape for small values of Bo. The above non-dimensional groups or a combination of them are used to identify threshold values for the different drop impact regimes and to predict drop impact characteristics, such as maximum spreading ratio, by correlations.

If heat transfer is considered, the Prandtl and Jakob number might become important. The Prandtl number is a material property of the fluid and relates the viscosity to thermal properties

$$Pr = \frac{c\mu}{k}, \tag{1.4}$$

using c_l, μ_l, and k_l for the liquid and $c_{p,\mathrm{v}}$, μ_v, and k_v for the vapour Prandtl number. The thermal heat capacity and the thermal conductivity of the phase are denoted by c and k, respectively. The Jakob number relates the sensible to the latent heat

$$Ja = \frac{c_\mathrm{l} \Delta T}{\Delta h_\mathrm{v}}, \tag{1.5}$$

with Δh_v being the latent heat of vaporisation and $\Delta T = T_\mathrm{w} - T_\mathrm{sat}$ the wall superheat, which is defined as the difference of wall temperature T_w and saturation temperature T_sat of the liquid. If the drop is

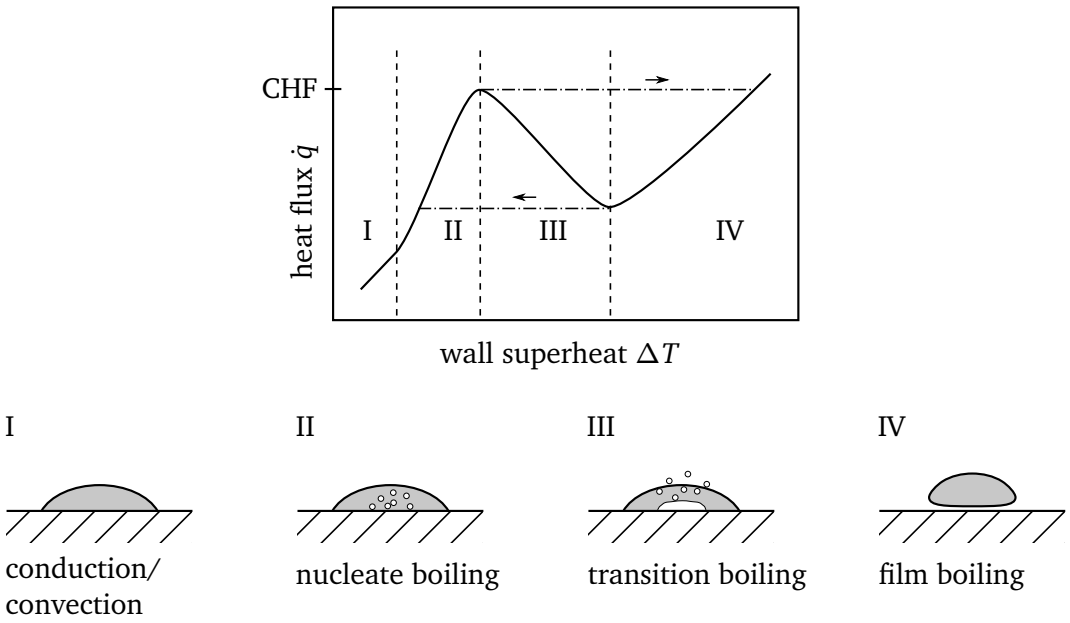

Figure 1.1.: Boiling curve of a drop [72, 82].

sub-cooled below saturation temperature, a term has to be added in the enumerator to account for the conductive heat transport.

In the context of compressible fluid flows, an important non-dimensional number is the Mach number

$$Ma = \frac{u_0}{a}, \tag{1.6}$$

where a denotes the speed of sound within the medium.

Heat transfer mechanisms

The different heat transfer regimes can be described by the Nukiyama boiling curve. In [72], Nukiyama summarised the entire boiling process and described the heat flux $\dot{q}$ as a function of wall superheat ΔT. The well-known boiling curve is often used to describe the phenomena in pool boiling, but can be used analogously for drops [82] and is sketched in Figure 1.1. A gently deposited or sessile drop on a hot solid surface passes through different heat transfer mechanisms:

- **Conduction/convection (phase I):** For small heat fluxes, the thermal energy between the wall and the liquid drop is transferred by conduction and also by natural convection. Most of the transferred energy is used for evaporation across the liquid-vapour interface. Nevertheless, a superheating of the liquid, i.e. the temperature of the liquid exeeds the saturation temperature, is possible [16, Ch. 5]. In spray cooling, phase I is sometimes called single phase cooling [6, 71, 76] or film evaporation [63].
- **Nucleate boiling (phase II):** If the heat flux is sufficiently high and nucleation sites are activated, small bubbles inside the drop start to form. This is the onset of nucleate boiling and the beginning of phase II in Figure 1.1. During this phase, the wall superheat rises slowly since thermal energy is used for evaporation to create and grow vapour bubbles. Possible bubble departure from the wall enhances the heat transfer. Phase II ends with the critical heat flux (CHF), a local maximum in the Nukiyama curve.

- **Transition boiling (phase III):** At CHF, besides ongoing bubble formation, an unstable vapour layer forms between wall and liquid. The vapour layer in phase III is not complete and parts of the liquid drop are in contact with the wall. A slight increase in the heat flux above the CHF leads to a sudden increase in the wall superheat and therefore to the next heat transfer mechanism.
- **Film boiling (phase IV):** Within this phase, a fully developed vapour layer hinders the drop from touching the solid surface. The superheat is high enough to cause instant evaporation of the liquid close to the wall. Nevertheless, it is reported that a very short contact between the solid wall and the liquid can occasionally happen [13, 82]. The Leidenfrost temperature is the lowest achievable solid surface temperature at which a fully developed vapour layer can exist. This marks the transition point between transition and film boiling. The Leidenfrost temperature of a fluid is known to be influenced by surface properties and impact velocity of the drop. Further details on Liedenfrost phenomena and influencing parameters can be found in the review articles by Quéré [81] and Brutin et al. [14].

The boiling curve of a drop in Figure 1.1 is depicted only quantitatively, because the individual boiling curve for drop impact depends not only on the material properties of the wall and the fluid, the heater's geometry and surface structuring, but also on the impact parameters of the drop [51, 52].

For a drop impacting on a hot surface, additional heat transfer mechanisms become important. Immediately after the initial drop-wall contact, high heat fluxes across the liquid-surface interface might arise from convective heat transfer. Besides the evaporation at the free liquid-vapour interface, the evaporation in the vicinity of the three-phase contact line, where solid, liquid and vapour meets, is important [2, 33, 46, 63]. Within a small region around the visible drop-wall contact, a considerable amount of heat is transferred, because the highest temperature gradients exist in this region. The contact angle and consequently the drop dynamics are influenced by the heat transfer at the three-phase contact line. Therefore, the investigations in the present thesis have a strong focus on fluid dynamics and heat and mass transfer within the vicinity of the three-phase contact line.

Fluid dynamics

Among others, recently Breitenbach et al. [13] investigated the drop impact on a hot, smooth wall in a boiling and non-boiling regime. In contrast to drop impact on a surface with the same temperature as the fluid, different drop impact regimes were observed and it was concluded that the fluid dynamics during impact is influenced by the heat transfer.

For boiling conditions, the outcome of the drop impact on hot walls was categorised in four different drop impact regimes. Snapshots of the different drop impact regimes can be found in Figure 1.2. The following regimes are identified:

- **Deposition:** After the initial contact with the wall, the drop starts to spread and, eventually, recedes again. The liquid stays permanently in contact with the solid.
- **Dancing:** For sufficient high wall temperature in the transition boiling regime, bubbles nucleate, grow, coalesce and eventually collapse. The formation and collapsing of bubbles forces the liquid to move and the drop appears to dance on the surface. Small secondary drops are formed, which accelerate away from the drop and solid surface.
- **Thermal atomisation:** For high wall temperatures in the transition boiling regime, enhanced formation of secondary drops occurs. It was reported by the authors that the high heat transfer enables the spreading drop lamella to levitate.
- **Rebound:** Due to a mostly stable gas/vapour layer between drop and solid surface, the drop repels from the surface. The gas/vapour layer is mainly found to occur in the film boiling regime.

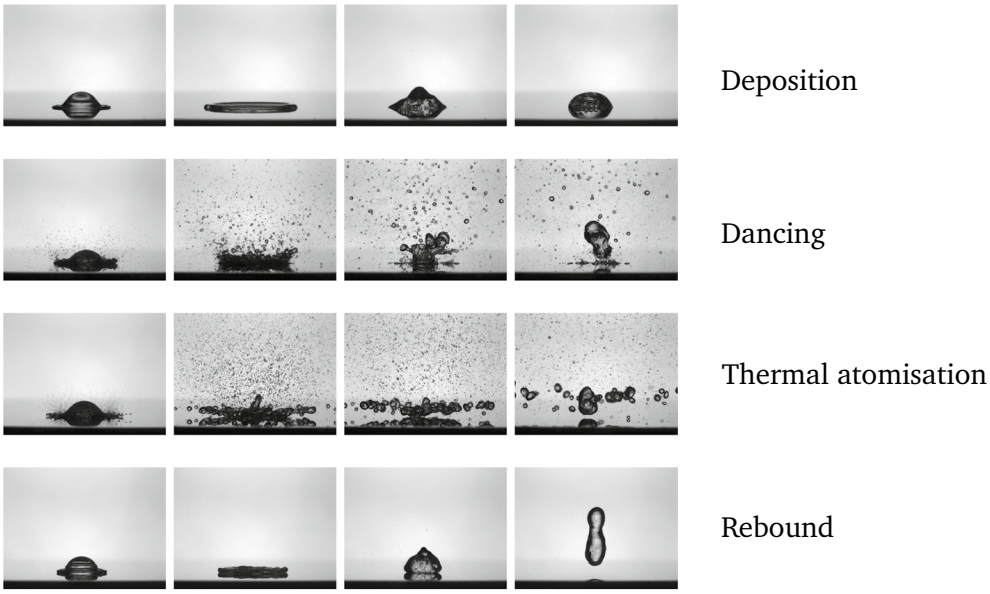

Figure 1.2.: Morphology of drop impact on a hot, dry surface from [13]. Reprinted by permission from Springer Nature Customer Service Centre GmbH.

1.3 State of the art

Spray cooling received much attention in recent years due to promising capabilities for transfering remarkably high heat fluxes [93]. There exist excellent review papers for spray cooling [21, 71, 93] and for single drop impact [5, 63, 71, 108]. For spray cooling efficiency, several important factors were identified, such as volumetric flow rate, Sauter mean diameter and spray orientation.

For single drop impact, numerous studies were conducted to investigate the influence of impact parameters (drop velocity and diameter, inclination of impact), material properties (viscosity, newtonian/non-newtonian fluids), surface material (wettability, roughness) and surface structure (micro and macro structured surfaces). These studies help to widen the understanding of the physics involved in fluid dynamics behaviour during and after the impact. A very popular study in this field was published by Rioboo et al. [84] that clearly described the outcome from a drop impact on solid surfaces. Rioboo et al. varied not only impact parameters, such as impact velocity and drop diameter, but also the surface structure (smooth/rough, hydrophil/hydrophob). Among many publications, drop impact on hot surfaces was published in [18–20, 33, 34, 46, 51, 75, 104]. An impressive series of pictures for the drop impact on hot walls was obtained by the experimental studies by Breitenbach [11] and Breitenbach et al. [12, 13]. The focus in these studies was identifying different drop impact regimes. Reynolds and Weber numbers, as well as the wall temperature were used to distinguish between the different regimes.

Various ambient pressures during a single drop impact event, however, have not been sufficiently addressed.

1.3.1 Experimental work

Spray cooling under various ambient pressures

The influence of the chamber pressure on the heat transfer characteristics of spray cooling was investigated by Liu et al. [64] using the refrigerant R134-a for cooling a plain copper surface. By varying the chamber pressure from $p = [0.2 \ldots 0.4]\,\mathrm{MPa}$, they obtained results for the heat flux, critical heat flux and spray efficiency. For constant wall superheat, they observed larger heat fluxes at higher chamber

pressures. The maximum CHF was found at the highest investigated chamber pressure. For the same flow rate, they concluded that spray cooling efficiency increases with increasing chamber pressure.

Recently, sprays at high ambient pressures were investigated experimentally by Costa et al. [24]. The study was motivated by the processes in internal combustion chambers in which a spray hits the chamber wall. The chamber pressure ranges between $p = [1 \ldots 30]$ bar. They used liquid water drops on stainless steel in a nitrogen atmosphere and considered two scenarios: constant wall temperature ($T_w = 260\,°C$; wall superheat decreases with increasing pressure) and constant initial wall superheat ($\Delta T = T_w - T_{sat} = 45\,K$; wall temperature increases with increasing pressure). In the case of constant wall temperature they observed the highest initial heat flux at 10 bar. For pressures above 10 bar, they reported a decrease in initial heat fluxes concluding an interaction between spray drops and the gas at elevated density. For constant wall superheat they showed a maximum initial heat flux at 20 bar. It is noteworthy that for both scenarios a maximum initial heat flux was not observed at the highest investigated pressure. Furthermore, for increasing ambient pressures, they observed broader spray angles and a higher uniformity degree but at the same time smaller generated drop sizes and decreased impact velocities of the drops. Both latter facts, smaller drop sizes and slower impact velocities, lead to a suppression of splash and rebound mechanisms and favour a deposition mechanism.

Drop impact on walls under various ambient pressures

An early experimental study of drop impact on a hot wall under elevated ambient pressures was published by Emmerson in 1975 [28]. The author studied the maximum evaporation time and Leidenfrost point for water drops deposited on different surface materials. The evaporation time is reduced as the pressure is increased because of the decrease in latent heat of vaporisation. The Leidenfrost temperature was found to increase with increasing pressure. However, the difference between Leidenfrost temperature and saturation temperature at each investigated pressure level stays roughly constant. In a follow-up study, Emmerson and Snoek [29] extended the experiments to other fluids having a lower critical point than water. In [29] they concluded a pressure dependence for the Leidenfrost temperature with respect to the fluid's critical pressure. Except for water, they reported for the organic fluids that the Leidenfrost temperature equals the critical temperature when the critical pressure is reached.

The influence of the ambient pressure on the drop hydrodynamics was reported by Mishra et al. [69]. They conducted drop impact experiments for different fluids, in which the temperature of the drop and surface was equal and pressures were ranging from atmospheric to 12 bar. During drop generation they observed high drop distortion at high pressures and different impact velocities for increased pressures due to increased gas drag. In their studies, the maximum spread diameter was found to be independent from the ambient pressure for all fluids considered. Interestingly, deposition was observed for low pressures whereas the drops start to splash for elevated pressure levels.

Buchmüller [15] conducted studies for water drop impacting on hot walls ranging from ambient pressure to 25 bar. In the thesis of Buchmüller, the evaporation time and the transition between several heat transfer mechanisms was investigated. For increasing pressures, a transition between the different heat transfer mechanisms was observed at increased surface temperatures.

Concerning low ambient pressure, a pioneering work of Xu et al. [107] was published in 2005. They studied different liquids having similar densities but different viscosities. To investigate the role of the surrounding gas, they varied the composition of the gas by using similar viscosities but different molar masses. The threshold pressure, at which the transition between deposition and splashing occurs, was found to be influenced by the impact velocity of the drop, the viscosity of the liquid, and the molar mass of the gas. Later, Stevens and co-worker [97, 98] extended the studies of Xu et al. [107] to low liquid viscosity drops.

Orejon et al. [74] studied the drop impact regimes on hot surfaces for different substrate materials and various low pressure levels. The heat transfer mechanisms varied from nucleate boiling to film boiling.

Table 1.1.: Overview of experimental studies on drop impact under various ambient pressures.

	Reference	hot wall	pressure range	liquids	gas
$> 1\,\text{bar}$	Emmerson (1975) [28]	yes	$0.1 - 0.5\,\text{MPa}$	water	air + N_2
	Emmerson et al. (1978) [29]	yes	$0.1 - 0.7\,\text{MPa}$	water	air + N_2
	Emmerson et al. (1978) [29]	yes	$0.1 - p_{cr}$	Freon C51-12, Freon 113, carbon tetrachloride, chloroform	air + N_2
	Mishra et al. (2011) [69]	no	$0.1 - 1.2\,\text{MPa}$	methanol, ethanol, propanol, cetane, diesel	air + N_2
	Buchmüller (2014) [15]	yes	$0.1 - 2.5\,\text{MPa}$	water	air
$< 1\,\text{bar}$	Xu et al. (2005) [107]	no	$1 - 100\,\text{kPa}$	methanol, ethanol, propanol	He, Kr, SF_6, air
	Stevens et al. (2014) [97, 98]	no	$5 - 101\,\text{kPa}$	ethanol, fluorinert, water-glycerol mixtures, silicone oils	He, SF_6, air
	Orejon et al. 2014 [74]	yes	$5 - 101\,\text{kPa}$	water, iso-octane, n-heptane, α-methylnaphthalene, n-hexadecane	n.a.
	Van Limbeek et al. (2018) [102]	yes	$13 - 100\,\text{kPa}$	ethanol	air
	Yu et al. 2019 [109]	yes	$0.2 - 20\,\text{kPa}$	water	air
	Hatakenaka et al. 2019 [45]	yes	$1 - 101\,\text{kPa}$	water	gas

Interestingly, they proposed a scaling law for the Leidenfrost temperature depending on the pressure analogously to the Clausius-Clapeyron equation, which describes the saturation temperature as function of pressure.

Van Limbeek et al. [102] studied different boiling regimes ranging from evaporation to film boiling for drop impact at ambient pressures below 1 bar. Van Limbeek et al. observed smaller Leidenfrost temperatures for decreasing ambient pressure. It was proposed that the escaping vapour has to do less work against smaller ambient pressures.

Recently, Yu et al. [109] studied water drop impact regimes on a hot silicon surface at low ambient pressures. The heat transfer mechanisms varied from film evaporation to Leidenfrost. They discovered a new drop impact regime that they called "explosive bouncing" which occurs after the deposition but before the boiling regime. Using a measurement technique to distinguish between wetted and non-wetted at the solid-fluid interface, the so-called frustrated total internal reflection (FTIR), they showed that an entrapped bubble grows and lifts up the drop entirely from the surface.

In the same year as Yu et al., Hatakenaka et al. [45] published a drop impact regimes study for water on a hot silicon wafer at low ambient pressures and different impact velocities. They confirmed the findings of Yu et al. and the new drop impact regime is referred to "magic carpet bouncing" in their studies. From their results it can be concluded that the transition between deposition and other impact regimes tends to appear for larger wall superheats. For a constant wall superheat this implies a better wettability for decreasing ambient pressures.

In Table 1.1, an overview of the reviewed literature regarding experimental studies on drop impact under various ambient pressures is given. Most of the studies describe the outcome of the drop impact. If heat transfer is present, much emphasis is put on the Leidenfrost temperature. There is a clear scientific gap in experimental work on single drop impact in a non-splashing regime with non-boiling but evaporative heat transfer mechanism under various ambient pressures. Even though boiling regimes were addressed

by most of the publications reviewed here, high spatial and temporal measurements of the temperature distribution at the solid-fluid interface during the drop impact are not available in the current literature. A detailed study of heat transfer mechanisms that provides insight into the underlying physical processes is missing.

1.3.2 Numerical work

With increasing computational power, numerical simulations and modelling of the relevant physical phenomena became a standard tool for the investigation of systems. Different numerical works investigating the drop impact were published. The numerical simulations differ in the underlying equations (Euler/Navier-Stokes) and assumptions, in the discretisation methods of the equations (finite differences/elements/volume methods), and in the applied solution algorithms. In case of two-phase flows, the tracking of the liquid-vapour interface is of interest. Several methods exist for tracking or capturing the interface. A popular interface capturing method is the concept of volume of fluid (VoF, see Hirt and Nichols [49]). Since evaporation is important for drop impact on hot walls, an appropriate evaporation model is required. The vicinity of the evaporating three-phase contact line was proved to strongly influence the fluid dynamics of the drop, as well as the heat and mass transfer [2, 33, 46]. In case of high pressure, compressibility effects might become important. In compressible fluid flows, the density is no longer assumed to stay constant within each phase. For the model, an additional equation is necessary to link the density of a phase to the thermodynamic properties. Commonly, equations of state (EoS) are used, especially the so-called barotropic EoS [23, 53, 57–61, 68] in which the density is solely a function of pressure. A popular barotropic EoS is the Tait equation. However, the choice of an appropriate EoS that accurately reflects the thermodynamic behaviour of the fluid is mandatory. In Table 1.2, an overview of the reviewed numerical studies is given.

Drop impact on hot walls

In 2001, Pasandideh-Fard et al. [76] developed a numerical model of heat transfer during drop impact. In the numerical simulations, the VoF method to capture the liquid-gas interface was used. Energy equations were solved within the fluid and the solid. However, evaporation was neglected and the contact angle was kept constant during all simulation runs.

The evaporation across the free liquid-vapour interface and in the vicinity of the three-phase contact line was included in the numerical model published by Herbert et al. [46, 47] and described in detail in the thesis of Batzdorf [2]. In the simulations, incompressible Navier-Stokes equations were solved, as well as energy equations for the fluid and the solid substrate. Using a subscale model, the dynamic contact angle was calculated as a function of wall superheat and the contact line velocity. In Herbert et al. [47], the drop impact on hot surfaces was investigated for a range of Reynolds, Weber, Bond, and Prandtl numbers. Also, the transferred heat across the fluid-solid surface was analysed.

Teodori et al. [100] conducted numerical simulations for the heat transfer during drop cooling using VoF interface capturing and validated the model against experiments with water. The numerical model accounted for the conjugated heat transfer between solid and fluid but neglected any evaporation effects. A constant contact angle was assumed during the drop impact process.

Drop impact at variable ambient pressures

The role of liquid viscosity on the splashing behaviour observed in the experiments of Xu et al. [107] and Stevens et al. [98] was investigated numerically by Boleans and de Pablo [8]. A finite volume method with VoF interface capturing was utilised for the drop impact studies on high and low viscosity fluids at atmospheric and low ambient pressure. Incompressible Navier-Stokes equations were solved while any temperature effects were neglected. Boleans and de Pablo [8] imposed a Navier-Slip boundary condi-

Table 1.2.: Overview of numerical studies on drop impact on heated surfaces. Interface representation methods: volume of fluid (VoF), locally grid-based (LGB) front tracking method. Equations of state (EoS) for liquid (l), gas (g), or vapour (v): stiffened gas, ideal gas, Tait, other barotropic EoS, Peng-Robinson (PR).

	Interface representation	*Evaporation included*	*Contact line model*	*Liquid phase*	*Gas phase*	*Compressibility included*	EoS
Pasandideh-Fard et al. (2001) [76]	VoF	no	no	water	air	no	–
Herbert et al. (2013)[46, 47]	VoF	yes	yes	FC-72	pure vap.	no	–
Teodori et al. (2017) [100]	VoF	no	no	water	air	no	–
Boelens et al. (2018) [7]	VoF	no	no	ethanol	air	no	–
Boelens and de Pablo (2018) [8]	VoF	no	no	ethanol, silicone oil	air	no	–
Haller et al. (2002, 2003) [40, 41]	LGB	no	no	water	air	yes	l: stiffened gas g: ideal gas
Chizhov and Takayama (2004) [23]	–	no	–	nitrogen	pure vap.	yes	l: Tait v: Tait
Kyriazis et al. (2018) [57]	VoF	yes	no	water	air/vap.	yes	l: barotropic g: ideal gas
present thesis	VoF	yes	yes	FC-72	pure vap.	yes	l: linearised PR v: linearised PR

tion away from the three-phase contact line and a so-called generalised Navier boundary condition [38] at the three-phase contact line. The generalised Navier boundary condition restores line-tension force whenever the dynamic angle deviates from the static contact angle. The initial conditions and material properties were chosen in accordance to the experiments from [98, 107]. From the numerical simulations, Boleans and de Pablo [8] concluded for early impact times that the low and high viscosity fluids share the same physics and therefore the drop dynamics are similar. However, for later instances after impact, the liquid sheet formation and the breakup is different for low and high viscosity liquids. Furthermore, to investigate splashing for an impacting drop at atmospheric or low ambient pressures, the influence of impact velocity, liquid viscosity, and surface tension were studied numerically by Boelens and co-workers [7].

Drop impact and compressible fluid flow

Compressible fluid flow is considered for high speed drop impact. The impact velocity of the drop is in the same order of magnitude as the speed of sound in the liquid. At the instance of impact a region in which the liquid is compressed is created [40, 41, 48]. Within the compressed liquid region, the pressure is higher than in the liquid bulk of the drop. The shock front that separates the high pressure region from the rest of the liquid remains attached to the three-phase contact line during a first stage. Later on, liquid jets form at the contact edge due to the high pressure in the compressed liquid region. The delay between initial wall contact and formation of the jet is of interest. Experimental [48] and theoretical [48, 54] work on high speed drop impact were published in the past century.

Chizhov and Schmidt [22] numerically investigated a high-speed water drop impact surrounded by air. In [22], the liquid and the wall have the same temperature. Later, Chizhov and Takayama [23] studied the drop impact on hot walls. In case of hot wall drop impact [23], the fluid was nitrogen and they considered a stable vapour layer between wall and drop. The mathematical model is based on compressible Navier-Stokes equations using a finite difference method in the vapour layer and a finite elements method in the liquid drop. For the equation of state, the Tait equation was chosen. Because both, the wall temperature and the pressure of the compressed liquid at the instant of drop impact, are above the critical point of the nitrogen, no liquid-vapour interface is present between the drop and the vapour layer. Surface tension, gravitational forces, and evaporation were neglected in the model. Chizhov and Takayama [23] proposed a heat flux calculation across the solid-fluid surface using an one-dimensional heat conduction equation within the vapour layer assuming a constant wall temperature.

Haller et al. [40, 41] used Euler equations to describe the compressible fluid flow. Evaporation, surface tension, and viscosity were neglected. A finite differences method was used in combination with a locally grid-based (LGB) front tracking approach. The equations of state were stiffened gas for liquid (water) and ideal gas for air.

Cavitation is the formation of bubbles in a liquid caused by high acceleration, high velocities or pressure waves. When the bubbles collapse high pressure and temperature peaks develop, which might cause erosive material damage for surrounding solid surfaces. During high speed drop impact, a high pressure wave, i.e. a shock wave, propagates away from the compressed liquid region. The high pressure wave is followed by a rarefaction wave that can locally change the thermodynamic equilibrium and may cause instant phase change, forming a cavitating bubble.

Kyriazis et al. [57] studied the bubble formation after high velocity drop impact on solid surfaces. They augmented an existing density-based solver of OpenFOAM for low Mach numbers enabling the solver to handle a broad *Ma* range from 10^{-2} to 10^{2}. The investigated Reynolds and Weber numbers are in the order of 10^{5} to 10^{6} and 10^{5} to 10^{7}, respectively. The model neglected surface tension, viscosity effects, and gravitation, as well as any temperature effects. Pressure-driven evaporation was included in the model. The compressible Euler equations were solved using a finite volume method with a VoF-like phase representation. Regarding EoS, the isothermal change of state of an ideal gas for the gas phase and a common barotropic equation for the liquid/vapour mixture was chosen. Kyriazis et al. [57] showed that cavitating bubbles can be formed by drop impact velocities from $u_0 = 27.5\,\mathrm{m\,s^{-1}}$ and above.

In the field of cavitating bubbles, remarkable numerical investigations using a finite volume method with VoF interface capturing were performed in [53, 58–61, 68].

Up to now, no attempt has been made to investigate the drop impact on a hot wall for various ambient pressures taking compressible fluid flow into account. For evaluating the heat transfer across the solid-fluid surface in a non-boiling but still evaporative system, evaporation across the free liquid-vapour interface, as well as the fluid dynamics, and the heat and mass transfer in the vicinity of the three-phase contact line is of interest.

1.4 Research objectives and outline of this thesis

The scope of the thesis is to investigate single drop impact and evaporation on a heated solid substrate under various ambient pressures. The ambient pressure ranges from below to above the atmospheric pressure of 1 bar but is kept below the critical pressure of the fluid. The liquid drop is initially at saturation temperature and the wall superheat varies but stays in the order of 10 K above the saturation temperature. The utilised fluid properties are those of FC-72, a fully fluorinated hexane. FC-72 is applied in industry as electronics coolant liquid for single or two-phase cooling methods [4, 35, 39, 78].

The focus for the drop impact is the deposition regime, in which no splashing, no fingering, and no Leidenfrost effects occur. Therefore, a numerical method is developed to account for the compressibility of the fluid and to take both, evaporation and three-phase contact line phenomena, into account.

Three research questions arise from the outlined drop impact scenario:

- **Question 1:** Does low/high ambient pressure influence the hydrodynamics after drop impact?
- **Question 2:** How does low/high ambient pressure influence the fluid dynamics and heat and mass transfer?
- **Question 3:** How large is the modelling error that might arise from the assumption of incompressible fluid flow?

The first two questions identify if and to which extent various ambient pressures influence the heat and mass transfer of both, the macroscopic drop impact and the microscopic three-phase contact line. The last question determines which situations benefits the most from the developed compressible solver.

The outline of the thesis is the following:

- **Chapter 2.** The mathematical model to simulate the macroscopic drop impact is introduced. The model is based on the compressible Navier-Stokes equations. The implementations and the solution procedure are described. The overall macroscopic model includes the effects of the evaporative three-phase contact line.
- **Chapter 3.** The subscale model, the so-called micro region model, is presented. It describes the fluid dynamics and heat and mass transfer in the vicinity of an evaporative three-phase contact line. The mathematical model is augmented by an additional thermal resistance between solids and fluids, the Kapitza resistance. Its contribution to the heat transfer and the apparent contact angle is analysed.
- **Chapter 4.** The macroscopic drop impact model takes compressible fluid flow and evaporation into account. The evaporation across the free liquid-vapour interface for the developed solver is verified against analytical solutions available in the literature. The overall macroscopic model, including the effects of the three-phase contact line, is validated against single drop impact experiments from literature.
- **Chapter 5.** In preparation for parameter studies, a reference case is defined and the fluid flow as well as the heat and mass transfer is shown in detail.
- **Chapter 6.** Several parameter studies are conducted to investigate the influence of low and high ambient pressures. For that, two distinct parameter studies are performed. In the first parameter study, impact parameters such as drop diameter, impact velocity, and wall superheat are kept constant. Due to the influence of ambient pressure on the material properties of the fluid, non-dimensional groups change. In a second parameter study, non-dimensional groups such as Re, We, Bo, Pr, and Ja are kept constant. Beside the two parameter studies for various ambient pressures, further studies are performed to investigate the influence of compressibility and the vapour phase material properties on the drop impact.
- **Chapter 7.** Finally, a summary and conclusion of the present thesis and suggestions for future research are given.

CHAPTER 2

Numerical Model of the CFD Simulations (Macro Model)

The numerical model is based on the work of Kunkelmann and Stephan [56], as well as Herbert et al. [46] and is extended to compressible fluid flow within this work. Most numerical methods of the model are thoroughly described in the theses of Kunkelmann [55] and Batzdorf [2]. In order to account for possible pressure effects, compressible conservation equations are the basis for the governing equations. Processes in the vicinity of the evaporating three-phase contact line are modelled in a subscale model and are described in detail in the next Chapter. However, the results of the subscale model are included in the macro model. Standard, modified, and newly implemented libraries of OpenFOAM are utilised to solve the set of partial differential equations. The CFD model consists of the following parts and is described in this Chapter, unless specified otherwise:

- **Governing equations: Full compressible model**. Compressible continuity equations for mass, momentum, and energy are the base of the macro CFD model.
- **Implementation and numerical methods**. This section gives an overview of the utilised methods. OpenFOAM is used as a framework to solve the resulting partial differential equations. Consequently, a finite volume approach is applied for spatial discretisation. Within this thesis, methods developed in earlier studies [2, 26, 55] are deployed. Methods regarding the compressibility are described in detail. The coupling of the results of the micro region model with the macro CFD model is presented in this section. Temporal and spatial discretisation is discussed. Finally, a walk-through of the complete numerical application is described.
- **Analysis of the CFD macro model**. The aim of this step is to quantify arising uncertainties and to collect evidence for the reliability and confidence of the macro CFD model. The verification of the evaporation across the free liquid-vapour interface is conducted in Chapter 4.1. Due to insufficient availability of experimental data for the drop impact on hot walls under various ambient pressures, the validation of the CFD macro model is challenging and a topic of ongoing efforts. However, the validation of the drop impact on a hot surface under atmospheric ambient pressure is shown in Chapter 4.2.
- **Results of the CFD macro model**. A reference scenario is described in Chapter 5 and serves as base for the comparison with the results of low and high ambient pressure drop impact. A systematic parameter study is conducted to indicate the influence of low and high ambient pressures on the outcome of drop impact on heated walls. The results and discussion of the CFD macro model are part of Chapter 6.

Before the governing equations of the full compressible model are presented, a brief introduction to compressible fluid flow related to the present thesis is given.

2.1 Fundamentals of compressibile fluid flow

Compressible fluid flow

From a thermodynamic point of view, all real fluids are compressible to some extent. Gases are more compressible than liquids and compressibility can be considered as a material property, which is a function of temperature, pressure and, in case of a mixture, composition. In fluid dynamics, the flow of a real fluid can be considered to be incompressible under certain conditions. Typically, three necessary conditions need to be fulfilled at the same time to assume incompressible fluid flow [94, pp. 161–162]:

- **Low Mach number.** The most prominent condition for incompressibility is the Mach number $Ma = u_0 a^{-1}$, with u_0 being the characteristic velocity that is the drop impact velocity in the present study and a being the speed of sound of the fluid. For incompressibility, the relation

$$\frac{u_0^2}{a^2} = Ma^2 \ll 1 \tag{2.1}$$

  must hold true. The impact velocity is in the order of $1\,\mathrm{m\,s^{-1}}$ and the speed of sound is in the order of $100\,\mathrm{m\,s^{-1}}$ for liquid or vaporous phase, respectively (c.f. Figure A.2 in the appendix). Consequently, the velocities investigated in the present work are small enough to ensure small Mach numbers.

- **Short length scales.** Another necessary condition to assume incompressible fluid flow reads

$$\frac{g\,L}{a^2} \ll 1 \tag{2.2}$$

  with g as the gravitational acceleration and L the problem specific length scale. For g in the order of $10\,\mathrm{m\,s^{-1}}$, the ratio a^2/g is about $10^3\,\mathrm{m}$. Thus, the assumption of incompressible flow is justified for length scales L well below $10^3\,\mathrm{m}$, which is always the case in the present work. The length scale of the drop is in the order of $10^{-3}\,\mathrm{m}$, the computational domain maximal $10^{-2}\,\mathrm{m}$.

- **Slow wave propagation.** The third necessary condition to assume incompressible fluid flow is

$$\frac{L^2 f^2}{a^2} \ll 1 \tag{2.3}$$

  with f being a characteristic frequency and L denoting a characteristic length scale. In case of oscillating waves, L can be considered as the problem specific wave length. Acoustic and shock waves propagate with the speed of sound. Clearly, acoustics and cavitation belong to the research field of compressible fluid flow. In this thesis, it is assumed that acoustics has no influence on the fluid dynamics, as well as on heat and mass transfer. For the non-splashing drop impact and for the heat transfer regime investigated in this thesis, strong pressure waves can not be excluded a priory. However, for the drop impact velocities used in the present work, strong pressure waves are highly unlikely to occur. Consequently, it is expected that condition 2.3 holds true in the present thesis.

To sum up, all conditions (2.1–2.3) to assume incompressible fluid flow are fulfilled in all cases in the present thesis. Compressible fluid flow is not expected during drop impact on a heated wall under various ambient pressures within the investigated parameter range.

However, the assumption of incompressible fluid flow is an approximation of a real fluid behaviour to limit the complexity of the underlying physical models. One research objective of the present thesis is to estimate the error that arises from the assumption of an incompressible fluid flow on the drop impact under various pressures (see research question 3 in Chapter 1.4).

In compressible fluid flow, the density ρ of the fluid is no longer assumed to stay constant in space and time. Combining the temporal and spatial derivative, the material derivative of the density denoted by $\mathrm{D}\rho/\mathrm{D}t$ reads

$$\frac{\mathrm{D}\rho}{\mathrm{D}t} = \frac{\partial \rho}{\partial t} + \mathbf{u} \cdot \nabla \rho \tag{2.4}$$

is non-zero. In this work, it is investigated what influence the compressibility of both phases, liquid and vapour, has on the outcome of the drop impact. In particular, the influence of the compressibility on the fluid dynamics, as well as on the heat and mass transfer is discussed.

It is expected that the pressure dependence of the density is not relevant for the fluid motion. But it might be relevant to heat and mass transfer. To investigate the relevance of a pressure-depended density for the heat and mass transfer, it is necessary to describe the fluid flow as compressible. From a numerical prospective the mass, the momentum, and the energy equations are coupled by the phase change and velocity field.

Compressibility

Compressibility is a change of density due to a change in pressure or temperature. Several definitions of compressibility exist in the field of fluid dynamics and thermodynamics. The definitions that are used in this thesis are outlined in the following:

- **Isothermal compressibility.** A thermodynamically consistent description of the isothermal compressibility χ_T reads

$$\chi_T = -\frac{1}{v}\left(\frac{\partial v}{\partial p}\right)_T = -\frac{1}{V}\left(\frac{\partial V}{\partial p}\right)_T . \tag{2.5}$$

  The isothermal compressibility is used to determine the mathematical compressibility.

- **Isentropic compressibility.** A similar description is given for the compressibility at constant entropy χ_S by

$$\chi_S = -\frac{1}{v}\left(\frac{\partial v}{\partial p}\right)_S = -\frac{1}{V}\left(\frac{\partial V}{\partial p}\right)_S . \tag{2.6}$$

  Using fundamental thermodynamic relations, the isothermal and isentropic compressibility are related by the fraction of constant pressure heat capacity c_p and constant volume heat capacity c_v, known as adiabatic index or isentropic exponent κ

$$\frac{\chi_T}{\chi_S} = \frac{c_p}{c_v} = \kappa . \tag{2.7}$$

  The isentropic compressibility χ_S is closely connected to the speed of sound. In literature, more data about the speed of sound for a fluid is available than about the compressibility. Therefore, χ_S is used to validate the compressibility against the speed of sound, which can be found in the Appendix A.1.

- **Mathematical compressibility.** For a single component fluid with a constant number of molecules, the density is a function of pressure p and temperature T. The total derivative is given by

$$\mathrm{d}\rho = \left(\frac{\partial \rho}{\partial p}\right)_T \mathrm{d}p + \left(\frac{\partial \rho}{\partial T}\right)_p \mathrm{d}T . \tag{2.8}$$

The change in temperature is expected to be much smaller than the change in pressure within the investigated parameter range and can be neglected. Consequently, the derivative of the density is a function of pressure only and is henceforth referred to as the mathematical compressibility ψ that reads

$$\psi = \left(\frac{\partial \rho}{\partial p}\right)_T . \tag{2.9}$$

The mathematical compressibility is implemented in the compressible fluid flow model by the linearised equation of state, introduced in Section 2.3.1. The mathematical and isothermal compressibility are connected via the density

$$\psi = \rho \chi_T . \tag{2.10}$$

- **Compressibility factor.** Another thermodynamic quantity that exists is the compressibility factor

$$Z = \frac{p v}{\mathrm{R} T} \tag{2.11}$$

that describes the deviation of a real gas from an ideal gas behaviour. Because Z is not an appropriate quantity for the two phase problems dealt with in this work, it is not considered further.

2.2 Governing equations: Full compressible model

The physical process of the drop impact with evaporation is considered as a continuum mechanics problem and the mathematical description of the phenomena is based on the conservation laws of mass, momentum, and energy. The following assumptions are made

- the fluid is compressible,
- the fluid properties are continuous,
- the fluid is Newtonian,
- the viscous dissipation can be neglected,
- only heat conduction, heat convection, and heat transfer due to phase change is relevant for the energy equation. Radiation, as well as changes in potential and kinetic energy are neglected.

The fluid phases, liquid and vapour, are assumed to be immiscible and no slip between the phases is present. No slip between the phases means that liquid and vapour share the same velocity at the liquid-vapour interface. Consequently a single moment equation and velocity field applies to model both phases. Thus, the mass, momentum, and energy equations read

$$\nabla \cdot \mathbf{u} = \dot{\Sigma}_\chi + \dot{\Sigma}_\mathrm{V} , \tag{2.12}$$

$$\frac{\partial (\rho \mathbf{u})}{\partial t} + \nabla \cdot (\rho \mathbf{u}\mathbf{u}) = -\nabla p + \nabla \left(-\frac{2}{3} \mu \nabla \cdot \mathbf{u} \right) + \nabla \cdot \left(\mu \left[\nabla \mathbf{u} + (\nabla \mathbf{u})^\mathrm{T} \right] \right) + \mathbf{f}_g + \mathbf{f}_\sigma , \tag{2.13}$$

$$\frac{\partial (\rho c T)}{\partial t} + \nabla \cdot (\rho c \mathbf{u} T) - \nabla \cdot (k \nabla T) = \dot{\Sigma}_\mathrm{e} . \tag{2.14}$$

In the above set of differential equations, μ, σ, c, and k denote the fluids properties of dynamic viscosity, surface tension, specific heat capacity, and thermal conductivity, respectively. They are assumed to be

independent of pressure and temperature. ρ describes the density, $\mathbf{u}$ the velocity, p and T the absolute pressure and temperature.

The first source term on the right-hand side of Equation 2.12, $\dot{\Sigma}_\chi$, is a result of the compressibility of the fluid. The second source term on the right-hand side of the same equation, $\dot{\Sigma}_\mathrm{V}$, accounts for the volume change due to evaporation and condensation if liquid and vapour differ in density. Both contributions enforce the phase-averaged flow velocity $\mathbf{u}$ not to be divergence free.

It is worth to note that the second term on the right-hand side of Equation 2.13 does not vanish due to the non-zero divergence of the velocity field. The surface tension force is substituted by a volume force

$$\mathbf{f}_\sigma = \sigma K \nabla \alpha \,. \tag{2.15}$$

where K denotes the curvature and α the volume fraction of a phase which is discussed later. Another volume force is the force caused by the gravitational field

$$\mathbf{f}_\mathrm{g} = \rho \mathbf{g} \,. \tag{2.16}$$

The energy conservation in Equation 2.14 is obtained by neglecting variations in kinetic and potential energy and applying Fourier's law. The source term $\dot{\Sigma}_\mathrm{e}$ arises from the phase change.

In the solid region, the energy conservation equation reduces to

$$\rho c \frac{\partial T}{\partial t} - \nabla \cdot (k \nabla T) = 0 \tag{2.17}$$

because of the absence of convection and phase change within the solid material. The solid properties density, thermal conductivity, and heat capacity are assumed to be independent of temperature and pressure and to be isotropic.

Equation of state

The density in compressible fluid flow, governed by the Equations 2.12–2.14, is no longer considered as constant. Hence, at least one additional equation is needed to describe the relation between density, pressure, and temperature. While the temperature changes are comparably small within the cases described in this thesis, the change in pressure is assumed to be large, e.g. at the impact of the drop on the wall. For FC–72, it turned out that the saturation curve is approximated best by the Peng-Robinson equation of state. Results for the comparison of different equations of state can be found in the Appendix A.1. For further information on different EoS for pure fluids, the reader is referred to a textbook covering this field, e.g. Poling et al. [79].

The Peng-Robinson equation of state is a three parameter cubic EoS and is commonly expressed by

$$p = \frac{\bar{R} T}{(\bar{v} - b)} - \frac{a_\mathrm{cr} \cdot \alpha(T)}{\bar{v}^2 + 2b\bar{v} - b^2} \tag{2.18}$$

with the Peng-Robinson parameters

$$\begin{aligned} a_\mathrm{cr} &= 0.45724 \frac{\bar{R}^2 T_\mathrm{cr}^2}{p_\mathrm{cr}}, \qquad \alpha(T) = \left[1 + m\left(1 - \sqrt{T/T_\mathrm{cr}}\right)\right]^2, \qquad b = 0.07780 \frac{\bar{R} T_\mathrm{cr}}{p_\mathrm{cr}}, \\ m &= 0.37464 + 1.54226\omega - 0.269992\omega^2 \,. \end{aligned} \tag{2.19}$$

The molar gas constant and the molar volume are denoted by $\bar{R}$ and $\bar{v}$. The acentric factor ω is a non-dimensional value of the pure fluid that expresses the deviation of a molecule's geometry from a perfect sphere

$$\omega = -1 - \log_{10}\left(\frac{p_{\mathrm{sat}}}{p_{\mathrm{cr}}}\right)_{(\mathrm{T}/\mathrm{T_{cr}})=0.7} . \tag{2.20}$$

Equations 2.18–2.20, however, result in a non-linear function for the molar volume $\bar{v}$ and consequently for the density $\rho = \bar{M}/\bar{v}$, with $\bar{M}$ being the molar mass of the material. In combination with the differential Equations 2.12–2.14, the non-linearity is not suitable for being solved within a finite volume method[1]. Instead, a linearised density as function of pressure is presented in Section 2.3.1.

Volume of fluid method for compressible flow with phase change

In order to follow the liquid-vapour interface, the volume of fluid (VoF) method proposed by Hirt and Nichols [49] is used. The volume V_{l} of the liquid phase is divided by the actual cell volume V_{c} to define the scalar volume fraction $\alpha = V_{\mathrm{l}}/V_{\mathrm{c}}$. Cells containing solely liquid phase have a value of unity, whereas the volume fraction is equal to zero for cells completely filled with vapour. Cells that contain both, liquid and vapour, have values between both extrema. For readability, the volume fraction is set to $\alpha = \alpha_1$ which is the volume fraction of the liquid phase. The volume fraction of the vapour phase is denoted as α_2. The sum of both volume fractions is unity:

$$1 = \alpha_1 + \alpha_2 . \tag{2.21}$$

To describe the evolution of the VoF field, a mathematical description is mandatory. The original equation for the volume fraction field is a conservation equation neglecting the diffusive term. It is extended by an additional compression term proposed by Weller [106]. Furthermore, the equation is augmented to account for volume fraction source terms that arise from compressibility and phase change. The transport equation for the VoF field for the liquid reads

$$\frac{\partial \alpha_1}{\partial t} + \nabla \cdot (\alpha_1 \mathbf{u}) + \nabla \cdot [c_\alpha \mathbf{u}_{\mathrm{r}} \alpha_1 (1-\alpha_1)] - \alpha_1 (\nabla \cdot \mathbf{u}) = -\alpha_1 \alpha_2 \left[\frac{1}{\rho_1}\frac{\mathrm{D}\rho_1}{\mathrm{D}t} - \frac{1}{\rho_2}\frac{\mathrm{D}\rho_2}{\mathrm{D}t}\right] \tag{2.22}$$

with the expression for $\mathbf{u}_{\mathrm{r}}$

$$\mathbf{u}_{\mathrm{r}} = |\mathbf{u}| \mathbf{n}_{\mathrm{int}} , \tag{2.23}$$

in which $\mathbf{n}_{\mathrm{int}}$ denotes the vector for the liquid-vapour interface normal and is defined later in this section. In Equation 2.22, the third term on the left-hand site is a compression term to counteract numerical diffusion close to the liquid-vapour interface, as proposed by Weller [106]. The compression acts only for α values between zero and unity and acts always perpendicular to the liquid-vapour interface.

The right-hand side of Equation 2.22 arises from the compressibility of the fluid. This part acts only in the interfacial region and vanishes in the bulk of the phases. $\mathrm{D}\rho/\mathrm{D}t$ is the material derivative of the density.

[1] In finite volume methods, after spatial and temporal discretisation, a system of linear algebraic equations is assembled and solved [30, 87].

Source terms, arising from the compressibility and the phase change, occur in the divergence of the velocity, which is the last term on the left-hand side of 2.22. As mentioned earlier, the velocity field is not divergence free, see Equation 2.12. The source term caused by compressibility is

$$\dot{\Sigma}_\chi = -\frac{\alpha_1}{\rho_1}\frac{\mathrm{D}\rho_1}{\mathrm{D}t} - \frac{\alpha_2}{\rho_2}\frac{\mathrm{D}\rho_2}{\mathrm{D}t}\,. \tag{2.24}$$

The derivation of Equation 2.22 can be found in the Appendix B. In the appendix, the consistent reduction of the VoF transport equation is shown, which accounts for solely phase change or solely compressibility. The reduced VoF transport equations were used in former studies and in studies found in literature.

All material properties γ introduced in the conservation equations are volume weighted averages of the material properties of the individual phase,

$$\gamma = \alpha_1\gamma_\mathrm{l} + (1-\alpha_1)\gamma_\mathrm{v}\,. \tag{2.25}$$

2.3 Implementation and numerical methods

The model is implemented in the OpenFOAM[2] framework, uses parts of the features developed in [2, 26, 55], and is historically an interFOAM based solver augmented by the effects due to compressibility. In the CFD code, the main development steps resulting from this thesis are in the field of compressible fluid flow with evaporation. Focusing on the newly achieved developments, the existing parts of the model will be explained briefly and references for descriptions elsewhere are given. Simulating the drop impact on a hot surface includes several subroutines that are described in detail in the following:

- **Linearised density and compressibility:** the density is a linear function of pressure. The linearisation factor is derived by the means of Peng-Robinson EoS.
- **Interface capturing and contact line:** the temperature gradient based evaporation model requires information about the position of the liquid-vapour interface in space. The contact line position, speed, and length is obtained within this subroutine.
- **Modelling of evaporation:** mass, volume, and energy source terms due to evaporation are determined and distributed within this step. The source terms are formulated implicitly regarding temperature. Therefore, an iteration loop with the next subroutine is performed until convergence is reached.
- **Conjugate heat transfer and coupling of the subscale model:** once the energy source term is obtained, the energy equation is solved for the temperature. Fluid-solid coupling is performed iteratively and contact line evaporation is taken into account.

2.3.1 Linearised density and compressibility

The thermodynamic compression χ introduced in Section 2.1 is not used in the computations due to the strong non-linearity. Instead, a linearised approximation of density as function of pressure is chosen that reads

$$\rho_{\mathrm{lin,l/v}} = \rho_{0,\mathrm{l/v}} + \psi_{\mathrm{l/v}}(p - p_0) \tag{2.26}$$

[2] The OpenFOAM Foundation Ltd using the rolling release OpenFOAM-dev with the commit from January 26th, 2017 0dd9616dcf30a0bdc89fea6f0209211c6bf4cb8e

with ρ_0 and p_0 representing the reference density and reference pressure, respectively. Within this work, the reference pressure for the liquid and the vapour phase is set to the ambient pressure $p_0 = p_{\text{sat}}$ as the ambient conditions are in saturation conditions. Accordantly, the reference densities for liquid and vapour are equal to the densities at saturation conditions. ψ is the slope of the density, which is now a linear function of pressure. Therefore,

$$\psi = \left[\left(\frac{\partial \rho}{\partial p}\right)_T\right]_{p=p_0} \tag{2.27}$$

represents the change in density with the change in pressure, which can be considered as the mathematical compressibility of the phase. The density of a phase, i.e. liquid or vapour, varies piecewise linear from the reference pressure. The link between the mathematical and the thermodynamic compressibility is given by

$$\psi = [\rho \chi_T]_{p=p_0} \tag{2.28}$$

$$= \left[-\frac{\rho}{\rho \bar{M}}\left[-\frac{\bar{R}T}{\left(\bar{M}-b\rho\right)^2} + \frac{\Theta\left(2\bar{M}+\delta\rho\right)\rho}{\left(\bar{M}^2+\delta\bar{M}\rho+\varepsilon\rho^2\right)^2}\right]^{-1}\right]_{p=p_0} . \tag{2.29}$$

The above equation is a common expression for the mathematical compressibility for different EoS with the parameters Θ, δ, b, and ε listed in Table A.1 in the appendix. Evaluating Equation 2.29 at $p = p_{\text{sat}}(T)$ for the Peng-Robinson EoS, the mathematical compressibility reads

$$\psi_{\text{l/v}} = -\frac{1}{\bar{M}}\left[-\frac{\bar{R}T}{\left(\bar{M}-b_{\text{PR}}\rho_{0,\text{l/v}}\right)^2} + \frac{2a_{\text{PR}}(T)\left(\bar{M}+b_{\text{PR}}\rho_{0,\text{l/v}}\right)\rho_{0,\text{l/v}}}{\left(\bar{M}^2+2b_{\text{PR}}\bar{M}\rho_{0,\text{l/v}}-b_{\text{PR}}^2\rho_{0,\text{l/v}}^2\right)^2}\right]^{-1} . \tag{2.30}$$

The parameters $a_{\text{PR}}(T) = a_{\text{cr}} \cdot \alpha(T)$ and b_{PR} are listed in Equation 2.19. An overview of the calculated values for the isothermal compressibility $\chi_{T,\text{PR}}$ and mathematical compressibility ψ used in this work is given in Table A.4 in the appendix.

To sum up, the density function in Equation 2.26 in combination with Equation 2.29 is a linear approximation, or first degree Taylor polynomial, of an arbitrary equation of state. For computations in this work with the Peng-Robinson EoS, Equations 2.26 and 2.30 are employed separately for the liquid and vapour phase. In fact, other values for ψ based on any equation of state, which is appropriate for the fluid, can be utilised. Setting the value of ψ to zero results into an incompressible fluid flow.

In compressible drop impact scenarios [31, 32, 41, 48, 62, 99], the maximum pressure difference in the liquid, which is present at the instant of drop impact, is estimated by the means of water hammer pressure $p_{\text{waterhammer}}$ that reads

$$p_{\text{waterhammer}} = \rho_{\text{l}} u_0 a\,. \tag{2.31}$$

The error $(\rho_{\text{lin,l}} - \rho_{\text{PR,l}})/\rho_{\text{PR,l}}$ induced by the linearisation of the Peng-Robinson EoS for the density is less than 0.1 % for the investigated parameter range.

2.3.2 Volume fraction transport and capturing of the interface

Advection of the VoF field

The advection of VoF field is mathematically described by Equation 2.22. To solve for the VoF field α, the so-called MULES algorithm is used together with an interface compression scheme. The MULES algorithm history reaches back to the 1970s. Formally, MULES is based on the work of Zalesak [110] who extended the flux-corrected transport (FCT) algorithm published by Boris and Book [9] to fully multi-dimensional form. MULES tries to keep boundedness of scalar fields, here the VoF field. OpenFOAM utilises MULES with a compression scheme to prevent the interface from diffusing and, therefore, aims for a reduction of numerical diffusion at the interface. This combination of the pure MULES algorithm and interface compression scheme, however, does not have an own name. For simplicity, the combination of both mentioned algorithms is called MULES in the following. A detailed description and validation of the MULES algorithm can be found in [25].

The transport equation for the VoF field is solved in three sub-cycles to increase accuracy in combination with the implicit Euler scheme for the interpolation in time. The compression factor c_α in Equation 2.22 is set to unity. A momentum predictor is called within each sub-cycle to use an updated version of the velocity field.

Reconstruction of liquid-vapour interface and calculation of interface data

Once the α field is obtained, it can be used to determine the position of the liquid-vapour interface in space. From the reconstructed interface, the interface normals are obtained. The interface normals, in turn, are used to calculate the curvature, which is an important quantity used to model the surface tension force within the momentum equation. Another quantity arising from the interface reconstruction is the distance between the liquid-vapour interface to a computational cell centroid. The distance is utilised for computing the temperature gradient used in the evaporation model. The reconstruction of the liquid-vapour interface, as well as the calculation of interface data such as the size, the normal, and the distance of the reconstructed interface is explained in the following.

In literature, the VoF method is sometimes used in combination with a piecewise linear interface construction (PLIC) method. Within PLIC, the normals based on the α field are computed first. The PLIC interface is then shifted parallel to the interface normals to match the volume fraction value in the computational cell. The edges of two adjacent PLIC reconstructed interfaces do not necessarily match and might not be continuous. It was shown, however, that a temperature gradient-based evaporation model benefits from a continuous interface.

The reconstruction of the liquid-vapour interface is based on the reconstruction using an $\alpha = 0.5$ iso-surface.[3] The used reconstruction of the liquid-vapour interface is the same as proposed by Kunkelmann [55]. To reconstruct the interface, the following steps are performed:

- interpolation of volume-centred α values to the vertices of a cell,
- determination of N_p intersection points $\mathbf{x}_{\mathrm{p,i}}$ of $\alpha = 0.5$ along a connecting edge between two vertices. All intersection points that belong to a common computational cell span a polygon that represents a segment of the total liquid-vapour interface,
- calculation of the size of the segment.

[3] original implementation by Kunkelmann [55], further developed by Batzdorf [2] and reimplemented by Rettenmaier [83]

It should be noted that the polygon within a computational cell might not be exactly planar. The mathematical description of the segment calculation, proposed by López and Hernández [65], reads

$$\mathbf{S}_{\text{int}} = \frac{1}{2}\sum_{i=1}^{N_\text{p}} \left(\mathbf{x}_{\text{p,i}} \times \mathbf{x}_{\text{p,i+1}}\right) . \tag{2.32}$$

With $\mathbf{x}_{\text{p},N_\text{p}+1} = \mathbf{x}_{\text{p},1}$ at the end of the sum the polygon is closed. Mathematically, $\mathbf{S}_{\text{int}}$ is a surface vector of dimension m^2. The liquid-vapour interface normal is calculated by the reconstructed interface

$$\mathbf{n}_{\text{int}} = \frac{\mathbf{S}_{\text{int}}}{|\mathbf{S}_{\text{int}}|} \tag{2.33}$$

which is always pointing into the liquid phase. The centroid $\mathbf{x}_\Sigma$ of the segment is calculated via a triangulation of the polygon. The centroid is used in the evaporation model.

The distance D_{int} between a cell centroid $\mathbf{x}_\text{c}$ and the interface segment is determined using the dot product with the interface normal

$$D_{\text{int}} = \frac{1}{N_\text{p}}\sum_{i=1}^{N_\text{p}} \left[\left(\mathbf{x}_\text{c} - \mathbf{x}_{\text{p,i}}\right) \cdot \mathbf{n}_{\text{int}}\right] . \tag{2.34}$$

The need for averaging arises from a potentially not exact planarity of the interface segment. The sign of the distance follows the position of the cell centroid $\mathbf{x}_\text{c}$ to the interface segment

$$D_{\text{int}} = \begin{cases} > 0, & \mathbf{x}_\text{c} \text{ in liquid phase} \\ < 0, & \mathbf{x}_\text{c} \text{ in vapour phase} \end{cases} . \tag{2.35}$$

Distribution of the interface normals $\mathbf{n}_{\text{int}}$ and the distance D_{int}

Within the interface reconstruction subroutine, the information about the normals of the interface and the distance of the interface from a cell centroid exists solely in cells containing a liquid-vapour interface segment. For various reasons, this information needs to be passed to a narrow band of several cells away of the cell, which contains the interface segment. One reason is that the VoF field around the liquid-vapour interface is diffuse and spreads usually a few cells[4]. The calculation of the surface tension force, to be more precise the determination of the curvature K, requires knowledge of the interface normals in cells where $0 < \alpha < 1$ holds true, even if they do not contain a segment of the interface. A second reason for a distribution of the interface information arises from the usage of the temperature-gradient based phase change model. The phase change model requires the information about the interface distance in the vicinity of the interface. The information about the distance from the interferace in the particular cell containing an interface segment is not sufficient. The distribution of the normals and distances follows the numerical method proposed by Batzdorf [2].

For the interface normals $\mathbf{n}_{\text{int}}$, direct neighbours that share an internal face with the data owner cell will receive the same normal. If this neighbour receives more than one normal, the final normal is calculated by arithmetic averaging, including optional normalising. The passing to neighbours is continued at least until all neighbouring cells with $0 < \alpha < 1$ attain a normal. The distributed normals are used for the curvature calculations.

[4] In the majority of the simulations the spreading is one cell in each direction, resulting in an inter-phase band of three cells.

On principal, the same procedure is used to distribute the distance D_{int}. Neighbours with a common internal face are selected to receive data. The interface distance of an interface segment to a potentially shared internal face is recalculated with $\mathbf{x}_{\text{f}}$, the centroid of the internal face. If the receiving cell retrieves data from more than one donating cell, the receiving cell chooses the smallest absolute value of internal face projected distance. Furthermore, the distance is re-calculated again using the cell centroid of the selected neighbour. The calculation of the distance requires the interface segment normal. Therefore, the distance field needs to be distributed together with the normals.

Curvature and surface tension force

Finally, the curvature is calculated based on the distributed normals, as proposed in [55]

$$K = -\nabla \cdot \mathbf{n}_{\text{int}} \,. \tag{2.36}$$

The following procedure is performed in order to reduce spourious currents arising from the curvature calculation, as suggested in [2]. The curvature is kept solely in cells containing a segment of the liquid-vapour interface, all other curvature data is eliminated. A median filter is applied to the remaining curvature field for smoothing. At last, the smoothed curvature field is again re-distributed within a narrow band around cells containing an interface segment.

Finally, the surface tension force is determined by the continuum surface force (CSF) model by Brackbill et al. [10] shown in Equation 2.15.

Contact line: position, angle, velocity, and length

The contact line exists where an liquid-vapour interface segments hits the fluid-solid surface. The VoF value on fluid-solid boundaries is manipulated to match a prescribed contact angle θ. The contact line position is calculated by interpolating the manipulated VoF value at the face centroid to the edges of the computational cell at the wall. This procedure is similar to the procedure described for the iso-surface reconstruction for the liquid-vapour interface. The contact line length within a computational cell is calculated by the vector difference between the interpolated edge values of the VoF field.

The contact line velocity u_{cl} is determined by the contact line position at the current and last time step, $\mathbf{x}_{\text{cl}}^{n}$ and $\mathbf{x}_{\text{cl}}^{n-1}$, respectively. The contact line velocity calculation reads

$$u_{\text{cl}} = -\frac{1}{\Delta t}\left(\mathbf{x}_{\text{cl}}^{n} - \mathbf{x}_{\text{cl}}^{n-1}\right) \cdot \left(\frac{\mathbf{n}_{\text{int}} - (\mathbf{n}_{\text{f}} \cdot \mathbf{n}_{\text{int}})\,\mathbf{n}_{\text{f}}}{|\mathbf{n}_{\text{int}} - (\mathbf{n}_{\text{f}} \cdot \mathbf{n}_{\text{int}})\,\mathbf{n}_{\text{f}}|} \right), \tag{2.37}$$

with Δt being the time step size and $\mathbf{n}_{\text{f}}$ the normal vector of the face at the fluid-solid surface. Consequently, the contact line velocity is based on the liquid-vapour interface reconstruction rather than on the volume-averaged velocity in the particular contact line cell.

The contact angle is a function of contact line velocity and wall temperature. Its specific calculation will be described in the next Chapter. However, the contact line velocity itself depends on the position of the iso-surface, which, in turn, depends on the interpolation of the VoF field. Therefore, a few iteration steps of the procedure are required until a convergence of the contact angle is achieved.

2.3.3 Modelling of phase change

The gathered information about the VoF field, the reconstructed interface, the contact line, and the (temporary) temperature field is used to calculate the source terms arising from the phase change and to update the temperature field. The following procedure is executed until a convergence of the temperature field is achieved. The implicit description of the phase change utilised in this work is built on the

works of Kunkelmann and Stephan [56] and Herbert et al. [46]. The distribution of the source terms follows the method proposed by Hardt and Wondra [44]. The phase change procedure is described in detail by Batzdorf [2] and briefly in this section.

The liquid-vapour interface is assumed to be at saturation temperature $T_{\mathrm{int}} = T_{\mathrm{sat}}$ of the corresponding ambient bulk pressure $p_\infty = p\,(T_{\mathrm{sat}})$. Consequently, the energy balance at the interface reads

$$0 = \dot{q}_{\mathrm{l,int}} + \dot{q}_{\mathrm{v,int}} - \dot{m}_{\mathrm{evap}} \Delta h_{\mathrm{v}} \tag{2.38}$$

while the temperature of the interface stays constant. $\dot{q}_{\mathrm{l,int}}$ and $\dot{q}_{\mathrm{v,int}}$ are conductive heat fluxes towards the interface from the liquid and vapour, respectively.

Two major numerical tasks arise from the above equation: the determination of the conductive heat flux based on an appropriate temperature gradient and the localisation of the initial mass flux $\dot{m}_{\mathrm{evap}}$. Mass needs to be destructed in one area and created in another area of the computational domain.

Both, the temperature gradient and the initial mass flux $\dot{m}_{\mathrm{evap}}$ are not evaluated in cells containing a reconstructed interface segment. Instead, neighbouring cells close to it are selected, which meet the following conditions:

- the neighbouring cell must share at least one common mesh point with the cell containing an interface segment,
- the neighbouring cell must be mostly filled with either liquid or vapour, and
- the angle between $\mathbf{n}_{\mathrm{int}}$ and the centroid-to-centroid connecting vector, from the cell containing an interface segment to the neighbouring cell, is less than 90 deg.

A simple approach for estimating the temperature gradient could be based on the temperature of an interface segment containing cell and a neighbouring cell in the direction of the steepest temperature slope. This, however, results in inaccurate estimations since the temperature of an interface segment containing cell is a cell average temperature. Instead, information about the position of the interface and the interface temperature is used. The temperature gradient is a weighted function taking into account the distance from the interface, $D_{\mathrm{int},i}$, and the deviation from the interface normal direction, w_i.

Since no energy sources or sinks are evaluated in interface segment containing cells j, the energy sources in the neighbouring cells i are determined

$$\text{liquid:} \quad \dot{\Sigma}_{\mathrm{e,l},i} = -\frac{\dot{Q}_{\mathrm{evap,l},i}}{V_{\mathrm{cell},i}} = -\frac{1}{V_{\mathrm{cell},i}} \frac{k_{\mathrm{l}}\,(T_i - T_{\mathrm{sat}})}{D_{\mathrm{int},i}} \sum_j w_{i,j} S_{\mathrm{int},j}\,, \tag{2.39}$$

$$\text{vapour:} \quad \dot{\Sigma}_{\mathrm{e,v},i} = -\frac{\dot{Q}_{\mathrm{evap,v},i}}{V_{\mathrm{cell},i}} = -\frac{1}{V_{\mathrm{cell},i}} \frac{k_{\mathrm{v}}\,(T_i - T_{\mathrm{sat}})}{D_{\mathrm{int},i}} \sum_j w_{i,j} S_{\mathrm{int},j}\,. \tag{2.40}$$

$D_{\mathrm{int},i}$ is a signed distance according to Equation 2.35. S_{int} denotes the liquid-vapour area which is the size of the interface segment obtained from Equation 2.32 within the interface reconstruction procedure. The weighting factor w_i scales with the angle β_i between the reconstructed interface normal direction and the centroid of the neighbouring cell i by

$$w_i = \frac{\cos\beta_i}{\sum_j \cos\beta_j}\,. \tag{2.41}$$

Consequently, the initial mass flux due to phase change is determined using the sum of the energy sinks/sources on liquid and vapour side

$$\dot{m}_{\mathrm{evap}} = \frac{\dot{Q}_{\mathrm{l,int}} + \dot{Q}_{\mathrm{v,int}}}{\Delta h_{\mathrm{v}} S_{\mathrm{int}}} = \frac{V_{\mathrm{cell}} \left(\dot{\Sigma}_{\mathrm{e,l}} + \dot{\Sigma}_{\mathrm{e,v}} \right)}{\Delta h_{\mathrm{v}} S_{\mathrm{int}}} = \frac{\dot{Q}_{\mathrm{evap}}}{\Delta h_{\mathrm{v}} S_{\mathrm{int}}} \tag{2.42}$$

The index i is suppressed to increase readability. The mass flux is positive in case of evaporation and negative in case of condensation.

Distributing the mass source terms

For stability reasons, the source terms are re-distributed. The initial mass source term $\dot{\rho}_0$ in $\mathrm{kg\,s^{-1}\,m^{-3}}$ reads

$$\dot{\rho}_0 = \frac{\dot{m}_{\mathrm{evap}} S_{\mathrm{int}}}{V_{\mathrm{cell}}} \,. \tag{2.43}$$

The distributed mass source term $\dot{\rho}^*$ is calculated according to the diffusion equation

$$\tilde{D} \nabla^2 \dot{\rho}^* = \dot{\rho}^* - \dot{\rho}_0 \,. \tag{2.44}$$

$\tilde{D}$ denotes a constant, which is chosen approximately as $(4\Delta x)^2$ for each simulation. The distributed mass, volume, and energy source terms are defined in the Equations 2.45–2.47, respectively

$$\dot{\rho} = \left[N_{\mathrm{v}} (1-\alpha)\, \mathrm{H}(\alpha_0 - \alpha) - N_{\mathrm{l}} \alpha \mathrm{H}(\alpha_0 - 1 + \alpha) \right] \dot{\rho}^* \,, \tag{2.45}$$

$$\dot{\Sigma}_{\mathrm{V}} = \dot{\rho} \left[\frac{\mathrm{H}(\alpha_0 - \alpha)}{\rho_{\mathrm{v}}} - \frac{\mathrm{H}(\alpha_0 - 1 + \alpha)}{\rho_{\mathrm{l}}} \right] , \tag{2.46}$$

$$\dot{\Sigma}_{\mathrm{e,sens}} = \left[N_{\mathrm{v}} (1-\alpha)\, \mathrm{H}(\alpha_0 - \alpha)\, c_{\mathrm{v}} - N_{\mathrm{l}} \alpha \mathrm{H}(\alpha_0 - 1 + \alpha)\, c_{\mathrm{l}} \right] \dot{\rho}^* \, T \,. \tag{2.47}$$

$\mathrm{H}(x)$ denotes the Heaviside function and α_0 is a cut-off value[5], both guaranteeing no overlapping of the source term regions for the individual phases, liquid and vapour. The scaling factors N_{v} and N_{l} are chosen to ensure global mass conservation and read

$$N_{\mathrm{v}} = \left[\iiint_V \dot{\rho}_0 \, \mathrm{d}V \right] \left[\iiint_V (1-\alpha)\, \mathrm{H}(\alpha_0 - \alpha)\, \dot{\rho}^* \, \mathrm{d}V \right]^{-1} , \tag{2.48}$$

$$N_{\mathrm{l}} = \left[\iiint_V \dot{\rho}_0 \, \mathrm{d}V \right] \left[\iiint_V \alpha \mathrm{H}(\alpha_0 - 1 + \alpha)\, \dot{\rho}^* \, \mathrm{d}V \right]^{-1} . \tag{2.49}$$

2.3.4 Conjugate heat transfer and coupling of the subscale model

Heat flux and heat flow in contact line cells and other wall cells

The heat flux in a computational cell that contains a part of the three-phase contact line is composed of two contributions. One contribution arises from the subscale model and the transferred heat within the micro region. The other contribution is the heat transfer within the liquid part. The latter part is referred

[5] $\tilde{D} = 2.56 \cdot 10^{-10}$ for a $4\,\mu$m grid and $\alpha_0 = 0.1$ are used

to as transition zone. The transition zone is the liquid enclosed between the liquid-vapour interface and the wall deducting the width of the contact line region. The contact line position, speed, and length is taken from the interface reconstruction step.

The heat flux within the transition zone takes into account the thermal resistance caused by phase change R_{int} at the liquid-vapour interface. The heat flux is calculated by

$$\dot{q}_{\text{trans}} = \frac{T_{\text{w,mic}} - T_{\text{sat}}}{\frac{\delta}{k_{\text{l}}} + \frac{R_{\text{int}}}{\tan\theta}} \tag{2.50}$$

in which $T_{\text{w,mic}}$ denotes the wall temperature. The heat flux $\dot{q}_{\text{trans}}$ must be integrated over the wall face area covered by the transition zone to obtain the heat flow $\dot{Q}_{\text{trans}}$. $\dot{q}_{\text{trans}}$ is a function of liquid height δ and, therefore, depends on the local alignment of the liquid-vapour interface and liquid-wall surface. A detailed description of the integration method for an arbitrary mesh can be found in [2].

Finally, the heat flux in a contact line cell $\dot{q}_{\text{clc}}$ is the sum of the integrated heat flux per contact line length $\dot{Q}_{\text{mic}}$ multiplied by the length of the contact line region L_{cl} and the heat flow across the transition zone $\dot{Q}_{\text{trans}}$ divided by the entire wall face area of the contact line cell $|\mathbf{S}_{\text{f,w}}|$.

$$\dot{q}_{\text{clc}} = \frac{\dot{Q}_{\text{mic}} L_{\text{cl}} + \dot{Q}_{\text{trans}}}{|\mathbf{S}_{\text{f,w}}|} \tag{2.51}$$

Within the contact line cell, heat transferred from the wall to the vapour is neglected.

The remaining heat fluxes at the fluid-solid coupled boundary are covered by Fourier's law using the thermal conductivity of the fluid (c.f. Equation 2.25) with respect to the volume fraction field

$$\dot{q}_{\text{w,fluid}} = \begin{cases} \dot{q}_{\text{w,clc}}, & \text{in contact line cells} \\ k_{\text{w,fluid}} \left(\nabla T_{\text{w,fluid}} \cdot \mathbf{n}_{\text{w}} \right), & \text{elsewhere}. \end{cases} \tag{2.52}$$

To sum up, the fluid-sided heat flux $\dot{q}_{\text{w,fluid}}$ at the wall is a function of current temperature field of the fluid and the solid-sided wall temperature. The current $\dot{q}_{\text{w,fluid}}$ is used as boundary condition to solve for the temperature field of the solid in the next time step.

Fluid-solid coupling

Solving the energy equations for the temperature field of the fluid and solid domain is an iterative process since they have direct contact and interact with each other. In Table 2.1 an overview of the boundary conditions and the calculated values is given. In summary, the following steps are performed:

- solving the energy equation of the **fluid** domain with the boundary condition $T_{\text{w,fluid}} = T_{\text{w,solid}}$ to obtain the temperature field of the fluid,
- calculation of the heat flux field of the **fluid** $\dot{q}_{\text{w,fluid}}$ from the temperature field of the fluid,
- solving the energy equation of the **solid** domain with the boundary condition $\dot{q}_{\text{w,solid}} = \dot{q}_{\text{w,fluid}}$ to obtain the temperature field of the solid,
- calculation of the heat flux field of the **solid** $\dot{q}_{\text{w,solid}}$ from the temperature field of the solid domain,
- comparison of the temperature fields of the fluid and the solid at the solid-liquid surface. If the difference is larger than a threshold value[6], re-start with the first step; otherwise the energy equation is considered converged and the iteration ends.

[6] In this work, the threshold for the absolute temperature difference is set to 10^{-4} K.

Table 2.1.: Boundary conditions for and calculated quantities from the energy equations of the fluid and the solid domain, respectively.

	Fluid domain	Solid domain
Boundary condition for the energy equation	$T_{\mathrm{w,fluid}} = T_{\mathrm{w,solid}}$	$\dot{q}_{\mathrm{w,solid}} = \dot{q}_{\mathrm{w,fluid}}$
Calculated from the energy equation	$\dot{q}_{\mathrm{w,fluid}}$	$T_{\mathrm{w,solid}}$

Coupling of the parametrised results of the micro region

When the drop is in contact with the wall, the apparent contact angle θ is prescribed according to the results of the micro region model, which will be described in detail in the next Chapter. The results for the transferred heat in the vicinity of the three-phase contact line, $\dot{Q}_{\mathrm{mic}}$, and the film thickness at the end of the micro region, δ_{end}, are also obtained in the micro region model. The micro region model is evaluated for a set of wall superheats, contact line velocities, and ambient pressures. For each pressure level, θ, $\dot{Q}_{\mathrm{mic}}$, and δ_{end} are given as a parametrised regression according to the procedure described in [2, p. 56]. The parameters can be found in Appendix C.

2.3.5 Temporal and spatial discretisation

In order to solve the set of partial differential equations numerically, a numerical grid is necessary. The computational domain is divided into a finite number of volumes and is block-structured. Besides a number of validation scenarios, all drop impact simulations are performed in a quasi 2D manner. The grid is locally refined and the number of cells stays constant within a simulation run. Further details on the numerical grid can be found in the individual sections for validation and simulation cases.

Furthermore, interpolation schemes and approximations for the derivatives of cell values are needed to compute the gradients, divergences, and the Laplace operator for the unknown variables. A summary of the used numerical schemes can be found in Appendix C.

For time integration of the volume fraction field, a Crank-Nicholson method is utilised. For time integration of all other quantities, a first order Euler implicit method is used.

The Courant number Co is a key quantity for the choice of the time step size Δt. The Courant number scales the time step size Δt with the characteristic convection time $\Delta x \, |\mathbf{u}|^{-1}$

$$\frac{|\mathbf{u}|}{\Delta x} \Delta t = Co < 1 \,. \tag{2.53}$$

The initial drop impact velocity is in the order of $1\,\mathrm{m\,s^{-1}}$, the grid size in the order of $10^{-6}\,\mathrm{m}$. To ensure a Courant number smaller than unity, a time step size Δt in the order of $10^{-6}\,\mathrm{s}$ is required. Throughout the thesis, Co is less than 0.1 everywhere in the computational domain at every time during the simulation.

In some situations during drop impact, capillary waves at the drop's liquid-vapour interface might develop and evolve. To temporally capture capillary waves, the capillary Courant number Co_Φ, originally introduced by Brackbill [10], is used

$$\frac{2\left[\dfrac{\sigma\pi}{(\rho_{\mathrm{l}}+\rho_{\mathrm{v}})}\right]^{1/2}}{\Delta x^{3/2}} \Delta t_\Phi = Co_\Phi < 1 \,. \tag{2.54}$$

At atmospheric pressure, for example, the surface tension σ is in the order of $10^{-2}\,\mathrm{N\,m^{-1}}$, the liquid's density is in the order of $10^{3}\,\mathrm{kg\,m^{-3}}$. To guarantee a capillary Courant number smaller than unity, a time step size Δt_Φ in the order of $10^{-6}\,\mathrm{s}$ is required. The capillary Courant number stays constant within one

simulation case but varies with ambient pressure. However, Co_Φ stays in the same order of magnitude within the pressure range investigated.

To capture compressible effects, such as a shock wave, much smaller time step sizes are mandatory. Pressure waves propagate with the speed of sound a across the computational domain. A definition of the acoustic Courant number Co_a is applied in [53]

$$\frac{a}{\Delta x}\Delta t = Co_\mathrm{a} < 1\,. \tag{2.55}$$

At 1 bar and saturation temperature, the speed of sound a is in the order of $400\,\mathrm{m\,s^{-1}}$ for liquid and $100\,\mathrm{m\,s^{-1}}$ for vaporous FC–72 [42, 67]. An acoustic Courant number smaller than unity and a minimal grid spacing of $\Delta x = 4\,\mu\mathrm{m}$ results in a time step in the order of $\Delta t = 10^{-8}\,\mathrm{s}$ and smaller. Since no tremendous influence of the compressibility on the fluid flow is expected (see Section 2.1), the requirements arising from the acoustic Courant number seem to be too strict. Hence, the acoustic Courant number is not considered in this work. Consequently, even if a compressible effect occurred, its propagation would not be resolved temporally[7]. Further discussions about the speed of sound can be found in Appendix A.2.

The utilised adaptive time step size in the numerical simulations is a choice of Co and Co_Φ

$$\Delta t = \min\left\{0.1\frac{\Delta x}{u_\mathrm{mean}},\quad \left[\frac{(\rho_\mathrm{l}+\rho_\mathrm{v})}{4\sigma\pi}\right]^{1/2}\Delta x^{3/2}\right\}. \tag{2.56}$$

Calculations for this research were conducted on the Lichtenberg high performance computer of the TU Darmstadt. With the proposed temporal and spacial discretisation, as well as a case specific number of CPU cores varying between 12 and 196 cores, the computational time ranges from 10 h to one week for a single simulation run.

2.4 Model overview

An overview of the overall solution procedure of the CFD simulation is given in Figure 2.1. After initialising all relevant fields and setting the time step according to Equation 2.56, the transport equation of the VoF field is solved using the MULES algorithm. From the obtained VoF field, the liquid-vapour interface can be reconstructed and the contact line position, speed, and length is obtained. The evaporation procedure calculates source terms for energy, mass, and volume. The evaporation procedure is iteratively coupled with the solution algorithm of the energy equation to obtain the temperature fields. For solving the momentum coupled with the mass conservation equation, Equations 2.12 and 2.13, solving for the velocity and the pressure field, the pressure-implicit split-operator (PISO) algorithm is used.

[7] With increasing computational power, small time step simulations for long time scales, such as the drop impact including shock wave propagation, might become feasible in the future.

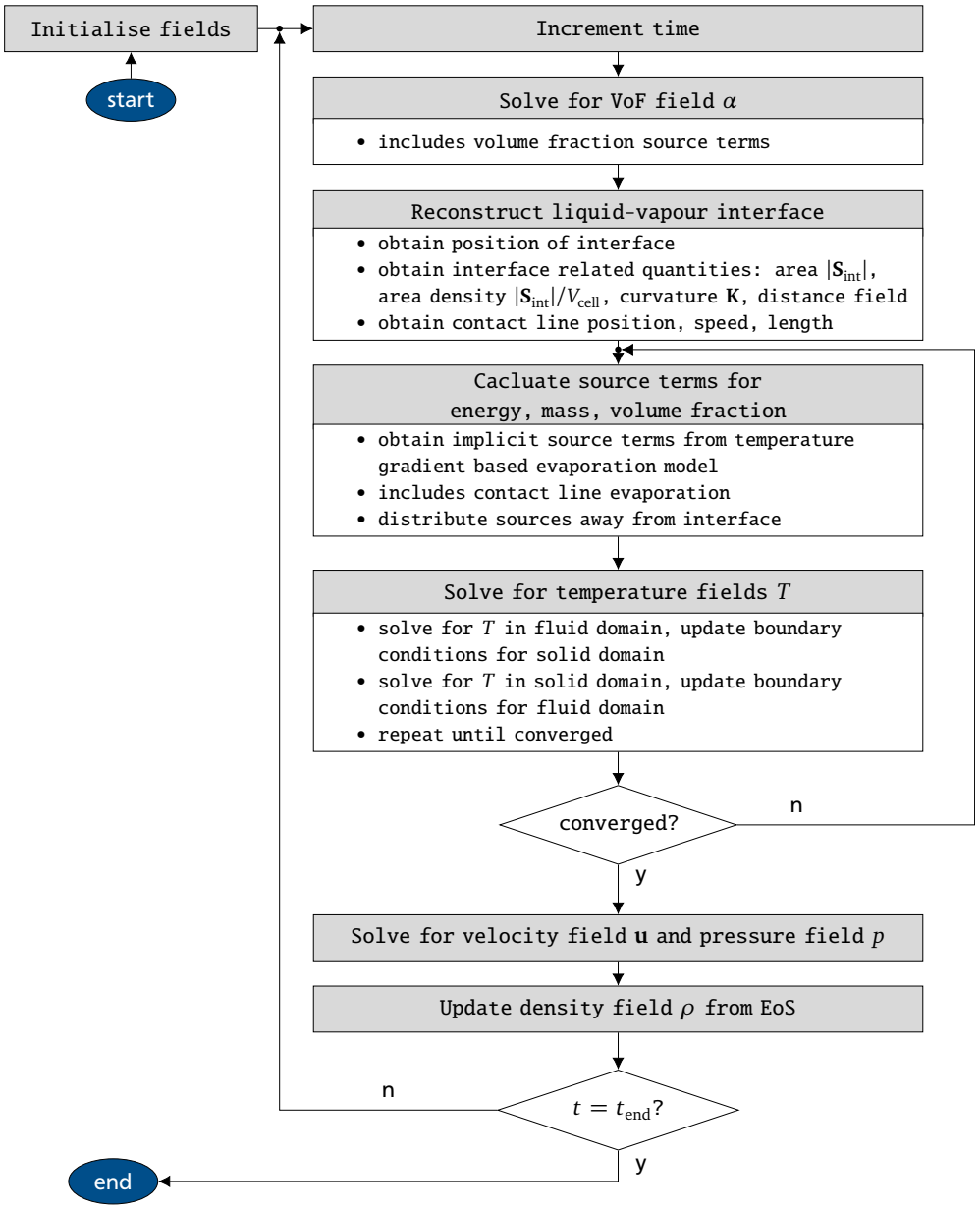

Figure 2.1.: Flowchart of the evaporative, compressible, two phase solver compressibleEvapVOF with contact line handling.

CHAPTER 3

Modelling of the Evaporating Three-Phase Contact Line (Micro Region)

In the vicinity of the three-phase contact line, fluid dynamics and thermodynamic phenomena occur that are influencing each other. The fluid dynamics affects the transferred heat. The transferred heat influences the apparent contact angle. The contact angle in turn dominates the fluid dynamics. To capture these effects in a macro-scale CFD model, high spatial resolution close to the three-phase contact line is necessary. To avoid high numerical effort, a special treatment of the small area around the three-phase contact line is applied, namely the concept of the micro region. The results from the micro region model are coupled with the CFD model. In the micro region model, short-scale effects like the disjoining pressure and the Kapitza resistance are taken into account. The model development is clustered into the following steps which are described in this Chapter unless otherwise specified.

- **Mathematical description of the micro region model**. The governing equations of the micro region model are the conservation laws of mass, momentum, and energy. Physical assumptions reduce the complexity of the underlying mathematical model. The most important assumptions are incompressibility, the lubrication approximation, and quasi-stationarity. Together with the necessary boundary conditions, the derived solution is a 4th order differential equation for the micro region model. In this thesis, the Kapitza resistance is introduced to the micro region model.
- **Solution procedure of the micro region model**. The differential equation for the micro region has no analytical solution and needs to be solved numerically. For numerical reasons, the differential equation together with the initial conditions are re-arranged non-dimensionally. The numerical scheme for the solution algorithm of the micro region model is a combination of a shooting and Runge-Kutta method.
- **Analysis of the micro region model**. Validation in terms of comparison with experimental results is not possible for the stand-alone micro region model with state-of-the-art experimental equipment. Nevertheless, sensitivity analyses regarding material properties and non-dimensional groups are performed to reinforce the results arising from the micro region model.
- The **Results of the micro region model** are the evolution of the micro region film thickness, the apparent contact angle, and the transferred heat. These quantities are functions of wall superheat, the contact line velocity, and material properties of the fluid. A parameter study is performed evaluating the influence of pressure on the results of the micro region model. A pressure range of $0.005 \leq p/p_{\mathrm{cr}} < 1$ is considered and results are discussed in Chapter 6.

3.1 Micro region model with Kapitza resistance

When investigating evaporating drops on hot surfaces, it is mandatory to take processes at the three-phase contact line into account. The liquid height and hence the thermal resistance within the liquid is small. The liquid-vapour interface is approximately at saturation temperature whereas the wall is superheated. Strong temperature gradients exist close to the three-phase contact line enhancing evaporation. Moving three-phase contact lines exist during drop impact and during bubble growth in nucleate boiling.

Instead of a sharp contact between the liquid-vapour interface and the wall, Potash and Wayner [80] introduced an alternative concept. This concept proposes the existence of a thin adsorbed layer of fluid molecules at the apparently dry parts of the solid surface. The adsorbed layer gradually transforms into the adjacent liquid bulk forming the apparent contact angle. The concept was originally called "interline region" [105]. The concept was adopted by Stephan [95] and Stephan and Busse [96], who coined the term micro region due to its small characteristic length scales.

The model proposed by Stephan, as well as Stephan and Busse was used with modifications by Kunkelmann [55]. Additionally, Batzdorf augmented the model for moving contact lines [2, 46] and applied it to drop impact [47] and pool boiling phenomena [26]. In the present thesis, the micro region model is further extended by an additional thermal resistance at the solid–liquid surface.

Before introducing the mathematical description of the micro region, it is helpful to address two quantities separately. The first quantity is the capillary pressure p_c. The capillary pressure is the pressure difference between the vapour pressure and the liquid pressure close to the liquid-vapour interface and reads

$$p_c = \sigma K - \dot{m}_{evap}^2 \left[\frac{1}{\rho_v} - \frac{1}{\rho_l} \right] + \frac{A}{\delta^3} . \tag{3.1}$$

The first term on the right-hand side is the pressure difference caused by the local curvature K of the liquid-vapour interface. The second term on the right-hand side is the recoil pressure due to phase change. It contains the evaporated mass flux $\dot{m}_{evap}$ across the liquid-vapour interface. The last term on the right-hand side arises from adhesion forces between the fluid and the solid molecules and is referred to as disjoining pressure. A is the dispersion constant[1] while δ denotes the local film height between solid surface and liquid-vapour interface. The capillary pressure changes the thermodynamic equilibrium at the liquid-vapour interface locally leading to higher pressures and consequently higher temperatures at which evaporation can occur. Therefore, evaporation across the liquid-vapour interface can occur only if the temperature at the liquid-vapour interface T_{int} exceeds the temperature of thermal equilibrium at the interface $T_{sat}(p_v + p_c)$ and the saturation temperature of the vapour bulk $T_{sat}(p_v)$, i.e. $T_{int} > T_{sat}(p_v + p_c) > T_{sat}(p_v)$.

The second quantity is the evaporated mass flux $\dot{m}_{evap}$ across the liquid-vapour interface itself. Schrage [90] proposed a description of the net evaporated mass flux across an evaporating interface from a molecular kinetics perspective. With several assumption that are

- the linearisation of the correction term in the original proposed mass flux,
- the use of the ideal gas law for substitution of the vapour density,
- the use of the Clausius-Clapeyron equation to estimate the saturation temperature, and
- assuming $\rho_v \ll \rho_l$

[1] For the combination of FC-72 and chromium, the dispersion constant is estimated to $A = 4.37 \cdot 10^{-21}$ J [2].

the net mass flux across the interface for a single component fluid becomes

$$\dot{m}_{\mathrm{evap}} = \frac{2f}{2-f} \frac{\rho_{\mathrm{v}} \Delta h_{\mathrm{v}}}{T_{\mathrm{sat}} \sqrt{2\pi R_{\mathrm{gas}} T_{\mathrm{sat}}}} \left[T_{\mathrm{int}} - T_{\mathrm{sat}} \left(1 + \frac{p_{\mathrm{c}}}{\Delta h_{\mathrm{v}} \rho_{\mathrm{l}}} \right) \right]. \tag{3.2}$$

T_{sat} denotes the saturation temperature according to the vapour bulk pressure $T_{\mathrm{sat}} = T_{\mathrm{sat}}(p_{\mathrm{v}})$. Δh_{v}, ρ_{v}, ρ_{l}, and R_{gas} denote the material properties latent heat of vaporisation, density of the vapour and liquid, as well as the individual gas constant, respectively. The parameter f is referred to as condensation coefficient[2] and represents the ratio of the number of condensed molecules to the total number of vapour molecules hitting the liquid-vapour interface.

Governing equations

The governing equations for the mathematical description of the micro region are incompressible, two-dimensional, stationary conservation laws of mass, momentum, and energy. Additionally, in order to reduce the complexity of the model, a dimension analysis is conducted, suggesting the assumptions:

- In the liquid layer, the spatial extension is much higher along the wall than perpendicular to it. In addition, the Reynolds number is small (lubrication approximation).
- The wall temperature within the micro region is uniform.
- The heat transfer is one-dimensional.

An extra term to account for the disjoining pressure normal to the wall is added to the lubrication approximation. The system of differential equations reads

$$0 = \frac{\mathrm{d}u_{\xi}}{\mathrm{d}\xi} + \frac{\mathrm{d}u_{\eta}}{\mathrm{d}\eta}, \tag{3.3}$$

$$0 = -\frac{\mathrm{d}p_{\mathrm{l}}}{\mathrm{d}\xi} + \mu_{\mathrm{l}} \frac{\mathrm{d}^2 u_{\xi}}{\mathrm{d}\eta^2}, \tag{3.4}$$

$$0 = -\frac{\mathrm{d}p_{\mathrm{l}}}{\mathrm{d}\eta} - \frac{3\,A}{\eta^4}, \tag{3.5}$$

$$0 = \frac{\mathrm{d}^2 T}{\mathrm{d}\eta^2}. \tag{3.6}$$

In Figure 3.1 a sketch of the micro region (left) and the boundary conditions for the conservation laws (right) are shown. For negative values of ξ, an adsorbed layer of liquid that cannot evaporate exists. At the end of the micro region, the film transitions into a constant slope, which forms the apparent contact angle θ. The value of ξ_{end} is chosen to ensure a larger film height compared to the thickness of the adsorbed layer. For a large film height the effect of adhesion forces on the thermal equilibrium diminishes. Additionally, the thermal resistance within the liquid is dominating and reduces the heat flux. Throughout this thesis, the end of the micro region is considered to be at $\xi_{\mathrm{end}} = 0.5\,\mu\mathrm{m}$. The value of ξ_{end} is chosen to guarantee a smooth transition to the macroscopic meniscus [2, 26, 55]. All material properties are expected to be independent of temperature and pressure within the computational domain.

Energy conservation

The differential Equation 3.6 is the one-dimensional energy equation. The thermal energy is transferred across the solid-liquid surface, through the liquid film, and across the liquid-vapour interface.

[2] The condensation coefficient is considered constant throughout the thesis and is $f = 0.5$ [2].

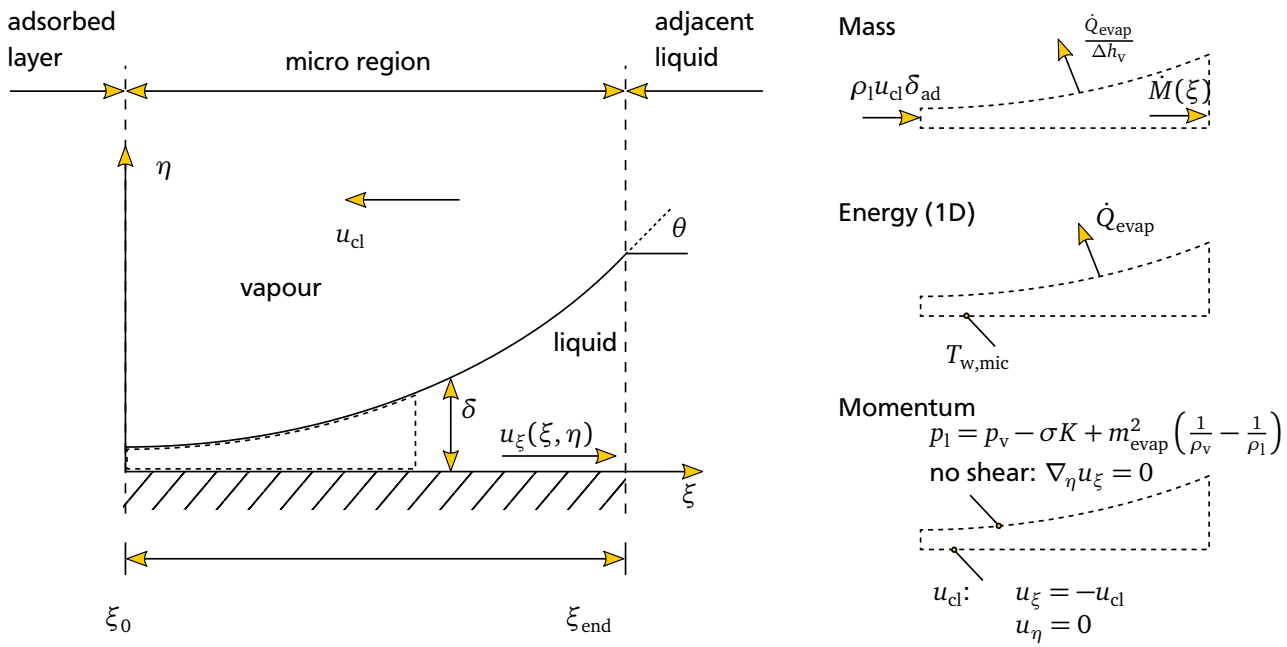

Figure 3.1.: Sketch of the micro region (left) and boundary conditions (right).

At the solid-liquid surface the so-called Kapitza resistance is present. The Kapitza resistance is an additional thermal resistance arising from the direct contact of two different materials. In 1941, Kapitza studied the heat flux between copper and liquid helium for very low temperature [89]. In the experiments, Kapitza observed a temperature discontinuity across the solid-liquid surface. Recently, molecular dynamic simulations were conducted determining the thermal resistance and the reciprocal, the thermal conductance, across the solid-fluid interface [43]. For the investigated pressure range, the Kapitza resistance R_{Kap} is assumed to be constant as proposed in [43].

Within the pure liquid film, only heat conduction is present. The thermal resistance R_{liq} scales with the local thickness of the film. The description of evaporation across the liquid-vapour interface is boiled down to a thermal resistance R_{int}. The evaporative heat flux $\dot{q}_{evap}$ can be calculated by

$$\dot{q}_{evap} = \dot{m}_{evap} \Delta h_v \,, \tag{3.7}$$

using the evaporated mass flux given in Equation 3.2.

In summary, there are three different regions in which the energy Equation 3.6 is applied:

- **I: Heat transfer across the solid-liquid surface.** The temperature at the surface on the solid side is $T_{w,mic}$ whereas the temperature at the surface at the liquid side is T_{Kap}. The heat flux $\dot{q}_{mic}$ across the solid-liquid surface can be determined by

$$\dot{q}_{mic} = \frac{T_{w,mic} - T_{Kap}}{R_{Kap}} \,. \tag{3.8}$$

- **II: Conductive heat transfer in the liquid film.** The temperature at the liquid-vapour interface on the liquid side is T_{int}. Using Equation 3.6 and applying $T = T_{Kap}$ at $\eta = 0$ and $T = T_{int}$ at $\eta = \delta$ results in the heat flux within the liquid film

$$\dot{q}_{mic} = \frac{T_{Kap} - T_{int}}{R_{liq}} \,. \tag{3.9}$$

The local thermal resistance of the liquid is given by

$$R_{\mathrm{liq}} = \frac{\delta}{k_{\mathrm{l}}}, \tag{3.10}$$

with k_{l} denoting the thermal conductivity of the liquid.

- **III: Evaporation across the liquid-vapour interface.** The thermodynamic equilibrium is shifted towards higher pressure and temperature at the interface due to the capillary pressure inside the micro region. This results in a raised temperature at the interface on the vapour side being at the same time the minimum temperature for evaporation to occur at the interface, $T_{\mathrm{int,min}} = T_{\mathrm{sat}}\left(1 + \frac{p_{\mathrm{c}}}{\Delta h_{\mathrm{v}} \rho_{\mathrm{l}}}\right)$. The evaporative heat flux $\dot{q}_{\mathrm{evap}}$ across the liquid-vapour interface reads

$$\dot{q}_{\mathrm{evap}} = \frac{T_{\mathrm{int}} - T_{\mathrm{int,min}}}{R_{\mathrm{int}}}, \tag{3.11}$$

with R_{int} denoting the thermal resistance caused by evaporation. R_{int} can be determined using the above equation, as well as Equations 3.2 and 3.7 to

$$R_{\mathrm{int}} = \frac{2-f}{2f} \frac{T_{\mathrm{sat}} \sqrt{2\pi R_{\mathrm{gas}} T_{\mathrm{sat}}}}{\rho_{\mathrm{v}} \Delta h_{\mathrm{v}}^2}. \tag{3.12}$$

Note that the R_{int} is solely a function of material properties, the condensation coefficient, and the saturation temperature at a given vapour bulk pressure.

Due to the slope of the liquid-vapour interface, the area of the liquid-vapour interface is larger than the area of the solid-liquid surface. Nevertheless, the heat flow across the different areas is equal

$$\dot{Q}_{\mathrm{mic}} = \dot{Q}_{\mathrm{evap}}. \tag{3.13}$$

Due to the one-dimensional assumption of energy transfer in the micro region, which is perpendicular to the wall, no lateral heat flow exists. The area correction for the liquid-vapour interface can be taken into account by the arc length of the liquid film height function by

$$\dot{q}_{\mathrm{mic}} = \dot{q}_{\mathrm{evap}} \sqrt{1 + \delta'^2}. \tag{3.14}$$

The prime indicates the derivative with respect to ξ.

The Equations 3.8, 3.9 and 3.11, as well as the introduced area correction in Equation 3.14 can be rewritten in one common equation for the heat flux that reads

$$\dot{q}_{\mathrm{mic}} = \frac{T_{\mathrm{w,mic}} - T_{\mathrm{int,min}}}{R_{\mathrm{Kap}} + R_{\mathrm{liq}} + \frac{R_{\mathrm{int}}}{\sqrt{1+\delta'^2}}}. \tag{3.15}$$

Mass and momentum conservation

Applying mass conservation for the control volume depicted in Figure 3.1 gives

$$\dot{M}_{\mathrm{evap}} = \frac{\dot{Q}_{\mathrm{mic}}}{\Delta h_{\mathrm{v}}} = \dot{M}(\xi) - \dot{M}(\xi_0) \tag{3.16}$$

for the mass flow per contact line length in $\mathrm{kg\,m^{-1}\,s^{-1}}$. The mass flow per contact line length at the adsorbed film, $\dot{M}(\xi_0)$, is determined by

$$\dot{M}(\xi_0) = -\rho_\mathrm{l} u_\mathrm{cl} \delta_\mathrm{ad} \,. \tag{3.17}$$

u_cl and δ_ad denote the contact line velocity and the height of the adsorbed film, respectively. The mass flow per contact line length at other positions than the adsorbed film, $\dot{M}(\xi)$, needs to be evaluated with respect to the velocity profile, which varies in the direction normal to the wall. Therefore, the mass flux $\rho_\mathrm{l} u_\xi$ through the cross sectional area is integrated over the film height

$$\dot{M}(\xi) = -\int_0^\delta \rho_\mathrm{l} u_\xi \mathrm{d}\tilde{\eta} \,. \tag{3.18}$$

The velocity profile u_ξ can be expressed [2] by

$$u_\xi = -\frac{1}{\nu_\mathrm{l}\rho_\mathrm{l}} \frac{\mathrm{d}p_\mathrm{c}}{\mathrm{d}\xi} \left(\frac{\eta^2}{2} - \delta\eta \right) + u_\mathrm{cl} \,. \tag{3.19}$$

The above equation is determined by integrating the momentum Equation 3.4 twice with respect to η. A constant contact line velocity at the wall and the absence of shear at the liquid-vapour interface, i.e. $\left(\mathrm{d}u_\xi/\mathrm{d}\eta\right)_{\eta=\delta} = 0$, are used as boundary conditions resulting in Equation 3.19. Additionally, from the momentum Equation 3.5 it can be shown that the derivative of the pressure in the liquid is linear to the derivative of the capillary pressure, i.e $(\mathrm{d}p_\mathrm{l}/\mathrm{d}\xi) = -(\mathrm{d}p_\mathrm{c}/\mathrm{d}\xi)$, which is already applied in Equation 3.19.

Substituting Equation 3.19 into Equation 3.18 and solving the integral of Equation 3.18 leads to the mass flow $\dot{M}(\xi)$ at the position ξ that reads

$$\dot{M}(\xi) = -\frac{\delta^3}{3\nu_\mathrm{l}} \frac{\mathrm{d}p_\mathrm{c}}{\mathrm{d}\xi} - \rho_\mathrm{l} u_\mathrm{cl} \delta \,. \tag{3.20}$$

Now, the mass balance in Equation 3.16 can be rewritten using Equations 3.17 and 3.20 that reads

$$\dot{M}_\mathrm{evap} = \frac{\dot{Q}_\mathrm{mic}}{\Delta h_\mathrm{v}} = -\frac{\delta^3}{3\nu_\mathrm{l}} \frac{\mathrm{d}p_\mathrm{c}}{\mathrm{d}\xi} - \rho_\mathrm{l} u_\mathrm{cl} (\delta - \delta_\mathrm{ad}) \,. \tag{3.21}$$

Re-arranging the above equation and differentiating the heat flow per contact line length, $\dot{Q}_\mathrm{mic}$, with respect to ξ finally leads to a second formulation for the heat flux across the micro region

$$\dot{q}_\mathrm{mic} = \frac{\mathrm{d}\dot{Q}_\mathrm{mic}}{\mathrm{d}\xi} = \frac{\mathrm{d}}{\mathrm{d}\xi} \left[-\frac{\Delta h_\mathrm{v}}{3\nu_\mathrm{l}} \delta^3 \frac{\mathrm{d}p_\mathrm{c}}{\mathrm{d}\xi} - \Delta h_\mathrm{v} \rho_\mathrm{l} u_\mathrm{cl} (\delta - \delta_\mathrm{ad}) \right] . \tag{3.22}$$

Complete differential equation for the micro region

The capillary pressure introduced in Equation 3.1 uses the curvature of the liquid-vapour interface. The curvature K can be determined utilising the film thickness δ

$$K = \frac{\delta''}{[1 + \delta'^2]^{1.5}} \,. \tag{3.23}$$

Combining Equations 3.15 and 3.22 yields

$$\frac{T_{\mathrm{w,mic}} - T_{\mathrm{int,min}}}{R_{\mathrm{Kap}} + R_{\mathrm{liq}} + \frac{R_{\mathrm{int}}}{\sqrt{1+\delta'^2}}} = \frac{\mathrm{d}}{\mathrm{d}\xi}\left[-\frac{\Delta h_{\mathrm{v}}}{3\nu_{\mathrm{l}}}\delta^3\frac{\mathrm{d}p_{\mathrm{c}}}{\mathrm{d}\xi} - \Delta h_{\mathrm{v}}\rho_{\mathrm{l}}u_{\mathrm{cl}}(\delta - \delta_{\mathrm{ad}})\right]. \tag{3.24}$$

Using Equation 3.24 together with the auxiliary Equations 3.1, 3.2, 3.10, 3.12, and 3.23 results in a single 4th order, non-linear, ordinary differential equation (ODE). The expression

$$\frac{\mathrm{d}}{\mathrm{d}\xi}\left(\frac{\mathrm{d}p_{\mathrm{c}}}{\mathrm{d}\xi}\right) = \mathrm{f}(\delta'''', \delta''', \delta'') \tag{3.25}$$

contains the fourth derivative of the film thickness δ.

3.2 Solution procedure of the micro region model

The resulting non-linear ODE 3.24 has no analytical solution. For solving the ODE numerically, the single equation is split into a system of linear ODE. The system of differential equations including the Kapitza resistance reads

$$\begin{aligned}
\frac{\mathrm{d}\delta}{\mathrm{d}\xi} &= \delta' \\
\frac{\mathrm{d}\delta'}{\mathrm{d}\xi} &= \frac{\left(1+\delta'^2\right)^{1.5}}{\sigma}\left(p_{\mathrm{c}} - \frac{A}{\delta^3} + \frac{1}{\Delta h_{\mathrm{v}}^2}\left[\frac{T_{\mathrm{w,mic}} - T_{\mathrm{sat}}\left(1 + \frac{p_{\mathrm{c}}}{\Delta h_{\mathrm{v}}\rho_{\mathrm{l}}}\right)}{\left(R_{\mathrm{Kap}} + \frac{\delta}{k_{\mathrm{l}}}\right)\sqrt{1+\delta'^2} + R_{\mathrm{int}}}\right]^2\left(\frac{1}{\rho_{\mathrm{v}}} - \frac{1}{\rho_{\mathrm{l}}}\right)\right) \\
\frac{\mathrm{d}p_{\mathrm{c}}}{\mathrm{d}\xi} &= -\frac{3\nu_{\mathrm{l}}}{\delta^3\Delta h_{\mathrm{v}}}\left[\dot{Q}_{\mathrm{mic}} + \rho_{\mathrm{l}}\Delta h_{\mathrm{v}}u_{\mathrm{cl}}(\delta - \delta_{\mathrm{ad}})\right] \\
\frac{\mathrm{d}\dot{Q}_{\mathrm{mic}}}{\mathrm{d}\xi} &= \dot{q}_{\mathrm{mic}} = \frac{T_{\mathrm{w,mic}} - T_{\mathrm{sat}}\left(1 + \frac{p_{\mathrm{c}}}{\Delta h_{\mathrm{v}}\rho_{\mathrm{l}}}\right)}{R_{\mathrm{Kap}} + \frac{\delta}{k_{\mathrm{l}}} + \frac{R_{\mathrm{int}}}{\sqrt{1+\delta'^2}}}.
\end{aligned} \tag{3.26}$$

The four initial conditions for the above ODE system are defined at the beginning of the micro region, adjacent to the non-evaporating adsorbed layer

$$\delta_{\mathrm{ad}} = \delta(\xi = 0) = \left(\frac{A}{p_{\mathrm{c,ad}}}\right)^{1/3}, \tag{3.27}$$

$$\delta'_{\mathrm{ad}} = \delta'(\xi = 0) = 0, \tag{3.28}$$

$$p_{\mathrm{c,ad}} = p_{\mathrm{c}}(\xi = 0) = \left(\frac{T_{\mathrm{w,mic}}}{T_{\mathrm{sat}}} - 1\right)\Delta h_{\mathrm{v}}\rho_{\mathrm{l}}, \tag{3.29}$$

$$\dot{Q}_{\mathrm{ad}} = \dot{Q}_{\mathrm{mic}}(\xi = 0) = 0. \tag{3.30}$$

The adsorbed layer is parallel to the wall and has no slope, which is represented by Equation 3.28. At the same time, the adsorbed layer's curvature is equal to zero. The capillary pressure reduces to the contribution of the disjoining pressure in Equation 3.27. Due to the high capillary pressure at the adsorbed layer, no evaporation across the micro region occurs, which is reflected by Equation 3.30. The capillary pressure at the adsorbed layer can be computed using Equation 3.15 with zero heat flux across the micro region, which results in Equation 3.29.

The system of equations 3.26 varies strongly in the order of magnitudes. It is reasonable to non-dimensionalise the system of equations, as well as the initial conditions. The non-dimensional quantities read

$$\xi^* = \frac{\xi}{\delta_{\mathrm{ad}}}, \tag{3.31}$$

$$\delta^* = \frac{\delta}{\delta_{\mathrm{ad}}}, \tag{3.32}$$

$$\delta'^* = \delta', \tag{3.33}$$

$$p_{\mathrm{c}}^* = \frac{p_{\mathrm{c}}}{p_{\mathrm{c,ad}}}, \tag{3.34}$$

$$\dot{Q}^* = \frac{\dot{Q}_{\mathrm{mic}}}{k_{\mathrm{l}}\left(T_{\mathrm{w,mic}} - T_{\mathrm{sat}}\right)}. \tag{3.35}$$

The coordinate along the wall, ξ, as well as the film thickness δ are scaled with the thickness of the adsorbed layer δ_{ad}. The maximum pressure within the micro region occurs at the adsorbed layer $p_{\mathrm{c,ad}}$. Therefore, the capillary pressure is scaled with $p_{\mathrm{c,ad}}$. The maximum heat that can be transferred by thermal conduction within the liquid scales with the maximum temperature difference that can occur $\left(T_{\mathrm{w,mic}} - T_{\mathrm{sat}}\right)$. Consequently, the integrated heat flux per contact line length, $\dot{Q}_{\mathrm{mic}}$, is scaled with the maximum conductive heat flux per contact line length.

The system of differential equations in non-dimensional form reads

$$\begin{aligned}
\frac{\mathrm{d}\delta^*}{\mathrm{d}\xi^*} &= \delta'^* \\
\frac{\mathrm{d}\delta'^*}{\mathrm{d}\xi^*} &= D_1\left(1+\delta'^{*2}\right)^{1.5}\left[p_{\mathrm{c}}^* - \frac{1}{\delta^{*3}} + D_5\left(\frac{\left(1-p_{\mathrm{c}}^*\right)}{\left(D_6+\delta^*\right)\sqrt{1+\delta'^{*2}}+D_3}\right)^2\right] \\
\frac{\mathrm{d}p_{\mathrm{c}}^*}{\mathrm{d}\xi^*} &= -\frac{D_2\dot{Q}^* + D_4\left(\delta^*-1\right)}{\delta^{*3}} \\
\frac{\mathrm{d}\dot{Q}^*}{\mathrm{d}\xi^*} &= \frac{1-p_{\mathrm{c}}^*}{D_6+\delta^*+D_3\dfrac{1}{\sqrt{1+\delta'^{*2}}}}.
\end{aligned} \tag{3.36}$$

D_1–D_6 are non-dimensional groups defined as

$$\begin{aligned}
D_1 &= \frac{\delta_{\mathrm{ad}} p_{\mathrm{c,ad}}}{\sigma}, & D_4 &= \frac{3\mu_{\mathrm{l}} u_{\mathrm{cl}}}{\delta_{\mathrm{ad}} p_{\mathrm{c,ad}}}, \\
D_2 &= \frac{3\nu_{\mathrm{l}}}{\Delta h_{\mathrm{v}}}\frac{k_{\mathrm{l}}\left(T_{\mathrm{w,mic}} - T_{\mathrm{sat}}\right)}{\delta_{\mathrm{ad}}^2 p_{\mathrm{c,ad}}}, & D_5 &= \frac{k_{\mathrm{l}}^2\left(T_{\mathrm{w,mic}} - T_{\mathrm{sat}}\right)^2}{p_{\mathrm{c,ad}}\delta_{\mathrm{ad}}^2\Delta h_{\mathrm{v}}^2}\left(\frac{1}{\rho_{\mathrm{v}}} - \frac{1}{\rho_{\mathrm{l}}}\right), \\
D_3 &= R_{\mathrm{int}}\frac{k_{\mathrm{l}}}{\delta_{\mathrm{ad}}}, & D_6 &= R_{\mathrm{Kap}}\frac{k_{\mathrm{l}}}{\delta_{\mathrm{ad}}}.
\end{aligned} \tag{3.37}$$

The additional non-dimensional group D_6 arises from the Kapitza resistance and occurs in two out of four equations within the system of differential equations 3.36.

Using the non-dimensional quantities, the non-dimensional initial conditions read

$$\delta^*(\xi^* = 0) = 1\,, \tag{3.38}$$
$$\delta^{*\prime}(\xi^* = 0) = 0\,, \tag{3.39}$$
$$p_c^*(\xi^* = 0) = 1\,, \tag{3.40}$$
$$\dot{Q}^*(\xi^* = 0) = 0\,. \tag{3.41}$$

In addition, the model shall satisfy constrains within the micro region. From the adsorbed layer, the film thickness is growing. Hence, δ has to be greater than the adsorbed layer and the slope of the film thickness is always positive. However, the slope of the film thickness shall stay below 90 deg, i.e. $\tan^{-1}(\delta^{*\prime}_{\max}) < 90\,\text{deg}$, and therefore the maximum slope is limited to $\delta^{*\prime}_{\max} = 1000$ in this thesis. The capillary pressure is maximal at the adsorbed layer and decreases with increasing film thickness. In summary, the following constrains need to be satisfied within the entire micro region

$$\delta^* \geq 1\,, \tag{3.42}$$
$$\delta^{*\prime} \geq 0\,, \tag{3.43}$$
$$\delta^{*\prime} \leq \delta^{*\prime}_{\max}\,, \tag{3.44}$$
$$p_c^* \leq 1\,. \tag{3.45}$$

Solving the system of ODEs 3.36 in combination with the non-dimensional groups defined in the set of Equations 3.37 and applying the initial boundary conditions of Equations 3.38–3.41, however, runs into the trivial solution. The adsorbed layer fulfils the model, the boundary conditions, and the additional constrains specified in Equations 3.42–3.45.

Hence, the initial condition for the film is slightly perturbed by a constant offset ε_1

$$\delta^*(\xi^* = 0) = 1 + \varepsilon_1\,. \tag{3.46}$$

This situation, having a system of ODE to solve with initial boundary conditions including at least one parameter, is a standard situation found in two-point boundary value problems (TP-BVP). In TP-BVP, boundary conditions are prescribed a priory on two sides of the computational domain, i.e. at the beginning and at the end. The so-called shooting method is a numerical method to solve TP-BVP. Three steps are involved in shooting methods. First, find boundary conditions for the dependent variables at only one side of the domain. This might include unknown values, i.e. parameters, for the boundary conditions. Second, solve the ODE with a method of choice. Compare the results with the desired boundary conditions at the end of the domain. Repeat the first two steps with modified parameters. The last step is the optimisation of the parameters to find the parameters for which the results are closest to the boundary conditions defined at the end of the domain. Consequently, the parameters chosen for the boundary conditions are no arbitrary values but rather additional unknown quantities. The solutions of these quantities are obtained within the optimisation step.

The perturbation is $0 < \varepsilon_1 \ll 1$ and is set to $\varepsilon_1 = 10^{-3}$ in this work. Technically, the integration starts in the micro region where the film thickness has already increased slightly. Consequently, the remaining three boundary conditions must be adapted. However, the problem can be reduced to only one unknown boundary condition for the integrated heat flux $\dot{Q}_{\text{mic}}$ whereas the remaining boundary conditions for p_c^* and $\delta^{*\prime}$ are expected to encounter solely negligible variations. Hence, the boundary condition for the integrated heat flux becomes

$$\dot{Q}^*(\xi^* = 0) = \varepsilon_2\,. \tag{3.47}$$

Using the shooting method for the micro region, a boundary condition needs to be specified at the end of the micro region. The boundary condition might be the non-dimensional slope or the derivative of it. However, a combination of the two quantities is chosen that is represented by the curvature at the end of the micro region. The curvature at this position is the macroscopic curvature K_{mac} the value of which is set to $K_{\mathrm{mac}} = 10^5\,\mathrm{m}^{-1}$. Its actual value does not influence the results of the micro region as long the macroscopic curvature is smaller than the maximal curvature within the micro region [2, 55].

During the shooting method, the algorithm deployed in the present thesis includes the solution of the system of ODE using a Runge-Kutta method while the optimisation is performed applying the bisection method. A two-parameter optimisation for ε_1 and ε_2 was proposed in [96] whereas other authors [2, 26, 55] used a one-parameter optimisation for ε_2 only. The latter option is used in the present thesis, as well.

The initial guess for $\varepsilon_{2,0}$ is important and is $1 \gg |\varepsilon_{2,0}| \geq |\varepsilon_2|$ while its sign depends on the ratio of D_2 and D_4. For large values of ε_2, the film thickness tends to become negative. For small values of ε_2, the slope reaches almost infinity. The optimal value for ε_2 is found if the obtained results fulfil the constrains expressed in Equations 3.42–3.45 while the curvature at the end of the micro region convergences[3]. However, in some situations, ε_2 gets smaller than the computational accuracy. In these situations the concept of part intervals is adopted which was proposed by Stephan [96] and applied by Batzdorf [2]. A small portion of 1 % of the current interval is stored, $\varepsilon_{2,0}$ is increased, and the solving of the ODE system, as well as the optimisation restarts.

The final solution of the micro region is continuous in δ^*, $\delta^{*\prime}$ and p_{c}^* but discontinuous in the integrated transferred heat flux $\dot{Q}_{\mathrm{mic}}^*$ due to the optimisation process of ε_2. The integrated transferred heat flux obtains small jumps at the boundaries of the part intervals, which are small compared to the integrated transferred heat flux within the entire micro region.

3.3 Analysis of the micro region model

In this section, the results from the micro region model for the variation of different quantities is discussed. In the present thesis, the micro region model is augmented by the Kapitza resistance. The influence of the Kapitza resistance on the results is analysed in detail. Furthermore, the thesis considers variable ambient pressures, which causes changing material properties. The influence of the individual material properties, as well as the non-dimensional groups $D_1 - D_6$ is discussed in this section whereas the influence of various ambient pressures is presented in detail in Chapter 6.

3.3.1 Influence of the Kapitza resistance

The Kaptiza resistance for the material combination of FC-72 and chromium was obtained by molecular dynamics simulations published in [43]. In the molecular dynamics simulations, the thermal conductance G_{Kap} across the solid-fluid surface was determined to $G_{\mathrm{Kap}} = 9.27 \cdot 10^6\,\mathrm{W\,m^{-2}\,K^{-1}}$ for the pressure range investigated in the present thesis. A pressure dependence of the thermal conductance across the solid-fluid surface was observed in [43]. However, this pressure dependence was observed for much larger pressures than considered in the present thesis. Consequently, the thermal conductance and, hence, the thermal resistance $R_{\mathrm{Kap}} = G_{\mathrm{Kap}}^{-1}$ is constant within the present thesis if not stated otherwise. From the assumptions made in the molecular dynamics simulations it is expected that the value of R_{Kap} is a conservative estimation for perfect ambient conditions. This implies that the value for R_{Kap} obtained by experiments under perfect conditions probably stays between zero and R_{Kap} obtained by molecular dynamics simulations. For more details about the molecular dynamics simulations, the reader is referred to the publication of Han et al. [43]. However, the Kapitza resistance is a result of a short distance force acting between fluid and solid molecules and is considered only in the micro region model. Consequently, the Kapitza resistance is neglected in the macroscopic CFD simulations.

[3] Convergence for the optimisation of ε_2 is reached if the curvature at ξ_{end}^* differs less than 5 % from K_{mac}.

In Figure 3.2 results are shown calculated by the micro region model for different values of the Kapitza resistance ranging from zero to ten times the Kapitza resistance value. The latter limit can be considered as parameter study in terms of any thermal resistance existing between the hot wall and the liquid. A thermal resistance in the order of magnitude of $10R_{\mathrm{Kap}}$ may be caused by a nano-sized surface roughness or by an imperfect smooth surface.

Three key quantities that are obtained by the micro region model and used later in the macroscopic CFD simulations are the film thickness δ, the apparent contact angle θ and the integrated heat flux $\dot{Q}_{\mathrm{mic}}$ at the end of the micro region. In Figure 3.2(a) and (b), the evolution of δ and the slope is plotted along the micro region. For both quantities, a difference between a zero and unity R_{Kap} is hardly visible. As depicted in Figure 3.2(d), $\dot{Q}_{\mathrm{mic}}$ is influenced more strongly by the Kapitza resistance and the curves differ to a larger extent. In Table 3.1, the values at the end of the micro region are listed. The relative deviation from the unity Kapitza resistance, $\varepsilon = |\phi_{\cdot\mathrm{Kap}} - \phi_{1\mathrm{Kap}}|/\phi_{1\mathrm{Kap}}$, with ϕ being one of the considered quantities δ, θ, or $\dot{Q}_{\mathrm{mic}}$, is larger for $\dot{Q}_{\mathrm{mic}}$ than for δ and θ.

Table 3.1.: Influence of the Kapitza resistance at the end of the micro region $\xi_{\mathrm{end}} = 0.5\,\mu\mathrm{m}$ for contact line velocity $u_{\mathrm{cl}} = 0\,\mathrm{m\,s^{-1}}$, wall superheat $\Delta T = 5\,\mathrm{K}$, and material properties at atmospheric pressure $p = 1.013\,\mathrm{bar}$.

	δ in $10^{-7}\,\mathrm{m}$	θ in deg	$\dot{Q}_{\mathrm{mic}}$ in $\mathrm{Wm^{-1}}$
$0R_{\mathrm{Kap}}$	2.209	28.739	0.955
$0.01R_{\mathrm{Kap}}$	2.203	28.613	0.955
$0.1R_{\mathrm{Kap}}$	2.198	28.581	0.951
$1R_{\mathrm{Kap}}$	2.143	28.105	0.916
$10R_{\mathrm{Kap}}$	1.774	24.692	0.669
$100R_{\mathrm{Kap}}$	0.904	15.843	0.171

The local heat flux within the micro region is shown in Figure 3.2(e). The highest local heat flux is observed for zero Kapitza resistance at the location of highest film curvature. The local curvature of the film is plotted in Figure 3.2(c).

Different temperatures within the micro region model are depicted in Figure 3.2(f). The solid-sided wall temperature T_{w}, the liquid-sided liquid-vapour interface temperature T_{int}, and the minimal temperature to enable evaporation across the liquid-vapour interface $T_{\mathrm{int,min}}$ are plotted.

On the one hand, the Kapitza resistance leads to a temperature jump across the solid-fluid surface that scales linearly with the heat flux, c.f. Equation 3.8. The liquid at the wall in the micro region experiences a smaller wall temperature with Kapitza resistance than without. It can be expected that a Kapitza resistance influences the results more strongly if the wall superheat is increased. High heat fluxes caused by large wall superheats might lead to stronger temperature jumps across the solid-liquid surface. On the other hand, the Kapitza resistance is small and can only influence the results of the micro region if it is in the same order of magnitude as the other thermal resistances. This is the case if the film thickness is comparably small because the thermal resistance within the liquid is small, as well. Small film thicknesses are especially encountered for large receding contact line velocities.

The following analysis answers the question if high wall superheats and/or small film thicknesses intensifies the influence of the Kapitza resistance on the results of the micro region model. Therefore, the contact line velocity, as well as the wall superheat are varied using the micro region model. Both, u_{cl} and ΔT influence the film thickness and the transferred heat within the micro region.

In Figure 3.3, the influence of the Kapitza resistance on the apparent contact angle and on the integrated heat flux is shown as function of wall superheat. For small wall superheats, the apparent contact angle, as well as the transferred heat is small. Generally, for increasing wall superheat, the apparent contact

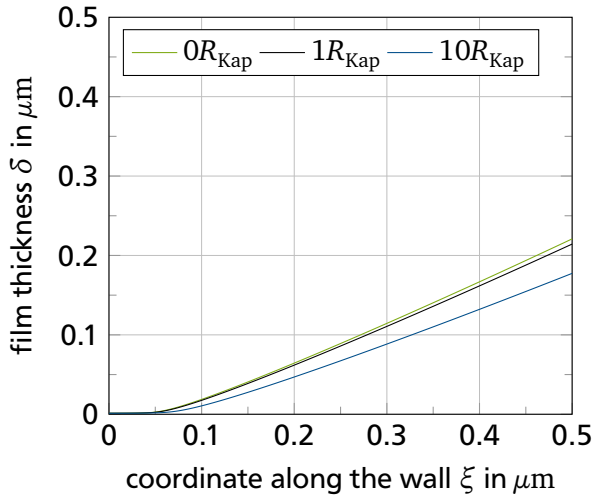

(a) Film thickness δ.

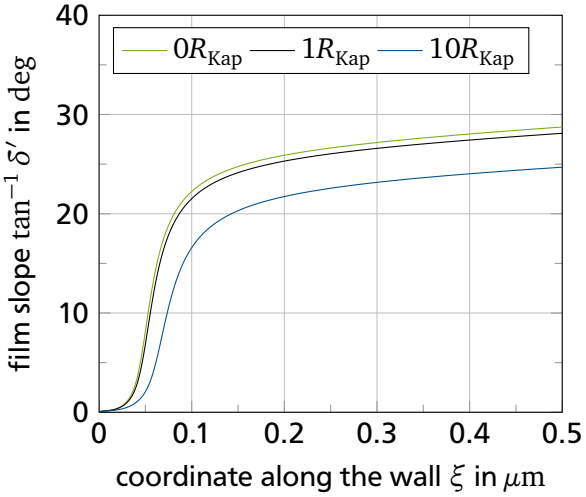

(b) Film slope δ'.

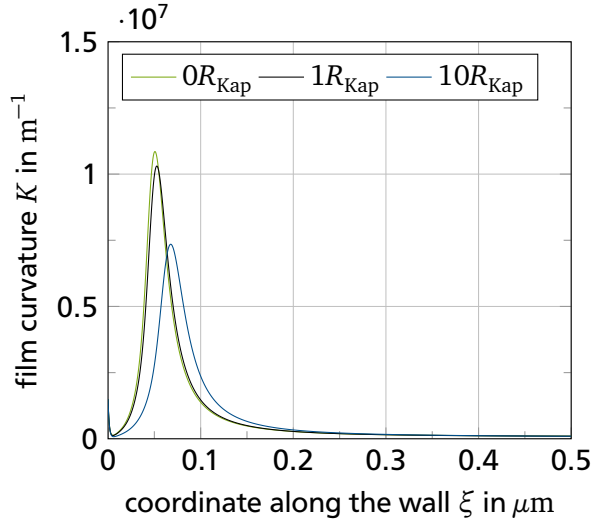

(c) Film curvature K.

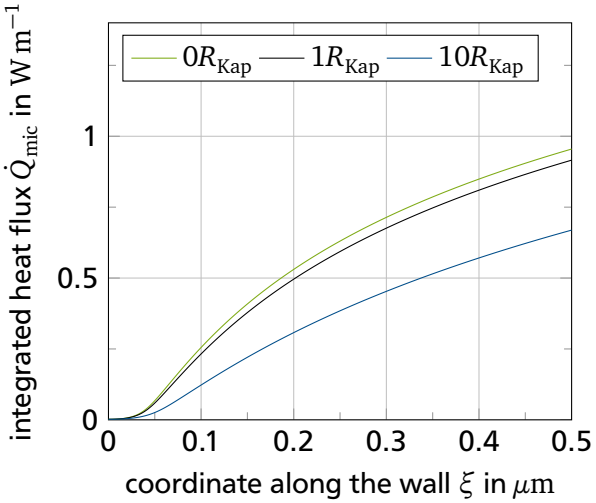

(d) Integrated heat flux $\dot{Q}_{\mathrm{mic}}$.

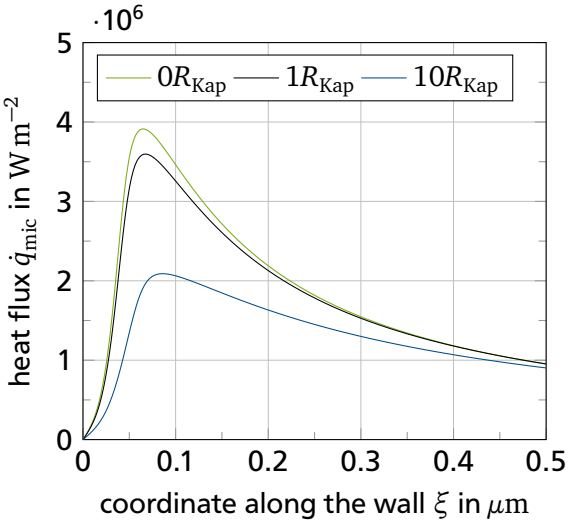

(e) Heat flux $\dot{q}_{\mathrm{mic}}$.

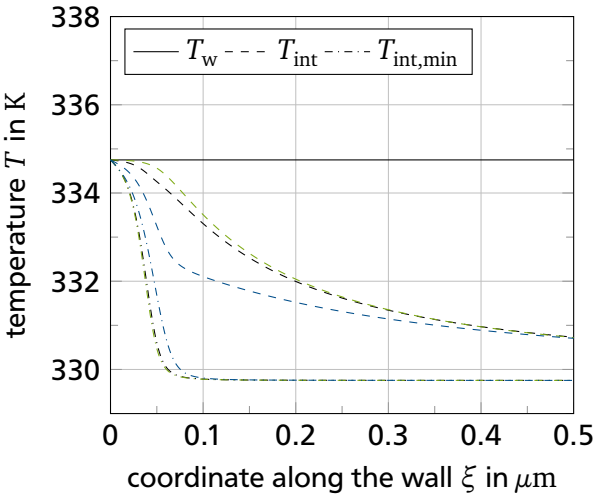

(f) Temperatures T.

Figure 3.2.: Influence of the Kapitza resistance ($R_{\mathrm{Kap}} = \left[9.27 \cdot 10^6\,\mathrm{W\,m^{-2}\,K^{-1}}\right]^{-1}$) on quantities of the micro region. Results obtained for contact line velocity $u_{\mathrm{cl}} = 0\,\mathrm{m\,s^{-1}}$, wall superheat $\Delta T = 5\,\mathrm{K}$, and material properties of FC-72 at atmospheric pressure $p = 1.013\,\mathrm{bar}$.

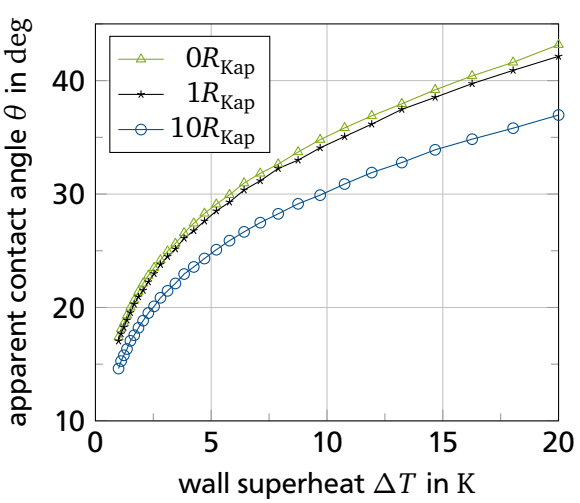

(a) Apparent contact angle θ as a function of wall superheat ΔT.

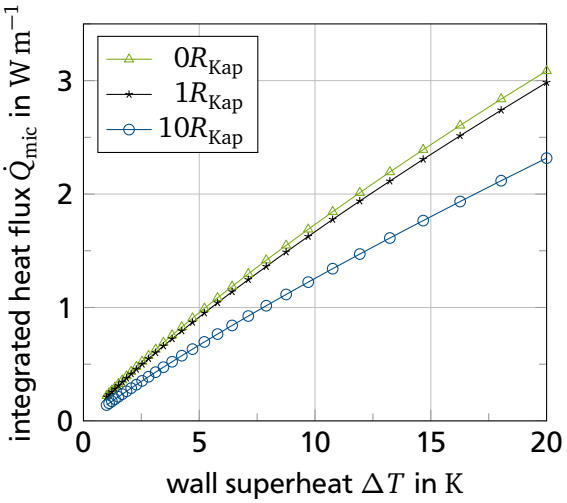

(b) Integrated heat flux $\dot{Q}_{\mathrm{mic}}$ across the micro region as a function of wall superheat ΔT.

Figure 3.3.: Influence of the Kapitza resistance on the apparent contact angle and on the integrated heat flux from the micro region model for different wall superheats at $u_{\mathrm{cl}} = 0\,\mathrm{m\,s^{-1}}$ and $p = 1.013\,\mathrm{bar}$.

angle, as well as the transferred heat increases. In [96], the influence of the wall superheat on the evolution of the micro region was discussed.

Both the apparent contact angle and the integrated heat flux decrease with increasing Kapitza resistance. To quantify the influence of the wall superheat on the results, it is helpful to inspect not only the absolute but also the relative deviation. Focussing on the influence of Kapitza resistance on the apparent contact angle, the relative deviation[4] $|\theta_{\cdot\mathrm{Kap}} - \theta_{1\mathrm{Kap}}|/\theta_{1\mathrm{Kap}}$ stays constant over the analysed wall superheat range. For the integrated heat flux, the relative deviation $|\dot{Q}_{\mathrm{mic},\cdot\mathrm{Kap}} - \dot{Q}_{\mathrm{mic},1\mathrm{Kap}}|/\dot{Q}_{\mathrm{mic},1\mathrm{Kap}}$ decreases with increasing wall superheat. It can be concluded that an increasing wall superheat does not amplify the influence of the Kapitza resistance on the results of the micro region.

In Figure 3.4, the influence of the Kapitza resistance on the apparent contact angle and on the integrated heat flux is shown as function of contact line velocity. Negative values of the contact line velocity refer to a receding motion of the contact line whereas positive values refer to an advancing motion. Generally, for large receding contact line velocities, the apparent contact angle is small and the transferred heat is large compared to high advancing contact line velocities. For increasing contact line velocity, the apparent contact angle increases whereas the transferred heat decreases. In [2], the influence of the contact line velocity on the evolution of the micro region was discussed.

The Kapitza resistance influences both, the apparent contact angle and the integrated heat flux for different contact line velocities. An increasing Kapitza resistance has an increasing influence on the contact angle and on the integrated heat flux. However, for the apparent contact angle, the influence of the Kapitza resistance as function of contact line velocity has a non-monotonic behaviour. At the lowest and highest contact line velocities in the investigated velocity range, it is observed that the absolute and relative deviation $|\theta_{\cdot\mathrm{Kap}} - \theta_{1\mathrm{Kap}}|/\theta_{1\mathrm{Kap}}$ is small compared to low receding, spreading or static contact line motions. However, the maximum deviation within the analysed velocity range is found at low receding contact line velocities. Regarding the integrated heat flux, the maximum absolute and relative deviation is found for high receding contact line velocities. For increasing advancing contact line velocities, the relative deviation $|\dot{Q}_{\mathrm{mic},\cdot\mathrm{Kap}} - \dot{Q}_{\mathrm{mic},1\mathrm{Kap}}|/\dot{Q}_{\mathrm{mic},1\mathrm{Kap}}$ stays constant.

[4] The index ·Kap refers to the results 0Kap and 10Kap based on zero and ten-fold Kapitza resistance, respectively.

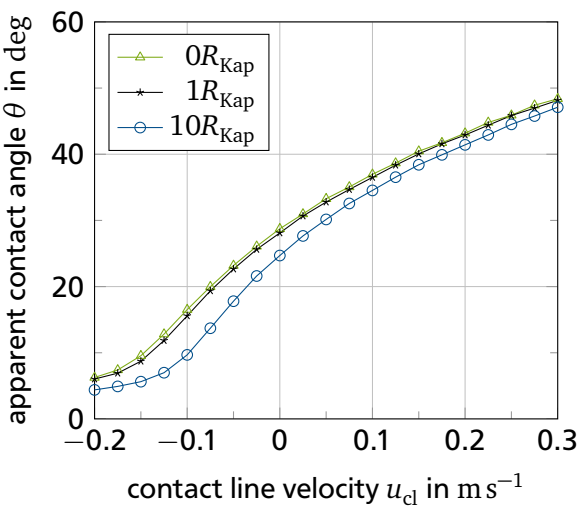

(a) Apparent contact angle θ as a function of contact line velocity u_{cl}.

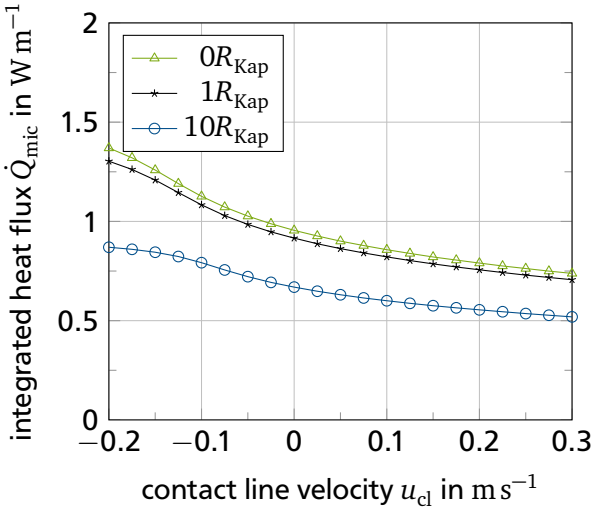

(b) Integrated heat flux $\dot{Q}_{\mathrm{mic}}$ across the micro region as a function of contact line velocity u_{cl}.

Figure 3.4.: Influence of the Kapitza resistance on the apparent contact angle and on the integrated heat flux from the micro region model for different u_{cl} at $\Delta T = 5\,\mathrm{K}$ and $p = 1.013\,\mathrm{bar}$.

For the analysed velocity range, it can be concluded that the highest receding velocities result in the thinnest film thickness. However, for small film thicknesses no clear trend for the influence of the Kapitza resistance can be stated for the apparent contact angle. On the contrary, small film thicknesses amplify the influence of the Kapitza resistance on the integrated heat flux.

It can be concluded that the Kapitza resistance does have an impact on the processes within the micro region. However, the influence of the Kapitza resistance obtained by molecular dynamics simulations, $1R_{\mathrm{Kap}}$, in comparison to zero Kapitza resistance is small. Nevertheless, if any thermal resistance[5] at the solid-liquid surface is larger than the Kapitza resistance, its influence might be large.

If not stated otherwise, a Kapitza resistance of $R_{\mathrm{Kap}} = \left[9.27 \cdot 10^6\,\mathrm{W\,m^{-2}\,K^{-1}}\right]^{-1}$ is used in the following.

3.3.2 Influence of material properties

For all numerical studies in the present thesis, the material properties of FC-72 are used. In this section, the influence of the material properties on the micro region is investigated. Key material properties are identified that have a large impact on the results of the micro region model. The reason for analysing the material properties individually is two-fold. Firstly, it indicates how sensitive the micro region model reacts on specific material properties and supports theories when evaluating the influence of the ambient pressure later in this thesis. Secondly, each measurement of a material quantity contains measurement uncertainties. However, for the used material properties, which are mostly measured, no measurement uncertainty is available. Therefore, a sensitivity analysis for each material property helps to quantify the influence of possible measurement uncertainties on the results of the micro region model. Before the sensitivity analysis for the material properties is presented, the pressure dependence of the material properties of FC-72 is addressed. The references for the used material properties are listed in Table 3.2.

Material properties of FC-72

In Figure 3.5 different material properties are shown for the liquid, vapour, and further properties as function of pressure. All values refer to saturation conditions at the given pressure $T_{\mathrm{sat}} = T(p)$. All mate-

[5] A thermal resistance that might be caused by a nano-sized surface roughness or by an imperfect smooth surface.

Table 3.2.: References for material properties of FC-72.

liquid	ρ_l, ν_l, k_l, $c_{p,\mathrm{l}}$, Pr_l: [92]
vapour	ρ_v: [92]; ν_v, k_v, $c_{p,\mathrm{v}}$: [33]; Pr_v calculated
further material properties	T_sat, σ, Δh_v: [92]

rial properties in Figure 3.5 are scaled to their respective values at atmospheric pressure $p = 1.013\,\mathrm{bar}$, which is indicated by dashed lines. The pressure at the critical point of the used fluid is $p_\mathrm{cr} = 18.41\,\mathrm{bar}$. It is useful here and for further analyses to scale the absolute ambient pressure with the critical pressure of the fluid. Wherever useful, the absolute ambient pressure is given at the top abscissa in addition to the ratio of pressure p/p_cr used at the bottom abscissa.

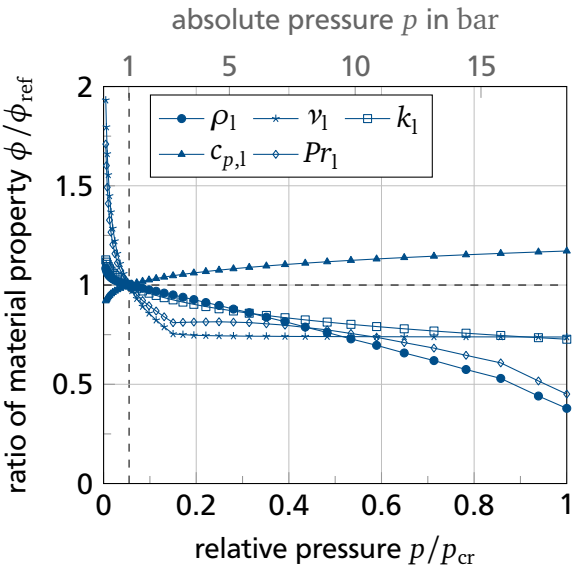

(a) Material properties of the liquid.

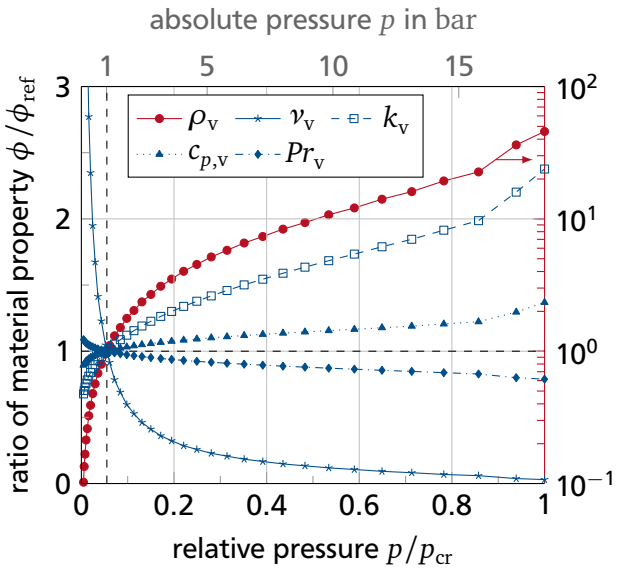

(b) Material properties of the vapour.

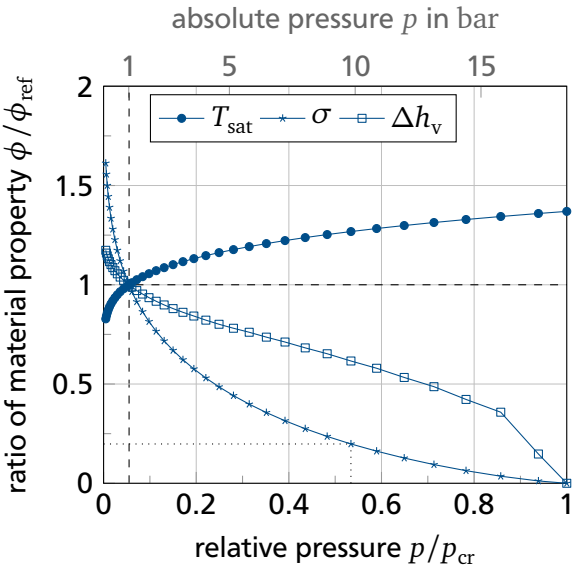

(c) Further material properties.

Figure 3.5.: Material properties of FC-72 as function of pressure at saturation conditions. All material properties are scaled with their respective value at atmospheric pressure $p = 1.013\,\mathrm{bar}$.

The material properties of the liquid as functions of pressure are plotted in Figure 3.5(a). For increasing pressure the heat capacity increases, whereas the density, the thermal conductivity, the kinematic viscosity, and the Prandtl number decrease. The properties of the saturated vapour are shown in Figure 3.5(b). With increasing pressure, the thermal conductivity and the heat capacity increase. The Prandtl number and the kinetic viscosity are decreasing with increasing pressure. The vapour density is plotted against a semi-logarithmic scale and increases with increasing pressure by a factor of more than 30.

The saturation temperature, surface tension, and latent heat of vaporisation are depicted in Figure 3.5(c). While the saturation temperature increases with increasing pressure, the surface tension and the latent heat of vaporisation decrease and drop to zero at the critical point.

Sensitivity of the micro region model on material properties of FC-72

The evaluation of the influence of individual material properties is performed using a reference case. For the reference case of the micro region model, material properties for the atmospheric pressure $p = 1.013\,\mathrm{bar}$ and a wall superheat of $\Delta T = 5\,\mathrm{K}$ are chosen. Since most technical applications are designed for atmospheric pressure, the choice of the reference ambient pressure is intuitive. The reference wall superheat is chosen arbitrarily. However, it is within the range of the investigated wall superheat in the present thesis. This allows for a broad variation of material properties since the key output quantities of the micro region model, the film thickness, the apparent contact angle, as well as the integrated heat flux for the reference case are far from the physical limits induced by the underlying assumptions of the micro region model.

Results from the sensitivity analysis for moving contact lines can be found in the Appendix D in Figure D.1. The results for a static contact line are discussed in the following.

In Figure 3.6 the influence of different material properties is plotted. The abscissa reflects the ratio of any material property ϕ to its reference value ϕ_{ref}. Please note the logarithmic scale used for the abscissa. The ordinate reflects the ratio of the apparent contact angle or of the integrated heat flux to the value at reference conditions. Solid lines indicate the variation of the material property within the physical range of the material properties of FC-72 available in the literature. Dashed lines are additional variations of the particular material property beyond the physical range of the material properties of FC-72. The dashed lines can be considered as parameter variations for an arbitrary fluid that has the combination of material properties. Besides material properties, the condensation coefficient f, the Kapitza resistance R_{Kap}, as well as the dispersion constant A are included in Figure 3.6.

The following example shall illustrate how Figure 3.6 is to be read. Varying the surface tension by a ratio of $\phi/\phi_{\mathrm{ref}} = \sigma/\sigma_{\mathrm{ref}} = 0.2$, the contact angle increases approximately by a factor of 1.5 compared to the contact angle at reference conditions. Additionally, a surface tension ratio of $\sigma/\sigma_{\mathrm{ref}} = 0.2$ shown in Figure 3.5(c) corresponds to a pressure ratio of about $p/p_{\mathrm{cr}} = 0.53$. This pressure ratio represents an absolute ambient pressure of about $p = 10\,\mathrm{bar}$ for FC-72 at saturation condition. This example is indicated by dotted lines in both figures.

As already discussed earlier and confirmed here, the Kapitza resistance has a small impact on both, the apparent contact angle and the integrated heat flux for $R_{\mathrm{Kap}}/R_{\mathrm{Kap,ref}}$ smaller than unity. However, the influence on both quantities increases for increasing Kapitza resistance.

The condensation coefficient f has larger impact on the integrated heat flux than on the apparent contact angle. However, the impact of f increases for θ especially for receding contact lines. In Figure D.1(a) in Appendix D the apparent contact angle increases by a factor of about 1.9 compared to the contact angle at the reference case if the condensation coefficient is doubled. For advancing contact lines, contrarily, the influence of f on the apparent contact angle hardly varies by more than 10 %.

The dispersion constant A influences the results of the micro region considerably only if it varies by more than one order of magnitude above its reference value.

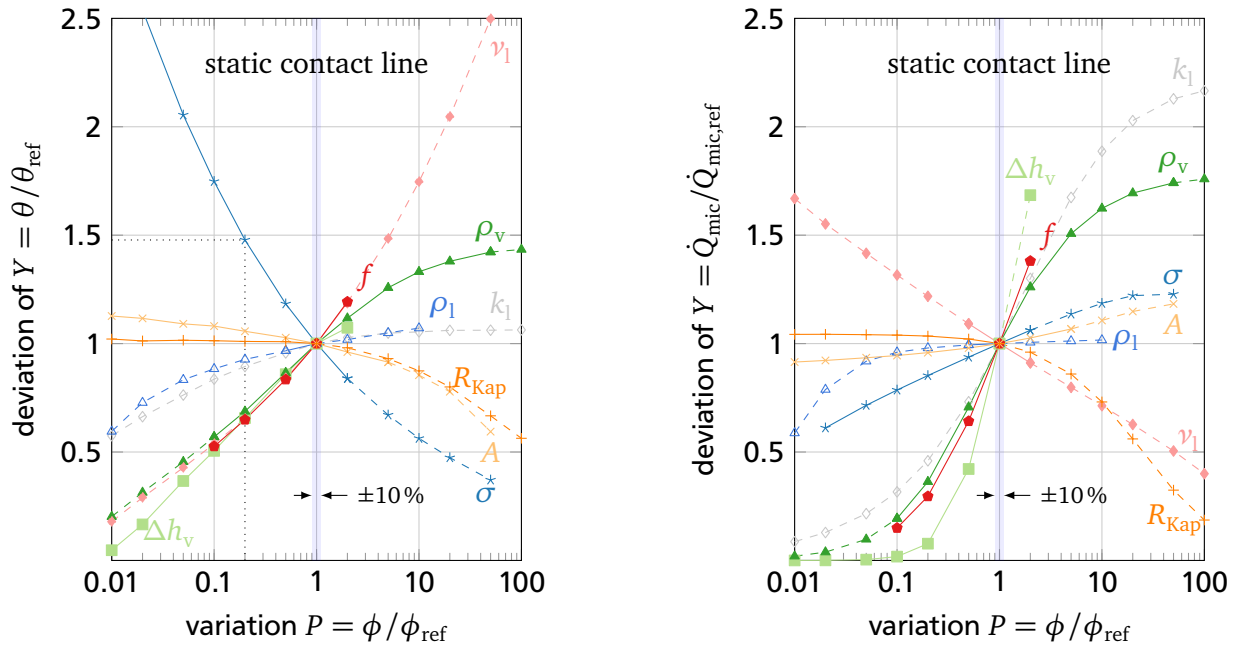

(a) Apparent contact angle θ.

(b) Integrated heat flux $\dot{Q}_{\mathrm{mic}}$.

Figure 3.6.: Influence of material properties on the apparent contact angle θ (left) and on the integrated heat flux $\dot{Q}_{\mathrm{mic}}$ across the micro region (right). The reference case is $p = 1.013\,\mathrm{bar}$, $\Delta T = 5\,\mathrm{K}$, $u_{\mathrm{cl}} = 0\,\mathrm{m\,s^{-1}}$, which results in $\theta_{\mathrm{ref}} = 28.2\,\mathrm{deg}$ and $\dot{Q}_{\mathrm{mic,ref}} = 0.9\,\mathrm{W\,m^{-1}}$.

The saturated vapour density undergoes one of the largest variations when varying the ambient pressure. Its influence on the apparent contact angle for a static contact line is ±50 % regarding the variation of ρ_{v} within physical limits. The influence on the transferred heat exceeds ±50 %.

The influence of the viscosity ν_{l} and the thermal conductivity k_{l} of the liquid on the micro region model is of interest. It can be seen from Figure 3.6 that both variations bring along large deviations of θ and $\dot{Q}_{\mathrm{mic}}$. However, both physical variation ranges are small and therefore the deviation of θ and $\dot{Q}_{\mathrm{mic}}$ are comparably small, as well.

It can be concluded that the variation of some material properties induce high deviations of the contact angle and of the integrated heat flux from the investigated reference cases. However, the sensitivity analysis indicates that measurement uncertainties result in comparably small deviations of the apparent contact angle and of the integrated heat flux computed from the micro region model, as long as measurement uncertainties do not vary in the order of magnitudes. A material property variation of ±10 %, which could be a typical uncertainty, is indicated by a narrow band around $\phi/\phi_{\mathrm{ref}} = 1$ in Figure 3.6. Increasing the ambient pressure results in the variation of multiple material properties that might have contrary influence on the micro region model when varied individually. Therefore, cross-effects are expected when changing the ambient pressure. Nevertheless, the performed sensitivity analysis can be used for further discussion on influencing parameters.

3.3.3 Influence of non-dimensional groups

Instead of varying each material property individually, the non-dimensional groups D_1–D_6 specified in Equation 3.37 introduced for solving the system of differential Equations 3.36 can be analysed. In Figure 3.7 the results of the sensitivity analysis for the non-dimensional groups are plotted for the case of a static contact line.

The contact angle decreases with increasing D_3 and D_6 and the contact angle increases with increasing D_1 and D_2. The contact angle stays (almost) constant for a variation of D_4 and D_5.

The integrated heat flux $\dot{Q}_{\mathrm{mic}}$ decreases monotonously for any increasing variation of D_1–D_3 and D_6. For the non-dimensional group D_4, the integrated heat flux stays constant at $\dot{Q}_{\mathrm{mic}}/\dot{Q}_{\mathrm{ref,mic}} = 1$. The integrated heat flux differs less than 1 % for the variation of D_5 in the investigated range and is hardly visible in the plot.

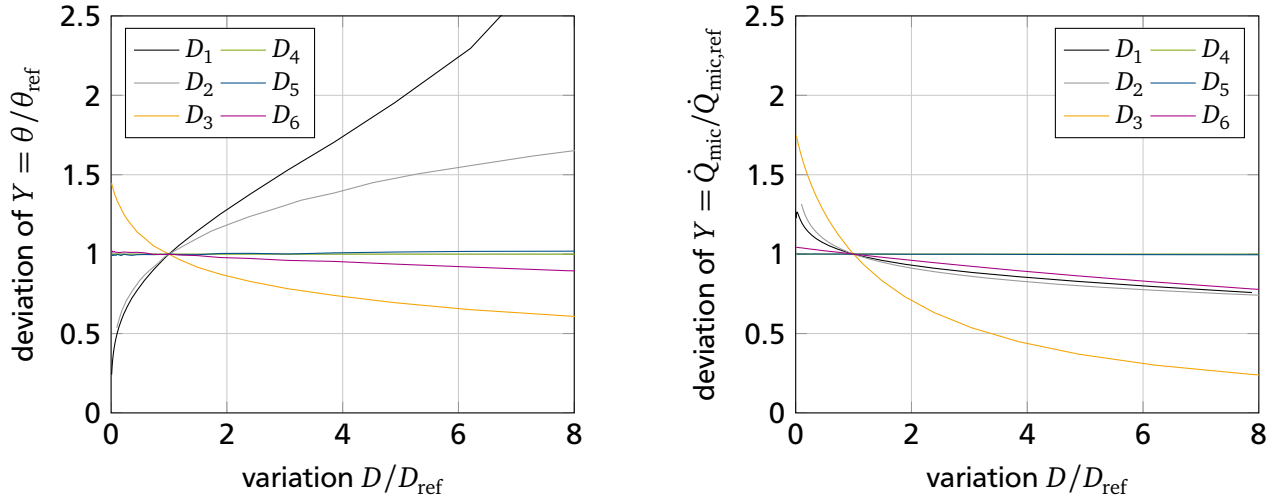

(a) Apparent contact angle θ.

(b) Integrated heat flux $\dot{Q}_{\mathrm{mic}}$.

Figure 3.7.: Influence of the non-dimensional groups D_1–D_6 on the apparent contact angle θ (left) and on the integrated heat flux $\dot{Q}_{\mathrm{mic}}$ across the micro region (right). The reference case is $p = 1.013\,\mathrm{bar}$, $\Delta T = 5\,\mathrm{K}$, and $u_{\mathrm{cl}} = 0\,\mathrm{m\,s^{-1}}$ which results in $\theta_{\mathrm{ref}} = 28.2\,\mathrm{deg}$ and $\dot{Q}_{\mathrm{mic,ref}} = 0.9\,\mathrm{W\,m^{-1}}$.

3.3.4 Review of model assumptions

The micro region model is a powerful tool to estimate the fluid dynamics and thermodynamic behaviour of a three-phase contact line. During the derivation of the mathematical description, several assumptions are necessary to limit the complexity of the underlying physics. These assumptions should be considered when evaluating the results of the micro region model.

Lubrication approximation

The most prominent and at the same time the most limiting assumption arises from the usage of the lubrication approximation. The lubrication approximation can be used only if the spatial extension in the direction of the flow is much larger than perpendicular to it, i.e. $L \gg \bar{h}$. L is the characteristic length scale that is equal to the width of the micro region ξ_{end}. $\bar{h}$ is the characteristic length scale perpendicular to L, which can be the film thickness δ or the mean film thickness $\bar{\delta}$ [94]. For the most conservative assumption, $\bar{\delta} = 0.5\delta$, the contact angle is limited[6] to $\theta < 63.4\,\mathrm{deg}$. Results from the micro region model with contact angles that exceed this limit encounter increasing errors in the capillary pressure calculation and, therefore, increasing errors in all results of the micro region model. However, results from the micro region model that exceed the contact angle limit are not necessarily wrong. The errors need to be taken into account appropriately.

[6] For $\bar{h} = 0.5\delta$, the lubrication approximation results in an upper limit for the contact angle $\theta < \tan^{-1}(2)$.

One-dimensional energy transport

Within the micro region model, the heat is assumed to be transferred one-dimensionally, normal to the wall. Only conductive heat transport is considered whereas energy storage and convective heat transfer are neglected.

Batzdorf et al. [3] conducted direct numerical simulations for the microscale fluid flow and heat transfer in the three-phase contact line region during evaporation. The Navier-Stokes and the energy equation including evaporation are solved in a moving reference frame. For the investigated parameter range, which is similar to the one of the present thesis, it was concluded that the lubrication approximation is appropriate to simplify the momentum equation. In [3], the maximum contact angle limit of 45 deg for the application of the lubrication model to accurately describe the flow within the liquid film was concluded. However, the assumption of solely one-dimensional conductive heat transfer is not fully valid but the results are in an acceptable range. The one-dimensional heat transfer used in the micro region model underestimates the transferred heat. The computational effort for the direct numerical simulations was evaluated about two orders of magnitude higher than the effort for solving the micro region model. Therefore, it is reasonable to accept the errors introduced by the micro region model in order to conduct large parameter variations.

Wall surface structure

For the micro region model, a molecular smooth liquid-solid surface is assumed. Any technical surface entails surface roughness, which might influence the fluid flow and the heat transfer in the vicinity of the three-phase contact line.

To investigate the influence of wall topology on static contact lines, Batzdorf et al. [3] conducted simulations for well defined nano-structured surfaces. It was concluded that the resulting contact angle for structured surfaces varies less than 3 % compared to the one for smooth surfaces. Therefore, the structure has no important influence. It was also emphasised that the situation might change for moving contact lines.

With the additional thermal resistance at the liquid-solid surface introduced in the present thesis, however, it is possible to include any thermal resistance that might arise from structured surfaces within the micro region model. This could be coupled with a slip boundary condition for the fluid flow to include the effects of surface roughness. A slip length was applied in the work of Ojha et al. [73].

Fluid properties

Within the micro region model, the fluid is assumed to consist of a single component, to have constant material properties, and to form a sharp liquid-vapour interface. Furthermore, the Clausius-Clapeyron equation is used to estimate the saturation pressure as a function of temperature. Consequently, the ideal gas law for the vapour and $\rho_\mathrm{v} \ll \rho_\mathrm{l}$ is applied.

The present thesis is restricted to single component evaporation to reduce cross-effects that arise from mixtures. The single component assumption in the micro region model is used in the expression for evaporated net mass flux in Equation 3.2 and in the underlying Navier-Stokes equations. Besides a description for the net mass flux for single component evaporation processes, Schrage also proposed a description of the net mass flux for multi-component evaporation, which can be found in [90]. Furthermore, the condensation coefficient f might be influenced by mixtures and by the presence of impurities.

The material properties are assumed to be independent of temperature and pressure within the micro region. The assumption seems to be reasonable since the maximum temperature difference always stays below 20 K. In the majority of cases the temperature difference amounts to about 10 K. From the sensitivity analysis for material properties, it was concluded that small variations in material properties only result in small deviations of contact angle and integrated heat flux. However, it is emphasised that

effects enforced by variation of the surface tension, the Marangoni effect, was not studied explicitly and no conclusion can be drawn regarding possible Marangoni effects. The Marangoni effect describes the fluid flow induced by the variation of surface tension, which is caused by temperature or concentration variations.

One focus of the present thesis is the investigation of heat and mass transfer at high ambient pressures. However, several assumptions are made within the micro region model that are crucial for the investigation of high pressure effects for which errors are not feasible. Increasing the pressure towards the critical point, the sharp liquid-vapour interface assumption is questionable. Instead, a transition region exists which is called diffuse interface in literature. Several studies exist that describe evaporating diffuse interfaces [36, 37]. In the thoroughly conducted studies, however, the models are based on equations of state which are not suitable for FC-72. In Appendix A.1, a comparison is made between material properties calculated by different EoS and experimentally determined material properties. It is also shown that the ideal gas law is not appropriately representing the vapour phase for high pressures. Consequently, it is not reasonable to extend the high pressure analyses for the micro region model far beyond a pressure ratio of about $p/p_{\mathrm{cr}} = 0.6$ for FC-72.

CHAPTER 4

Verification and Validation

The verification and validation of the numerical CFD model introduced in Chapter 2 is addressed in this Chapter. Validation is the process, which answers the question of if the proper equations are solved. Verification of a numerical model answers the question of if the equations are solved properly [87].

The combined evaporating compressible two-phase flow with hot wall interaction is too complex to verify as a whole. Therefore, the verification focusses on the evaporation process with the augmented compressible solver. The phase change process across the free liquid-vapour interface is compared to an analytical solution proposed in the literature. The validation of the CFD macro model is a remaining task due to insufficient availability of experimental data for the drop impact on hot walls under various ambient pressures in literature. However, the validation of the drop impact on a hot surface under atmospheric ambient pressure is presented in this Chapter.

4.1 Verification: Evaporation model

Scriven [91] formulated differential equations for radial bubble growth in an infinite pool of superheated liquid driven by heat and mass transfer and solved them analytically. The analytical solution is used to verify the compressible solver in terms of precise computation of the evaporation process across the free liquid-vapour interface. Following the assumptions and simplifications made in the formulation of Scriven, surface tension, external forces, and compressibility are neglected.

The sketches of different computational domains are depicted in Figure 4.1. The outer blue box indicates the bounding box of the computational domain. The maximal size of the computational domain in radial

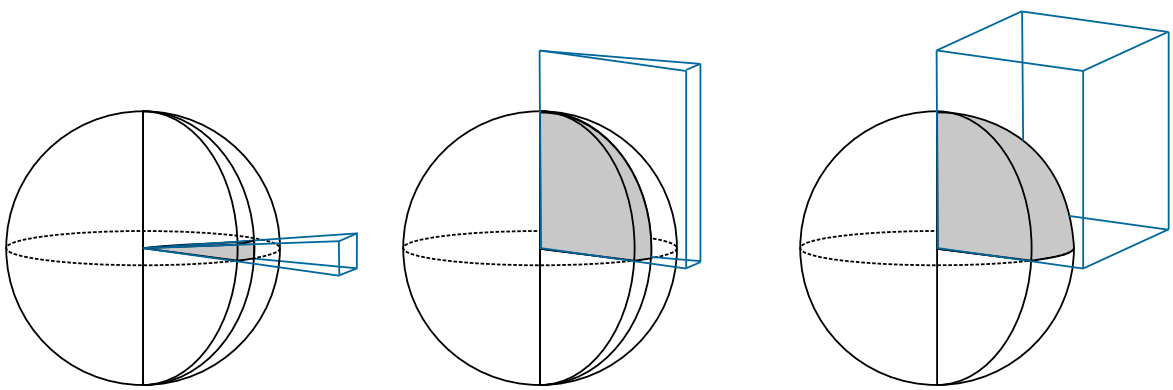

(a) Spherical symmetry (1d). **(b)** Axial symmetry (2d). **(c)** Quarter hemisphere (3d).

Figure 4.1.: Computational domain for (a) quasi one-, (b) quasi two-, and (c) three-dimensional simulation for phase change across an interface. The sphere indicates the vapour bubble.

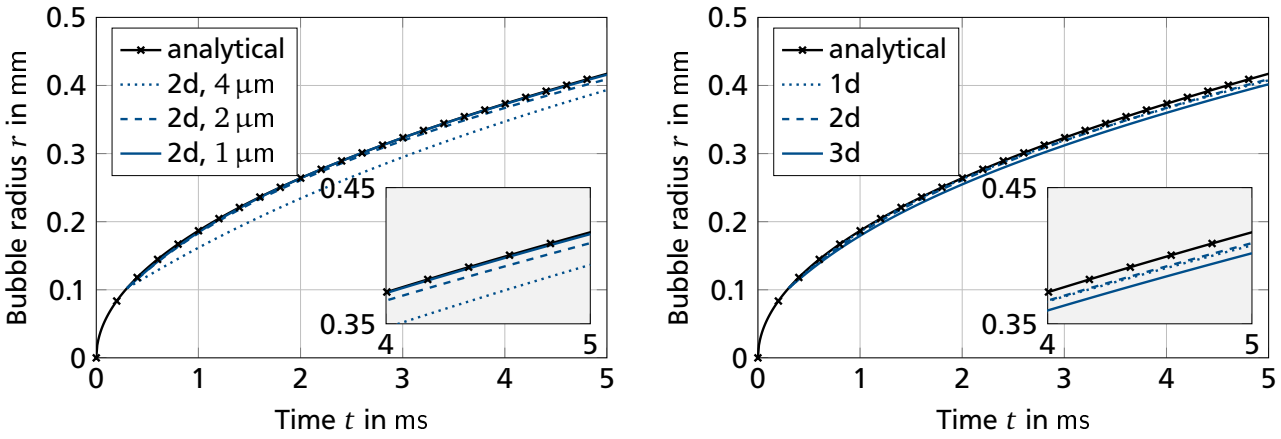

(a) 2d, different mesh resolution.

(b) $\Delta x = 2\,\mu$m, different dimensions.

Figure 4.2.: Evaporation across the free liquid-vapour interface. Comparison with the analytical solution derived by Scriven [91].

direction (x-direction) is 0.8 mm. For the quasi one-dimensional CFD simulations, the extension of each tangential direction (y- and z-direction) is one cell thickness employing an equidistant resolution in radial direction. For the quasi two-dimensional simulations, axial symmetry is applied. In this case, the tangential direction extends by one cell thickness, whereas both, the radial and axial directions are divided into equidistant cells. A fully equidistant mesh in x-, y-, and z-direction is used for the three-dimensional simulations. Although only structured meshes are shown for the verification cases, the evaporation algorithm is not restricted to structured meshes as demonstrated by Batzdorf [2].

The center of an initial bubble is located at the origin of each computational domain with an initial bubble radius R_0 at the start of the simulation at $t_0 = 0.3$ ms. For FC-72 at $p = 1.013$ bar and a liquid superheat of $\Delta T = 10$ K, the initial bubble radius is approximately $R_0 = 0.1022$ mm. Scriven provides the solution for the temperature field within the liquid and consequently a thermal boundary layer exists close to the liquid-vapour interface at the liquid side. The initial thermal boundary layer is approximately $\delta_{\text{th}} = 13.52\,\mu$m while 99 % of ΔT is within the first $6\,\mu$m distance from the liquid-vapour interface. Most boundaries of the different computational domains have symmetry boundary conditions. Dirichlet boundary conditions for pressure and temperature, and Neumann boundary conditions for velocity and volume fraction field are applied to the remaining boundaries.

In Figure 4.2, the evolution of the bubble radius is shown. Different mesh resolutions of the axial symmetry case are depicted in Figure 4.2(a). The coarsest mesh resolution with $\Delta x = 4\,\mu$m shows the largest deviation from the analytical results derived by Scriven. With increasing mesh resolution, the deviation decreases. Results obtained by different computational domains for a constant mesh resolution of $\Delta x = 2\,\mu$m can be found in Figure 4.2(b). For all different computational domains, good agreement between simulation and analytical results are obtained. An axial symmetrical mesh (2d) is chosen for all following numerical studies.

It can be concluded that the compressible solver for a quasi two-dimensional grid even for the coarsest applied resolution represents evaporation across the free liquid-vapour interface reasonably well.

4.2 Validation: Single drop impact

The compressible solver taking into account evaporation across the liquid-vapour interface as well as the evaporating three-phase contact line is validated. Single drop impact experiments at atmospheric pressure published in [46] and described in detail in [33] are selected as validation cases. The experimental set-up from those experiments in the literature is described briefly in the following.

4.2.1 Experimental set-up

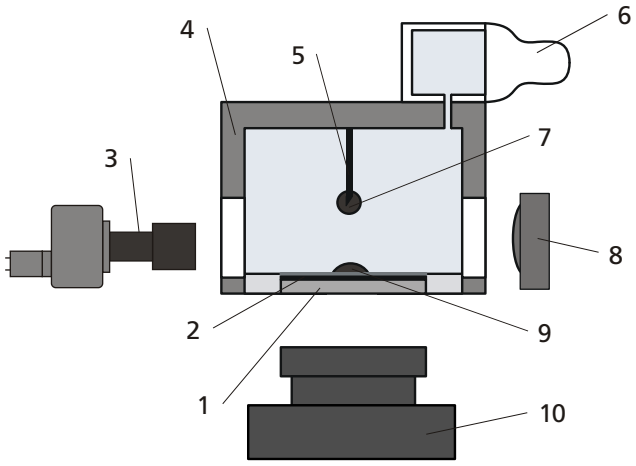

1 heater substrate/crystal
2 heating layer
3 high speed b/w camera
4 tempered walls
5 sub-cooled needle
6 pressure equalisation chamber
7 recondensing drop
8 light source
9 evaporating drop
10 high speed IR camera

Figure 4.3.: Experimental test cell [33].

For the single drop impact experiments discribed in [33], the drop generator and the heater are enclosed in a container to allow for precise control of the experimental ambient conditions. The drop generator is a sub-cooled needle. Needles with different diameters allow for different drop sizes. Due to condensation from the saturated vapour atmosphere, liquid phase gathers at the sub-cooled needle. The drop detaches and falls trough quiescent vapour, once gravitational forces overcome capillary forces. The needle is variable in height to control the impact velocity.

The utilised heater's base material is a 2 mm thick calcium fluoride CaF_2 crystal that is transparent for infra-red light. The crystal is covered by an approximately 400 nm thin layer of calcium nitride CaN for increasing emissivity. The CaN layer is coated by an approximately 400 nm thin layer of pure chromium Cr via physical vapour deposition (PVD). The Cr layer is used as Joule heater, hence providing a heat source at the top of the heater. During drop impact experiments, the drop is in direct contact with the pure chromium layer.

The high speed infra-red camera with a spatial resolution of 29.27 μm at a frame rate of 1 kHz is installed beneath the crystal and aligned with the drop impact area. The IR camera captures the temperature field at the CaF_2-CaN boundary. Neglecting thermal storage and resistance within the two thin layers, the measured temperature field is assumed to be very similar to the temperature field that would result from a direct drop-crystal contact [47]. Calibration of the IR camera is performed in-situ for each pixel prior to the experimental run. Since both layers are very thin compared to the thickness of the CaF_2 crystal, they are not taken into account in the numerical simulations. The high speed b/w camera installed from the side allows to capture the drop's shape, diameter, and impact velocity with a spatial resolution of 37.11 μm at a frame rate of 1 kHz.

The test cell surrounding walls are tempered at saturation temperature to support thermodynamic equilibrium and counteract thermal losses. The pressure equalisation chamber suppresses a pressure drop inside the test cell.

Besides the temperature field, the heat flux across the fluid-solid surface during the drop impact process is a quantity of interest. Therefore, the time-dependent temperature field obtained by the IR camera is post-processed with a transient, three-dimensional heat conduction simulation within the crystal substrate. The calculations are performed with OpenFOAM assuming adiabatic boundary conditions everywhere except at the solid-fluid surface. At the solid-fluid surface, the measured temperature field from the IR camera is imposed. The resulting heat flux across the fluid-solid surface is the superposition of the heat flux estimated from the measured electrical current of the Joule heater and the calculated heat flux from

the transient heat conduction calculation. Further details on the postprocessing procedure are given in [33, 34].

The evolution of the contact line position is another quantity of interest. In general, the b/w camera is capable of detecting the three-phase contact line position. However, for various reasons (e.g. synchronisation, error propagation) it is helpful to retrieve experimental data from a unique data set. The IR camera provides data from which the local heat flux distribution, as well as the contact line position is post-processed. The contact line is assumed to be present at locations of highest heat flux rate.

From the experiments, two scenarios are selected that serve as validation cases for the compressible fluid flow solver with evaporation and contact line handling. The same experiments were used in former studies [2] for code validation and hence can be utilised as benchmark cases for the different fluid flow solvers.

4.2.2 Computational domain, initial and boundary conditions

The accurately designed and conducted experiments minimise the occurrence of perturbations. Effects like fingering, splashing and boiling are not observed within the investigated parameter range. Moreover, the obtained results show symmetrical behaviour, allowing for axially symmetrical simulations. The computational domain is a wedge of two different regions: solid and fluid. Both regions have identical spatial extents. Their size is chosen in a way that boundaries of the computational domain do not induce any artificial disturbance to the velocity, pressure, or temperature field. Geometrical aspects for the heater are also represented. Therefore, the height and width of the fluid region is set to twice and four times the initial drop diameter, respectively. The region of interest concentrates on the solid-fluid surface and fluid-vapour interface. Instead of a dynamic mesh refinement, a static mesh refinement is selected. The region covered by the maximum spreading is, therefore, the region with highest resolution. For the finest mesh, two levels of refinement based on the coarse mesh are defined. Figure 4.4(a) illustrates the spatial extent of the computational domain and the refinement regions I–III.

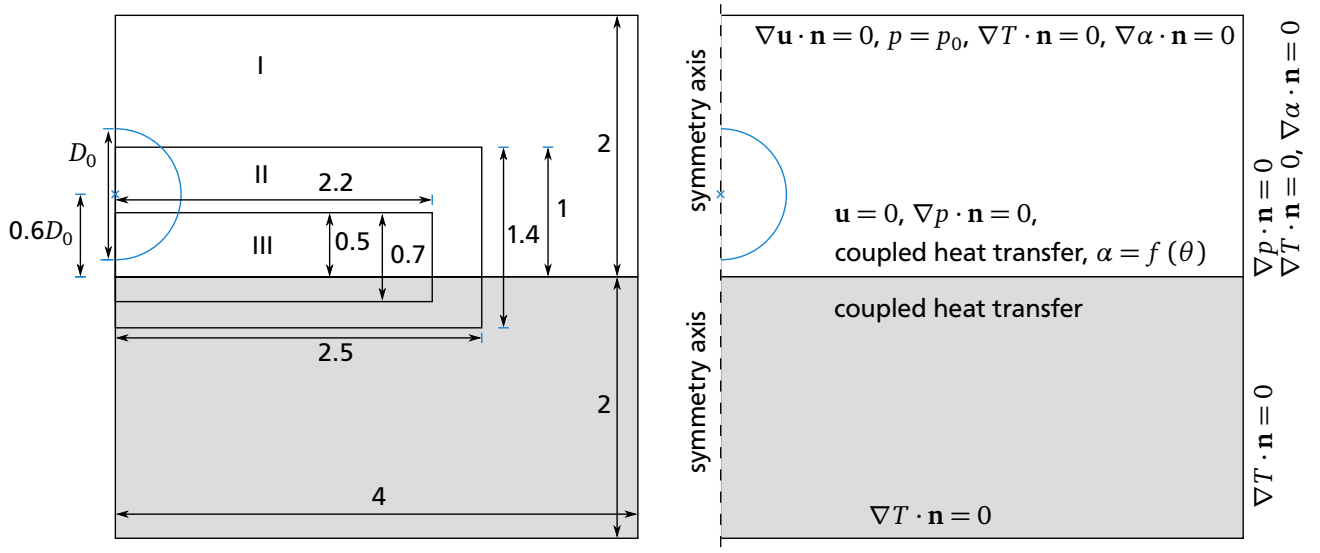

(a) Computational domain, dimensions given in 10^{-3} m. **(b)** Boundary conditions.

Figure 4.4.: Computational domain and boundary conditions for the validation case and for the reference case.

In Figure 4.4(b), the boundary conditions are indicated. At the top of the computational domain, a Dirichlet boundary condition for the pressure at saturation and Neumann boundary conditions with zero gradient for the temperature, velocity, and volume fraction fields are chosen. It is assumed that heat transfer parallel to the solid surface is negligible. Hence, an adiabatic boundary condition is set at the

opposite side of the symmetry axis. There, the gradient is zero for the pressure and the volume fraction. The temperature field of the fluid and the solid is coupled via conjugated heat transfer at the solid-fluid boundary. The heat flux which arises from the Joule heater, $\dot{q}_{\mathrm{in}}$, is added. All other boundaries within the solid are assumed to be adiabatic.

In the initial state, the center of mass of the drop is aligned with the rotational axis and is $0.6\,D_0$ above the solid wall. The drop has an initial diameter, velocity, and temperature of D_0, u_0, and T_{sat}, respectively. The initial parameters for the two different scenarios A and B can be found in Table 4.1. In the vapour phase, the temperature is set to account for a thermal boundary layer of thickness δ_{th} close to the hot solid wall. The thickness of the thermal boundary layer is determined as proposed in [2] which is based on the Nusselt number for laminar natural convection over a horizontal plate. Within the thermal boundary layer, the temperature is assumed to have a linear gradient normal to the wall.

Table 4.1.: Initial parameters for the validation cases using the properties of liquid FC-72 and its vapour. Material properties are taken at atmospheric pressure.

scenario	p bar	D_0 mm	u_0 $\mathrm{m\,s^{-1}}$	ΔT_{w} K	δ_{th} mm	$\dot{q}_{\mathrm{in}}$ $\mathrm{W\,m^{-2}}$	Re	We	Bo	Pr	Ja
A	1.013	1.02	0.262	13.7	0.793	4000	954	13.7	0.50	9.55	0.17
B	1.013	0.977	0.584	17.4	0.745	9500	2037	65.2	0.46	9.55	0.23

The validation cases are simulated using different mesh resolutions. The computational mesh is block structured, i.e. different regions are selected for decreasing the grid spacing Δx, compare Figure 4.4(a). The coarsest region I consists of a uniform grid spacing of $\Delta x = 8\,\mu$m in radial and axial direction. For medium and fine meshes, regions II and III consist of values that differ from the coarsest mesh. In Table 4.2, an overview is given for the grid spacing and the resulting number of computational cells in the fluid and solid region for the different mesh resolutions.

Table 4.2.: Grid size and number of computational cells for different mesh resolutions.

mesh	grid size Δx in 10^{-6} m region I	region II	region III	number of cells N_{c} fluid	solid
coarse	8	8	8	125 000	125 000
medium	8	4	4	242 375	148 475
fine	8	4	2	448 625	254 450

4.2.3 Results and discussion

Once gravitational forces dominate over capillary forces, the drop falls off the sub-cooled needle towards the dry, smooth, superheated target. In Figure 4.5(a) and (b), the evolution of the drop's contact line radius is depicted for the two different scenarios and for different resolution of the computational mesh. After the initial contact with the wall at $t = 0$, the drop spreads along the surface, until a maximum dilatation $R_{\mathrm{cl,max}}$ is reached. During spreading, inertia and viscous forces are dominant. When the inertia and viscous forces decay, surface tension forces try to minimise the surface energy, causing the drop to recede. A minimum drop footprint is obtained, before the drop oscillates around a quasi sessile drop state. During the impact process, evaporation takes place and after a waiting period, the drop will be evaporated completely. For both scenarios, the evolution of the contact line radius stays mostly within the specified measurement uncertainty, indicated by the error bars.

As soon as the contact of the drop with the wall is established, a strong rise in the heat flux at the solid-fluid surface is recognised for both, experiments and numerical simulations. In Figure 4.5(c) and (d),

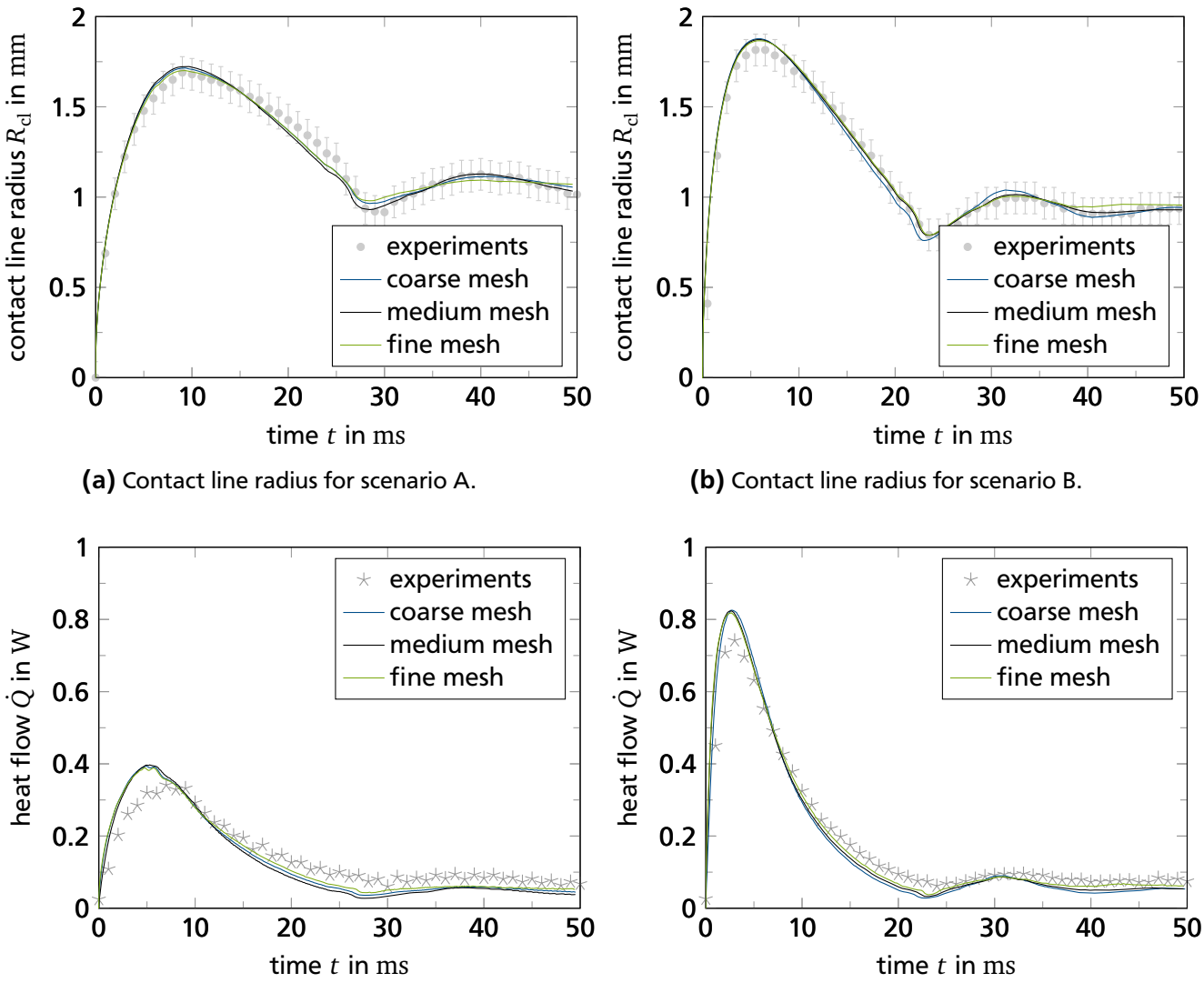

(a) Contact line radius for scenario A.

(b) Contact line radius for scenario B.

(c) Transferred heat for scenario A.

(d) Transferred heat for scenario B.

Figure 4.5.: Evolution of contact line radius and transferred heat. Experimental data taken from [33].

the evolution of the total heat flow at the solid-fluid surface covered by the liquid is shown for both scenarios and different resolutions of the computational mesh. Comparing the results without measurement uncertainties, the numerical simulations seems to overpredict the maximum peak in heat flow and to undershoot the experimentally obtained results at later instances. In scenario B, the peak of the heat flow is larger than the peak in scenario A. In scenario B, the combination of larger impact velocity resulting in stronger convective heat transport, as well as larger initial wall superheat are reasons for the higher heat flow peak.

Grid convergence

For drop impact characterisation, the maximum extent after drop impact is of interest. The compressible fluid flow solver is able to capture fluid dynamics reasonably well. For the different mesh resolutions, $R_{cl,max}$ differs less than 4 % (scenario B) and even less than 2 % (scenario A) in comparison to the experimental results. The best agreement in terms of fluid dynamics behaviour is found to be achieved with the finest mesh resolution. For the heat transfer $\dot{Q}_{cum,r}$, the heat transferred from the initial drop-wall contact until the instance of minimum spreading including the entire spreading and receding phase, is chosen for comparison with the experiments. The cumulative heat flow is chosen due to the high energy

transfer within a short characteristic time scale after drop impact. In contrast to $R_{\mathrm{cl,max}}$, the cumulative heat flow does not converge with increasing mesh resolution. However, the largest relative deviation stays below 7 % for the coarse mesh and below 4 % for medium mesh resolution. Hence, a medium mesh resolution is identified as reasonable compromise between accuracy and computational cost for further investigations. A summary of the maximum contact line radius and cumulative heat flow until minimum contact line radius after spreading for different mesh resolutions is given in Table 4.3.

Table 4.3.: Grid convergence study. Relative error $\varepsilon = \left|(\cdot)_i - (\cdot)_{\mathrm{exp}}\right| / (\cdot)_{\mathrm{exp}}$.

scenario	mesh	$R_{\mathrm{cl,max}}$ in 10^{-3} m	$\dot{Q}_{\mathrm{cum,r}}$ in 10^{-3} W	ε_{R} in %	ε_{Q} in %
A	coarse	1.7225	5.2449	1.9	6.5
	medium	1.7134	5.4197	1.4	3.3
	fine	1.6991	5.5625	0.56	0.79
	exp.	1.6896	5.6068		
B	coarse	1.877	7.2668	3.4	2.3
	medium	1.872	7.4695	3.2	0.43
	fine	1.865	7.6368	2.8	2.7
	exp.	1.815	7.4375		

CHAPTER 5

Drop Impact Reference Case

The objective of the present thesis is to investigate single drop impact onto a heated solid substrate under various ambient pressures. Different parameter studies using CFD simulations are conducted and presented in the next Chapter. In preparation for the parameter studies, a reference case is introduced. The reference case is used within all parameter studies and scenarios of the performed CFD simulations. The reference case serves as launching point from which different aspects are varied to identify influencing parameters on the evaporative drop impact process. Due to the key role of the reference case, its numerical set-up is described and its simulation results are shown in detail.

5.1 Definition of the reference case

The selection of the reference case is based on different criteria. The reference case is chosen to cover a representative standard scenario in technical applications. Most technical applications are operated at atmospheric ambient pressure. Furthermore, the reference case represents the middle of a parameter spectrum in which the numerical model is validated against experimental results. Additionally, the reference case is close to a scenario used in former studies enabling a direct comparison of the results. Consequently, the drop has an initial diameter of $D_0 = 1.0241\,\mathrm{mm}$ and an impact velocity of $u_0 = 0.2735\,\mathrm{m\,s^{-1}}$ at a constant wall superheat of $\Delta T_\mathrm{w} = 10\,\mathrm{K}$. The ambient pressure is set to 1.013 bar and all material properties of the fluid are evaluated at atmospheric pressure. The values for the reference case are summarised in Table 5.1 and the values for the non-dimensional groups in Table 5.2.

Table 5.1.: Initial parameters of the reference case for the CFD simulations using the properties of liquid FC–72 and its vapour. All material properties are evaluated at atmospheric pressure.

p bar	T_sat K	D_0 mm	u_0 $\mathrm{m\,s^{-1}}$	ΔT_w K	g $\mathrm{m\,s^{-2}}$	c_l $\mathrm{J\,(kg\,K)^{-1}}$	Δh_v $\mathrm{J\,(kg)^{-1}}$	k_l $\mathrm{mW\,(m\,K)^{-1}}$
1.013	329.75	1.0241	0.2735	10	9.74	1098.41	84510.9	52.16

Table 5.2.: Non-dimensional groups of the reference case for the CFD simulations.

p/p_cr	Re	We	Bo	Pr	Ja
0.055	1000	15	0.5	9.55	0.13

Further material properties of the fluid and the solid can be found in Table C.3. The utilised compressibility for FC-72 is listed in Table A.4. The correlation coefficients from the micro region model can be found in Table C.2. All aforementioned tables are listed in the appendix.

The micro region model and the macro CFD simulations focus on different length scales and distinct phenomena. For this reason, the reference cases differ for the individual models. For example, the impact velocity u_0 for the macro CFD simulation is set to a certain value. For the micro region model, in contrast, the results for a non-moving contact line $u_{cl} = 0$ are of particular interest. Hence, there is no global reference case that covers the micro region model and macro CFD simulation.

5.2 Computational domain, boundary and initial conditions

The computational domain is similar to the one used for the validation scenarios in the previous Chapter. A sketch of the computational domain is shown in Figure 4.4. The computational domain is a wedge but in contrast to the validation case only the fluid domain is considered while the solid domain is neglected. Instead, a constant temperature is imposed as boundary condition at the wall. The size of the computational domain is chosen such that boundaries of the computational domain do not induce any artificial disturbances. Therefore, the height and width of the fluid region is set to twice and four times the initial drop diameter, respectively. The region of interest concentrates on the wall-fluid surface and the liquid-vapour interface. Instead of a dynamic mesh refinement, a static mesh refinement is selected. The region covered by the maximum spreading is, therefore, the region with the highest resolution. For the medium mesh, which is used in the reference case, one level of refinement is applied.

Numerical experiments have shown that drop deformation and internal drop flow during the falling time has only little effect on the spreading and heat transfer. Furthermore, a thermal boundary layer in the vapour phase close to the wall was observed to have only little influence on the heat transfer. Consequently, no thermal boundary layer is prescribed. The center of the drop is placed at a hight of $0.6D_0$ above the solid surface. The drop is initially spherical and the complete fluid domain is at saturation temperature. The drop has an initial velocity u_0. Any change in kinetic energy until the first drop-wall contact is neglected and, therefore, the initial velocity is the impact velocity. Since no vapour bubble formation was observed during the experiments in [46], any numerical, artificially induced vapour entrapment inside the drop is neglected.

5.3 Results for the reference case

The fluid dynamics of a drop hitting a surface can be analysed by the evolution of the three-phase contact line of the drop. In Figure 5.1(a), the contact line radius is plotted over time. During the deposition of a non-splashing drop, the evolution of the contact line can be summarised in three phases:

- **Phase I, spreading:** the initial point of the phase is the first contact of the drop with the wall. The motion of the drop is driven by inertia and viscous forces and the drop spreads. Over time, inertia and viscous forces decay and capillary forces are increasingly influencing the drop motion. The end of phase I is reached when the drop reaches its maximum spreading.
- **Phase II, receding:** the receding phase starts at the drop's maximum spreading diameter and ends at the drop's minimal footprint after spreading. During this phase, surface tension is dominant, forcing the drop to contract. In this phase, capillary forces and wetting properties are influencing the fluid dynamics more strongly than in phase I.
- **Phase III, sessile stage:** the motion of the contact line is small in comparison with the spreading and receding phase. The drop might oscillate around a quasi-stationary position.

During all phases of fluid dynamics heat and mass transfer is present. In Figure 5.1(b), different contributions to the heat flow $\dot{Q}$ are shown as a function of time. The heat flow across the solid-fluid surface is denoted by $\dot{Q}_{drop}$. It is the amount of heat being transferred to a single drop. During the spreading phase a strong increase in $\dot{Q}_{drop}$ can be observed. High velocities of the cold liquid result in high convective heat transfer between the solid and the drop. The peak in $\dot{Q}_{drop}$ is reached before the maximum spreading of the drop is reached. Between the heat flow peak and the maximum spreading, indicated by

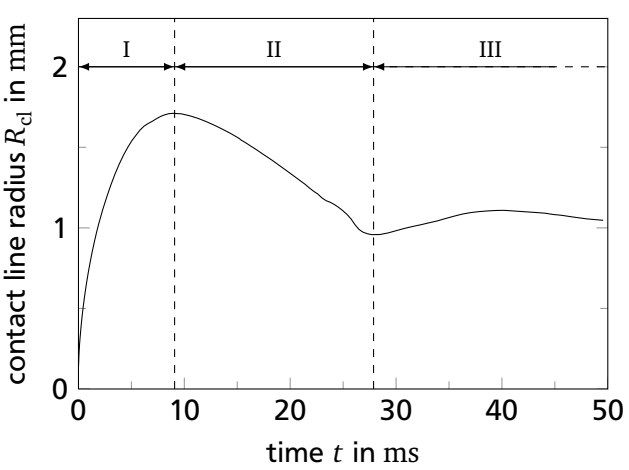

(a) Contact line radius.

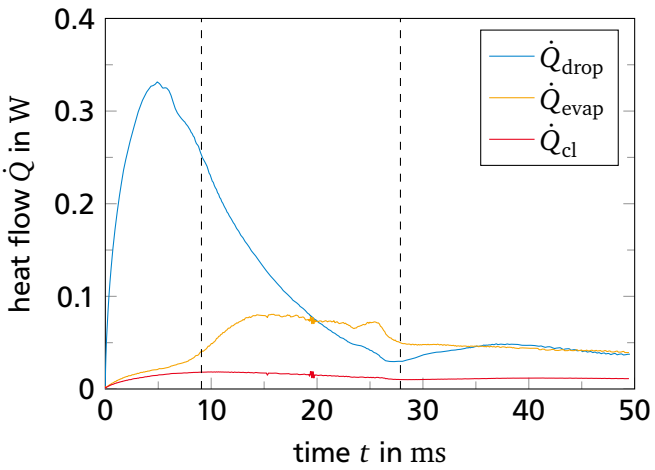

(b) Transferred heat.

Figure 5.1.: Results for the reference case.

the first dashed line, the liquid is still moving but at the same time a growing thermal boundary layer in the liquid suppresses heat transfer. When the drop starts to contract the warm liquid inside the thermal boundary layer causes the heat transfer to further decay during the receding phase. In the sessile stage, the heat transfer is low in comparison with the other phases of drop motion.

The heat flow that is transferred by evaporation is denoted by $\dot{Q}_{evap}$. It includes the evaporation across the three-phase contact line and across the free liquid-vapour interface. In some drop impact events, as in the reference case, $\dot{Q}_{evap}$ can temporarily exceed the heat flow to a single drop $\dot{Q}_{drop}$. During the convective heat transfer in phase I, most of the energy is converted into sensible heat of the liquid, leading to an increase in liquid temperature rising above the saturation temperature. During receding, phase II, hot liquid from the wall is transferred to the liquid-vapour interface and a strong evaporation rate is observed. The strong evaporation rate decays, as soon as the fluid transport with hot liquid from the wall to the liquid-vapour interface decreases, which is just before the transition from phases II to III.

The heat flow across the micro region is denoted by $\dot{Q}_{cl}$. The magnitude of $\dot{Q}_{cl}$ during the spreading phase is small compared to the convective heat transfer. However, as soon as the convective heat transfer decays, the heat transferred by evaporation across the contact line becomes important for heat transfer.

In Figure 5.2, cumulative heat flows of different heat transfer mechanisms are visualised for the spreading and the receding phase. During the spreading phase, most of the transferred energy between the

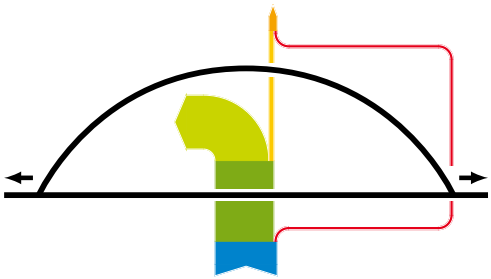

(a) Spreading phase.

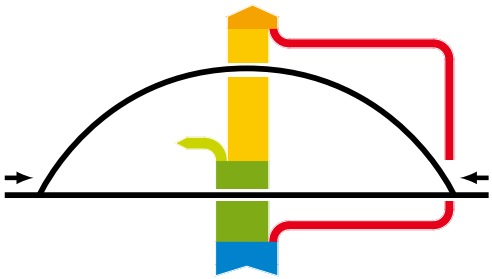

(b) Receding phase.

Figure 5.2.: Chart of cumulative heat flow over time during the spreading and the receding phase. The colours refer to ■ sensible heat from the wall (Q_{drop}), ■ convective and conductive heat transfer, ■ sensible heat of the drop, ■ contact line evaporation (Q_{cl}), ■ evaporation across the free liquid-vapour interface, and ■ evaporation to bulk vapour (Q_{evap}).

wall and the drop turns into sensible heat of the liquid drop. Only a small amount of the transferred heat from the wall evaporates across the three-phase contact line and the free liquid-vapour interface. However, the situation is different during the receding phase. During the receding phase the amount of energy, which directly evaporates across the free liquid-vapour interface, is higher than the amount of energy, which turns into sensible heat of the drop. The contact line evaporation becomes noticeable. Interestingly, the cumulative energy being transferred from the wall to a single drop, indicated by the width of the blue arrow in Figure 5.2, is approximately the same for both phases, spreading and receding.

Constant wall temperature

In contrast to the validation scenarios, a constant wall temperature is imposed as boundary condition at the wall for the reference case. In Figure 5.3, results are shown for constant wall temperature, as well as for conjugated heat transfer at the wall. The conjugated heat transfer accounts for the local cooling of the wall and the transient heat transfer within the solid substrate. The evolution of the contact line radius is presented in Figure 5.3(a). During spreading, the contact line radii differ insignificantly and almost the same maximum spreading is reached for both cases. Due to dominating inertia and viscous forces during the spreading phase, the contact angle influences the motion of the drop less than during the receding phase. The contact line radii differ less than 8 % during the receding phase. In the case of conjugated heat transfer, the local cooling of the wall is influencing the contact angle. The colder wall temperature leads to a smaller receding contact angle and, hence, a slower contraction of the drop. Additionally, the minimum contact line radius is slightly larger in the case of conjugated heat transfer because of the smaller contact angle.

In Figure 5.3(b) the cumulative heat flow Q is shown as function of time. For obtaining Q, the heat flow to a single drop $\dot{Q}_{\mathrm{drop}}$ is cumulated over time. Conjugated heat transfer leads to lower values for the cumulative heat flow due to the local cooling of the wall and, therefore, lower temperature gradients. The cumulative heat flow differs less than 6 %. For comprehensive parameter studies, the usage of a

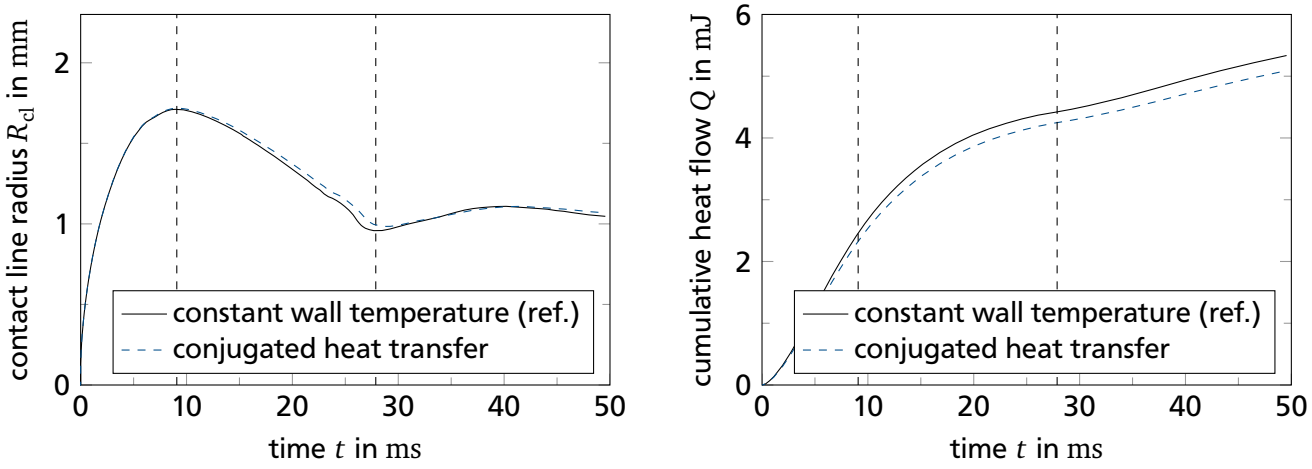

(a) Contact line radius.

(b) Cumulative heat flow.

Figure 5.3.: Comparison of results for the reference case assuming conjugated heat transfer.

constant wall temperature is considered to be a reasonable boundary condition for the wall material used here. Firstly, it saves computational resources[1]. Secondly, it reduces the problem by the parameters of the solid. If conjugated heat transfer is taken into account for the parameter studies, the material properties of the solid, such as thermal conductivity and heat capacity, are additional parameters.

[1] Simulation duration (execution time) for the reference case using parallel computations, 12 cores: constant wall temperature 39 565 s, conjugated heat transfer 51 120 s.

Non-dimensional quantities

For comparing different systems and drop impact situations, non-dimensional quantities are helpful. Common non-dimensional numbers such as Reynolds, Weber, Bond, Prandtl, and Jakob number are defined in Equations 1.1–1.5. The length and time scales, as well as the transferred heat and mass are presented in a non-dimensional form.

Non-dimensionalisation of the length scale is performed with the initial drop diameter. The non-dimensional spreading ratio S reads

$$S = \frac{2R_{\mathrm{cl}}}{D_0}. \tag{5.1}$$

The time scale is non-dimensionalised by the initial drop diameter and impact velocity u_0. The non-dimensional time reads

$$\tau = \frac{u_0 t}{D_0}. \tag{5.2}$$

The heat flow $\dot{Q}_{\mathrm{drop}}$ is cumulated over time and scaled by the maximum amount of energy, which can be transferred by completely evaporating a single drop with an initial diameter of D_0. The non-dimensional heat E^* reads

$$E^* = \frac{6Q}{\pi \rho_{\mathrm{l}} D_0^3 \Delta h_{\mathrm{v}}}. \tag{5.3}$$

If the liquid is initially sub-cooled, an additional term for the sensible heat needs to be taken into account in the denominator of Equation 5.3. Finally, the evaporated mass is scaled by the initial mass of the drop

$$M^* = \frac{6M_{\mathrm{evap}}}{\pi \rho_{\mathrm{l}} D_0^3}. \tag{5.4}$$

The evolution of the three-phase contact line for the reference case is replotted in non-dimensional form in Figure 5.4(a). The maximum and minimum spreading ratios are denoted by S_{max} and S_{min},

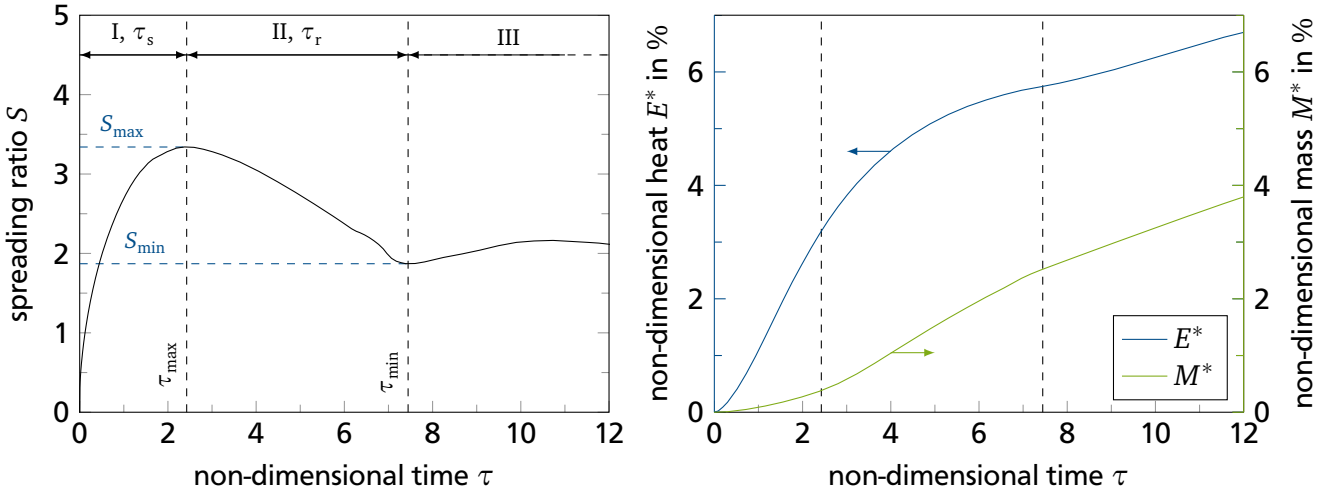

(a) Spreading ratio.

(b) Transferred heat and evaporated mass.

Figure 5.4.: Non-dimensional results of the reference case.

respectively. The instants of maximum and minimum spreading after an initial drop-wall contact are denoted by τ_{max} and τ_{min}, respectively. The spreading phase duration is denoted by τ_s whereas the receding phase duration is denoted by τ_r. The evolution of E^* and M^* is depicted in Figure 5.4(b).

5.4 Overview of the CFD simulations based on the reference case

Different parameter studies are conducted to identify parameters influencing the drop impact process. The parameter studies are presented and discussed in the next Chapter. The different parameter studies are:

- **Low and high ambient pressure with constant initial impact parameters (CIIP):** In this study, the dimensional impact parameters, such as D_0, u_0, ΔT_w, and g, are kept constant. The ambient pressure varies from below reference pressure to elevated ambient pressure. When the pressure changes, all material properties change as well and non-dimensional groups, such as Reynolds or Bond number, are not constant. The change in material properties is taken into account in the micro region model, as well as in the CFD simulations. The objective of this study is to investigate the influence of low and high ambient pressure on fluid dynamics and thermodynamics. Probably, this is the study with most practical relevance. It will answer the question what happens if solely the ambient pressure is varied, e.g. in a spray cooling chamber.
- **Low and high ambient pressure with constant non-dimensional groups (CNDG):** This parameter study is similar to the CIIP study. The ambient pressure and consequently the material properties change. In contrast to the former study, the non-dimensional groups, such as Reynolds, Weber, Bond, Prandtl, and Jakob number, stay constant. The dimensional impact parameters change. The objective of the CNDG parameter study is to identify the influencing parameters on the evaporative drop impact process for various ambient pressures that is not induced by the change of non-dimensional groups.
- **Compressibility:** The developed solver takes into account the compressibility of the vapour and liquid phase individually. The objective of the study is to investigate the influence of the compressibility on fluid dynamics and thermodynamics for different pressures. The compressibility is derived from thermodynamic principles. However, since this material property is not available as measured quantity, it needs to be considered as an additional, unknown input parameter. On the one hand, the sensitivity of the numerical model on the compressibility is shown for the drop impact process with evaporation. The study quantifies the error which arises from the assumption of incompressible instead of compressible fluid flow. On the other hand, the study helps to investigate the behaviour of fluids of different compressibility.
- **Material properties of the vapour phase:** Commonly, much emphasis is put on the material properties of the liquid for the drop impact and evaporation process. However, when varying the ambient pressure, the material properties of the vapour change, as well. Within this study, the influence of the vapour phase's viscosity, density, heat capacity, and Prandtl number on the evaporative drop spreading and receding process is investigated. Furthermore, not only the physical material properties of FC-72 are considered. A parameter study is conducted varying the viscosity and density of the vapour phase.

CHAPTER 6

Results and Discussion

In this Chapter, the results are presented and discussed for the variation of ambient pressure for different length scales. The various ambient pressures influence the material properties and, therefore, the fluid dynamics, as well as the heat and mass transfer.

The first part of the Chapter focuses on the shortest length scales investigated. The micro region model is used, which describes the processes in the vicinity of an evaporating three-phase contact line. Results are presented for static and moving contact lines covering a pressure range of about $p = [0.1 \ldots 15.5\,\text{bar}]$ ($p/p_{\text{cr}} = \left[5 \cdot 10^{-3} \ldots 0.9\right]$ for FC-72).

In the second part of the Chapter, the results of the macro CFD simulations of a single drop impact on a hot wall under various ambient pressures are presented and discussed. The compressible fluid flow solver, which takes phase change into account and uses dynamic contact line handling is applied for the CFD simulations. The results from the micro region are included as correlation coefficients. Several parameter studies are conducted to investigate the influence of low and high ambient pressure. The focus is the non-splashing drop-wall collision in a non-boiling, single-component evaporation regime. Ambient pressure ratios ranging between $p/p_{\text{cr}} = \left[8 \cdot 10^{-3} \ldots 0.5\right]$, non-dimensional numbers ranging between $Re = [600 \ldots 1300]$, $We = [10 \ldots 50]$, $Bo = [0.3 \ldots 1.6]$, $Pr = [7 \ldots 14]$, and $Ja = [0.1 \ldots 0.2]$ are investigated. The wall temperature is above saturation but below Leidenfrost temperature. The wall superheat is in the order of $\Delta T = 10\,\text{K}$.

6.1 Part I: Micro region model – variation of ambient pressure

This section is dedicated to the influence of various ambient pressures on the evaporating three-phase contact line. The results are obtained from the micro region model introduced in Chapter 3 using different ambient pressures and material properties of FC–72.

In Figure 6.1, the apparent contact angle and the transferred heat across the micro region is shown as a function of pressure for different contact line velocities. The displayed contact line velocities represent minimum and maximum velocities obtained during the macro scale simulations. Values for the contact line velocity $u_{\text{cl}} > 0$ refer to a spreading drop (wetting), whereas values for the contact line velocity $u_{\text{cl}} < 0$ refer to a receding drop (dewetting). A static contact line has zero velocity. A dashed vertical line indicates atmospheric pressure $p = 1.013\,\text{bar}$.

With increasing ambient pressure, the apparent contact angle increases monotonously for receding and static contact lines. Remarkably, the contact angle for higher values of advancing contact line speeds shows a local minimum at approximately $p = 1\,\text{bar}$, as depicted in Figure 6.1(a). However, during the spreading phase after drop impingement on a solid surface, the dynamic, advancing contact angle plays a sub-dominant role due to the inertia forces of the drop movement. Therefore, the results from the

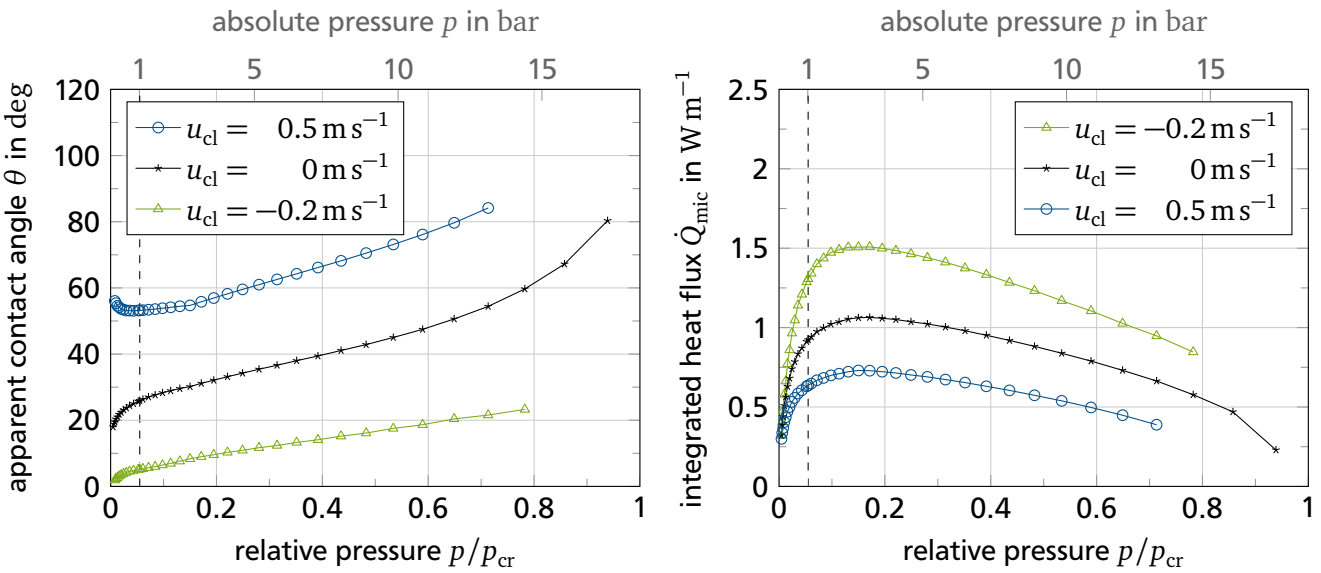

(a) Apparent contact angle as function of pressure.

(b) Integrated heat flux as function of pressure.

Figure 6.1.: Results from the micro region model evaluated for $\Delta T = 5\,\mathrm{K}$ and different contact line velocities. Atmospheric pressure $p = 1.013\,\mathrm{bar}$ is indicated by a dashed vertical line.

micro region model for the contact angle can be generally simplified to a single statement: the higher the pressure the higher is the contact angle.

From the material property study presented in Chapter 3 it was concluded that the material properties surface tension, vapour density, and latent heat of vaporisation undergo the largest changes when varying the pressure. At the same time, these three material properties have the largest impact on the contact angle and on the transferred heat. Since the contact angle is increasing with increasing pressure (Figure 6.1(a)), the decreasing surface tension and increasing vapour density are dominating over the influence of the decreasing latent heat of vaporisation (Figures 3.6(a), D.1(a), and D.1(c)). A decreasing latent heat of vaporisation decreases the contact angle in the micro region model.

The heat transferred across the micro region per meter contact line length is shown in Figure 6.1(b). With increasing contact line velocity, less heat is transferred due to increasing apparent contact angles. High values for θ result in high values for the thickness of the micro region and consequently high thermal resistances within the liquid. However, the monotonous trend from the contact angle over the ambient pressure does not directly translate to $\dot{Q}_{mic}$. The transferred heat across the micro region shows a local maximum over ambient pressure for all contact line velocities. The local maximum occurs at a pressure ratio of approximately $p/p_{cr} = 0.1$, which is explained in the following.

The heat transfer within the micro region model is assumed to be one-dimensional normal to the wall. Three thermal resistances are considered: the Kapitza resistance R_{Kap} located at the solid-liquid surface, the thermal resistance within the liquid R_{liq}, and the thermal resistance at the liquid-vapour interface R_{int} due to evaporation. The total thermal resistance within the micro region R_{mic} is the sum of the individual thermal resistances

$$R_{mic} = \sum_{i=1}^{3} R_i = R_{Kap} + R_{liq} + R_{int}\,. \tag{6.1}$$

While R_{Kap} is constant for all pressures investigated, R_{liq} and R_{int} are a function of both, pressure and film thickness δ within the micro region. The film thickness δ is varying within the micro region and, consequently, is a function of the coordinate along the wall ξ. A typical evolution of the film thickness

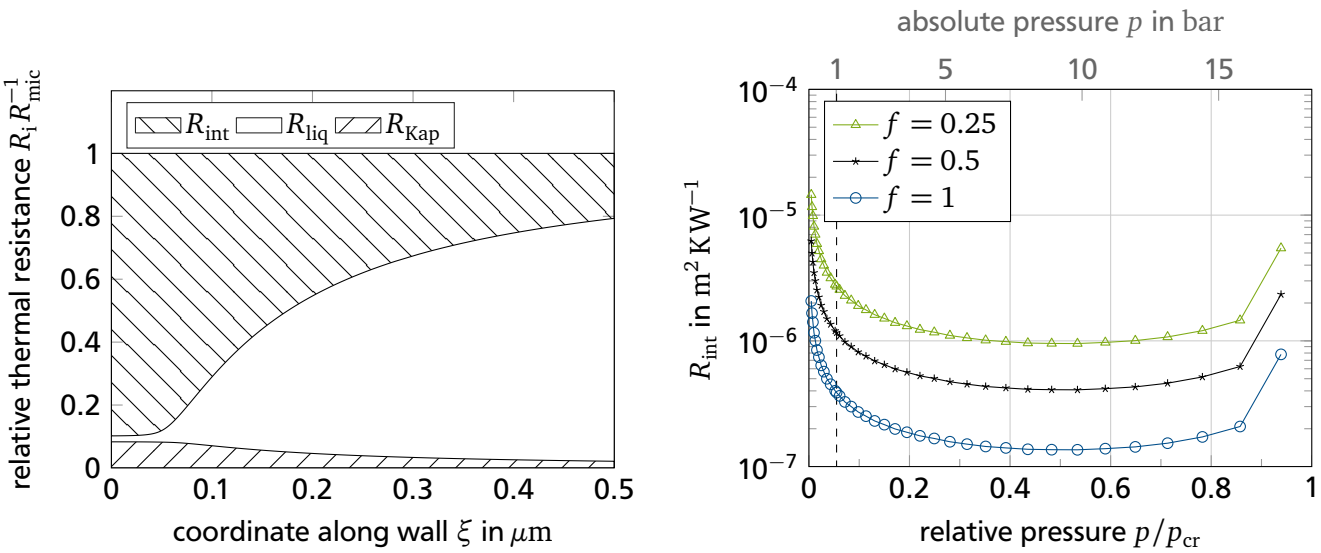

(a) Relative thermal resistances within the micro region for $\Delta T = 5\,\mathrm{K}$, $u_{\mathrm{cl}} = 0\,\mathrm{m\,s^{-1}}$, and $p = 1.013\,\mathrm{bar}$.

(b) Thermal resistance at the liquid–vapour interface due to phase change as function of pressure.

Figure 6.2.: Different thermal resistances. Both, the thermal resistance at the liquid–vapour interface and the thermal resistance within the liquid are a function of pressure and film thickness.

over the coordinate along the wall is shown in Figure 3.2(a). Hence, the ratio of an individual thermal resistance to the total thermal resistance is varying within the micro region.

In Figure 6.2(a), the individual thermal resistance normalised by the total thermal resistance is plotted over ξ. For negative values of ξ, the adsorbed film that cannot evaporate, exists. Close to the adsorbed film, the thermal resistance at the liquid-vapour interface is dominant. However, as soon as the thickness of the film develops, the thermal resistance within the liquid increases and the influence of both, the interfacial resistance as well as the Kapitza resistance is damped.

Additionally, R_{liq} and R_{int} are functions of pressure due to the pressure dependence of the material properties. In Figure 6.2(b), R_{int} is depicted as function of ambient pressure for different values of the condensation coefficient f. Starting from low pressure, R_{int} decreases with increasing pressure. The thermal resistance at the liquid–vapour interface stays approximately constant for the pressure range of about $p/p_{\mathrm{cr}} = [0.3 \ldots 0.7]$. With further increasing pressure, the interfacial resistance increases. The strong increase in R_{int} towards the end of the pressure range results from a sudden change in material properties (compare Figure 3.5), especially in the latent heat of vaporisation.

The heat flux per contact line length $\dot{Q}_{\mathrm{mic}}$ is integrated over the entire width of the micro region. The thermal resistance R_i depends on the position within the micro region, i.e $R_i = f(\xi)$. To compare the individual thermal resistances and $\dot{Q}_{\mathrm{mic}}$, it is reasonable to not only focus on the thermal resistances at the end of the micro region $R_i(\xi_{\mathrm{end}})$. This would overemphasise R_{liq} since the film thickness is the largest at the end of the micro region. Instead, a mean value over the entire micro region is more representative. The mean thermal resistance $\tilde{R}$ is obtained by the mean of a function

$$\tilde{R}_i = \frac{1}{\xi_{\mathrm{end}}} \int_0^{\xi_{\mathrm{end}}} R_i(\xi) \mathrm{d}\xi \,, \tag{6.2}$$

with $\xi_{\mathrm{end}} = 0.5\,\mu$m being the end of the micro region. In Figure 6.3, the mean thermal resistances for the liquid-vapour interface $\tilde{R}_{\mathrm{int}}$, the liquid $\tilde{R}_{\mathrm{liq}}$, and the Kapitza resistance $\tilde{R}_{\mathrm{Kap}}$ are plotted in a semi-logarithmic scale as a function of pressure for different contact line velocities. Since $\dot{Q}_{\mathrm{mic}} \propto \tilde{R}_{\mathrm{mic}}^{-1}$, the

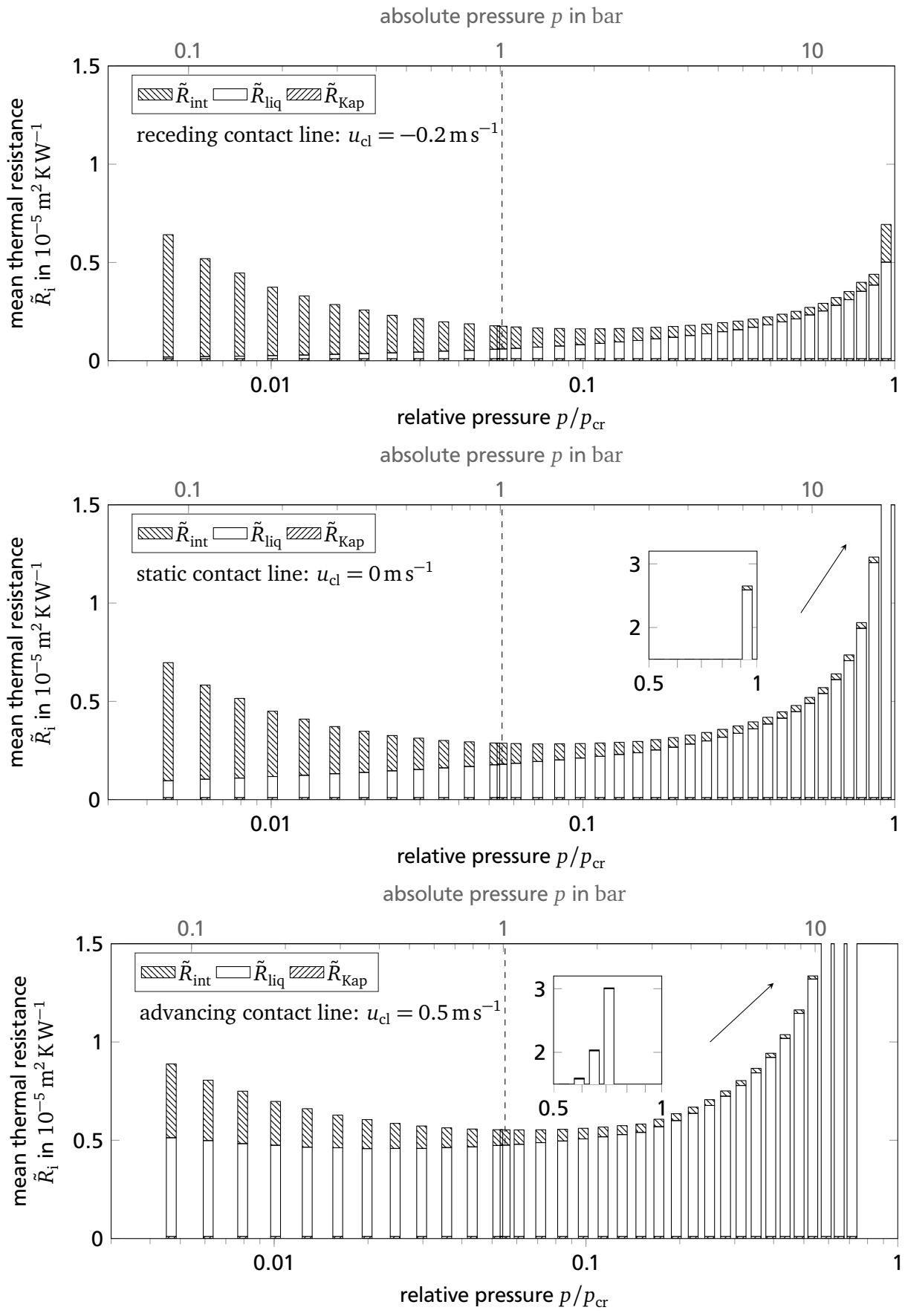

Figure 6.3.: Mean thermal resistance as function of pressure for $\Delta T = 5\,\mathrm{K}$, $f = 0.5$, and different contact line velocities. The dashed vertical line indicates $p = 1.013\,\mathrm{bar}$.

inverse behaviour of the transferred integrated heat flux within the micro region $\dot{Q}_{\mathrm{mic}}$ is represented in Figure 6.3. Due to its small contribution to the total thermal resistance, the Kapitza resistance is close to the abscissa and is not very pronounced in this presentation.

It can be clearly seen that for low pressure and in case of a receding or static contact line the thermal resistance at the liquid–vapour interface is dominating. On the one hand, R_{int} is high for low pressures (cf. Figure 6.2(b)). On the other hand, the contact angle for these situations and, hence, the thermal resistance within the liquid is low.

Noteworthy, the trend of the contact angle as function of pressure shown in Figure 6.1(a) can be identified for R_{liq} in Figure 6.3. For increasing contact angles, R_{liq} increases as well.

Summarising the influence of ambient pressure on evaporating three-phase contact lines, the higher the pressure, the higher is the contact angle. For FC-72, the integrated heat flux $\dot{Q}_{\mathrm{mic}}$ obtains a local maximum at a pressure ratio of approximately $p/p_{\mathrm{cr}} = 0.1$, independent from the contact line velocity.

Fischer [33] experimentally investigated the heat transfer for static and moving contact lines for different ambient pressures in a capillary slot with FC–72. A direct comparison is not the objective of this thesis. The analytically obtained results from the micro region model and the experimentally obtained results differ in spatial resolution by 1-2 orders of magnitude. However, for different ambient pressures and for a static contact line, a heat flux maximum at a pressure ratio of $p/p_{\mathrm{cr}} = 0.1$ was reported in [33] as well.

Xu et al. [107], Mishra et al. [69], Stevens [97], and Mitchell et al. [70], studied the threshold pressure between drop deposition and splashing regimes on flat substrates. They performed experiments for different ambient pressures. In case of high pressures, splash occurs and vanishes for lower ambient pressure. Although not reported in [69, 97, 107], it seems reasonable that the contact angle decreases with decreasing pressure, which results in better wetting characteristics and, therefore, suppresses splashing.

Sarmadivaleh et al. [85] conducted experiments for contact angles of a water/CO_2/quartz system and Al-Yaseri et al. [1] for receding and advancing contact angles of a brine/CO_2/quartz system. Both studies consider pressures up to $p = 200\,\mathrm{bar}$. In these studies, an increasing contact angles with increasing pressure was reported for both, dynamic and static contact angles. Even though the investigated fluid-solid combinations differ from the one considered in the present thesis, the results indicate a generally valid relation between contact angles and system pressure.

Non-dimensional results

To transfer the results from the analytical micro region model to other systems, a non-dimensional presentation of the results is preferable. Commonly, the contact angle is represented as function of Capillary number. The Capillary number adapted to the micro region reads

$$Ca = \frac{\mu_{\mathrm{l}} u_{\mathrm{cl}}}{\sigma}\,, \tag{6.3}$$

with u_{cl} being the velocity of the three-phase contact line. To enforce a constant Ca, u_{cl} varies with increasing pressure ratios, because the material properties are changing with pressure.

The integrated heat flux $\dot{Q}_{\mathrm{mic}}$ across the micro region is scaled with the maximum heat that can be transferred by thermal conduction within the liquid. Hence, the non-dimensional heat flux, which was introduced in Section 3.2, is recalled here

$$Q^* = \frac{\dot{Q}_{\mathrm{mic}}}{k_{\mathrm{l}}\left(T_{\mathrm{w,mic}} - T_{\mathrm{sat}}\right)}\,. \tag{3.35}$$

To investigate drop impact phenomena for constant non-dimensional groups, the micro region Jakob number

$$Ja = \frac{c_\mathrm{l}\left(T_\mathrm{w,mic} - T_\mathrm{sat}\right)}{\Delta h_\mathrm{v}} \tag{6.4}$$

and the Prandtl number

$$Pr = \frac{\mu_\mathrm{l} c_\mathrm{l}}{k_\mathrm{l}} \tag{6.5}$$

are kept constant resulting in a variation of wall superheat $\left(T_\mathrm{w,mic} - T_\mathrm{sat}\right)$ and an artificial thermal conductivity k_l of the liquid, respectively. The thermal conductivity of the liquid is artificially tuned to ensure constant Pr. Nevertheless, the artificial thermal conductivity stays in the same order of magnitude as the physical material property. The remaining material properties, μ_l, σ, c_l, and Δh_v are the physical material properties of FC-72.

The Jakob and Prandtl numbers are chosen in accordance with the reference case of the macro CFD simulations, i.e. $Ja = 0.13$ and $Pr = 9.55$. The Capillary number $Ca = 0.0274$ refers to the advancing contact line velocity $u_\mathrm{cl} = 0.5\,\mathrm{m\,s^{-1}}$ at reference pressure $p = 1.013\,\mathrm{bar}$ ($p/p_\mathrm{cr} = 0.055$). The Capillary number $Ca = -0.0110$ refers to the receding contact line velocity $u_\mathrm{cl} = -0.2\,\mathrm{m\,s^{-1}}$ at reference pressure.

In Figure 6.4(a), the apparent contact angle θ is plotted as function of pressure ratio p/p_cr. Interestingly, for advancing contact lines ($Ca > 0$), θ seems to be only weakly influenced by pressure in case of constant Prandtl and Jakob numbers. For static and receding contact lines, the apparent contact angle increases.

The non-dimensional heat flux is depicted in Figure 6.4(b). The non-dimensional heat flux increases with increasing pressure up to about $p/p_\mathrm{cr} = 0.2$. With further increasing pressure, Q^* decreases in case of a receding contact line. In contrast, Q^* stays almost constant for relative pressures higher than $p/p_\mathrm{cr} = 0.2$ in case of a static or advancing contact line.

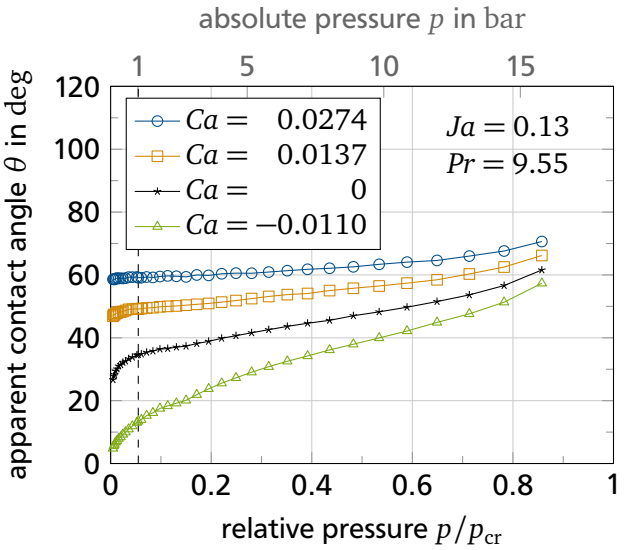

(a) Apparent contact angle θ as function of relative pressure p/p_cr.

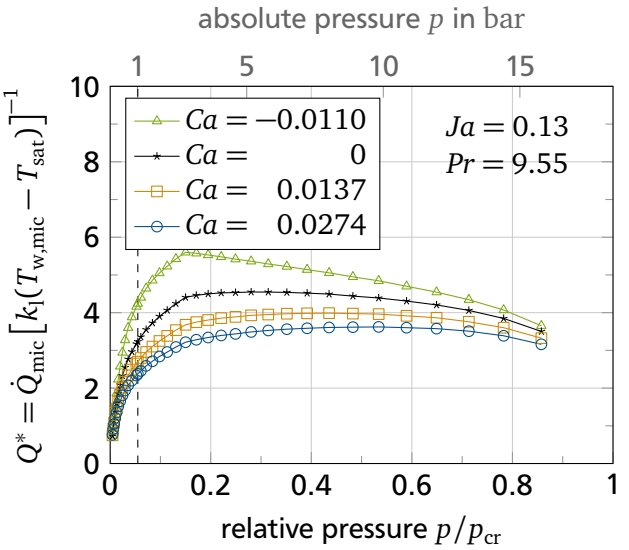

(b) Non-dimensional heat flux Q^* across the micro region as function of relative pressure p/p_cr.

Figure 6.4.: Results from the micro region model for constant Ja and Pr numbers.

6.2 Part II: CFD simulations of drop impact at low and high ambient pressure

Within this work, two different studies of drop impact on a hot wall are conducted to investigate the influence of ambient pressure. In the following, the results of the studies are described with a focus on fluid dynamics behaviour, as well as heat and mass transfer. The results are separately presented for low and high ambient pressures. The reference case at atmospheric pressure represents the cut-off pressure separating the low and high ambient pressure range.

Another study investigates the influence of compressibility on the evaporating drop impact process. Finally, material properties of the vapour are investigated in a separate study.

6.2.1 Parameter study for constant initial impact parameters (CIIP)

Within the parameter study, all initial and impact parameters, such as $D_0 = 1.0241\,\mathrm{mm}$, $u_0 = 0.2735\,\mathrm{m\,s^{-1}}$, $\Delta T = 10\,\mathrm{K}$, $g = 9.74\,\mathrm{m\,s^{-2}}$, are identical for each simulation run. However, when varying the ambient pressure, all material properties change and, consequently, all non-dimensional groups, such as Reynolds, Weber, Bond, Prandtl, and Jakob number are varying. All dimensional and non-dimensional parameters of the CIIP study are listed in Table C.4 in the appendix.

For the CIIP study and with increasing ambient pressure, *Re*, *We*, *Bo*, and *Ja* are increasing. Only *Pr* is decreasing with increasing pressure. Remarkably, with increasing pressure at constant drop diameter, the drop's inertia and volume forces decrease because the liquid's density decreases. However, viscous and surface forces decrease stronger with increasing pressure than inertia and volume forces resulting in rising *Re*, *We*, and *Bo* numbers. In Table 6.1, the changes of the non-dimensional numbers with pressure are summarised. The dynamic and static contact angles are increasing with increasing pressure.

Table 6.1.: Changes of non-dimensional groups as well as initial and impact parameters with ambient pressure, $\mathrm{d}(\cdot)/\mathrm{d}(p/p_{\mathrm{cr}})$, for the CIIP study.

Parameter study	*Re*	*We*	*Bo*	*Pr*	*Ja*	θ	D_0	u_0	ΔT	g
CIIP	>0	>0	>0	<0	>0	>0	0	0	0	0

For constant initial impact parameters, the following conclusions can be drawn: the higher the ambient pressure

- the higher is the maximum spreading ratio S_{max}.
- the smaller is the minimum spreading ratio S_{min} after receding.
- the higher is the transferred non-dimensional heat E^*.
- the higher is the non-dimensional evaporated mass M^*.

The duration of the spreading phase τ_{s} and the duration of the receding phase τ_{r} decreases with increasing pressure for the low pressure range. In case of high ambient pressure, τ_{s} and τ_{r} increase with increasing pressure. The spreading ratio, the non-dimensional heat, and the non-dimensional evaporated mass are shown in Figure 6.5 and are discussed in the following for the CIIP study.

Fluid dynamics

The temporal evolution of the non-dimensional contact line radius S (spreading ratio) over the non-dimensional time τ is presented in Figure 6.5(a) for low ambient pressures and in Figure 6.5(b) for high ambient pressures.

During the early spreading phase, the evolution of the non-dimensional contact line is similar for all cases. Maximum spreading S_{max} and minimum spreading S_{min} are influenced by ambient pressure. The

duration of the receding phase τ_r varies stronger than the duration of the spreading phase τ_s for the investigated pressure range.

The **maximum spreading ratio** S_{max} increases with increasing pressure for the CIIP study. An increase in *Re*, *We*, and *Bo* supports the increase in S_{max}. Viscous forces, which counteract the spreading, decrease with increasing pressure. Additionally, surface forces, which act contrary to the elongation of the drop, are decreasing within increasing pressure. With increasing pressures, these aforementioned effects are dominating over the influence of the *Pr* and *Ja* numbers, as well as over an increase in contact angle, which would lead to smaller S_{max}.

The **spreading duration** τ_s is influenced by two counteracting effects. If *We* increases, the spreading duration increases. If the contact angle θ increases, the spreading duration decreases. For the low pressure range, it can be clearly observed in Figure 6.5(a) that τ_s decreases with increasing pressure. Consequently, the increase in contact angle is dominating over the influence of the Weber number. However, for the high pressure range depicted in Figure 6.5(b), τ_s stays approximately constant up to a pressure ratio of about $p/p_{cr} = 0.15$. A further increase in ambient pressure results in an increase in τ_s. This indicates that the influence of *We* is dominating the spreading duration for large pressure ratios.

The **minimum spreading ratio** S_{min} decreases with increasing pressure. The influence of *Pr* and *Ja* numbers as well as an increase in contact angle with increasing pressure are dominating over the influence of the change in *Re*, *We*, and *Bo* numbers. A minor influence on decreasing S_{min} is attributed to the decrease of *Pr*. A thicker thermal boundary layer within the liquid drop develops with decreasing *Pr*. This has the effect that the temperature gradient normal to the liquid-vapour interface gets steeper, which results in strong evaporation, especially during receding. The strong evaporation results in less mass of the liquid drop. However, the major influence for decreasing S_{min} is the increase in *Ja* number and the increase in contact angle. The Jakob number influences the fluid motion indirectly. An increase in *Ja* results in larger contact angles [2]. Larger contact angles during receding forces the drop to contract more resulting in smaller values of S_{min}. For very low ambient pressures, in turn, S_{min} is not very pronounced and consequently the distinct boundary between the receding phase and sessile drop vanishes.

The **receding duration** τ_r is mostly influenced by Weber number and contact angle. Generally, large values for *We* result in long receding durations whereas large contact angles shorten the receding phase. Large Weber numbers are a result of low surface forces. Low surfaces forces, in turn, lead to weak contraction of the drop during receding and, hence, to a long receding duration. For the low pressure range shown in Figure 6.5(a), it can be seen that with increasing pressure τ_r decreases. Hence, the contact angle influences τ_r stronger than *We*. In contrast, τ_r increases for the high pressure range shown in Figure 6.5(b). High Weber numbers are dominating the receding duration in this pressure range.

Heat and mass transfer

Both, the heat and mass transfer, are influenced by the change in ambient pressure. For the CIIP study, the influence caused by a change in non-dimensional groups is larger than the influence caused by a change in the contact angle.

The **non-dimensional heat** E^* over the non-dimensional time is shown in Figures 6.5(c) and (d). For the low and high pressure range investigated, E^* increases with increasing pressure. With increasing pressure, *Pr* decreases whereas *Ja* increases, both leading to an increase in non-dimensional transferred heat. However, E^* needs to be interpreted carefully. For evaluating E^* the integrated heat flux Q is scaled with $M_0 \Delta h_v$ (c.f. Equation 5.3). With increasing pressure, the absolute value of Q decreases. In Figure 6.6(a) the evolution of the cumulative heat flow is shown for selected pressure ratios. The decrease in inertia forces leads to a decrease in convective heat transfer. Furthermore, the conductive heat transfer is decreasing with increasing pressure caused by smaller values for the thermal conductivity of the liquid. However, in case of CIIP, the initial mass of the drop M_0 and the latent heat of vaporisation Δh_v decrease even stronger with pressure than Q, which results in an increase in E^*.

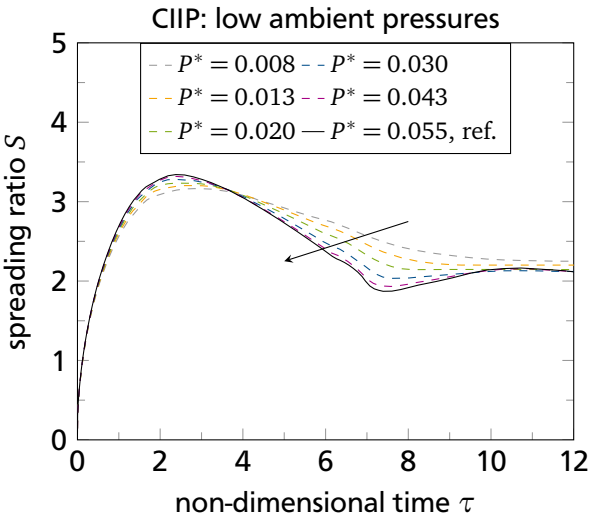

(a) Spreading ratio.

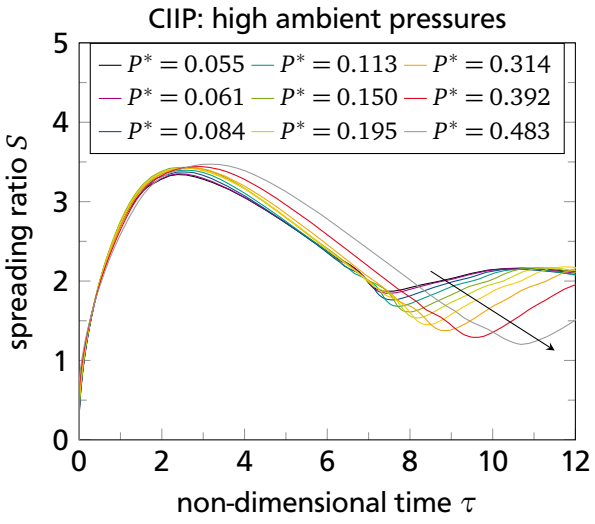

(b) Spreading ratio.

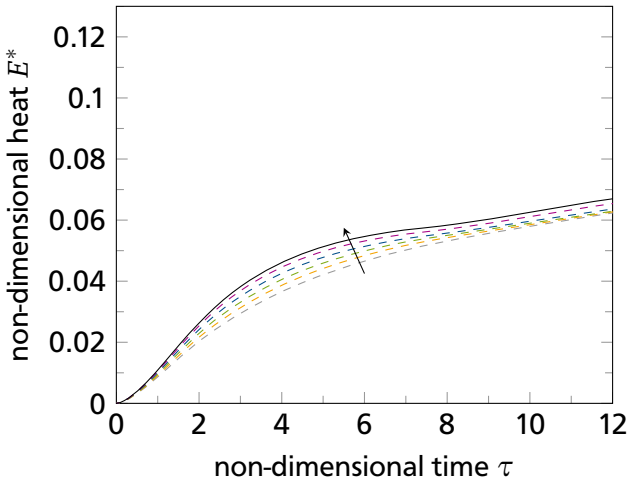

(c) Non-dimensional heat.

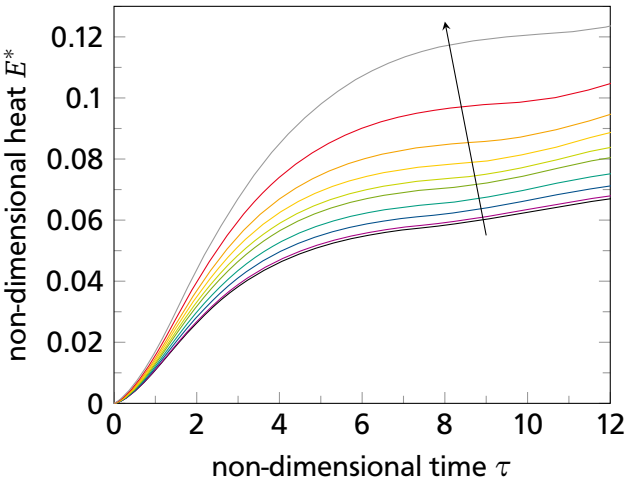

(d) Non-dimensional heat.

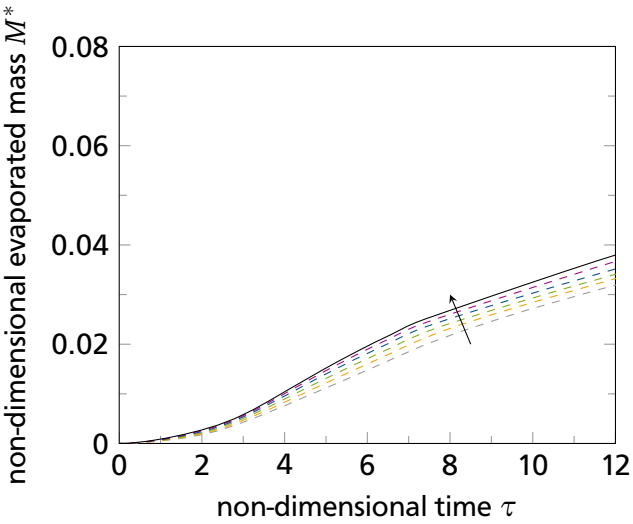

(e) Non-dimensional evaporated mass.

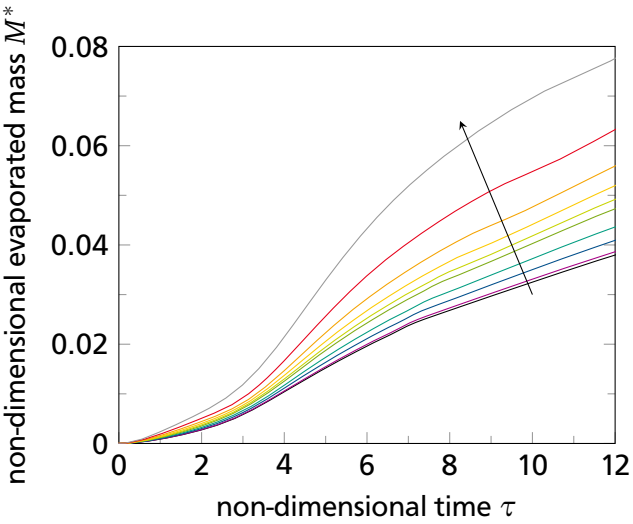

(f) Non-dimensional evaporated mass.

Figure 6.5.: Spreading ratio, non-dimensional heat and evaporated mass for constant initial impact parameters ($D_0 = 1.0241\,\mathrm{mm}$, $u_0 = 0.2735\,\mathrm{m\,s^{-1}}$, $\Delta T = 10\,\mathrm{K}$, $g = 9.74\,\mathrm{m\,s^{-2}}$). Results are depicted left for a low ambient pressure range and right for a high ambient pressure range. The reference case is at $P^* = p/p_{\mathrm{cr}} = 0.055$.

The **non-dimensional mass** M^* over the non-dimensional time is shown in Figures 6.5(e) and (f). For the pressure range investigated, M^* increases with increasing pressure. With increasing pressure, less energy is required for the phase change from liquid to vapour caused by decreasing Δh_v. Consequently, an increasing Jakob number results in increasing M^*. Furthermore, smaller Prandtl numbers result in increasing thermal boundary layer thicknesses in the liquid extending from the wall. As a result, the thermal boundary layer and the liquid-vapour interface are now much closer to one another. Consequently, a steeper temperature gradient close to the liquid-vapour interface develops, which enhances evaporation. In Figure 6.6(b), the evolution of the cumulative mass flow is shown. In contrast to the cumulative heat flow Q, the cumulative mass flow M_{evap} increases with increasing pressure.

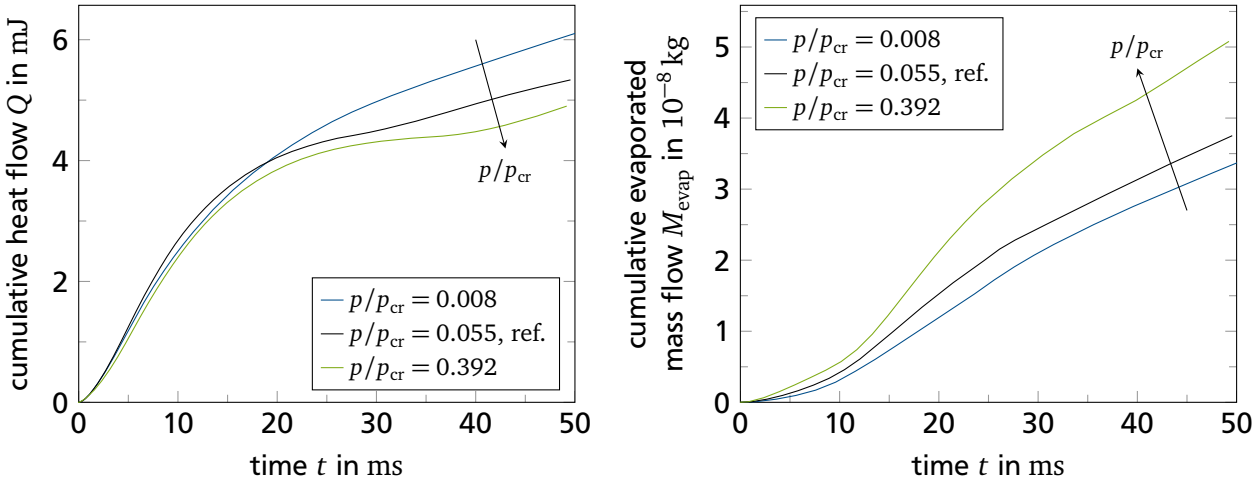

(a) Cumulative heat flow.

(b) Cumulative mass flow.

Figure 6.6.: Cumulative heat and mass flow for constant initial impact parameters study.

6.2.2 Parameter study for constant non-dimensional groups (CNDG)

Within this parameter study, all non-dimensional numbers are kept constant for all simulation runs. The non-dimensional numbers are $Re = 1000$, $We = 15$, $Bo = 0.5$, $Pr = 9.55$, and $Ja = 0.13$. The ambient pressure changes. To ensure constant non-dimensional groups, the initial and impact parameters, such as D_0, u_0, ΔT, and g, are varied. Additionally, to guarantee a constant Prandtl number for various ambient pressures, the thermal conductivity of the liquid k_l is artificially tuned. However, k_l stays in the same order of magnitude as the physical value. All dimensional and non-dimensional parameters of the CNDG study are listed in Table C.5 in the appendix.

For the CNDG study and increasing ambient pressure, the contact angle increases whereas the wall superheat decreases. The parameter D_0, u_0 and g show a non-monotonous behaviour. Starting from the lowest investigated pressure, D_0 decreases whereas u_0 and g increase with increasing pressure. However, towards the highest investigated pressures, D_0 increases whereas u_0 and g decrease with increasing pressure. Thus, $D_0(p)$ follows a convex function whereas $u_0(p)$ and $g(p)$ follow a concave function. In Table 6.2, the change of the initial and impact parameters with pressure is summarised.

Table 6.2.: Change of non-dimensional groups as well as initial and impact parameters with ambient pressure, $\mathrm{d}(\cdot)/\mathrm{d}(p/p_{cr})$, for the CNDG study.

Parameter study	Re	We	Bo	Pr	Ja	θ	D_0	u_0	ΔT	g
CNDG	0	0	0	0	0	>0	convex	concave	<0	concave

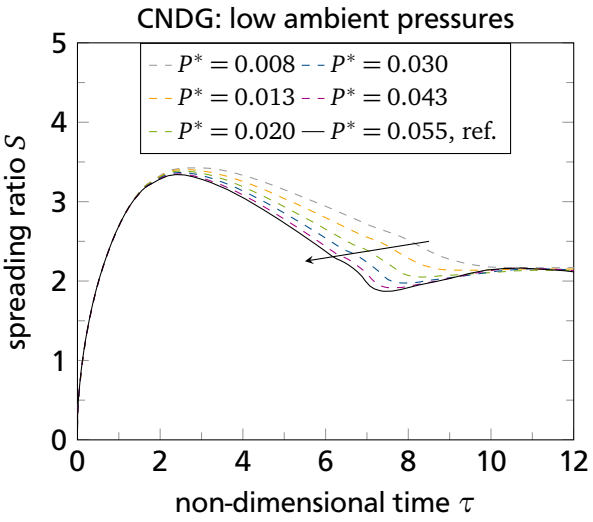

(a) Spreading ratio.

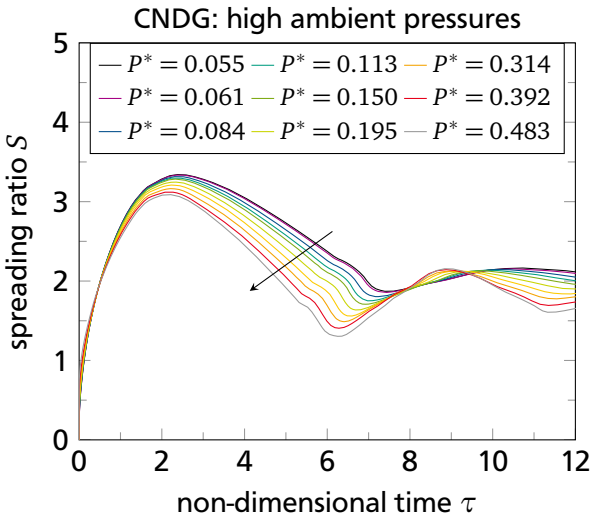

(b) Spreading ratio.

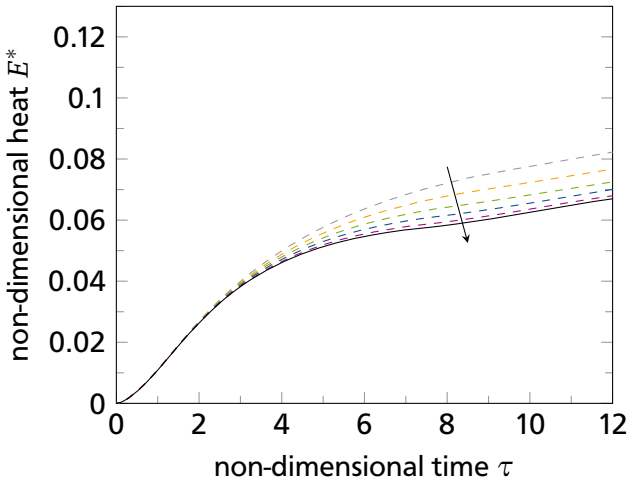

(c) Non-dimensional heat.

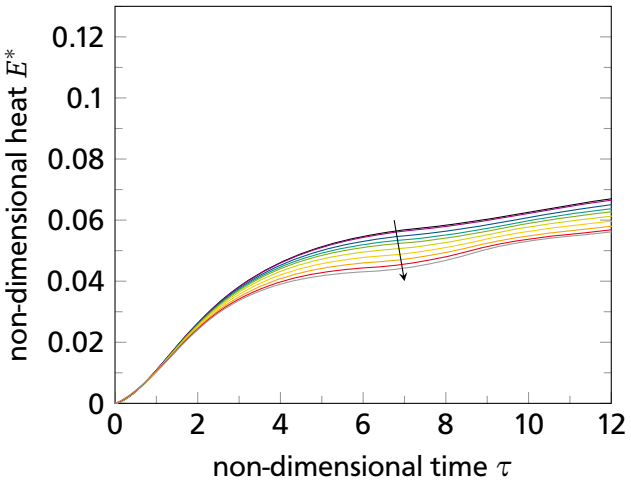

(d) Non-dimensional heat.

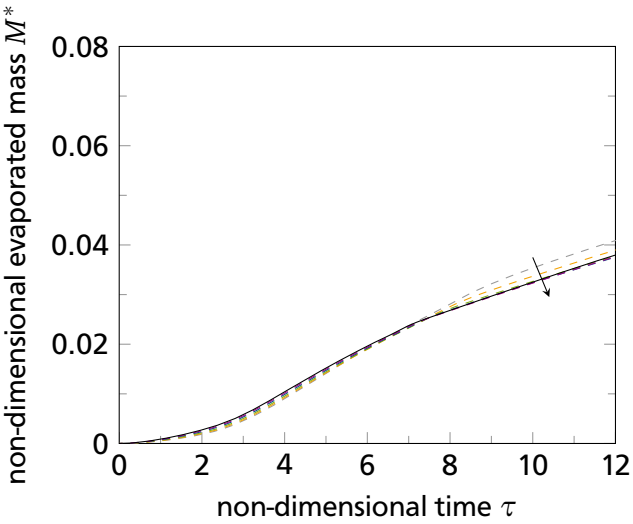

(e) Non-dimensional evaporated mass.

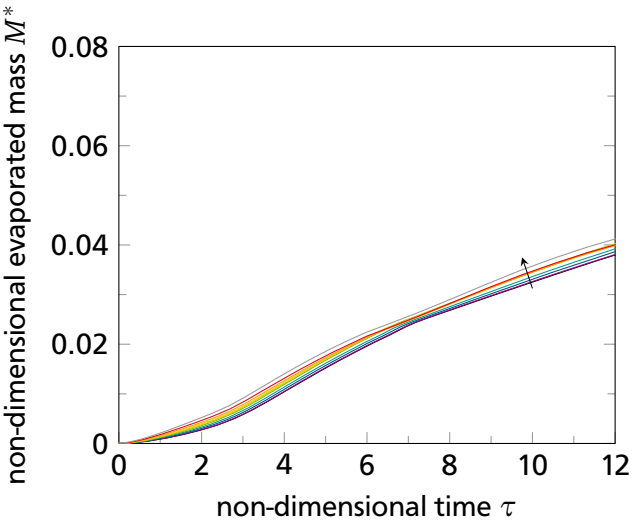

(f) Non-dimensional evaporated mass.

Figure 6.7.: Spreading ratio, non-dimensional heat, and non-dimensional evaporated mass for constant non-dimensional groups ($Re = 1000$, $We = 15$, $Bo = 0.5$, $Pr = 9.55$, $Ja = 0.13$). Results are depicted left for a low ambient pressure range and right for a high ambient pressure range. The reference case is at $P^* = p/p_{\mathrm{cr}} = 0.055$.

For constant non-dimensional groups, the following conclusions can be drawn: the higher the ambient pressure

- the lower is the maximum spreading ratio S_{max}.
- the shorter is the duration of the spreading phase τ_s.
- the smaller is the minimum spreading ratio S_{min} after receding.
- the shorter is the duration of the receding phase τ_r.
- the lower is the transferred non-dimensional heat E^*.

For the investigated pressure range, the non-dimensional evaporated mass M^* stays approximately constant and varies less than ±10 % in comparison to the reference case.

All non-dimensional groups of the macroscopic model stay constant and, therefore, the shift in acting forces is eliminated. Consequently, the influencing parameters can be limited to the contact angle, as well as the material properties that are not considered in the non-dimensional groups. These are the compressibility of liquid and vapour as well as all vapour material properties. The influence of the compressibility and the vapour material properties, however, are discussed in individual parameter studies. The spreading ratio, the non-dimensional heat, and the non-dimensional evaporated mass are shown in Figure 6.7 and are discussed in the following for the CNDG parameter study.

Fluid dynamics

The spreading ratio is shown in Figure 6.7(a) for the low pressure range and in Figure 6.7(b) for the high pressure range. S_{min} is influenced stronger than S_{max} for the investigated pressure ranges. The spreading and receding durations are influenced by the ambient pressure. In contrast to the CIIP study, S_{max}, S_{min}, τ_s, and τ_r show a monotonous behaviour with increasing ambient pressure.

The **maximum spreading ratio** S_{max} and the **spreading duration** τ_s decrease with increasing pressure. As the contact angle increases with increasing pressure, it hinders the drop from further spreading, resulting in a decreasing S_{max}. As a consequence, for constant non-dimensional groups, the maximum spreading is reached earlier and τ_s decreases for higher pressures.

During the receding phase wetting properties influence the fluid dynamics stronger than during the spreading phase. The **minimum spreading ratio** S_{min} and the **receding duration** τ_r decrease with increasing pressure.

The smaller spreading ratios, S_{max} and S_{min}, as well as the shorter spreading and receding durations result in a smaller footprint of the drop over time. The smaller the drop's footprint, the smaller is the wetted surface area, the shorter is the time-averaged three-phase contact line, the smaller is the liquid-vapour area, and the larger is the mean height of the drop. This, in turn, reduces the heat transfer between solid and liquid, as well as the heat and mass transfer across the liquid-vapour interface.

Heat and mass transfer

In Figure 6.7(c) and (d), the evolution of the **non-dimensional heat** E^* is depicted for the low and high pressure range, respectively. The higher the ambient pressure, the less non-dimensional heat is transferred to a single drop. This can be attributed to the reduction of wetted area between wall and the liquid of the drop, to a shorter three-phase contact line, as well as to a larger drop height (i.e. thicker liquid layer).

In Figure 6.7(e) and (f), the evolution of the **non-dimensional evaporated mass** M^* is shown for the low and high pressure range. It is observed that M^* decreases with increasing pressure within the low pressure range whereas M^* increases within the high pressure range. However, for both pressure ranges, the non-dimensional evaporated mass differs less than ±10 % and, therefore, M^* can be considered

to stay constant within the entire investigated pressure range. For CNDG, it can be concluded that the variation in ambient pressure and the resulting variation in wetting properties has only a minor influence on the evaporated mass. This result might appear counter-intuitive since E^* is decreasing with increasing pressure and it might be expected that the evaporated mass is directly linked to the trend of E^*, especially for receding motion of the drop. However, for increasing pressure, Δh_v is also reduced. Consequently, the same amount of M^* evaporates across the liquid-vapour interface with less E^*.

6.2.3 Comparison with correlations from literature

In this section, correlations for the maximum spreading ratio, the spreading duration, as well as the non-dimensional heat are presented. Existing correlations from literature are evaluated for the two parameter studies CIIP and CNDG. Additionally, the results from Batzdorf [2] are included, which describe the influence of the non-dimensional groups *Re*, *We*, *Bo*, *Pr*, and *Ja* on the evaporating drop impact based on numerical simulations. This sophisticated parameter spectrum allows for the evaluation of the correlations that cover a broad range of influencing phenomena on the evaporating, non-splashing, non-boiling single drop impact.

Maximum spreading ratio

The maximum spreading ratio S_{max} is of interest in drop impingement processes. In literature, an often used correlation to predict S_{max}, not only, but also in the context of ambient pressure influence on the drop impact, expresses S_{max} as function of Reynolds and Ohnesorge number. It reads

$$S_{max} = a(Re^2 Oh)^b = a(Re\sqrt{We})^b \,, \tag{6.6}$$

with the non-dimensional Ohnesorge number $Oh = \sqrt{We}/Re$. The two-parameter correlation was used in the studies of Scheller and Bousfield [88] and Mishra et al. [69], in which the pressure influence on the drop impact was investigated[1]. The parameters were obtained empirically and semi-empirically by Scheller and Bousfield [88] (empirical: $a = 0.61$, $b = 0.166$; semi-empirical: $a = 0.91$, $b = 0.133$). Mishra et al. [69] presented different parameters ($a = 0.91$, $b = 0.146$).

Equation 6.6 takes into account the changes in Reynolds and Weber number, but does not take into account the influence of Bond, Prandtl, and Jakob number, as well as the influence of wetting properties. Consequently, Equation 6.6 is not suitable for the CNDG study in which all non-dimensional groups are constant. The best fit for the CIIP study is reached for $a = 1.759$ and $b = 0.077$.

Figure 6.8(a) presents a comparison between the correlation of Equation 6.6 ($a = 1.759$, $b = 0.077$) and the results obtained for the different parameter studies. The abscissa represents the maximum spreading ratio for the CFD simulations obtained in the present thesis and taken from [2]. The ordinate is the estimated maximum spreading ratio based on Equation 6.6. The grey, filled circles represent the results from [2] whereas the coloured symbols represent the results obtained in the present thesis. For the CIIP and CNDG studies, empty symbols refer to the low pressure range whereas filled symbols refer to the high pressure range. The reference case, as well as the validation cases are included. The black, solid line through the origin indicates a perfect match between CFD simulations and the correlation equation. The dashed lines indicate a ±5% deviation.

The correlation predicts a constant maximum spreading ratio in case of CNDG evaluated in the present thesis, as well as for constant *Bo*, *Pr*, and *Ja* evaluated in [2]. However, a good fit is reached for the CIIP study in the low pressure range. Results for the high pressure range are within the ±5% deviation.

Besides (semi-) empirical correlations, such as Equation 6.6, analytically derived correlations exist for the maximum spreading ratio. Within these correlations, the change in kinetic, potential, and surface

[1] parameter range: $Re = \left[19 \ldots 16.4 \cdot 10^3\right]$ and $Oh = [0.002 \ldots 0.58]$ in [88]; $Re = \left[10^3 \ldots 10^4\right]$ in [69]

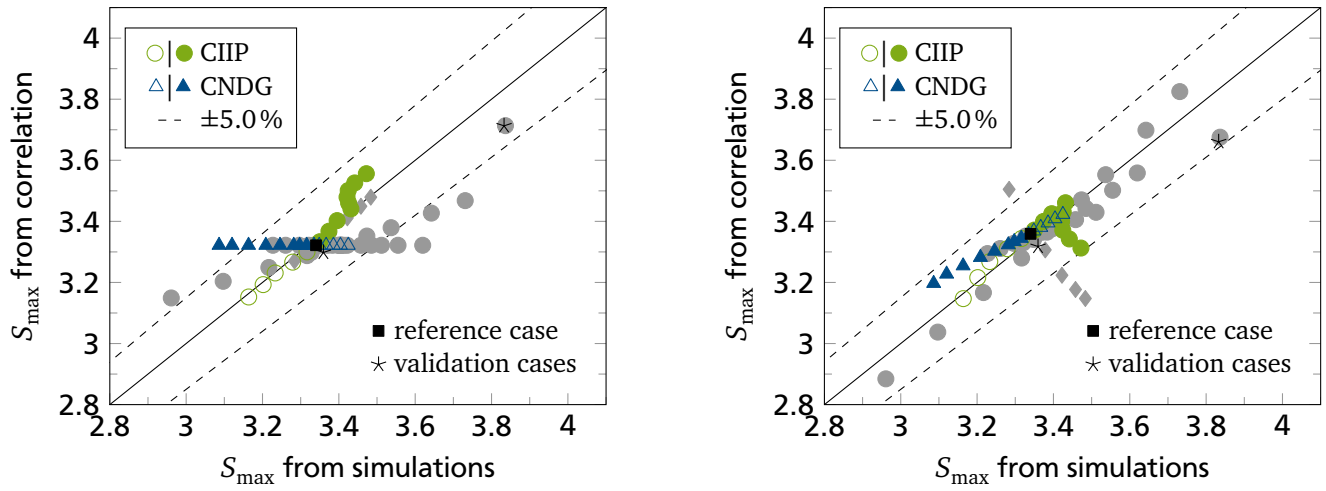

(a) Correlation from Eq. 6.6

(b) Correlation from Eq. 6.7

Figure 6.8.: Correlated versus simulated spreading ratios for low ambient pressure (empty symbols) and high ambient pressure (filled symbols). Additional data (grey symbols) taken from [2].

energy is balanced with the dissipation during the spreading. Chandra et al. [18], Pasandideh-Fard et al. [77], as well as Ukiwe et al. [101] proposed analytical correlations, which differ in the estimation of the dissipation. Batzdorf [2] accounts for the change in potential energy in the energy balance, as well as for the evaporated mass until maximum spreading. This approach is also used in the present correlation. After re-arranging in terms of non-dimensional groups, the energy balance reads

$$We + Bo + 12 - 3\,(1 - \cos\theta_0)\,S_{max}^2 = 12\frac{We}{Re\left(1 - M_s^*\right)}S_{max}^4\,. \tag{6.7}$$

M_s^* denotes the non-dimensional mass evaporated until the maximum spreading. From the above equation, the maximum spreading ratio S_{max} can be determined using the static contact angle θ_0.

In Figure 6.8(b), the comparison between the correlation resulting from Equation 6.7 and S_{max} computed by the CFD simulations is shown. The deviation of the correlation from the simulation results of the CIIP and CNDG parameter study is in a ±5% range. In [2] it was pointed out that the correlation predicts $dWe/dS_{max} < 0$ whereas the CFD simulations predict the opposite result, $dWe/dS_{max} > 0$. The results of the variation of We are represented by diamond shaped symbols in Figure 6.8(b). Within the CIIP study conducted in the present thesis, We increases with increasing pressure due to the decrease in surface tension especially in the high pressure range. At the same time, S_{max} is increasing with increasing pressure, i.e. $dWe/dS_{max} > 0$. Therefore, the trend of S_{max} obtained within the high pressure range of the CIIP study follows the trend of S_{max} obtained by the variation of We.

Spreading duration

The non-dimensional spreading duration τ_{max} is found in the present thesis to be proportional to $We^{0.25}$

$$\tau_{max} \propto \left(\frac{We}{(1 - \cos\theta_0)}\right)^{0.25}\left(1 - M_s^*\right). \tag{6.8}$$

Choosing a scaling factor to 0.84 all simulation data points are within a ±15 % range. In Figure 6.9(a) the comparison between the correlated and simulated non-dimensional spreading duration is presented.

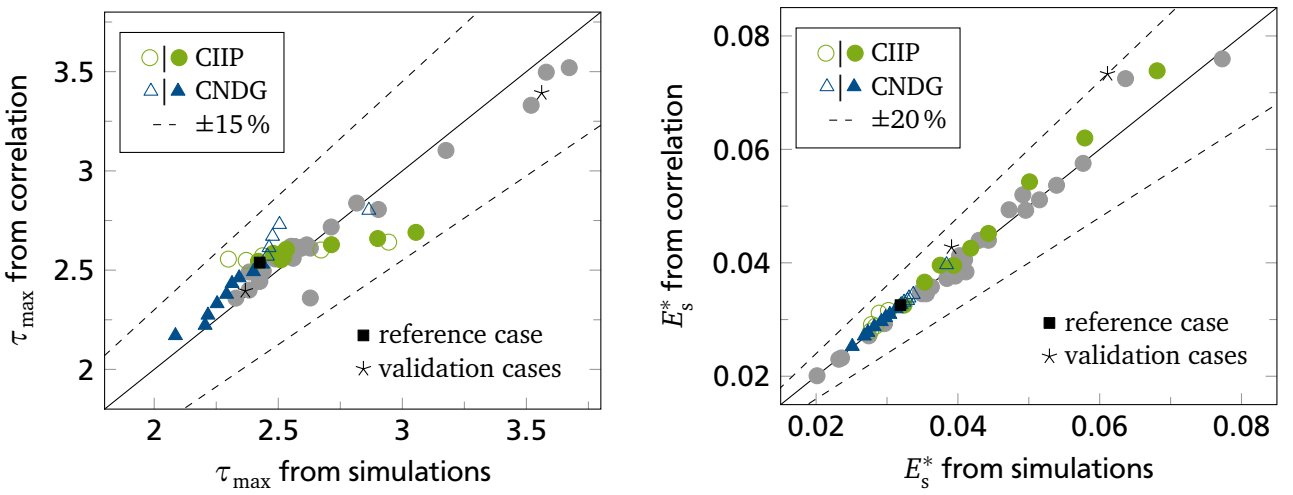

(a) Correlation from Eq. 6.8.

(b) Correlation from Eq. 6.9.

Figure 6.9.: Correlated versus simulated non-dimensional spreading duration (left) and non-dimensional heat during spreading (right) for low ambient pressure (empty symbols) and high ambient pressure (filled symbols). Additional data (grey symbols) taken from [2].

It is observed that the slope of the correlation is appropriate for the majority of the data points. However, the deviation is largest for the CIIP study.

Non-dimensional heat

The non-dimensional heat E_s^* during the spreading phase can be approximated using a correlation derived in [2]. The derivation of the correlation assumes that the heat from the solid to the drop is mainly transferred by the convection of the drop's liquid. Therefore, the transferred heat can be balanced with a Nusselt correlation for single, continuously impinging jets. The derived correlation for the non-dimensional heat E_s^* during the spreading phase reads

$$E_s^* = 3a \frac{S_{max}(S_{max}-1.1)}{(S_{max}-0.6)} \frac{\left(1+0.005Re^{0.55}\right)^{0.5} Ja}{Re^{0.5}Pr^{0.58}} \tau_{max}. \tag{6.9}$$

The maximum spreading ratio S_{max} and the spreading duration τ_{max} are taken from each simulation run. Choosing a pre-factor of $a = 4/3$ results in a maximum deviation of less than ±20 % for all data points. In Figure 6.9(b) the comparison between the correlated and simulated non-dimensional heat E_s^* during the spreading phase is presented. The highest deviation is found for one of the validation scenarios. However, for the validation scenarios, the conjugated heat transfer was utilised including local cooling of the solid. The local cooling affects the convective heat transfer between solid and liquid and results in less heat being transferred within the simulations.

Except for the validation scenario, it can be observed that the results of the high pressure range CIIP study show the highest deviations. As noticed in former studies [2], Equation 6.9 might not be accurate for strong variations in *We*, which are present in the high pressure range CIIP study.

6.2.4 Compressibility

In the present thesis, a compressible fluid flow solver is developed, which accounts for the phase change at the free liquid-vapour interface and for dynamic three-phase contact line handling. One objective of the present thesis is to investigate the influence of compressibility on the heat and mass transfer

during the evaporative drop impact process, especially at elevated ambient pressures. Therefore, two different compressibility studies are conducted. Within the first compressibility study, the CIIP and CNDG studies introduced in the previous section are re-calculated using zero compressibility. The deviation in spreading ratios, spreading and receding duration, as well as transferred heat and mass is compared and discussed. Within a second compressibility study, the compressibility of the fluid is artificially raised for the reference case up to a compressibility ratio of $\psi/\psi_{\mathrm{ref}} = 50$.

Compressible versus incompressible CIIP and CNDG study

Within this analysis, the studies of constant initial impact parameters (CIIP) and constant non-dimensional groups (CNDG) are re-calculated for incompressible fluid flow. Hence, the compressibility of the liquid and vapour phase is set to zero.

In Figure 6.10, results are shown for the spreading ratios S_{max} and S_{min}, as well as for the non-dimensional times τ_{max} and τ_{min}. The abscissa shows the results obtained from the compressible fluid flow simulations, whereas the ordinate shows the results obtained from the incompressible fluid flow simulations. For the maximum spreading ratio S_{max}, Figure 6.10(a), similar or lower values are

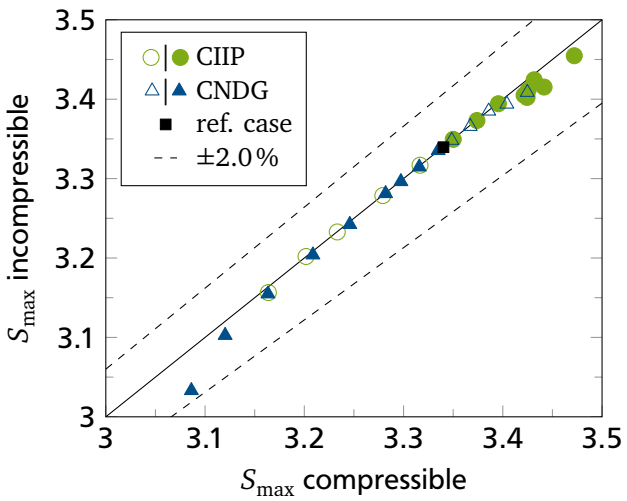

(a) Maximum spreading ratio.

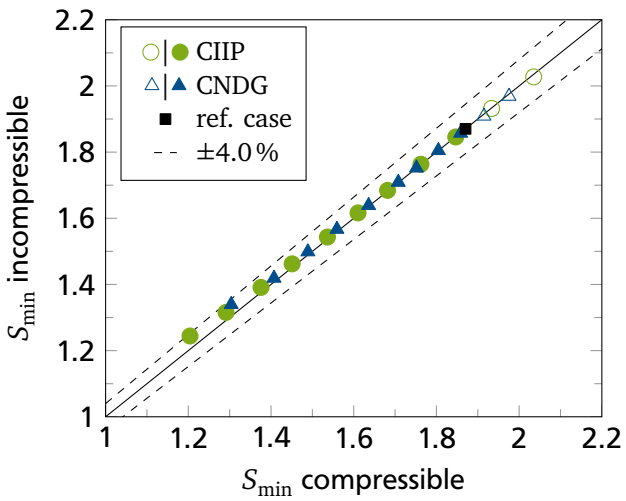

(b) Minimum spreading ratio.

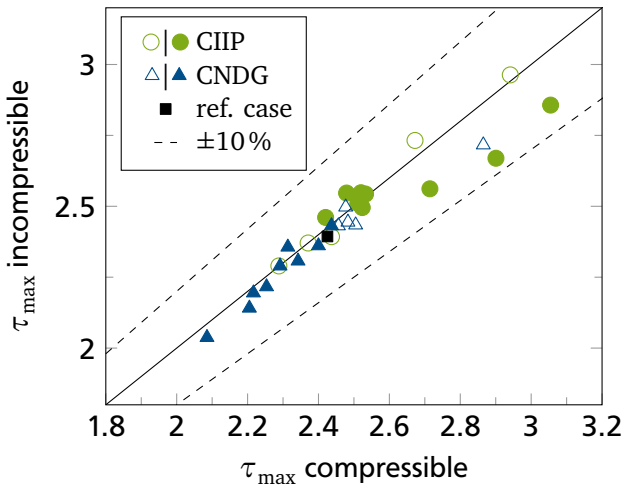

(c) Non-dimensional spreading duration.

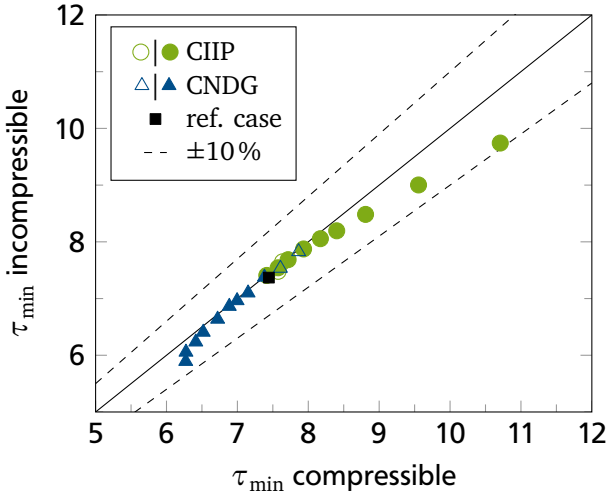

(d) Non-dimensional duration until S_{min}.

Figure 6.10.: Influence of the compressibility on the spreading characteristics for low ambient pressure (empty symbols) and high ambient pressure (filled symbols).

obtained for the incompressible fluid flow. The maximum deviation between incompressible and compressible fluid flow is 1.7 % for the CNDG study at the highest investigated pressure ratio $p/p_{cr} = 0.483$. The deviation in minimum spreading ratio after receding S_{min}, Figure 6.10(b), stays below 4 % (CIIP: 3.3 %; CNDG 2.7 %).

The duration from initial drop-wall contact until maximum or minimum spreading, τ_{max} and τ_{min}, shows larger deviations. The spreading duration τ_{max}, Figure 6.10(c), scatters the most but stays in a ±10 % range. However, the duration τ_{min} until the minimum spreading ratio is reached, Figure 6.10(d), shows a compact distribution over the pressure range. The deviation of τ_{min} is largest for the highest pressure ratio $p/p_{cr} = 0.483$ (CIIP: 9.0 %; CNDG: 6.1 %).

To summarise, the spreading and receding dynamics are influenced by compressibility for elevated pressures. However, no influence of compressibility is observed for the low pressure range as well as for small values of the high pressure range up to a pressure ratio of $p/p_{cr} = 0.195$.

The larger the ambient pressure, the stronger is the influence of the compressibility on the evaporated drop impact. Therefore, the high pressure ratio $p/p_{cr} = 0.483$ is analysed in detail in the following. In Figure 6.11 the spreading ratio and the non-dimensional evaporated mass is plotted for the CIIP and CNDG study, as well as for the reference case. The solid lines refer to the simulations based on compressible fluid flow whereas dashed lines refer to the simulations based on incompressible fluid flow. For the reference case, results based on incompressible and compressible fluid flow can hardly be distinguished. However, the results based on incompressible and compressible fluid flow at $p/p_{cr} = 0.483$ can be clearly distinguished. From the evolution of the spreading ratio over the non-dimensional time, Figure 6.11(a), it can be concluded that for the CIIP study the spreading ratio is influenced more strongly by the compressibility than for the CNDG study. For the CIIP study with compressible fluid flow, the drop recedes slowest resulting in the largest value for τ_{min}. Remarkably, at the same time the evaporated mass becomes largest for the same simulation case. The non-dimensional evaporated mass M^* is depicted in Figure 6.11(b). Even though the CIIP and CNDG study have identical material properties and compressibility factors for the same pressure ratio, the difference in non-dimensional evaporated mass between the simulations with compressible and incompressible fluid flow is higher for the CIIP study than for the CNDG study. This indicates that the influence of compressibility is not solely caused by the value of the compressibility factor. The influence of compressibility appears to be amplified by one or more

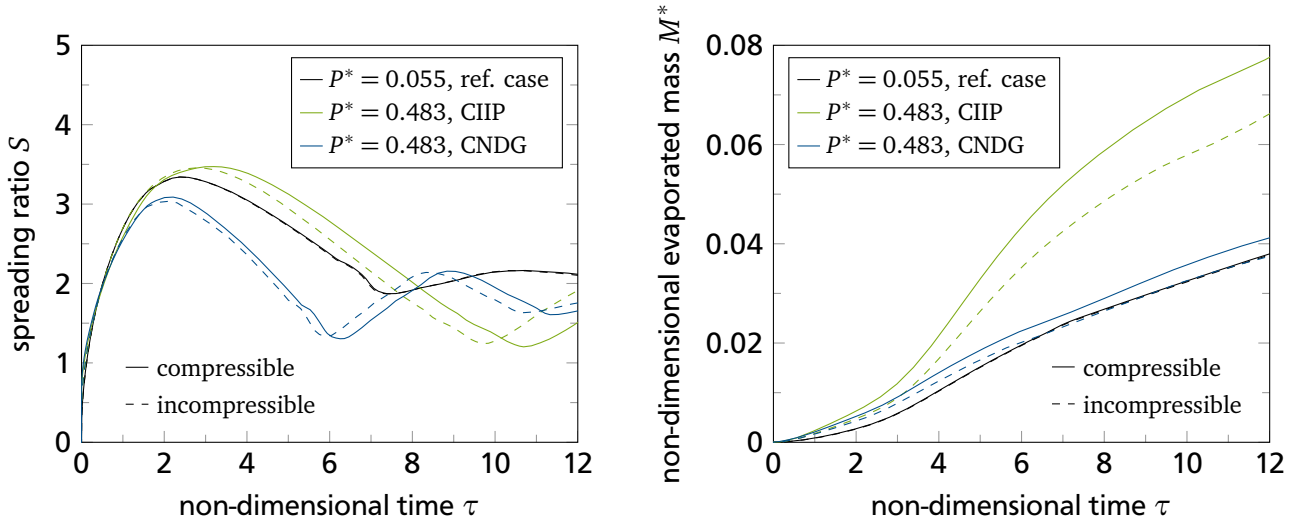

(a) Spreading ratio.

(b) Non-dimensional evaporated mass.

Figure 6.11.: Comparison of compressible and incompressible fluid flow for $P^* = p/p_{cr} = 0.483$ and the reference case.

non-dimensional group(s). Since the influence of compressibility is especially strong during receding, it is expected that the Weber number, which has the strongest impact on the receding phase (compare Figure D.2(b) in the appendix), amplifies compressibility effects. In summary, cross-over effects between fluid dynamics and heat and mass transfer cannot be excluded. It is reasonable that the compressibility does not directly influence the fluid motion under the investigated ambient conditions, c.f. Section 2.1. However, the compressibility affects the heat and mass transfer which, in turn, affects the fluid motion.

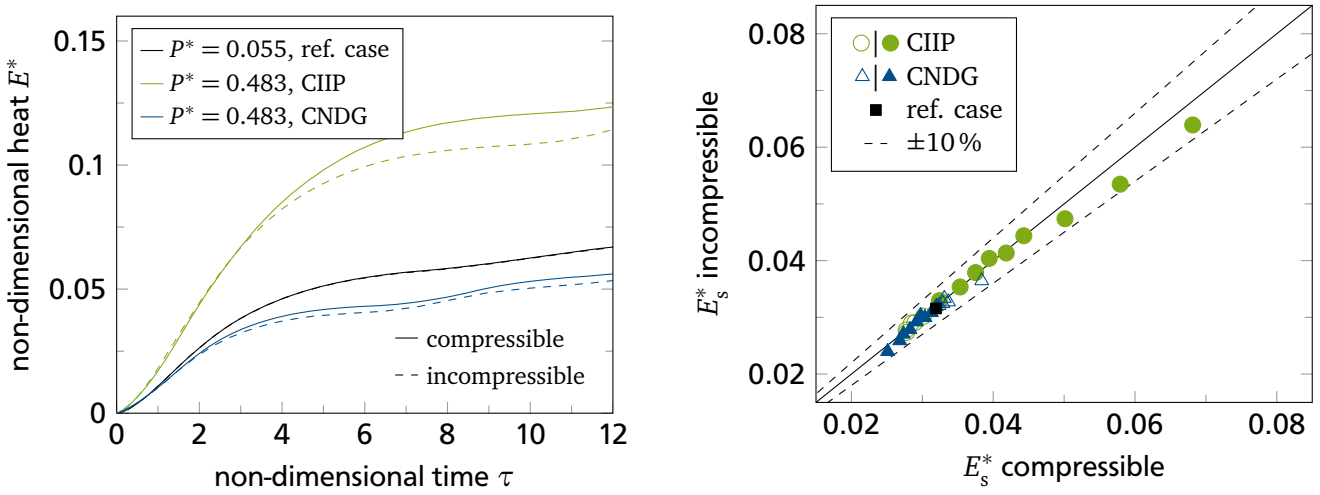

(a) Non-dimensional heat.

(b) Non-dimensional heat during spreading.

Figure 6.12.: Comparison of compressible and incompressible fluid flow for $P^* = p/p_{cr} = 0.483$ and reference case (a). Influence of the compressibility on the non-dimensional heat E_s^* during spreading for the CIIP and CNDG study (b) for low ambient pressure (empty symbols) and high ambient pressure (filled symbols).

In Figure 6.12(a), the evolution of the non-dimensional heat E^* is shown for compressible and incompressible fluid flow, for the pressure ratio $p/p_{cr} = 0.483$ and for the reference case. In case of incompressible fluid flow, less non-dimensional heat E^* is transferred. Again, the results from the CIIP study are influenced more strongly by the compressibility than the results from the CNDG study.

A quantity of interest is the transferred heat during the spreading phase since most energy is transferred from the wall by convection during the spreading phase. Figure 6.12(b) represents the non-dimensional heat during the spreading phase E_s^*, evaluated for compressible and incompressible fluid flow over the entire pressure range. The deviation between incompressible and compressible fluid flow varies within a ±10 % range. However, the data used for the correlation of E_s^* shown in Figure 6.9(b) varies in a wider range.

Consequently, for the proposed correlations of S_{max}, τ_{max}, and E_s^*, the compressibility of the fluid is concluded to play a sub-dominant role for the investigated parameter range. Additionally, the utilised compressibility factors (c.f. Table A.4 in the appendix) are an approximation of the compressibility's physical values. Extrapolated values from experiments indicate that the approximated compressibility factors might overestimate the physical values (c.f. Table A.3 in the appendix).

Reference case with high compressibility

Within a second compressibility study, the numerical set-up is identical to the reference case at $p/p_{cr} = 0.055$, but with different values for the compressibility of the liquid, ψ_l, and vapour phase, ψ_v. Within this study, the compressibility of both phases is varied at the same time by the same factor ψ/ψ_{ref}. A ratio of $\psi/\psi_{ref} = 0$ refers to an incompressible fluid flow. A ratio of $\psi/\psi_{ref} = 1$ is identical to the reference case. A compressibility ratio of $\psi/\psi_{ref} = 10$ is approximately the ratio of

the compressibility from the highest investigated pressure ($p/p_{cr} = 0.483$) to the reference pressure ($p/p_{cr} = 0.055$).

In Figure 6.13, the evolution of the spreading ratio and the non-dimensional heat E^* is shown for different ratios of compressibilities. The maximum spreading ratio S_{max} and the spreading duration τ_{max} varies only for a very high value of the compressibility ratio $\psi/\psi_{ref} = 50$, Figure 6.13(a). However, increasing the compressibility decreases the minimum spreading ratio S_{min} and increases τ_{min}. More non-dimensional heat is transferred from the solid to the drop for a high compressibility ratio than for the reference case, Figure 6.13(b).

It is worth to mention that the strong deviation between $\psi/\psi_{ref} = 0$ and $\psi/\psi_{ref} = 10$ observed in the previous paragraph is not reproduced in here. This supports the argument that the value of compressibility might not be the only influencing parameter for the results shown in Figures 6.11 and 6.12.

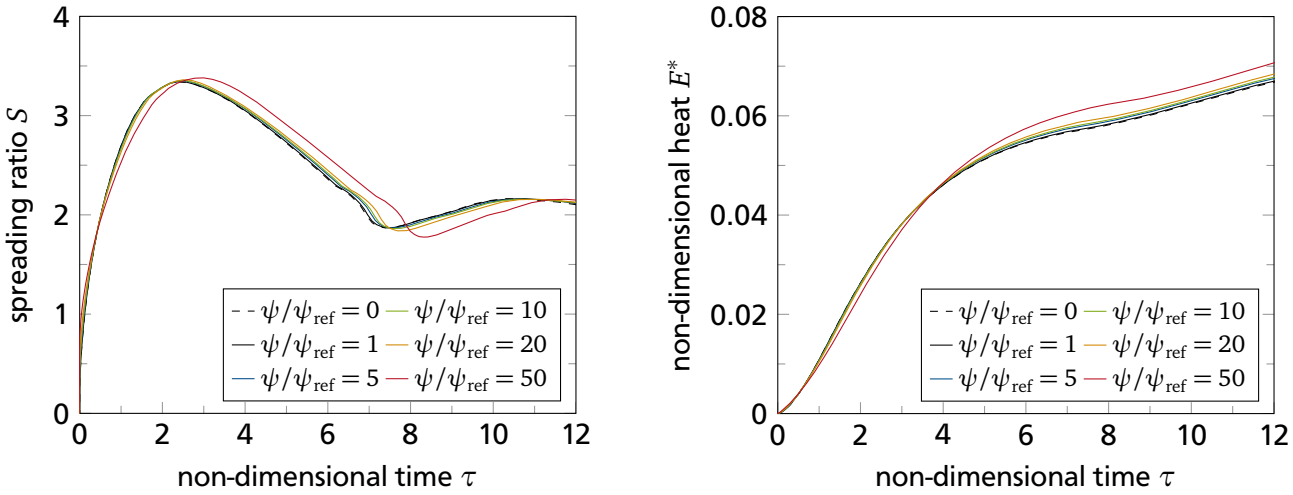

Figure 6.13.: Evolution of the spreading ratio and the non-dimensional heat based on the variation in compressibility for the reference case at $p/p_{cr} = 0.055$.

6.2.5 Material properties of the vapour

When simulating the drop impact with evaporation at different pressures, most attention is paid to the liquid phase. However, to investigate the influence of the vapour phase on the overall process, several parameter studies are conducted. The strong advantage of numerical simulation is the ease of varying parameters such as material properties and the possibility to vary them separately. In the following, the dynamic viscosity, the density, the heat capacity, and the Prandtl number of the vapour are modified.

Variation of viscosity and density within CIIP and CNDG study

In a first study, the same set-up as for the CIIP and CNDG study is considered. Within the CIIP and CNDG study, different pressures were investigated. In the present study, the individual physical material properties μ_v and ρ_v are substituted by the values of the reference case at $p_{ref} = 1\,\text{bar}$ ($p/p_{cr} = 0.055$). Consequently, the reference case remains the same whereas all other simulation cases obtain different values for μ_v and ρ_v than in the original CIIP and CNDG studies. The objective is to investigate the role of the vapour material properties on the evaporating drop impact process under various pressures. Both, the dynamic viscosity and the density of the vapour are varied separately.

The investigated FC-72 vapour properties show a monotonous behaviour over pressure (c.f. Figure 3.5(b)). This implies that the strongest deviation in results for the viscosity and density variation is to be expected at highest and at lowest pressure levels.

In Figure 6.14, the influence of the viscosity μ_v and density ρ_v on the drop spreading characteristics is presented. Results from the original CIIP and CNDG studies are shown on the abscissa. The ordinate refers to the results from the variation of the vapour material properties. For the maximum spreading ratio S_{max}, the most influencing vapour material property is found to be the density ρ_v at the highest investigated pressure ratio $p/p_{cr} = 0.483$ resulting in a maximum deviation of 1.1 % for the CIIP study (CNDG: 0.7 %). The maximum deviation in minimum spreading ratio S_{min} is found at $p/p_{cr} = 0.483$ but stays below 2 % (CIIP: 1.7 %; CNDG: 1.7 %). For the variation in dynamic viscosity of the vapour phase, the deviation in both, S_{max} and S_{min}, stays within ±0.3 % over the entire pressure range.

The deviation in τ_{max} and τ_{min} varies almost exclusively in a range of ±5 %. Only one high pressure CIIP simulation case exceeds the 5 % limit for τ_{max} slightly when changing ρ_v. This particular case, however, shows a rather long and flat plateau for the evolution of the spreading ratio at the maximum spreading. The deviation in τ_{min} stays below ±2.6 % when when varying ρ_v for the CIIP and CNDG study over the entire pressure range. The deviation in τ_{min} stays below ±0.7 % when varying μ_v for the CIIP and CNDG study over the entire pressure range. For the parameter range investigated, the viscosity and density of the vapour are concluded to have only minor influence on the drop spreading characteristics.

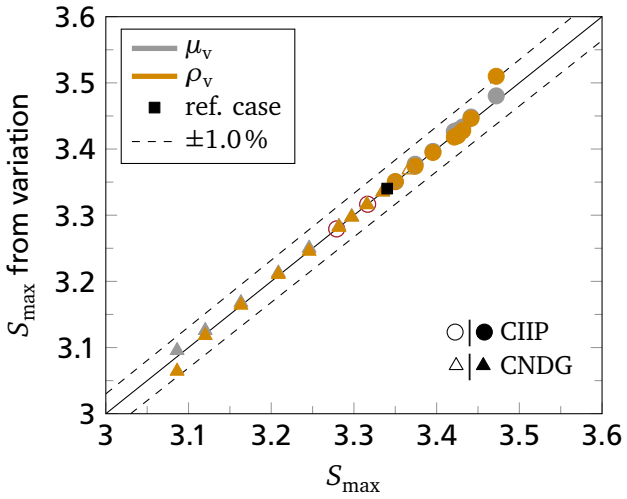

(a) Maximum spreading ratio.

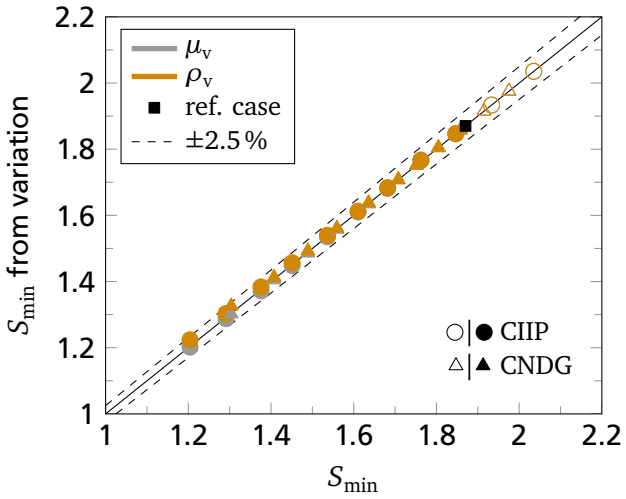

(b) Minimum spreading ratio.

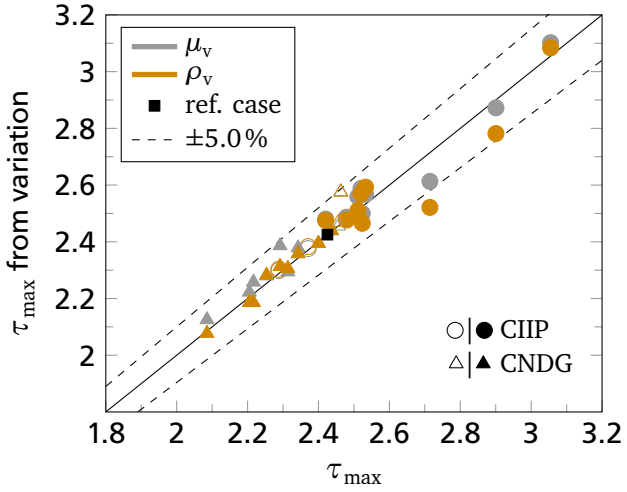

(c) Non-dimensional spreading duration.

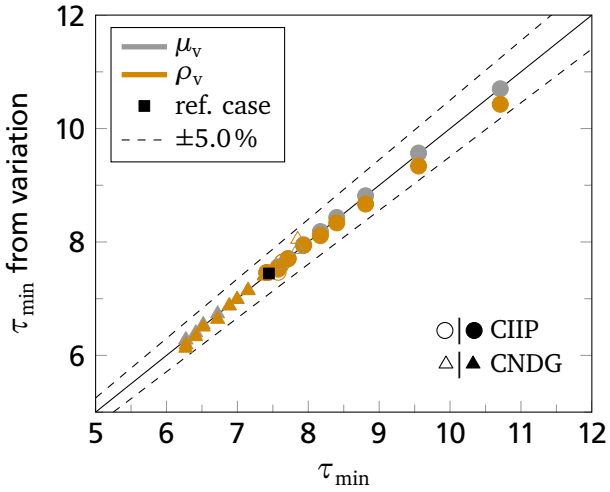

(d) Non-dimensional duration until minimum spreading ratio.

Figure 6.14.: Variation in density and viscosity of the vapour phase for the CIIP and CNDG study at low ambient pressure (empty symbols) and high ambient pressure (filled symbols).

Variation in viscosity and density for the reference case

In a second study of the material properties of the vapour, the numerical set-up is identical to reference case but with different values for the vapour density and, separately, for the vapour dynamic viscosity. Consequently, the ratio $\rho_v/\rho_{v,ref} = 1$ and $\mu_v/\mu_{v,ref} = 1$ is identical to the reference case. By varying the vapour density or viscosity, the proportion between the vapour and liquid material properties changes. Therefore, this study can be interpreted in terms of varying the proportion between vapour and liquid density or the proportion between vapour and liquid dynamic viscosity.

In Figure 6.15, the evolution of the spreading ratio and the evolution of the non-dimensional heat is shown for the variation of ρ_v. The ratio $\rho_v/\rho_{v,ref}$ varies between 0.1 and 20. A ratio of $\rho_v/\rho_{v,ref} = 10$ reflects approximately the vapour density that exists at the highest investigated pressure ratio $p/p_{cr} = 0.483$ during the CIIP and CNDG study. However, no strong influence of the variation in vapour density on the reference case can be observed for the investigated parameter range. The fluid dynamics, as well as the heat and mass transfer during the evaporative drop impact is not influenced by the vapour density.

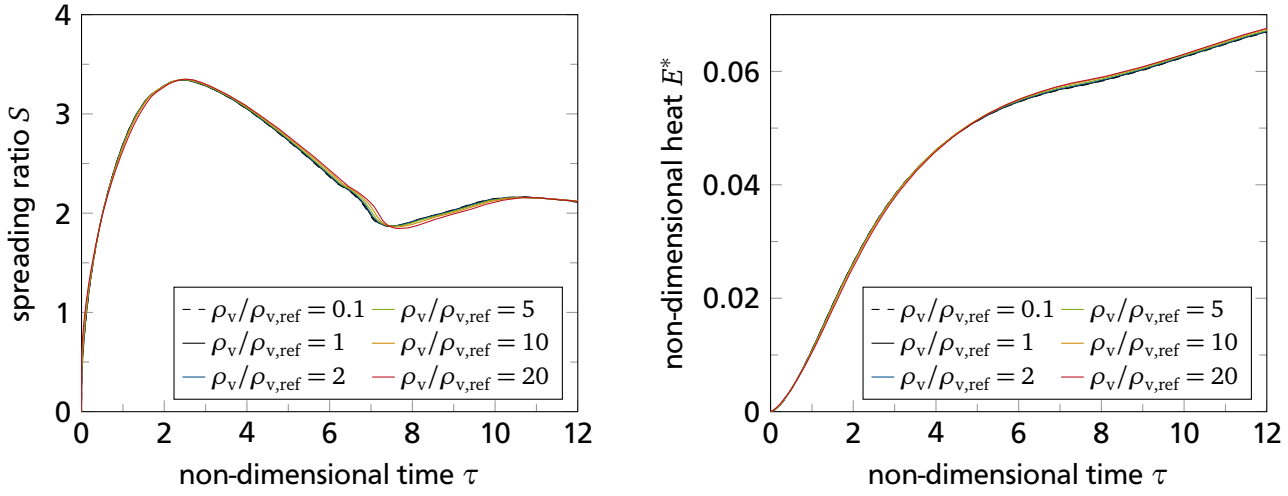

(a) Spreading ratio.

(b) Non-dimensional heat.

Figure 6.15.: Variation in density of the vapour phase for the reference case.

In Figure 6.16, the evolution of the spreading ratio and of the non-dimensional heat are shown for the variation of μ_v. The ratio $\mu_v/\mu_{v,ref}$ varies between 0.1 and 10. A ratio of $\mu_v/\mu_{v,ref} = 1.25$ reflects approximately the vapour viscosity that exists at the highest investigated pressure ratio $p/p_{cr} = 0.483$ during the CIIP and CNDG study. Similar to the results of the density variation, no strong influence of the variation in vapour viscosity on the reference case can be observed for the investigated parameter range. The fluid dynamics as well as the heat and mass transfer during the evaporative drop impact are not influenced by the vapour viscosity and density.

Variation in heat capacity and Prandtl number of the vapour phase

To investigate the influence of thermal properties of the vapour, such as heat capacity $c_{p,v}$ and the Prandtl number Pr_v, the individual material properties are substituted by the values of the reference case for the drop impact scenarios CIIP and CNDG. It is found that both thermal properties influence the maximum and minimum spreading ratios by less than 0.5 %. The duration between initial wall contact and maximum or minimum spreading varies by less than 1 %. Consequently, both, $c_{p,v}$ and Pr_v have very little influence on the evaporative drop impact process within the investigated parameter range.

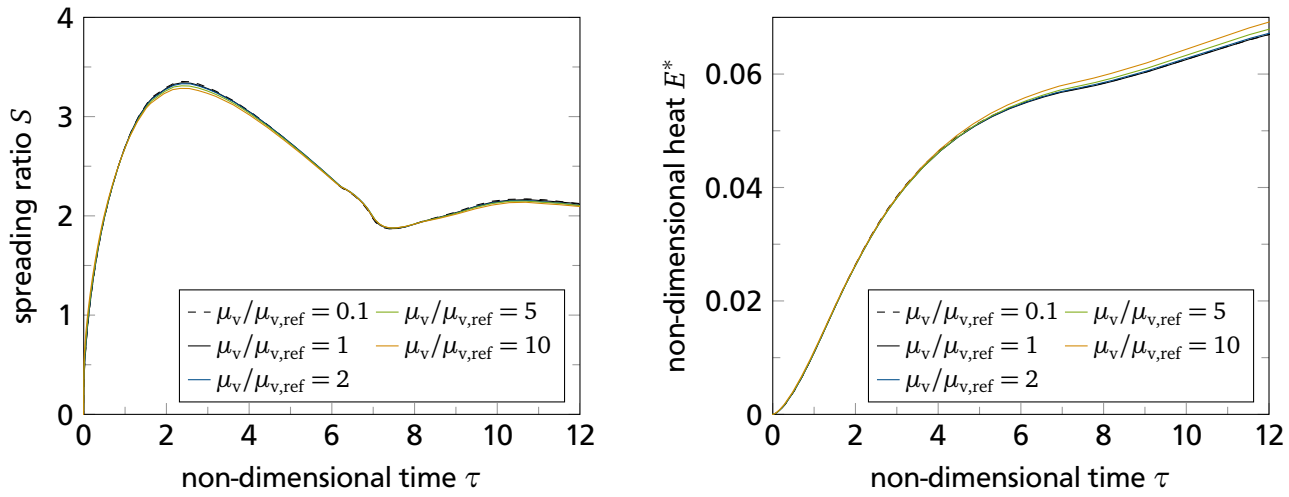

(a) Spreading ratio.

(b) Non-dimensional heat.

Figure 6.16.: Variation in dynamic viscosity of the vapour phase for the reference case.

6.3 Summary of the pressure influence on drop impact with evaporation

This section summarises the conducted studies and the main results. The research questions of the present thesis are answered. For detailed results, discussions and conclusions the reader is referred to the individual sections. Finally, comments on drop impact at very high pressures close to the critical point are given.

It is shown that the ambient pressure has an influence on the fluid dynamics and thermodynamics. The ambient pressure influences the processes on different length scales. In particular, the ambient pressure influences the material properties and, consequently, a shift in acting forces is observed, which leads to different spreading as well as heat and mass transfer behaviour during the drop impact.

The shortest length scale is studied within the micro region model which models the effects in the vicinity of an evaporating three-phase contact line. When varying the ambient pressure and, hence, the material properties, the micro region model predicts an increasing contact angle with increasing pressure, independent from the contact line velocity. Influences of the surface tension and the vapour density are dominating over the influence of the latent heat of evaporation. The dynamic contact angle as a function of pressure has an important effect on the macro CFD simulations. In contrast, the transferred heat calculated by the micro region model shows a non-monotonous behaviour over the pressure range revealing a maximum. The maximum is caused by a shift in dominating thermal resistances at the liquid-vapour interface and within the liquid.

Macroscopic length scales are investigated within CFD simulations computing the evaporative drop impact. The solver was augmented to take compressibility of the fluid into account. Within a first study, CIIP, results are obtained using constant initial impact parameters when varying the ambient pressure. It is observed that especially at very high ambient pressures up to $p/p_{cr} = 0.5$, the drop spreading is different from the drop spreading at low ambient pressures. This behaviour, however, is neither caused by the changing contact angle nor by the compressibility. Results show that the change in the spreading behaviour at very high ambient pressures in the CIIP study is related to the shift in acting forces and, consequently, is related to the changing non-dimensional numbers with increasing pressure. A second study, CNDG, focuses on constant non-dimensional groups for the drop impact at different ambient pressures. Here, the influence of the increasing apparent contact angle with increasing pressure can be clearly observed.

The influence of the compressibility is addressed in two distinct parameter studies. Within the first study, all parameter set-ups from the CIIP and CNDG are re-calculated assuming zero compressibility. It was observed that the highest deviation occurs at the highest investigated ambient pressure and, therefore, for the highest values of compressibility. It seems intuitive that the high values for the compressibility are the reason for the large deviations at high pressures. A second study takes the reference case and artificially increases the compressibility to very high values. This study, however, did not reproduce the high deviations observed during the comparison of the compressible and incompressible CIIP and CNDG study. Consequently, high compressibility values are not solely the reason for the high deviations; a cross-effect with other processes is expected to be present. However, this cross-effect is not studied in detail. Instead, the results from the compressible CIIP and CNDG study are compared against correlations from literature. In general, the simulation results and the results generated with the correlations are in good agreement. However, the deviations between the compressible and incompressible fluid flow simulations are smaller than the deviations between simulations and correlations. Consequently, for the investigated parameter and pressure range, compressible fluid flow can be neglected.

Additionally, similar to the investigations for the compressibility, the vapour phase material properties ρ_v, μ_v, c_{pv}, and Pr_v are individually investigated in two distinct studies. Within a first study for the material property of interest, the CIIP and CNDG study is re-calculated using the same material property as in the reference case. The deviation is expected to be largest at lowest and highest investigated pressure since the deviation of the material property is largest at these pressure limits. In a second study, the reference case is re-calculated with an artificially tuned value for the material property of interest. Two conclusions can be drawn for all investigated material properties of the vapour phase. Firstly, the investigated material properties do neither have a strong influence on the fluid dynamics behaviour of the drop nor on the evaporation process. Secondly, the presence of cross-effects is expected between the individual material properties of the vapour and other properties or parameters. The results from the modified CIIP and CNDG study are not fully reproducible in the artificially tuned reference case study. However, for the investigated parameter and pressure range, it is concluded that the material properties of the vapour influence the evaporative drop impact only to a very small extend.

The scenarios investigated in the present thesis are focused on the non-splashing, non-boiling, single component evaporative drop impact regime without Leidenfrost temperature effects. The studies cover a limited pressure range and a limited range of non-dimensional groups. However, up to now no attempt was made to conduct numerical simulations or experiments over a broad pressure range. Therefore, the findings obtained in the present thesis are believed to improve system design for spray cooling on an engineering scale.

Research questions and answers

The research questions formulated in Chapter 1.4 are recalled and short answers are given.

- **Question 1:** Does low/high ambient pressure influence the hydrodynamics after drop impact?

  The ambient pressure influences the material properties of the liquid and the vapour phase of a fluid. The material properties affect the fluid dynamics and thermodynamics of the evaporative drop impact process on different length scales.

  Question 2: How does low/high ambient pressure influence the fluid dynamics and heat and mass transfer?

  The influence of low/high ambient pressure on fluid dynamics and heat and mass transfer can not be completely generalized. For the shortest investigated length scales in the vicinity of the evaporating three-phase contact line, ambient pressure influences the contact angle and thus the wetting properties. Furthermore, the ambient pressure affects the contact line heat and mass transfer. Detailed results from the micro region model are presented in Section 6.1. For the macroscopic length

scales, a shift in acting forces is observed, which leads to a different spreading as well as a different heat and mass transfer behaviour during the drop impact. Detailed results from macroscopic CFD simulations can be found in Section 6.2.

- **Question 3:** How large is the modelling error that might arise from the assumption of incompressible fluid flow?

  The question is targeting the numerical deviation between compressible and incompressible fluid flow is answered in detail in Section 6.2.4. For the highest investigated pressure, the largest deviation between compressible and incompressible fluid flow is observed. However, these deviations are found to be small.

Drop impact at very high pressures close to the critical point

Several aspects lead to the upper limit of $p/p_{cr} = 0.5$ for the FC-72 drop impact studies presented in this thesis. These aspects concern the material properties, the validity of a sharp interface, and the estimation of the dynamic contact angle using the micro region model.

Generally, when increasing the pressure towards the critical point material properties vary strongly. The surface tension and latent heat of vaporisation become zero at the critical point whereas other material properties, such as the specific heat capacity, become infinite. Further material properties, such as viscosity and thermal conductivity, diverge at the critical point [17]. For FC-72, the best data available in literature for saturation conditions as function of pressure does not reflect the aforementioned behaviour for the viscosity, specific heat capacity, and thermal conductivity. The bend in the viscosity of the liquid as function of pressure at a relative pressure of about $p/p_{cr} = 0.15$ (c.f. Figure 3.5(a)) is very prominent. Furthermore, no measurement uncertainties are reported which makes it difficult to judge the accuracy of the measured material properties. However, saturation temperature and surface tension are in accordance with theoretical models, as reported in [33]. The densities for liquid and vapour can be reproduced in a good agreement with the Peng-Robinson EoS (c.f. Figure A.1 in the appendix).

With increasing pressure towards the critical point, the sharp liquid-vapour interface gradually turns in a diffuse interface. The diffuse interface is a transition region in which material properties vary continuously. At the critical point, the interface region vanishes completely. The diffuse interface affects the smallest investigated length scales first, i.e. the micro region. A mathematical reformulation of the micro region model in terms of a diffuse interface approach is desirable but yet challenging.

The surface tension influences the shape of the drop during the falling of the drop towards the wall. The higher the pressure, the lower is the surface tension and hence the larger become the Weber and Bond numbers (for constant drop diameter, impact velocity, and gravitational force). Large Weber and Bond numbers indicate a high possibility of large drop deformation and might result in drop disintegration. The VoF method used in the present thesis, however, is no effective tool to predict the merge or disintegration of a phase within two-phase simulations. For instabilities, which occur before drop disintegration, stochastic simulations are more suitable than the deterministic simulations conducted in the course of this thesis.

Several assumptions are made within the micro region model to finally estimate the contact angle as function of pressure. The validation of the micro region model with state-of-the-art measurement equipment is not possible. Consequently, the micro region model is believed to qualitatively predict the contact angle. However, model uncertainties are expected to increase with increasing pressure.

The drop impact investigations performed in this work are limited to a relative pressure of about $p/p_{cr} = 0.5$ for FC-72. Among the discussed aspects, the decreasing surface tension leading to an increasing probability of drop disintegration, as well as the contact angle limit of the micro region model are the main reasons for this limitation. Nevertheless, if the drop impact parameters are considered in a way which omits drop breakup (i.e. small drop diameter, low impact velocities), an appropriate

contact angle handling is utilised, and accurate material properties are available, then investigations of near-critical drop impact might become more reasonable. It might be of interest how the drop spreading and receding is influenced if liquid and vapour densities become similar with increasing pressure.

Chapter 7

Summary, Conclusion and Outlook

Within this thesis, single liquid drop impingement in saturated vapour on a hot wall is investigated for low and high ambient pressures of $p/p_{\mathrm{cr}} = \left[8 \cdot 10^{-3} \ldots 0.5\right]$. The focus is drop deposition for Reynolds and Weber numbers in the range of $Re = [600 \ldots 1300]$ and $We = [10 \ldots 50]$, respectively. The wall temperature is above saturation but below Leidenfrost temperature. The wall superheat is in the order of $\Delta T = 10\,\mathrm{K}$. Two-phase CFD simulations are performed with a finite volume discretisation using OpenFOAM, solving the Navier-Stokes equations. The numerical solver accounts for compressible fluid flow, for heat and mass transfer due to evaporation across the free liquid–vapour interface, for evaporation in the vicinity of the three-phase contact line, and for heat conduction within the solid substrate. The volume of fluid method is utilised in conjunction with a dynamic subscale model to account for a dynamic contact angle.

7.1 Conclusion

The influence of low and high ambient pressures is studied for different length scales. For the smallest length scales investigated, in the vicinity of the three-phase contact line, the results of the micro region model can be summarised:

- **Ambient pressure influences the wetting properties** of a specific fluid solid combination for moving and static evaporating contact lines. Specifically, the ambient pressure has an influence on the contact angle. The way the pressure influenced material properties interact within the micro region model is complex and may not be obvious. In the majority of cases, increasing ambient pressure leads to increasing apparent contact angles.
- **Ambient pressure affects the contact line heat and mass transfer**. The ambient pressure influences the material properties and, therefore, the thermal resistances within the liquid and at the liquid–vapour interface. For FC-72, the integrated heat flux obtains a local maximum at a pressure ratio of $p/p_{\mathrm{cr}} \approx 0.1$, independently of the contact line velocity.

For the macroscopic drop impact CFD simulations, different parameter studies are conducted exploring the influence of the different ambient pressures on the fluid dynamics and heat and mass transfer. Keeping the dimensional impact parameters constant, such as drop diameter, impact velocity, and wall superheat, the ambient pressure is varied. Most of the drop impact results can be explained by the shift of acting forces due to the variation in material properties. Therefore, an additional parameter study is performed keeping the non-dimensional groups, such as *Re*, *We*, *Bo*, *Ja*, and *Pr* constant while varying the pressure ratio p/p_{cr}. The following observations are made:

- **The maximum spreading ratio and receding duration decreases with increasing pressure.** Most probably, the dynamic contact angle, which is influenced by pressure, is the predominant rea-

son. Parameter studies varying the vapour phase material properties at different ambient pressures only indicate a weak influence on the fluid dynamics.

- **The heat transfer during drop impact decreases with increasing pressure,** especially after the maximum spreading ratio is reached. The mechanism behind this phenomena is believed to be three-fold: I) Higher contact angles result in less wetted area. The time-averaged footprint of the drop is smaller and, consequently, less heat transfer area between solid and liquid is present. II) Less wetted area implies a shorter three-phase contact line at which a noticeable amount of heat is being transferred. III) For larger contact angles, the average thickness of the liquid drop is higher, resulting in an increased thermal resistance within the liquid. At the same time, the evaporative mass transfer stays approximately constant for the pressure range investigated.

The parameter study investigating the impact of compressibility on the drop impingement process, however, indicates only minor effects on the fluid dynamics and heat and mass transfer for the investigated parameter range.

7.2 Outlook

A reasonable extension of the current compressible and incompressible solver developed might include an enhanced evaporation model that takes pressure-driven evaporation into account, e.g. including a pressure-depended evaluation of the saturation temperature. The enhanced evaporation model might enable the simulation of evaporation against vacuum, describe cavitation, and handle re-condensation within the vapour layer confined between drop and substrate immediately before impact.

In order to systematically investigate spray cooling processes, two- or multi-drop impingement onto hot surfaces is of interest. Spatial arrangement and frequency span a wide range of possible scenarios to investigate with regard to the cooling rate of the surface. Within the SFB/TRR–75[1], experimental and numerical investigations were started and will be continued in the future.

[1] Collaborative Research Center Transregio 75 "Droplet Dynamics Under Extreme Ambient Conditions", supported by the German Research Foundation

Bibliography

[1] A. Z. Al-Yaseri, M. Lebedev, A. Barifcani and S. Iglauer. Receding and advancing (CO2 + brine + quartz) contact angles as a function of pressure, temperature, surface roughness, salt type and salinity. *The Journal of Chemical Thermodynamics*, 93:416–423, 2016.

[2] S. Batzdorf. *Heat transfer and evaporation during single drop impingement onto a superheated wall*. Dissertation, TU Darmstadt, 2015.

[3] S. Batzdorf, T. Gambaryan-Roisman and P. Stephan. Direct Numerical Simulation of the Microscale Fluid Flow and Heat Transfer in the Three-Phase Contact Line Region During Evaporation. *Journal of Heat Transfer*, 140(3):1851, 2018.

[4] A. Becker. *[online] Bitcoin Mining Boosts Interest in Liquid Cooling*. https://bit.ly/2nOxTto (date: 30.09.2019), 2013.

[5] J. Bellan. Supercritical (and subcritical) fluid behavior and modeling: drops, streams, shear and mixing layers, jets and sprays. *Progress in Energy and Combustion Science*, 26(4-6):329–366, 2000.

[6] J. D. Bernardin and I. Mudawar. Film boiling heat transfer of droplet streams and sprays. *International Journal of Heat and Mass Transfer*, 40(11):2579–2593, 1997.

[7] A. M. P. Boelens, A. Latka and J. J. de Pablo. Observation of the pressure effect in simulations of droplets splashing on a dry surface. *Physical Review Fluids*, 3(6), 2018.

[8] A. M. P. Boelens and J. J. de Pablo. Simulations of splashing high and low viscosity droplets. *Physics of Fluids*, 30(7):072106, 2018.

[9] J. P. Boris and D. L. Book. Flux-corrected transport. I. SHASTA, a fluid transport algorithm that works. *Journal of Computational Physics*, 11(1):38–69, 1973.

[10] J. Brackbill, D. Kothe and C. Zemach. A continuum method for modeling surface tension. *Journal of Computational Physics*, 100(2):335–354, 1992.

[11] J. Breitenbach. *Drop and spray impact onto a hot substrate: Dynamics and heat transfer*. Dissertation, TU Darmstadt, 2019.

[12] J. Breitenbach, I. V. Roisman and C. Tropea. Heat transfer in the film boiling regime: Single drop impact and spray cooling. *International Journal of Heat and Mass Transfer*, 110:34–42, 2017.

[13] J. Breitenbach, I. V. Roisman and C. Tropea. From drop impact physics to spray cooling models: a critical review. *Experiments in Fluids*, 59(5), 2018.

[14] D. D. Brutin, editor. *Droplet wetting and evaporation: From pure to complex fluids*. Academic Press, London, 2015. ISBN 978-0-12-800722-8.

[15] I. Buchmüller. *Influence of pressure on Leidenfrost effect*. Dissertation, TU Darmstadt, 2014.

[16] V. P. Carey. *Liquid-vapor phase-change phenomena: An introduction to the thermophysics of vaporization and condensation processes in heat transfer equipment*. Taylor & Francis, New York and London, 2nd ed. edition, 2008. ISBN 978-1-59169-035-1.

[17] P. Carlès. A brief review of the thermophysical properties of supercritical fluids. *The Journal of Supercritical Fluids*, 53(1-3):2–11, 2010.

[18] S. Chandra and C. T. Avedisian. On the collision of a droplet with a solid surface. *Proceedings: Mathematical and Physical Sciences*, 432(1884):13–41, 1991.

[19] D. Chatzikyriakou, S. P. Walker, C. P. Hale and G. F. Hewitt. The measurement of heat transfer from hot surfaces to non-wetting droplets. *International Journal of Heat and Mass Transfer*, 54(7-8):1432–1440, 2011.

[20] W. Chaze, O. Caballina, G. Castanet and F. Lemoine. Spatially and temporally resolved measurements of the temperature inside droplets impinging on a hot solid surface. *Experiments in Fluids*, 58(8):2579, 2017.

[21] W.-l. Cheng, W.-w. Zhang, H. Chen and L. Hu. Spray cooling and flash evaporation cooling: The current development and application. *Renewable and Sustainable Energy Reviews*, 55:614–628, 2016.

[22] A. V. Chizhov and A. A. Schmidt. Impact of a high-velocity drop on an obstacle. *Technical Physics*, 45(12):1529–1537, 2000.

[23] A. V. Chizhov and K. Takayama. The impact of compressible liquid droplet on hot rigid surface. *International Journal of Heat and Mass Transfer*, 47(6-7):1391–1401, 2004.

[24] T. Costa, J. Martins, F. P. Brito, M. R. O. Panão and A. L. Moreira. The effect of ambient pressure on the heat transfer of a water spray. *Applied Thermal Engineering*, 152:490–498, 2019.

[25] S. S. Deshpande, L. Anumolu and M. F. Trujillo. Evaluating the performance of the two-phase flow solver interFoam. *Computational Science & Discovery*, 5(1):014016, 2012.

[26] J. Dietl. *Numerical Simulation of Pool Boiling from Reentrant Type Structured Surfaces*. Dissertation, TU Darmstadt, 2015.

[27] B. Duret, R. Canu, J. Reveillon and F. X. Demoulin. A pressure based method for vaporizing compressible two-phase flows with interface capturing approach. *International Journal of Multiphase Flow*, 108:42–50, 2018.

[28] G. S. Emmerson. The effect of pressure and surface material on the leidenfrost point of discrete drops of water. *International Journal of Heat and Mass Transfer*, 18(3):381–386, 1975.

[29] G. S. Emmerson and C. W. Snoek. The effect of pressure on the leidenfrost point of discrete drops of water and freon on a brass surface. *International Journal of Heat and Mass Transfer*, 21(8):1081–1086, 1978.

[30] J. H. Ferziger and M. Perić. *Numerische Strömungsmechanik*. Springer, Berlin and Heidelberg, 2008. ISBN 978-3-540-67586-0.

[31] J. E. Field, J. P. Dear and J. E. Ogren. The effects of target compliance on liquid drop impact. *Proceedings of the Royal Society A: Mathematical, Physical and Engineering Sciences*, 65(2):533–540, 1989.

[32] J. E. Field, M. B. Lesser and J. P. Dear. Studies of two-dimensional liquid-wedge impact and their relevance to liquid-drop impact problems. *Proceedings of the Royal Society of London. A. Mathematical and Physical Sciences*, 401(1821):225–249, 1985.

[33] S. Fischer. *Experimental investigation of heat transfer during evaporation in the vicinity of moving three-phase contact lines*. Dissertation, TU Darmstadt, 2015.

[34] S. Fischer, S. Herbert, T. Gambaryan-Roisman and P. Stephan. Local heat flux investigation during single drop impingement onto a heated wall. In *Proceedings of the 25th European Conference on Liquid Atomization and Spray Systems, Greece*, 2013.

[35] S. Freund, A. Pautsch, T. Shedd and S. Kabelac. Local heat transfer coefficients in spray cooling systems measured with temperature oscillation IR thermography. *International Journal of Heat and Mass Transfer*, 50(9):1953–1962, 2007.

[36] E. J. Gelissen, C. van der Geld, M. W. Baltussen and J. Kuerten. Modeling of droplet impact on a heated solid surface with a diffuse interface model. *International Journal of Multiphase Flow*, 123:103173, 2020.

[37] E. J. Gelissen, C. van der Geld, J. Kuipers and J. Kuerten. Simulations of droplet collisions with a Diffuse Interface Model near the critical point. *International Journal of Multiphase Flow*, 107:208–220, 2018.

[38] J.-F. Gerbeau and T. Lelièvre. Generalized Navier boundary condition and geometric conservation law for surface tension. *Computer Methods in Applied Mechanics and Engineering*, 198(5-8):644–656, 2009.

[39] J. L. Gess, S. H. Bhavnani and R. W. Johnson. Experimental investigation of a direct liquid immersion cooled prototype for high performance electronic Systems. *IEEE Transactions on Components, Packaging and Manufacturing Technology*, 5(10):1451–1464, 2015.

[40] K. K. Haller, D. Poulikakos, Y. Ventikos and P. Monkewitz. Shock wave formation in droplet impact on a rigid surface: lateral liquid motion and multiple wave structure in the contact line region. *Journal of Fluid Mechanics*, 490:1–14, 2003.

[41] K. K. Haller, Y. Ventikos, D. Poulikakos and P. Monkewitz. Computational study of high-speed liquid droplet impact. *Wear*, 92(5):2821–2828, 2002.

[42] G. Hallewell, V. Vacek and V. Vinš. Properties of saturated fluorocarbons: Experimental data and modeling using perturbed-chain-SAFT. *Fluid Phase Equilibria*, 292(1-2):64–70, 2010.

[43] H. Han, C. Schlawitschek, N. Katyal, P. Stephan, T. Gambaryan-Roisman, F. Leroy and F. Müller-Plathe. Solid-Liquid Interface Thermal Resistance Affects the Evaporation Rate of Droplets from a Surface: A Study of Perfluorohexane on Chromium Using Molecular Dynamics and Continuum Theory. *Langmuir*, 33(21):5336–5343, 2017.

[44] S. Hardt and F. Wondra. Evaporation model for interfacial flows based on a continuum-field representation of the source terms. *Journal of Computational Physics*, 227(11):5871–5895, 2008.

[45] R. Hatakenaka, J. Breitenbach, I. V. Roisman, C. Tropea and Y. Tagawa. Magic carpet breakup of a drop impacting onto a heated surface in a depressurized environment. *International Journal of Heat and Mass Transfer*, 145:118729, 2019.

[46] S. Herbert, S. Fischer, T. Gambaryan-Roisman and P. Stephan. Local heat transfer and phase change phenomena during single drop impingement on a hot surface. *International Journal of Heat and Mass Transfer*, 61:605–614, 2013.

[47] S. Herbert, T. Gambaryan-Roisman and P. Stephan. Influence of the governing dimensionless parameters on heat transfer during single drop impingement onto a hot wall. *Colloids and Surfaces A: Physicochemical and Engineering Aspects*, 432:57–63, 2013.

[48] F. J. Heymann. High–Speed Impact between a Liquid Drop and a Solid Surface. *Journal of Applied Physics*, 40(13):5113–5122, 1969.

[49] C. Hirt and B. Nichols. Volume of fluid (VOF) method for the dynamics of free boundaries. *Journal of Computational Physics*, 39(1):201–225, 1981.

[50] S. Jafari, J. F. Dunne, M. Langari, Z. Yang, J.-P. Pirault, C. A. Long and J. Thalackottore Jose. Control of spray evaporative cooling in automotive internal combustion engines. *Journal of Thermal Science and Engineering Applications*, 10(4):041011, 2018.

[51] J. Jung, S. Jeong and H. Kim. Investigation of single-droplet/wall collision heat transfer characteristics using infrared thermometry. *International Journal of Heat and Mass Transfer*, 92:774–783, 2016.

[52] J. Kim. Spray cooling heat transfer: The state of the art. *International Journal of Heat and Fluid Flow*, 28(4):753–767, 2007.

[53] M. Koch, C. Lechner, F. Reuter, K. Köhler, R. Mettin and W. Lauterborn. Numerical modeling of laser generated cavitation bubbles with the finite volume and volume of fluid method, using OpenFOAM. *Computers & Fluids*, 126:71–90, 2016.

[54] A. A. Korobkin. Asymptotic theory of liquid–solid impact. *Philosophical Transactions of the Royal Society of London. Series A: Mathematical, Physical and Engineering Sciences*, 355(1724):507–522, 1997.

[55] C. Kunkelmann. *Numerical Modeling and Investigation of Boiling Phenomena*. Dissertation, TU Darmstadt, 2011.

[56] C. Kunkelmann and P. Stephan. Numerical simulation of the transient heat transfer during nucleate boiling of refrigerant HFE-7100. *International Journal of Refrigeration*, 33(7):1221–1228, 2010.

[57] N. Kyriazis, P. Koukouvinis and M. Gavaises. Modelling cavitation during drop impact on solid surfaces. *Advances in colloid and interface science*, 260:46–64, 2018.

[58] W. Lauterborn, C. Lechner, M. Koch and R. Mettin. Bubble models and real bubbles: Rayleigh and energy-deposit cases in a Tait-compressible liquid. *IMA Journal of Applied Mathematics*, 83(4):556–589, 2018.

[59] C. Lechner, M. Koch, W. Lauterborn and R. Mettin. Pressure and tension waves from bubble collapse near a solid boundary: A numerical approach. *The Journal of the Acoustical Society of America*, 142(6):3649, 2017.

[60] C. Lechner, M. Koch, F. Reuter, K. Köhler, R. Mettin and W. Lauterborn. Numerical Modeling of Laser-Induced Cavitation Bubbles with a Finite Volume Method. *PAMM*, 15(1):515–516, 2015.

[61] C. Lechner, W. Lauterborn, M. Koch and R. Mettin. Fast, thin jets from bubbles expanding and collapsing in extreme vicinity to a solid boundary: A numerical study. *Physical Review Fluids*, 4(2):133, 2019.

[62] M. Lesser. The impact of a compressible liquid. In M. G. Velarde, M. Sayir, W. Schneider, B. Schrefler, G. Bianchi, C. Tasso and M. Rein, editors, *Drop-surface interactions*, volume 456 of *CISM International Centre for Mechanical Sciences*, pages 39–102. Springer Vienna, Vienna, 2002. ISBN 978-3-211-83692-7.

[63] G. Liang and I. Mudawar. Review of drop impact on heated walls. *International Journal of Heat and Mass Transfer*, 106:103–126, 2017.

[64] J. Liu, R. Xue, L. Chen, X. Liu and Y. Hou. Influence of chamber pressure on heat transfer characteristics of a closed loop R134-a spray cooling. *Experimental Thermal and Fluid Science*, 75:89–95, 2016.

[65] J. López and J. Hernández. Analytical and geometrical tools for 3D volume of fluid methods in general grids. *Journal of Computational Physics*, 227(12):5939–5948, 2008.

[66] A. Marcos, L. C. Chow, Du Jian-Hua, S. Lei, D. P. Rini and J. J. Lindauer. Spray cooling at low system pressure. In *Proceedings of Eighteenth Annual IEEE Semiconductor Thermal Measurement and Management Symposium, USA*, pages 169–175, 2002.

[67] J. N. Marsh, C. S. Hall, S. A. Wickline and G. M. Lanza. Temperature dependence of acoustic impedance for specific fluorocarbon liquids. *The Journal of the Acoustical Society of America*, 112(6):2858–2862, 2002.

[68] S. T. Miller, H. Jasak, D. A. Boger, E. G. Paterson and A. Nedungadi. A pressure-based, compressible, two-phase flow finite volume method for underwater explosions. *Computers & Fluids*, 87:132–143, 2013.

[69] N. K. Mishra, Y. Zhang and A. Ratner. Effect of chamber pressure on spreading and splashing of liquid drops upon impact on a dry smooth stationary surface. *Experiments in Fluids*, 51(2):483–491, 2011.

[70] B. R. Mitchell, T. E. Bate, J. C. Klewicki, Y. P. Korkolis and B. L. Kinsey. Experimental investigation of droplet impact on metal surfaces in reduced ambient pressure. *Procedia Manufacturing*, 10:730–736, 2017.

[71] A. Moreira, A. S. Moita and M. R. Panão. Advances and challenges in explaining fuel spray impingement: How much of single droplet impact research is useful? *Progress in Energy and Combustion Science*, 36(5):554–580, 2010.

[72] S. Nukiyama. The maximum and minimum values of the heat Q transmitted from metal to boiling water under atmospheric pressure. *Journal of the Japan Society of Mechanical Engineers*, 37(206):367–374, 1934.

[73] M. Ojha, A. Chatterjee, G. Dalakos, P. C. Wayner and J. L. Plawsky. Role of solid surface structure on evaporative phase change from a completely wetting corner meniscus. *Physics of Fluids*, 22(5):052101, 2010.

[74] D. Orejon, K. Sefiane and Y. Takata. Effect of ambient pressure on Leidenfrost temperature. *Physical review. E, Statistical, nonlinear, and soft matter physics*, 90(5-1):053012, 2014.

[75] J. Park and H. Kim. An experimental investigation on dynamics and heat transfer associated with a single droplet impacting on a hot surface above the Leidenfrost point temperature. *Kerntechnik*, 81(3):233–243, 2016.

[76] M. Pasandideh-Fard, S. D. Aziz, S. Chandra and J. Mostaghimi. Cooling effectiveness of a water drop impinging on a hot surface. *International Journal of Heat and Fluid Flow*, 22(2):201–210, 2001.

[77] M. Pasandideh-Fard, Y. M. Qiao, S. Chandra and J. Mostaghimi. Capillary effects during droplet impact on a solid surface. *Physics of Fluids*, 8(3):650–659, 1996.

[78] A. G. Pautsch and T. A. Shedd. Spray impingement cooling with single- and multiple-nozzle arrays. Part I: Heat transfer data using FC-72. *International Journal of Heat and Mass Transfer*, 48(15):3167–3175, 2005.

[79] B. E. Poling, J. M. Prausnitz and J. P. O'Connell. *The properties of gases and liquids*. McGraw-Hill, New York and London, 5th ed. edition, 2000. ISBN 0-07-011682-2.

[80] M. Potash and P. Wayner. Evaporation from a two-dimensional extended meniscus. *International Journal of Heat and Mass Transfer*, 15(10):1851–1863, 1972.

[81] D. Quéré. Leidenfrost Dynamics. *Annual Review of Fluid Mechanics*, 45(1):197–215, 2013.

[82] M. Rein. Interactions between drops and hot surfaces. In M. G. Velarde, M. Sayir, W. Schneider, B. Schrefler, G. Bianchi, C. Tasso and M. Rein, editors, *Drop-surface interactions*, volume 456 of *CISM International Centre for Mechanical Sciences*, pages 185–217. Springer Vienna, Vienna, 2002. ISBN 978-3-211-83692-7.

[83] D. Rettenmaier. *Numerical simulation of shear driven wetting*. Dissertation, TU Darmstadt, 2019.

[84] R. Rioboo, C. Tropea and M. Marengo. Outcomes from a drop impact on solid surfaces. *Atomization and Sprays*, 11(2):12, 2001.

[85] M. Sarmadivaleh, A. Z. Al-Yaseri and S. Iglauer. Influence of temperature and pressure on quartz-water-CO_2 contact angle and CO_2-water interfacial tension. *Journal of colloid and interface science*, 441:59–64, 2015.

[86] L. H. Saw, H. M. Poon, H. S. Thiam, Z. Cai, W. T. Chong, N. A. Pambudi and Y. J. King. Novel thermal management system using mist cooling for lithium-ion battery packs. *Applied Energy*, 223:146–158, 2018.

[87] M. Schäfer. *Computational Engineering — Introduction to Numerical Methods*. Springer-Verlag, Berlin/Heidelberg, 2006. ISBN 3-540-30685-4.

[88] B. L. Scheller and D. W. Bousfield. Newtonian drop impact with a solid surface. *AIChE Journal*, 41(6):1357–1367, 1995.

[89] C. Schmidt. *Kapitzawiderstand an Grenzflächen zwischen Festkörpern*. Dissertation, TH Karlsruhe, 1974.

[90] R. W. Schrage. *A theoretical study of interphase mass transfer*. Columbia University Press, New York, 1953.

[91] L. E. Scriven. On the dynamics of phase growth. *Chemical Engineering Science*, 10(1-2):1–13, 1959.

[92] A. Sielaff. *Experimental investigation of single bubbles and bubble interactions in nucleate boiling*. Dissertation, TU Darmstadt, 2014.

[93] P. Smakulski and S. Pietrowicz. A review of the capabilities of high heat flux removal by porous materials, microchannels and spray cooling techniques. *Applied Thermal Engineering*, 104:636–646, 2016.

[94] J. Spurk and N. Aksel. *Strömungslehre: Einführung in die Theorie der Strömungen*. Springer Berlin Heidelberg and Springer Vieweg, Berlin, Heidelberg, 9., aktual. aufl. 2019 edition, 2019. ISBN 978-3-662-58764-5.

[95] P. Stephan. *Wärmedurchgang bei Verdampfung aus Kapillarrillen in Wärmerohren*. VDI-Verlag, Düsseldorf, 1992. ISBN 3181459194.

[96] P. C. Stephan and C. A. Busse. Analysis of the heat transfer coefficient of grooved heat pipe evaporator walls. *International Journal of Heat and Mass Transfer*, 35(2):383–391, 1992.

[97] C. S. Stevens. Scaling of the splash threshold for low-viscosity fluids. *EPL (Europhysics Letters)*, 106(2):24001, 2014.

[98] C. S. Stevens, A. Latka and S. R. Nagel. Comparison of splashing in high- and low-viscosity liquids. *Physical review. E, Statistical, nonlinear, and soft matter physics*, 89(6):063006, 2014.

[99] Y. Tatekura, M. Watanabe, K. Kobayashi and T. Sanada. Pressure generated at the instant of impact between a liquid droplet and solid surface. *Royal Society open science*, 5(12):181101, 2018.

[100] E. Teodori, P. Pontes, A. Moita, A. Georgoulas, M. Marengo and A. Moreira. Sensible Heat Transfer during Droplet Cooling: Experimental and Numerical Analysis. *Energies*, 10(6):790, 2017.

[101] C. Ukiwe and D. Y. Kwok. On the maximum spreading diameter of impacting droplets on well-prepared solid surfaces. *Langmuir*, 21(2):666–673, 2005.

[102] M. A. J. van Limbeek, P. B. J. Hoefnagels, M. Shirota, C. Sun and D. Lohse. Boiling regimes of impacting drops on a heated substrate under reduced pressure. *Physical Review Fluids*, 3(5), 2018.

[103] M. Visaria and I. Mudawar. Application of two-phase spray cooling for thermal management of electronic devices. *IEEE Transactions on Components and Packaging Technologies*, 32(4):784–793, 2009.

[104] L. Wachters and N. Westerling. The heat transfer from a hot wall to impinging water drops in the spheroidal state. *Chemical Engineering Science*, 21(11):1047–1056, 1966.

[105] P. C. Wayner, Y. K. Kao and L. V. LaCroix. The interline heat-transfer coefficient of an evaporating wetting film. *International Journal of Heat and Mass Transfer*, 19(5):487–492, 1976.

[106] H. G. Weller. A new approach to VOF-based interface capturing methods for incompressible and compressible flow. *Technical report, OpenCFD Limited*, 2006.

[107] L. Xu, W. W. Zhang and S. R. Nagel. Drop splashing on a dry smooth surface. *Physical Review Letters*, 94(18):184505, 2005.

[108] A. L. Yarin. Drop impact dynamics: Splashing, spreading, receding, bouncing…. *Annual Review of Fluid Mechanics*, 38(1):159–192, 2006.

[109] X. Yu, R. Hu, X. Zhang, B. Xie and X. Luo. Explosive bouncing on heated silicon surfaces under low ambient pressure. *Soft Matter*, 15(21):4320–4325, 2019.

[110] S. T. Zalesak. Fully multidimensional flux-corrected transport algorithms for fluids. *Journal of Computational Physics*, 31(3):335–362, 1979.

APPENDIX A

Equation of state, speed of sound, and compressibility

A.1 Equation of state

Different equations of state have been tested to describe the thermodynamic relation of pressure, temperature, and density for FC-72. The aim is to find the most simple but at the same time accurate approximation for the fluid that describes both phases, liquid and vapour. However, it should be stated, that the solver is capable of handling different equations of state for the individual fluid phases. Nevertheless, to describe both phases with one single equation of state, cubic equations of state are chosen. They are suitable for unpolar species and are commonly used to describe the behaviour of the phases with adequate accuracy. Even though not a cubic equation of state, the ideal gas law is taken into account for comparison. As it will be shown below, the Peng-Robinson equation of state turned out to be sufficient for the purpose in the thesis. However, there might be another equation of state that describes the properties of FC-72 more accurately.

An expression commonly used for cubic equations of state is given by

$$p = \frac{\bar{R}T}{(\bar{v} - b)} - \frac{\Theta}{\bar{v}^2 + \delta\,\bar{v} + \varepsilon} \tag{A.1}$$

with co-volume b and the parameters Θ, δ, and ε listed in table A.1. The parameters are usually a function of critical pressure and critical temperature of the material and might be a function of temperature.

Table A.1.: Parameters for common cubic equations of state.

Equation of state	Θ	δ	ε	Parameters a, b
(ideal gas)	0	0	0	$b = 0$
Van der Waals	a	0	0	$a = a_{\mathrm{cr}};\ a_{\mathrm{cr}} = \frac{27}{64}\frac{\bar{R}^2 T_{\mathrm{cr}}^2}{p_{\mathrm{cr}}};\ \alpha = 1;\ b = \frac{1}{8}\frac{\bar{R}T_{\mathrm{cr}}}{p_{\mathrm{cr}}}$
Soave-Redlich-Kwong	$a(T)$	b	0	$a = a_{\mathrm{cr}} \cdot \alpha(T);\ a_{\mathrm{cr}} = 0.4278\frac{\bar{R}^2 T_{\mathrm{cr}}^2}{p_{\mathrm{cr}}};\ \alpha = \left[1 + m\left(1 - \sqrt{T/T_{\mathrm{cr}}}\right)\right]^2;$ $m = 0.48 + 1.574\omega - 0.176\omega^2;\ b = 0.08664\frac{\bar{R}T_{\mathrm{cr}}}{p_{\mathrm{cr}}}$
Peng-Robinson	$a(T)$	$2b$	$-b^2$	$a = a_{\mathrm{cr}} \cdot \alpha(T);\ a_{\mathrm{cr}} = 0.457\,24\frac{\bar{R}^2 T_{\mathrm{cr}}^2}{p_{\mathrm{cr}}};\ \alpha = \left[1 + m\left(1 - \sqrt{T/T_{\mathrm{cr}}}\right)\right]^2;$ $m = 0.37464 + 1.54226\omega - 0.26992\omega^2;\ b = 0.0778\frac{\bar{R}T_{\mathrm{cr}}}{p_{\mathrm{cr}}}$

The Soave-Redlich-Kwong and Peng-Robinson equation of state use the acentric factor (Pitzer factor) ω

$$\omega = -1 - \log_{10}\left(\frac{p_{\mathrm{sat}}}{p_{\mathrm{cr}}}\right)_{(\mathrm{T/T_{cr}})=0.7} . \tag{2.20}$$

The logarithmic term includes the ratio of the saturated pressure p_{sat} to the critical pressure p_{cr}. The saturated pressure is evaluated at the ratio of absolute temperature T to the critical temperature T_{cr} equal to 0.7. The acentric factor ω is a non-dimensional value of the pure fluid that expresses the deviation of a molecules geometry from a perfect sphere.

Taking the temperature and according saturation pressure from [92], the molar volume $\bar{v}$ and mass specific volume $v = \bar{v}/\bar{M} = 1/\rho$ can be determined. In Figure A.1(a), results for the different equations of state are shown together with literature data. The saturation pressure is plotted over the mass specific volume. The ideal gas law reflects the mass specific volume for the vapour phase reasonably well for low pressures. The deviation from the literature data increases for increasing pressure in case of the ideal gas law. The simplest cubic EoS investigated is the Van der Waals EoS. It well describes the vapour phase, even for higher pressures, compared to the ideal gas law. The Van der Waals EoS is able to quantify values for the liquid phase. However, the Van der Waals EoS performs worse than the other investigated cubic EoS for the liquid phase. The EoS of Soave-Redlich-Kwong, a two parameter EoS, has smaller deviation of the mass specific volume in the vapour phase, than Van der Waals. Furthermore, it is able to compute the liquid phase fairly well. However, the best results and smallest deviations for the mass specific volume are achieved with the Peng-Robinson equation of state. In Figure A.1 (b), the saturation curve obtained from the Peng-Robinson equation of state can be seen together with the literature data.

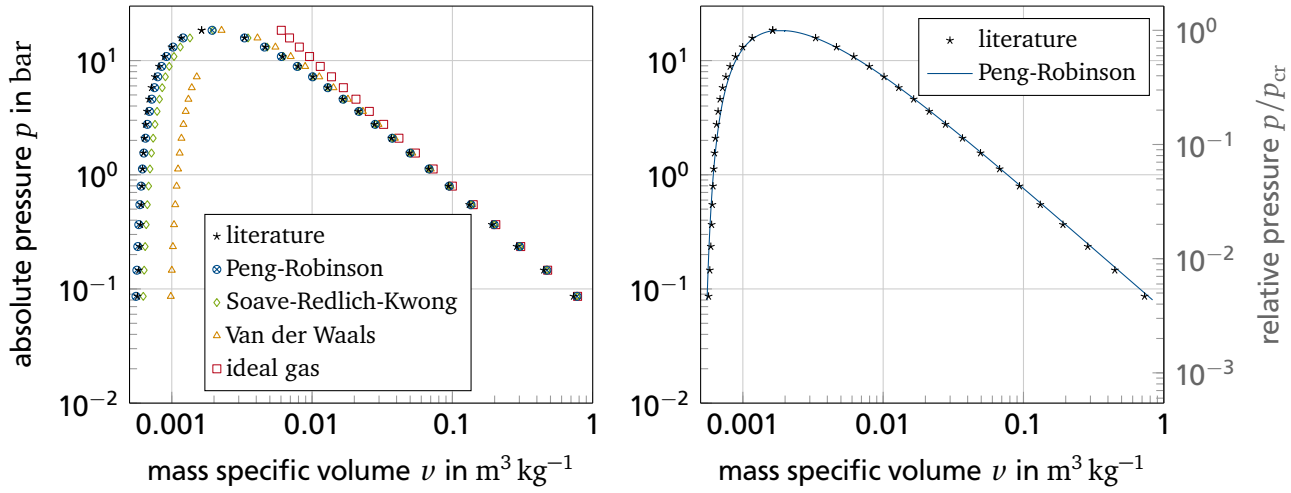

(a) Comparison of different EoS.

(b) Saturation curve.

Figure A.1.: (a) Comparison of different equations of state with measurement data for FC-72 taken from [92]. (b) Saturation curve with Peng-Robinson equation of state.

Instead of the molar volume, the density of the phases is of particular interest within the numerical simulations. Therefore, the relative error for the density

$$\varepsilon_{\mathrm{rel}} = \frac{|\rho - \rho_{\mathrm{lit}}|}{\rho_{\mathrm{lit}}} \tag{2.20}$$

is summarised in Table A.2 for different conditions. The first values are single point errors, which refer to atmospheric or critical pressure. The minimum, maximum, and mean values for the liquid and vapour phase are evaluated for the pressure range $p = [0.086 \ldots 15.786]\,\mathrm{bar}$. It is noteworthy that rather large

deviations at the critical point exist for all EoS. However, the pressures studied in the present thesis stay below the critical point. The relative errors confirm the small deviations of the Peng-Robinson EoS from literature data for FC-72. The mean relative error for densities in the liquid phase is 2.8 %, whereas the mean relative error in the vapour phase is only 1.9 %. Consequently, the Peng-Robinson EoS is chosen for the equation of state in the compressible fluid flow model.

Table A.2.: Relative error for the density $\varepsilon_{\mathrm{rel}} = |\rho - \rho_{\mathrm{lit}}|/\rho_{\mathrm{lit}}$ in %. The atmospheric pressure is taken at $p_{\mathrm{atm}} = 1.013\,25\,\mathrm{bar}$. Minimum, maximum, and mean values for the liquid and vapour phase do not contain the data of the critical point. Literature data from [92].

	ρ_{l} at p_{atm}	ρ_{v} at p_{atm}	ρ at p_{cr}	liquid min	liquid max	liquid mean	vapour min	vapour max	vapour mean
ideal gas		6.7	72.9				6.2	52.2	17.5
Van der Waals	43.8	3.3	27.8	41.9	49.8	44.8	3.3	19.1	7.7
Soave-Redlich-Kwong	11.0	1.0	17.3	8.5	16.1	12.5	1.0	5.7	2.6
Peng-Robinson	0.7	0.7	15.8	0.3	4.8	2.8	0.05	5.7	1.9

A.2 Isothermal compressibility and speed of sound

Within the numerical model for compressible flows employed in this thesis, the compressibility of a fluid is a key parameter. It is used to determine the density as function of pressure. The direct usage of an explicit EoS within the numerical model is not suitable for FVMs, due to the non-linearity of all EoS. Here, the derivation of the isothermal compressibility from an arbitrary equation of state is shown, as well as the isothermal compressibility of a particular EoS, Peng-Robinson. The computed mathematical and isothermal compressibilities used in the simulations are listed in Table A.4.

Starting from the common equation of state for cubic EoS

$$p = \frac{\bar{R}T}{(\bar{v} - b)} - \frac{\Theta}{\bar{v}^2 + \delta\,\bar{v} + \varepsilon}\,, \tag{A.1}$$

the partial derivation of p with respect to the molar volume $\bar{v}$ for constant temperature T reads

$$\left.\frac{\partial p}{\partial \bar{v}}\right|_{\mathrm{T}} = -\frac{\bar{R}T}{(\bar{v} - b)^2} + \frac{\Theta\,(2\bar{v} + \delta)}{(\bar{v}^2 + \delta\,\bar{v} + \varepsilon)^2}\,. \tag{A.2}$$

Rewriting Equation 2.5 for the isothermal compressibility χ_T, using the molar specific volume

$$\chi_T = -\frac{1}{\bar{v}}\left(\frac{\partial\,\bar{v}}{\partial p}\right)_T \tag{2.5}$$

and substituting Equation A.2 yields

$$\chi_T = -\frac{1}{\bar{v}}\left[-\frac{\bar{R}T}{(\bar{v} - b)^2} + \frac{\Theta\,(2\bar{v} + \delta)}{(\bar{v}^2 + \delta\,\bar{v} + \varepsilon)^2}\right]^{-1}\,. \tag{A.3}$$

For convenience, the above equation is rewritten in terms of density instead of molar volume. After rearranging, this results into

$$\chi_T = -\frac{\rho}{\bar{M}} \left[-\frac{\bar{R}T\rho^2}{\left(\bar{M} - b\rho\right)^2} + \frac{\Theta\rho^3\left(2\bar{M} + \delta\rho\right)}{\left(\bar{M}^2 + \delta\bar{M}\rho + \varepsilon\rho^2\right)^2} \right]^{-1} . \tag{A.4}$$

Both, Equations A.3 and A.4 are common expressions for the isothermal compressibility for different EoS used in this thesis. Using the parameters for b, Θ, δ, and ε from Table A.1, individual expressions for the compressibility are obtained.

For the ideal gas law ($b_{\mathrm{igl}} = 0$, $\Theta = 0$), the isothermal compressibility reads

$$\chi_{T,\mathrm{igl}} = -\frac{\rho}{\bar{M}} \left[-\frac{\bar{R}T\rho^2}{\bar{M}^2} \right]^{-1} = \frac{1}{p} . \tag{A.5}$$

Obviously, due to the limitation of the ideal gas law to describe only the vapour phase, $\chi_{T,\mathrm{igl}}$ is valid solely for the vapour phase.

Using Equation A.4 for the Peng-Robinson equation ($\Theta = a_{\mathrm{PR}}$, $\delta = 2b_{\mathrm{PR}}$, $\varepsilon = -b_{\mathrm{PR}}^2$), the isothermal compressibility reads

$$\chi_{T,\mathrm{PR}} = -\frac{\rho}{\bar{M}} \left[-\frac{\bar{R}T\rho^2}{\left(\bar{M} - b_{\mathrm{PR}}\rho\right)^2} + \frac{2a_{\mathrm{PR}}\rho^3\left(\bar{M} + b_{\mathrm{PR}}\rho\right)}{\left(\bar{M}^2 + 2b_{\mathrm{PR}}\bar{M}\rho - b_{\mathrm{PR}}^2\rho^2\right)^2} \right]^{-1} . \tag{A.6}$$

$\chi_{T,\mathrm{PR}}$ can be used for both phases, liquid and vapour, individually. Equation A.6 is used for the linear density approximation in the numerical CFD simulations, introduced in Section 2.3.1. The link between the mathematical and the thermodynamic compressibility is given by

$$\psi = \left[\rho\chi_T\right]_{p=p_0} . \tag{2.29}$$

Via Maxwell relations, the thermodynamic compressibilities and heat capacities are related:

$$\frac{\chi_T}{\chi_S} = \kappa = \frac{c_p}{c_v} , \tag{A.7}$$

κ is the isentropic expansion factor, c_p and c_v are specific heat capacities for constant pressure and volume, respectively.

The definition of the speed of sound a reads

$$a = \sqrt{\frac{1}{\rho\chi_S}} \tag{A.8}$$

$$= \sqrt{\frac{1}{\psi_S}} = \sqrt{\frac{\kappa}{\psi_T}} . \tag{A.9}$$

The speed of sound is a function of temperature and pressure. Generally, and in particular for flourinated hydorcarbons, such as FC-72 [42, 67], the dependencies read

$$\text{liquid:} \quad \left.\frac{\partial a}{\partial T}\right|_p < 0 \quad \text{and} \quad \left.\frac{\partial a}{\partial p}\right|_T < 0 \tag{A.10}$$

$$\text{vapour:} \quad \left.\frac{\partial a}{\partial T}\right|_p > 0 \quad \text{and} \quad \left.\frac{\partial a}{\partial p}\right|_T < 0\,. \tag{A.11}$$

Figure A.2(a) shows the speed of sound versus pressure for liquid and vapour in saturated conditions. In principal, moving along the saturation curve towards the critical point but not reaching it, both, the temperature and pressure increase. According to the relations for saturated liquid mentioned in Equation A.10, the speed of sound decreases for increasing pressure monotonously. This can be clearly seen in Figure A.2(a), as well. However, the saturated vapour shows a different, non-monotonic behaviour. Coming from low pressure, the speed of sound shows a maximum with increasing pressure and drops towards zero speed of sound at the critical point. The maximum is not visibly pronounced in Figure A.2(a) due to the scale. However, this behaviour of the speed of sound in saturated vapour is general and not restricted to the saturated vapour of perfluorocarbons. In Figure A.2(b), the mathematical compressibility of the saturated liquid and vapour is shown as a function of pressure. The compressibility scales with the speed of sound $\psi \propto a^{-2}$.

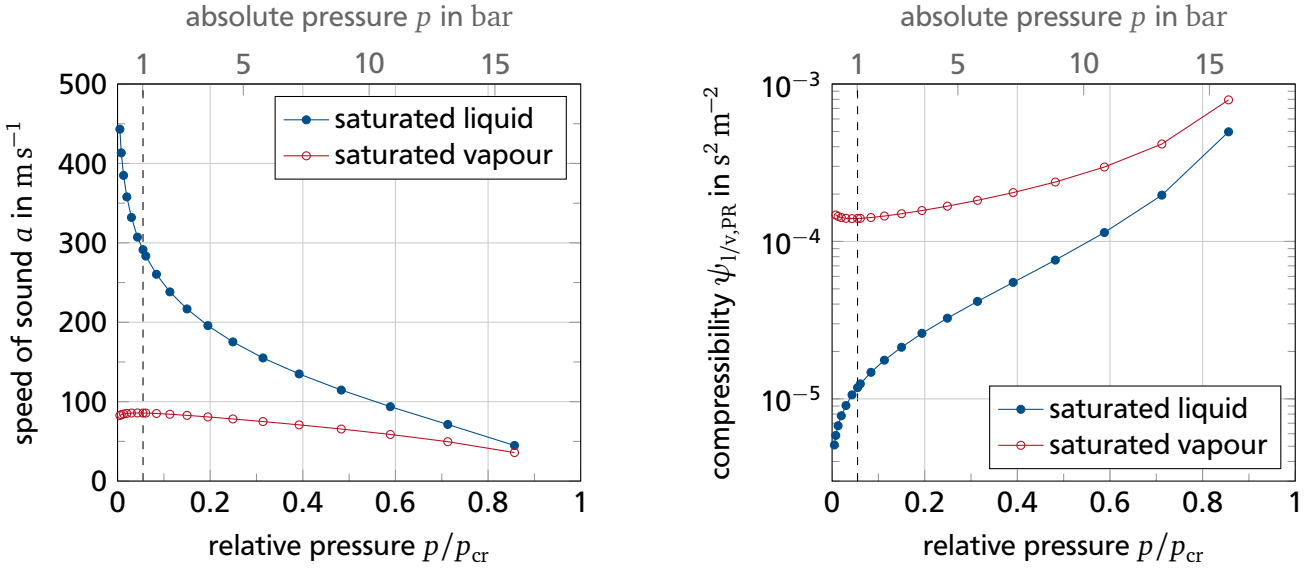

(a) Speed of sound.

(b) Mathematical compressibility.

Figure A.2.: Speed of sound and mathematical compressibility calculated from Peng-Robinson EoS for FC-72 evaluated at $p = p_{sat}(T)$. The dashed vertical line indicates the $p = 1.013\,\text{bar}$ isobar.

For liquid FC-72, computed data from the Peng-Robinson EoS used in this work and experimental data from literature for density, speed of sound and isentropic compressibliity are summarised in Table A.3. Hallewell et al. [42] conducted experiments to compare to the results obtained from the PC-SAFT equation of state. Marsh et al. [67] measured the speed of sound and density for pure liquid of seven different liquid fluorocarbons, including FC-72, at constant atmospheric pressure and a temperature range between 20 °C and 45 °C. Therefore, values for 56.6 °C are extrapolated from the linear function given in [42] and [67]. The compressibility in Table A.3 is calculated using Equation A.8 and setting the isentropic equal to the isothermal compressibility, which is a common assumption made for the compressibility of liquids.

Table A.3.: Density, speed of sound, and isentropic compressibility for pure liquid FC-72 evaluated for $p = 1.013\,\mathrm{bar}$.

	This work/P-Robinson			Hallewell et al. [42]			Marsh et al. [67]		
T_C °C	ρ_l kg m^{-3}	a_l s m^{-1}	χ_l 10^{-9} Pa^{-1}	ρ_l kg m^{-3}	a_l s m^{-1}	χ_l 10^{-9} Pa^{-1}	ρ_l kg m^{-3}	a_l s m^{-1}	χ_l 10^{-9} Pa^{-1}
25	1732.9	371.96	4.17	1682.8	510.70	2.28	1681.8	509.95	2.29
56.6	1619.7	291.40	7.27	1589.4*	413.73*	3.68	1584.3*	422.17*	3.54

* Extrapolated data points.

Obviously, both experimental data sets are similar, whereas the computed data from the Peng-Robinson EoS is quite off, especially for the speed of sound and compressibility. In other words, at least for FC-72, the Peng-Robinson is accurate enough for the determination of the densities but at the same time too inaccurate for the determination of the derivatives of the density that are used for the computation of the speed of sound and compressibility. Besides the inaccuracy of the Peng-Robinson EoS, it should be noted that the experimental apparatus used in [42] is calibrated with Xenon but not with a perfluorocarbon. Both studies focused on sub-cooled liquids at atmospheric pressure so that the saturation condition was out of the measurement range. Therefore, a direct comparison is difficult.

To summarise, the Peng-Robinson EoS determines the densities for the liquid and vapour phase reasonably well. However, it shows limited accuracy for the compressibility. The computed compressibilities are in the same order of magnitude as comparable literature data for $p = 1.013\,\mathrm{bar}$. Consequently, the Peng-Robinson EoS is believed to be the best approximation available for density and compressibility for both phases, saturated liquid and vapour, over a wide pressure and temperature range for FC-72.

To achieve a better approximation of the compressibility for future studies, it might be useful to determine the compressibility or the speed of sound experimentally for the fluid along the saturation curve for each phase, liquid and vapour, individually. Based on the experimentally obtained speed of sound, the compressibilities could be computed using Equation A.9.

Table A.4 lists the mathematical ψ and isothermal χ_T compressibility obtained from the Peng-Robinson EoS for different pressures. The compressibility obtained from the ideal gas law is shown for comparison but is not used for the numerical studies in the thesis.

Table A.4.: Compressibility as function of pressure computed from Peng-Robinson (PR) EoS and ideal gas law (igl) for FC-72. Mathematical compressibility ψ and isothermal compressibility χ_T evaluated at $p = p_{\mathrm{sat}}(T)$ individually for liquid (l) and vapour (v) phase.

p in bar	p/p_{cr} –	$\psi_{\mathrm{l,PR}}$ in $\mathrm{s^2\,m^{-2}}$	$\psi_{\mathrm{v,PR}}$ in $\mathrm{s^2\,m^{-2}}$	$\chi_{T,\mathrm{l,PR}}$ in $\mathrm{Pa^{-1}}$	$\chi_{T,\mathrm{v,PR}}$ in $\mathrm{Pa^{-1}}$	$\chi_{T,\mathrm{v,igl}}$ in $\mathrm{Pa^{-1}}$
0.086	0.005	$5.091 \cdot 10^{-6}$	$1.514 \cdot 10^{-4}$	$2.831 \cdot 10^{-9}$	$1.171 \cdot 10^{-4}$	$1.161 \cdot 10^{-4}$
0.146	0.008	$5.853 \cdot 10^{-6}$	$1.474 \cdot 10^{-4}$	$3.301 \cdot 10^{-9}$	$6.945 \cdot 10^{-5}$	$6.854 \cdot 10^{-5}$
0.235	0.013	$6.748 \cdot 10^{-6}$	$1.442 \cdot 10^{-4}$	$3.864 \cdot 10^{-9}$	$4.338 \cdot 10^{-5}$	$4.254 \cdot 10^{-5}$
0.366	0.020	$7.808 \cdot 10^{-6}$	$1.418 \cdot 10^{-4}$	$4.545 \cdot 10^{-9}$	$2.812 \cdot 10^{-5}$	$2.734 \cdot 10^{-5}$
0.547	0.030	$9.072 \cdot 10^{-6}$	$1.403 \cdot 10^{-4}$	$5.377 \cdot 10^{-9}$	$1.901 \cdot 10^{-5}$	$1.828 \cdot 10^{-5}$
0.795	0.043	$1.060 \cdot 10^{-5}$	$1.397 \cdot 10^{-4}$	$6.406 \cdot 10^{-9}$	$1.326 \cdot 10^{-5}$	$1.257 \cdot 10^{-5}$
1.013	0.055	$1.178 \cdot 10^{-5}$	$1.401 \cdot 10^{-4}$	$7.221 \cdot 10^{-9}$	$1.054 \cdot 10^{-5}$	$9.869 \cdot 10^{-6}$
1.124	0.061	$1.245 \cdot 10^{-5}$	$1.402 \cdot 10^{-4}$	$7.693 \cdot 10^{-9}$	$9.555 \cdot 10^{-6}$	$8.899 \cdot 10^{-6}$
1.549	0.084	$1.474 \cdot 10^{-5}$	$1.419 \cdot 10^{-4}$	$9.330 \cdot 10^{-9}$	$7.085 \cdot 10^{-6}$	$6.455 \cdot 10^{-6}$
2.089	0.113	$1.761 \cdot 10^{-5}$	$1.450 \cdot 10^{-4}$	$1.145 \cdot 10^{-8}$	$5.399 \cdot 10^{-6}$	$4.786 \cdot 10^{-6}$
2.762	0.150	$2.128 \cdot 10^{-5}$	$1.500 \cdot 10^{-4}$	$1.426 \cdot 10^{-8}$	$4.223 \cdot 10^{-6}$	$3.620 \cdot 10^{-6}$
3.588	0.194	$2.608 \cdot 10^{-5}$	$1.572 \cdot 10^{-4}$	$1.807 \cdot 10^{-8}$	$3.388 \cdot 10^{-6}$	$2.787 \cdot 10^{-6}$
4.589	0.249	$3.255 \cdot 10^{-5}$	$1.676 \cdot 10^{-4}$	$2.344 \cdot 10^{-8}$	$2.789 \cdot 10^{-6}$	$2.179 \cdot 10^{-6}$
5.789	0.314	$4.160 \cdot 10^{-5}$	$1.825 \cdot 10^{-4}$	$3.133 \cdot 10^{-8}$	$2.359 \cdot 10^{-6}$	$1.728 \cdot 10^{-6}$
7.211	0.391	$5.494 \cdot 10^{-5}$	$2.044 \cdot 10^{-4}$	$4.363 \cdot 10^{-8}$	$2.059 \cdot 10^{-6}$	$1.387 \cdot 10^{-6}$
8.887	0.482	$7.612 \cdot 10^{-5}$	$2.385 \cdot 10^{-4}$	$6.444 \cdot 10^{-8}$	$1.868 \cdot 10^{-6}$	$1.125 \cdot 10^{-6}$
10.852	0.588	$1.139 \cdot 10^{-4}$	$2.971 \cdot 10^{-4}$	$1.045 \cdot 10^{-7}$	$1.794 \cdot 10^{-6}$	$9.215 \cdot 10^{-7}$
13.132	0.712	$1.969 \cdot 10^{-4}$	$4.159 \cdot 10^{-4}$	$2.011 \cdot 10^{-7}$	$1.903 \cdot 10^{-6}$	$7.615 \cdot 10^{-7}$
15.786	0.856	$4.972 \cdot 10^{-4}$	$7.934 \cdot 10^{-4}$	$5.990 \cdot 10^{-7}$	$2.616 \cdot 10^{-6}$	$6.335 \cdot 10^{-7}$

APPENDIX B

Augmented transport equation for the VoF field

In the present model, energy, mass, and volume source terms in the governing equations are necessary to account for evaporation and condensation. Additional volume source terms arise from the compressibility of the fluid. The source terms enforce the divergence of the velocity to be non-zero. The original transport equation for the VoF field proposed by Hirt and Nichols [49] needs to be augmented by volume sources terms and the non-divergence free velocity field.

The evolution of the VoF field, assuming a divergence-free velocity field and absence of phase change, is originally [49] given by

$$\frac{\partial \alpha}{\partial t} + \mathbf{u} \cdot \nabla \alpha = 0 \,. \tag{B.1}$$

The transport equation of the volume fraction for the individual phases 1 and 2, including the source terms caused by compressibility and phase change on the right-hand side, reads

$$\frac{\partial \alpha_1}{\partial t} + \nabla \cdot (\alpha_1 \mathbf{u}) = -\frac{\alpha_1}{\rho_1} \frac{\mathrm{D}\rho_1}{\mathrm{D}t} + \alpha_1 \dot{\Sigma}_\mathrm{V} \tag{B.2}$$

$$\frac{\partial \alpha_2}{\partial t} + \nabla \cdot (\alpha_2 \mathbf{u}) = -\frac{\alpha_2}{\rho_2} \frac{\mathrm{D}\rho_2}{\mathrm{D}t} + \alpha_2 \dot{\Sigma}_\mathrm{V} \tag{B.3}$$

with $\mathrm{D}\rho_\mathrm{i}/\mathrm{D}t$ being the material derivative of the density of the individual phase i.The expression $\alpha_\mathrm{i}\dot{\Sigma}_\mathrm{V}$ accounts for the volume source terms of the individual phases during phase change. Combining the above equations and using $1 = \alpha_1 + \alpha_2$ results in the expression for the divergence of the velocity

$$\nabla \cdot \mathbf{u} = -\frac{\alpha_1}{\rho_1} \frac{\mathrm{D}\rho_1}{\mathrm{D}t} - \frac{\alpha_2}{\rho_2} \frac{\mathrm{D}\rho_2}{\mathrm{D}t} + \dot{\Sigma}_\mathrm{V} \,, \tag{B.4}$$

$$\nabla \cdot \mathbf{u} = \dot{\Sigma}_\chi + \dot{\Sigma}_\mathrm{V} \,. \tag{B.5}$$

Substracting $\alpha_1 (\nabla \cdot \mathbf{u})$ on both sides of Equation B.2 and substituting $\nabla \cdot \mathbf{u}$ with the Equation B.4 on the right-hand side results, after re-arranging, in the transport equation for compressible fluid flow

$$\frac{\partial \alpha_1}{\partial t} + \nabla \cdot (\alpha_1 \mathbf{u}) - \alpha_1 (\nabla \cdot \mathbf{u}) = -\alpha_1 \alpha_2 \left[\frac{1}{\rho_1} \frac{\mathrm{D}\rho_1}{\mathrm{D}t} - \frac{1}{\rho_2} \frac{\mathrm{D}\rho_2}{\mathrm{D}t} \right] . \tag{B.6}$$

The source term caused by evaporation, $\dot{\Sigma}_\mathrm{V}$, occurs only in $\alpha_1 (\nabla \cdot \mathbf{u})$ on the left-hand side of Equation B.6. The Equations B.4 and B.6 include both, source terms due to evaporation and due to compress-

ibility. Neglecting either one or the other of the source terms in the Equations B.4 and B.6 results in the transport equations which were used in other VoF based models in former studies and in literature. The consistent reduction of the Equations B.4 and B.6 is presented in the following. Two case distinctions can be made:

- **Solely compressibility:** no source terms caused by phase change are present in the divergence of the velocity and the VoF transport equation. The divergence of the velocity, Equation B.4, reduces to

$$\nabla \cdot \mathbf{u} = -\frac{\alpha_1}{\rho_1}\frac{\mathrm{D}\rho_1}{\mathrm{D}t} - \frac{\alpha_2}{\rho_2}\frac{\mathrm{D}\rho_2}{\mathrm{D}t}\,. \tag{B.7}$$

  The VoF transport equation reads

$$\frac{\partial \alpha_1}{\partial t} + \nabla \cdot (\alpha_1 \mathbf{u}) - \alpha_1 \nabla \cdot \mathbf{u} = -\alpha_1 \alpha_2 \left[\frac{1}{\rho_1}\frac{\mathrm{D}\rho_1}{\mathrm{D}t} - \frac{1}{\rho_2}\frac{\mathrm{D}\rho_2}{\mathrm{D}t}\right]. \tag{B.8}$$

  Note that the Equations B.6 and B.8 are mathematically identical. However, the divergence of the velocity field differs. Miller et al. [68] and Koch et al. [53] used a pressure-based method for their compressible fluid flow simulations without phase change. In both publications, $\nabla \cdot \mathbf{u}$ and the transport equation for the VoF field are mainly a function of pressure instead of density. Substituting the material derivative of the density with the material derivative of the pressure using the mathematical compressibility $\psi = \partial\rho/\partial p$,

$$\frac{\mathrm{D}\rho_1}{\mathrm{D}t} = \psi_1 \frac{\mathrm{D}p}{\mathrm{D}t} \tag{B.9}$$

$$\frac{\mathrm{D}\rho_2}{\mathrm{D}t} = \psi_2 \frac{\mathrm{D}p}{\mathrm{D}t} \tag{B.10}$$

  leads to an alternative but consistent expression for the Equations B.7 and B.8. As a result, the divergence of the velocity as function of pressure reads

$$\nabla \cdot \mathbf{u} = \left[-\frac{\alpha_1 \psi_1}{\rho_1} - \frac{\alpha_2 \psi_2}{\rho_2}\right]\frac{\mathrm{D}p}{\mathrm{D}t}\,. \tag{B.11}$$

  Combining Equations B.8–B.11 results in the alternative expression for the transport equation for the VoF field

$$\frac{\partial \alpha_1}{\partial t} + \nabla \cdot (\alpha_1 \mathbf{u}) - \alpha_1 \nabla \cdot \mathbf{u} = \alpha_1 \alpha_2 \left[\frac{\psi_1 \rho_2 - \psi_2 \rho_1}{\alpha_1 \psi_1 \rho_2 + \alpha_2 \psi_2 \rho_1}\right](\nabla \cdot \mathbf{u})\,, \tag{B.12}$$

  which is sometimes used for tracking the individual phases in pressure based methods [53, 68].

- **Solely phase change:** no source terms caused by compressibility are present in the divergence of the velocity and the transport equation. The divergence of the velocity, Equation B.4, reduces to

$$\nabla \cdot \mathbf{u} = \dot{\Sigma}_\mathrm{V}\,. \tag{B.13}$$

  The VoF transport equation reads

$$\frac{\partial \alpha_1}{\partial t} + \nabla \cdot (\alpha_1 \mathbf{u}) - \alpha_1 \nabla \cdot \mathbf{u} = 0\,. \tag{B.14}$$

Re-arranging the above equation and substituting the divergence of the velocity, the transport equation for the VoF field becomes

$$\frac{\partial \alpha_1}{\partial t} + \nabla \cdot (\alpha_1 \mathbf{u}) = \alpha_1 \dot{\Sigma}_\mathrm{V} \,. \tag{B.15}$$

In combination with an additional artificial compression term, Equations B.13 and B.15 were used by Kunkelmann [55], Batzdorf [2, 46], and by Dietl [26] and their related publications.

In this thesis, Equations B.4 and B.6 are functions of the density and its spatial and temporal derivative. They can be re-formulated as functions of pressure and its derivatives, which is sometimes used for pressure based methods in literature. The divergence of the velocity as function of pressure, accounting for compressibility and phase change, reads

$$\nabla \cdot \mathbf{u} = \left[-\frac{\alpha_1 \psi_1}{\rho_1} - \frac{\alpha_2 \psi_2}{\rho_2} \right] \frac{\mathrm{D}p}{\mathrm{D}t} + \dot{\Sigma}_\mathrm{V} \,. \tag{B.16}$$

The transport equation for the volume fraction field as a function of pressure reads

$$\frac{\partial \alpha_1}{\partial t} + \nabla \cdot (\alpha_1 \mathbf{u}) - \alpha_1 \nabla \cdot \mathbf{u} = \alpha_1 \alpha_2 \left[\frac{\psi_1 \rho_2 - \psi_2 \rho_1}{\alpha_1 \psi_1 \rho_2 + \alpha_2 \psi_2 \rho_1} \right] \left[(\nabla \cdot \mathbf{u}) - \dot{\Sigma}_\mathrm{V} \right] . \tag{B.17}$$

Duret et al. [27] investigated compressible two-phase flow with heat and mass transfer using pressure based methods. In their work, the derived transport equation for the phase fraction and the divergence of the velocity in their work differ from Equations B.16–B.17 only by the determination of the volume source term, denoted as $\dot{\Sigma}_\mathrm{V}$ here.

APPENDIX C

Material properties, parameters, and numerical schemes

Table C.1.: Numerical discretisation schemes used for the CFD simulations in the present thesis.

Operator	**Variable**	**Scheme**
Time derivative, $\mathrm{d}\Phi/\mathrm{d}t$	default	Euler implicit
	α	Crank Nicolson
Gradient, $\nabla\Phi$	default	Gauss linear
Divergence, $\nabla\cdot\Phi$	default	Gauss linear
	$\rho\mathbf{uu}$	Gauss limitedLinearV 1.0
	$\rho\alpha$	Gauss vanLeer
	$c_\alpha\mathbf{u}_\mathrm{r}(1-\alpha)\alpha$	Gauss limitedLinear 1.0
	$\rho c_\mathrm{p}\mathbf{u}T$, $\rho_\mathrm{l}\mathbf{u}$, $\rho_\mathrm{v}\mathbf{u}$	Gauss limitedLinear 1.0
	$\rho\,\nu_\mathrm{eff}(\nabla\mathbf{u})^\mathrm{T}$	Gauss linear
Laplacian, $\nabla\cdot\nabla\Phi$	default	Gauss linear corrected
Surface normal gradient, $\nabla\Phi\mathbf{n}_\mathrm{f}$	default	corrected

Table C.2.: Correlation coefficients for the contact line model evaluated for FC-72 at $p = 1.013\,\mathrm{bar}$ ($p/p_\mathrm{cr} = 0.055$), $5\,\mathrm{K} \leq \Delta T \leq 20\,\mathrm{K}$ and $-0.1\,\mathrm{m\,s^{-1}} \leq u_\mathrm{cl} \leq 2.0\,\mathrm{m\,s^{-1}}$ (Reference case). The parametrised regression procedure is described in [2, p. 56].

i	1	2	3	4	5	6	7	8
$a_{Q,T,i}$	-0.10419	24.559	-277.12	930.062	-1177.06	499.876	–	–
$a_{Q,u,i}$	1.0	-1.9426	7.1454	-22.4347	42.6939	-46.1249	26.057	-5.962
b_Q	-0.30543							
$a_{\theta,T,i}$	-16.5726	4274.4	-63449	242508	-331591	148294	–	–
$a_{\theta,u,i}$	1.0	19.094	-159.56	1016.81	-3999.84	9209.41	-11369	5802
b_θ	-0.925867							
$a_{\delta,T,i}/10^{-8}$	-5.59998	1719.0	-26220	101364	-139409	62563.8	–	–
$a_{\delta,u,i}$	1	4.5892	-6.14979	29.316	-65.4250	79.5793	-46.462	10.31
b_δ	-0.22005							

Table C.3.: Material properties for saturated FC-72 and for CaF_2.

		density ρ kg/m^3	**specific heat capacity** c J/(kg K)	**thermal conductivity** $k/10^{-3}$ W/(m K)	**dynamic viscosity** $\mu/10^{-6}$ N s/m^2	**latent heat of vaporisation** Δh_v J/(kg)	**surface tension** $\sigma/10^{-3}$ N/m
FC-72	liquid	1755.29	1011.01	58.77	949.6	99181.7	13.340
(0.086 bar, 0 °C)	vapour	1.371	795.01	6.03	8.414		
FC-72	liquid	1719.78	1026.45	57.60	800.0	96818.2	12.410
(0.146 bar, 10 °C)	vapour	2.234	812.38	6.49	8.732		
FC-72	liquid	1691.54	1041.89	56.43	686.8	94368.5	11.500
(0.235 bar, 20 °C)	vapour	3.484	829.37	6.98	9.051		
FC-72	liquid	1669.12	1057.34	55.26	601.1	91820.3	10.590
(0.366 bar, 30 °C)	vapour	5.231	846.01	7.48	9.369		
FC-72	liquid	1649.68	1072.78	54.10	535.3	89173.6	9.708
(0.547 bar, 40 °C)	vapour	7.589	862.32	7.99	9.688		
FC-72	liquid	1631.48	1088.22	52.93	483.1	86403.9	8.838
(0.795 bar, 50 °C)	vapour	10.683	878.32	8.53	10.006		
FC-72	liquid	1619.73	1098.41	52.16	453.7	84510.9	8.273
(1.013 bar, 56.6 °C)	vapour	13.396	888.79	8.90	10.215		
FC-72	liquid	1613.67	1103.66	51.76	438.8	83535.7	7.985
(1.124 bar, 60 °C)	vapour	14.793	894.08	9.09	10.323		
FC-72	liquid	1593.25	1119.11	50.59	398.2	80556.6	7.150
(1.549 bar, 70 °C)	vapour	20.238	909.66	9.68	10.640		
FC-72	liquid	1539.16	1149.99	48.26	324.9	74364.7	5.538
(2.762 bar, 90 °C)	vapour	35.976	940.38	10.91	11.270		
FC-72	liquid	1501.10	1165.44	47.09	314.0	71201.0	4.766
(3.588 bar, 100 °C)	vapour	46.996	955.63	11.57	11.584		
FC-72	liquid	1452.99	1180.88	45.92	302.8	67692.7	4.018
(4.589 bar, 110 °C)	vapour	60.625	970.88	12.26	11.896		
FC-72	liquid	1394.01	1196.32	44.75	289.8	64295.1	3.297
(5.789 bar, 120 °C)	vapour	77.496	986.24	12.98	12.207		
FC-72	liquid	1320.90	1211.77	43.58	274.2	60134.4	2.606
(7.211 bar, 130 °C)	vapour	98.550	1001.89	13.74	12.517		
FC-72	liquid	1232.78	1227.21	42.42	255.7	55148.8	1.952
(8.887 bar, 140 °C)	vapour	125.586	1018.21	14.55	12.825		
FC-72	liquid	1127.69	1242.65	41.25	233.7	48969.2	1.339
(10.852 bar, 150 °C)	vapour	162.044	1035.98	15.43	13.131		
FC-72	liquid	1003.25	1258.09	40.08	207.7	41127.7	0.779
(13.132 bar, 160 °C)	vapour	215.217	1057.03	16.43	13.435		
FC-72	liquid	857.72	1273.54	38.91	177.5	30258.0	0.294
(15.786 bar, 170 °C)	vapour	303.138	1086.64	17.68	13.738		
FC-72	liquid	613.50	1286.66	37.92	126.9	0.0	0.000
(18.411 bar, 178 °C)	vapour	612.502	1216.38	21.16	13.994		
CaF_2	solid	3180.0	854.0	$9.71 \cdot 10^3$			

Table C.4.: Constant initial impact parameters (CIIP) study.

p bar	p/p_{cr}	Re	We	Bo	Pr	Ja	D_0 mm	u_0 $m\,s^{-1}$	ΔT_w K	g $m\,s^{-2}$	k_l $mW\,(m\,K)^{-1}$
0.146	0.008	602	10.6	0.35	14.25	0.11	1.0241	0.2735	10	9.74	57.60
0.235	0.013	690	11.3	0.38	12.68	0.11	1.0241	0.2735	10	9.74	56.43
0.366	0.020	778	12.1	0.40	11.50	0.12	1.0241	0.2735	10	9.74	55.26
0.547	0.030	863	13	0.43	10.61	0.12	1.0241	0.2735	10	9.74	54.10
0.795	0.043	946	14.1	0.47	9.93	0.13	1.0241	0.2735	10	9.74	52.93
1.013	0.055	1000	15	0.5	9.55	0.13	1.0241	0.2735	10	9.74	52.16
1.124	0.061	1030	15.5	0.52	9.36	0.13	1.0241	0.2735	10	9.74	51.76
1.549	0.084	1121	17.0	0.57	8.81	0.14	1.0241	0.2735	10	9.74	50.59
2.089	0.113	1215	19	0.63	8.31	0.15	1.0241	0.2735	10	9.74	49.42
2.762	0.150	1327	21.3	0.71	7.74	0.15	1.0241	0.2735	10	9.74	48.26
3.588	0.195	1339	24.1	0.80	7.77	0.16	1.0241	0.2735	10	9.74	47.09
4.589	0.249	1344	27.7	0.92	7.79	0.17	1.0241	0.2735	10	9.74	45.92
5.789	0.314	1347	32.4	1.08	7.75	0.19	1.0241	0.2735	10	9.74	44.75
7.211	0.392	1349	38.8	1.3	7.62	0.20	1.0241	0.2735	10	9.74	43.58
8.887	0.483	1351	48.4	1.61	7.40	0.22	1.0241	0.2735	10	9.74	42.42

Table C.5.: Constant non-dimensional groups (CNDG) study.

p bar	p/p_{cr}	Re	We	Bo	Pr	Ja	D_0 mm	u_0 $m\,s^{-1}$	ΔT_w K	g $m\,s^{-2}$	k_l $mW\,(m\,K)^{-1}$
0.146	0.008	1000	15	0.5	9.55	0.13	1.9991	0.2327	12.3	3.61	85.95
0.235	0.013	1000	15	0.5	9.55	0.13	1.6166	0.2512	11.8	5.20	74.90
0.366	0.020	1000	15	0.5	9.55	0.13	1.3628	0.2643	11.3	6.83	66.52
0.547	0.030	1000	15	0.5	9.55	0.13	1.1928	0.2720	10.8	8.27	60.11
0.795	0.043	1000	15	0.5	9.55	0.13	1.0791	0.2744	10.3	9.30	55.02
1.013	0.055	1000	15	0.5	9.56	0.13	1.0241	0.2735	10	9.74	52.16
1.124	0.061	1000	15	0.5	9.55	0.13	0.9962	0.2730	9.8	9.97	50.69
1.549	0.084	1000	15	0.5	9.55	0.13	0.9279	0.2693	9.4	10.42	46.64
2.089	0.113	1000	15	0.5	9.55	0.13	0.8781	0.2626	8.9	10.47	42.96
2.762	0.150	1000	15	0.5	9.55	0.13	0.8256	0.2557	8.4	10.56	39.11
3.588	0.195	1000	15	0.5	9.55	0.13	0.9188	0.2277	7.9	7.52	38.30
4.589	0.249	1000	15	0.5	9.55	0.13	1.0470	0.1990	7.5	5.05	37.43
5.789	0.314	1000	15	0.5	9.55	0.13	1.2182	0.1707	7	3.19	36.29
7.211	0.392	1000	15	0.5	9.55	0.13	1.4561	0.1426	6.4	1.86	34.78
8.887	0.483	1000	15	0.5	9.55	0.13	1.8114	0.1145	5.8	0.97	32.84

APPENDIX D

Supplemental results

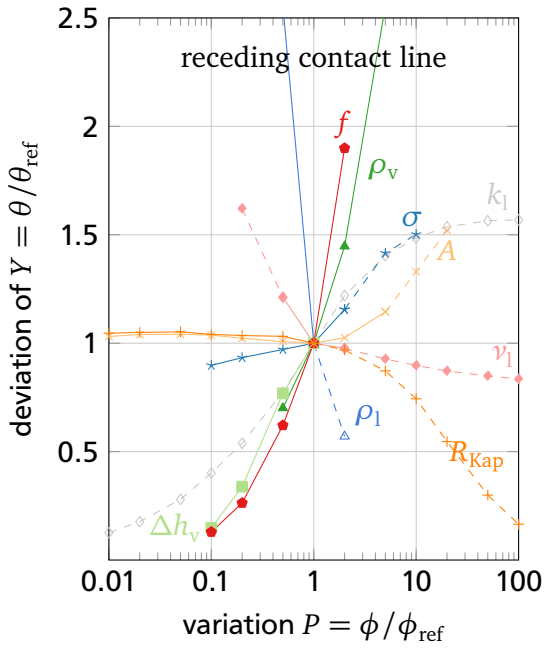

(a) Apparent contact angle θ.

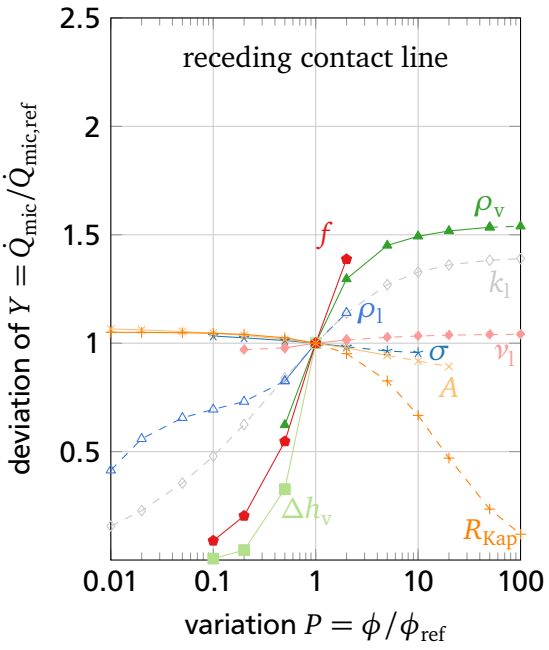

(b) Integrated heat flux $\dot{Q}_{\mathrm{mic}}$.

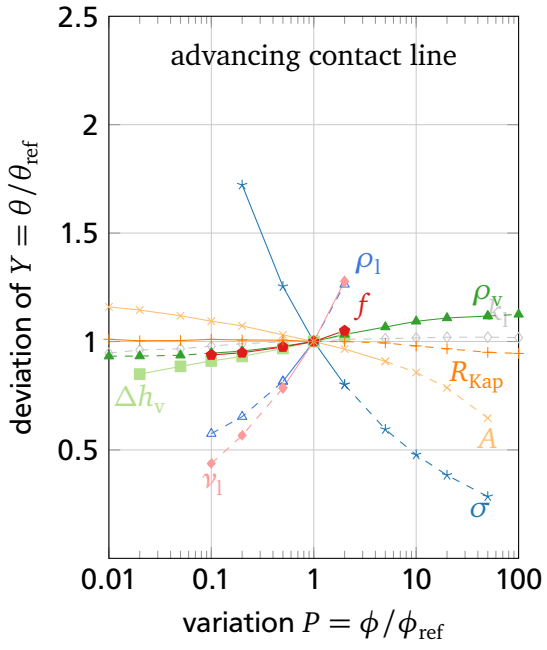

(c) Apparent contact angle θ.

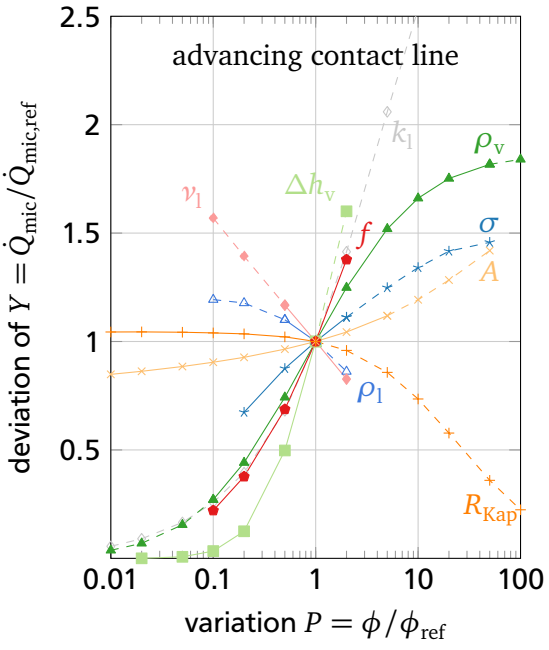

(d) Integrated heat flux $\dot{Q}_{\mathrm{mic}}$.

Figure D.1.: Influence of material properties on the apparent contact angle θ (left) and on the integrated heat flux $\dot{Q}_{\mathrm{mic}}$ across the micro region (right). The reference case is $p = 1.013\,\mathrm{bar}$, $\Delta T = 5\,\mathrm{K}$, and different contact line velocities. The receding contact line motion (top) at a contact line velocity of $u_{\mathrm{cl}} = -0.2\,\mathrm{m\,s^{-1}}$ results in $\theta_{\mathrm{ref}} = 5.9\,\mathrm{deg}$ and $\dot{Q}_{\mathrm{mic,ref}} = 1.3\,\mathrm{W\,m^{-1}}$. The advancing contact line motion (bottom) at a contact line velocity of $u_{\mathrm{cl}} = 0.3\,\mathrm{m\,s^{-1}}$ results in $\theta_{\mathrm{ref}} = 48.1\,\mathrm{deg}$ and $\dot{Q}_{\mathrm{mic,ref}} = 0.7\,\mathrm{W\,m^{-1}}$.

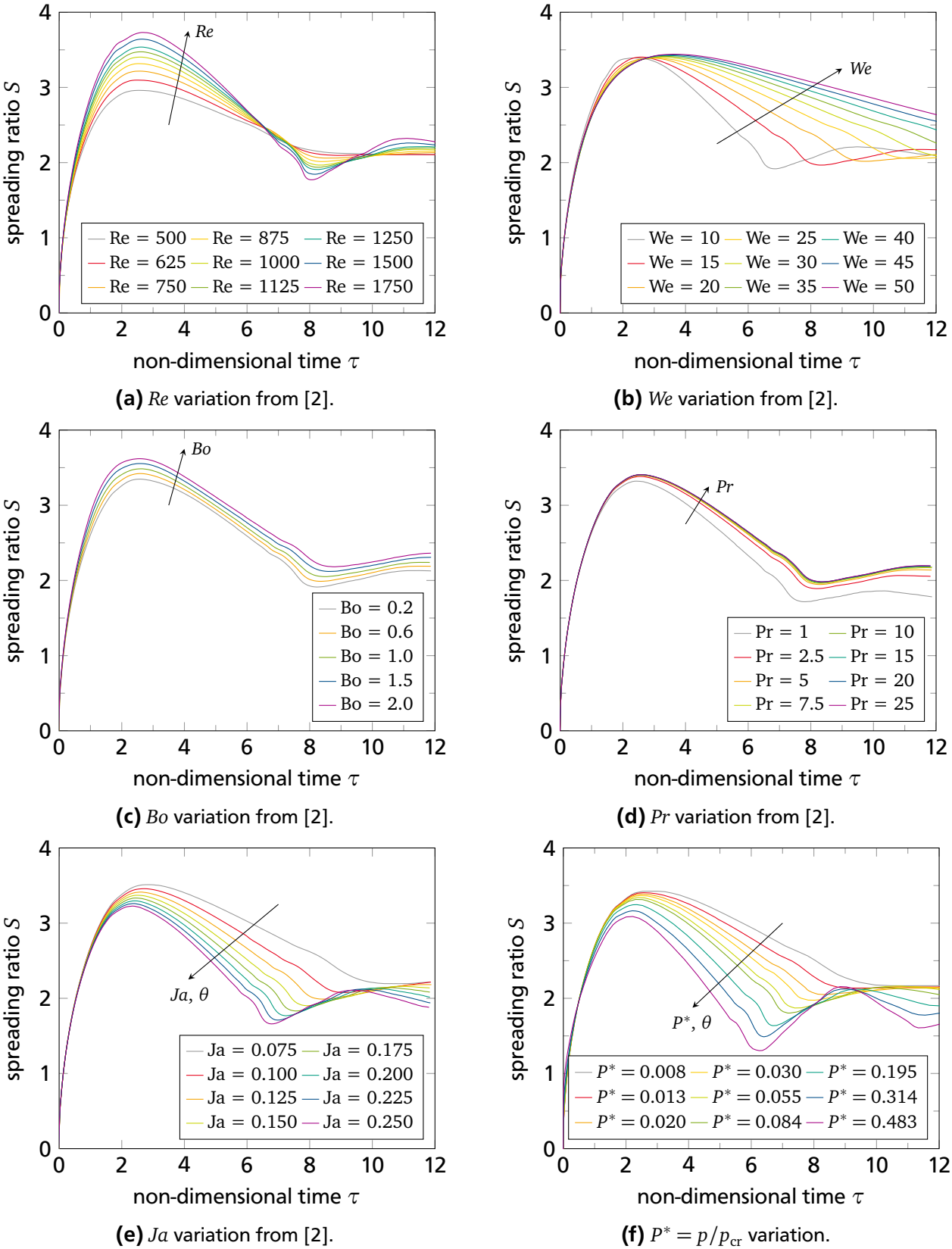

(a) *Re* variation from [2].

(b) *We* variation from [2].

(c) *Bo* variation from [2].

(d) *Pr* variation from [2].

(e) *Ja* variation from [2].

(f) $P^* = p/p_{cr}$ variation.

Figure D.2.: Evolution of spreading ratio S. Results of a)–e) taken from [2], results of f) obtained in this thesis. If not denoted otherwise, the constant non-dimensional groups are $Re = 1000$, $We = 15$, $Bo = 0.5$, $Pr = 9.55$, $Ja = 0.13$, $P^* = 0.055$.

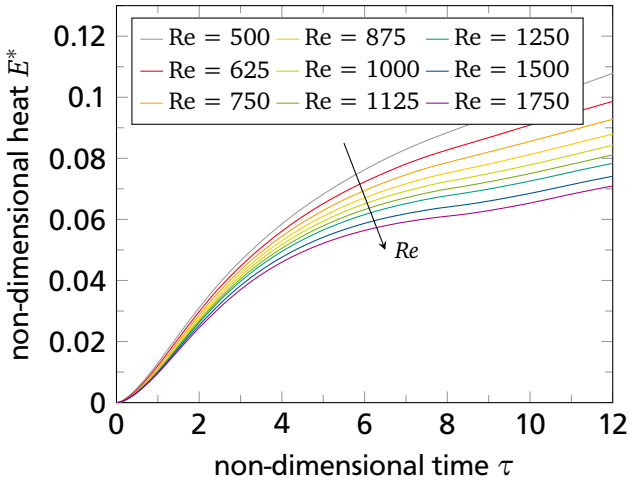

(a) *Re* variation from [2].

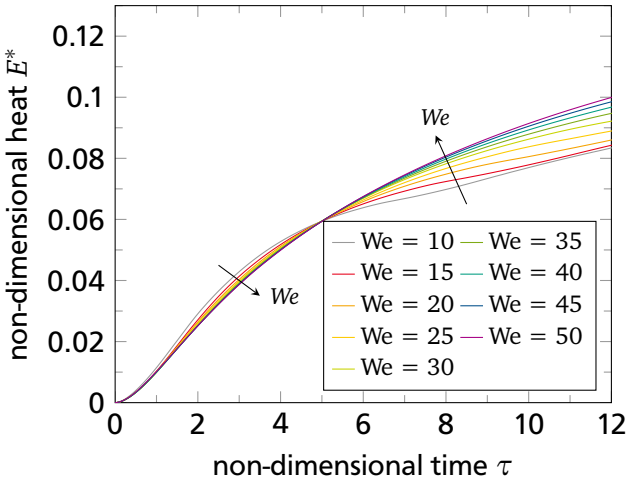

(b) *We* variation from [2].

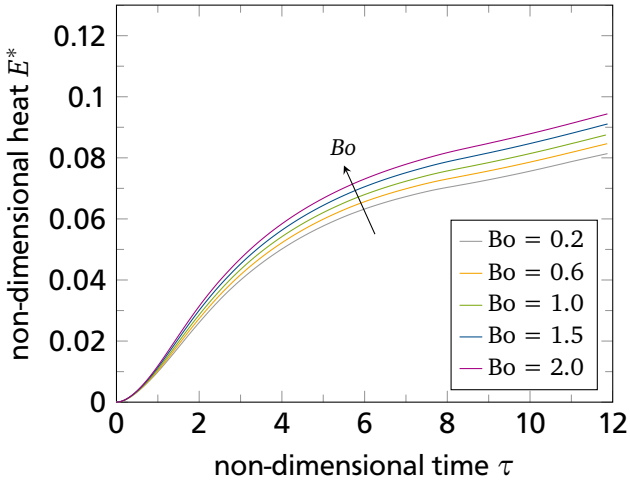

(c) *Bo* variation from [2].

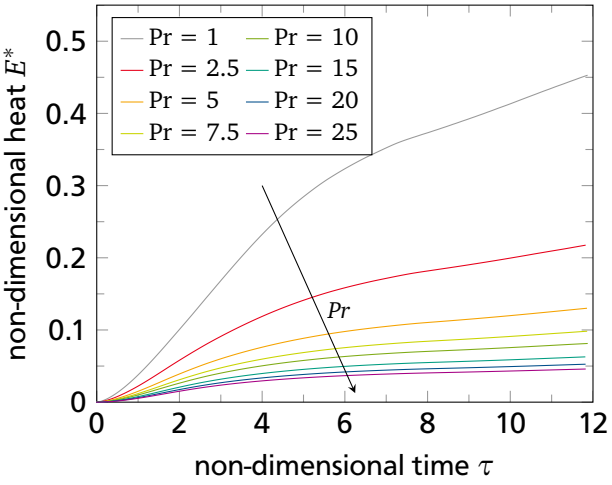

(d) *Pr* variation from [2].

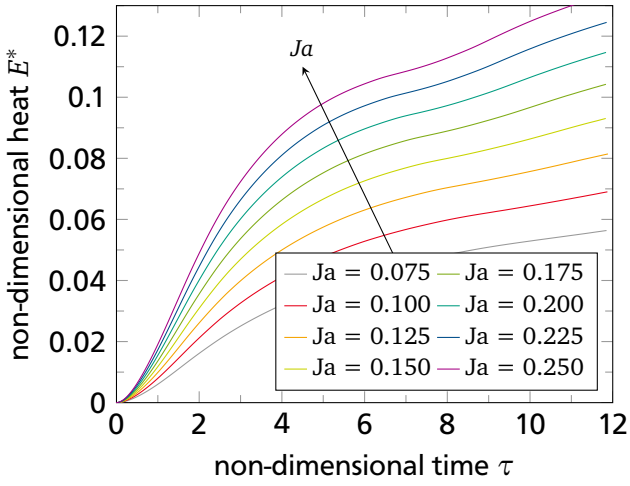

(e) *Ja* variation from [2].

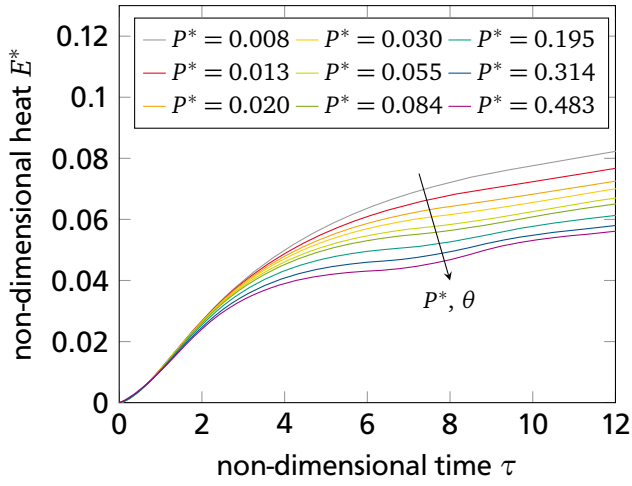

(f) $P^* = p/p_{cr}$ variation.

Figure D.3.: Evolution of non-dimensional heat E^*. Results of a)–e) taken from [2], results of f) obtained in this thesis. If not denoted otherwise, the constant non-dimensional groups are $Re = 1000$, $We = 15$, $Bo = 0.5$, $Pr = 9.55$, $Ja = 0.13$, $P^* = 0.055$.

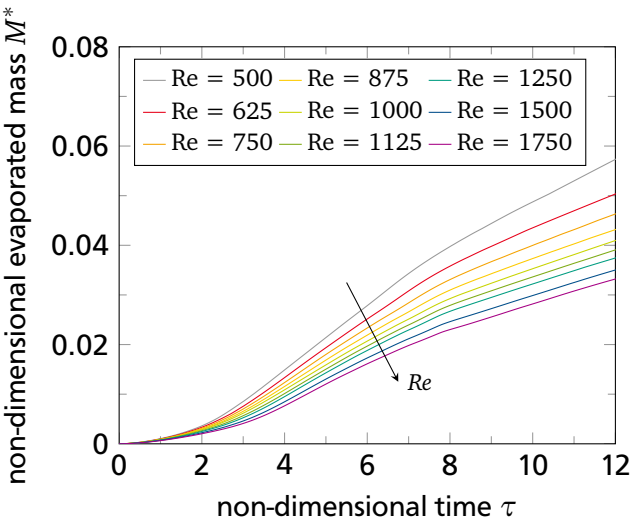

(a) *Re* variation from [2].

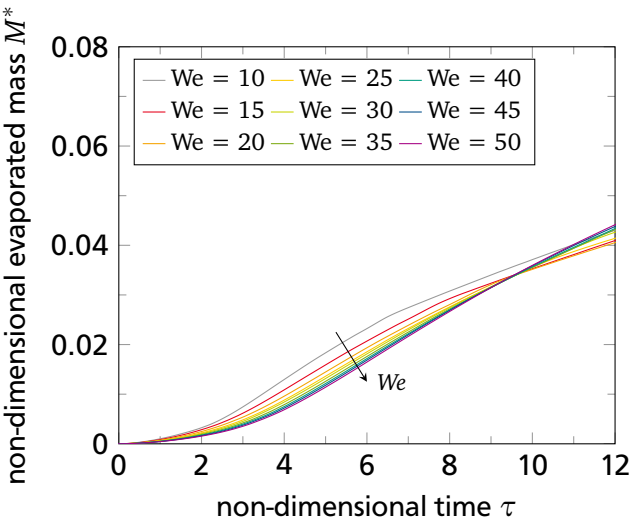

(b) *We* variation from [2].

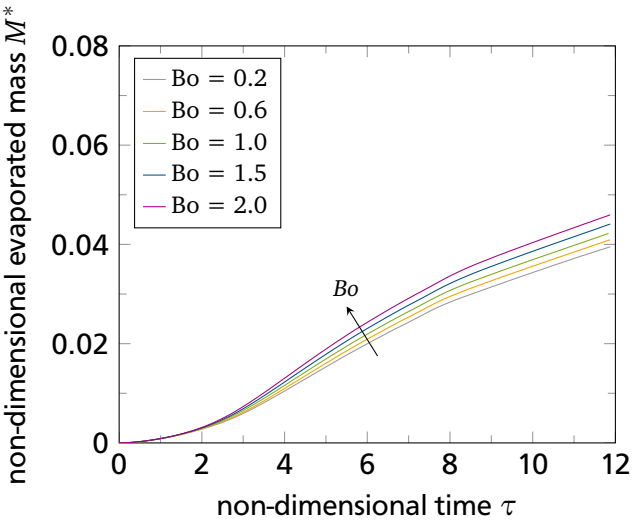

(c) *Bo* variation from [2].

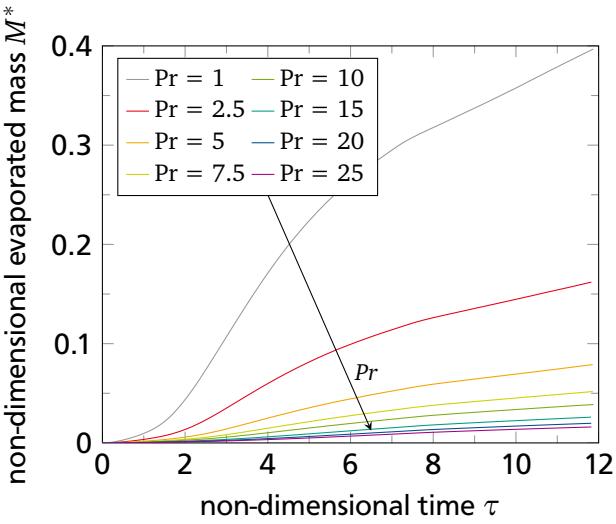

(d) *Pr* variation from [2].

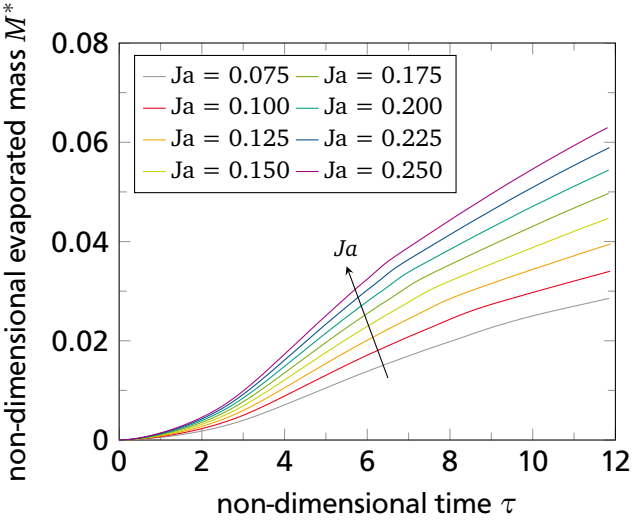

(e) *Ja* variation from [2].

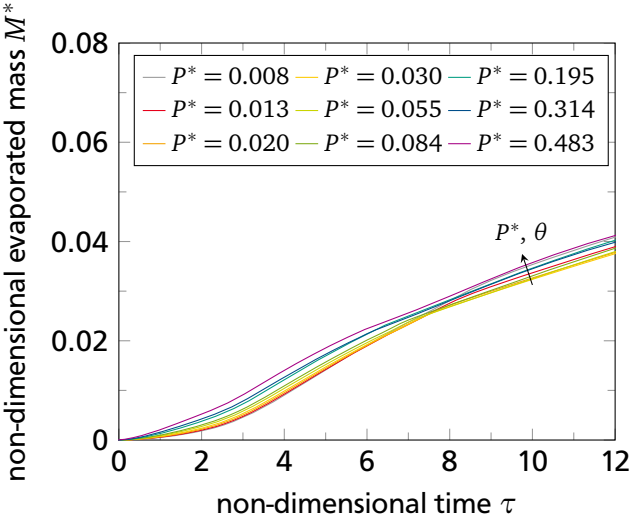

(f) $P^* = p/p_{cr}$ variation.

Figure D.4.: Evolution of non-dimensional evaporated mass M^*. Results of a)–e) taken from [2], results of f) obtained in this thesis. If not denoted otherwise, the constant non-dimensional groups are $Re = 1000$, $We = 15$, $Bo = 0.5$, $Pr = 9.55$, $Ja = 0.13$, $P^* = 0.055$.